HIGH-GRADIENT NANOMAGNET-ON-CANTILEVER FABRICATION FOR SCANNED PROBE DETECTION OF MAGNETIC RESONANCE

A Dissertation

Presented to the Faculty of the Graduate School

of Cornell University

in Partial Fulfillment of the Requirements for the Degree of

Doctor of Philosophy

by

Jonilyn Greta Longenecker

January 2013

HIGH-GRADIENT NANOMAGNET-ON-CANTILEVER FABRICATION FOR SCANNED PROBE DETECTION OF MAGNETIC RESONANCE

Jonilyn Greta Longenecker, Ph.D.

Cornell University 2013

Magnetic resonance force microscopy (MRFM) is a non-invasive, three-dimensional imaging technique that employs attonewton-sensitivity cantilevers to mechanically detect the interaction between the field gradient of a magnetic particle and magnetically-active sample spins. Achieving high sensitivity demands the use of a high field gradient. In order to study a wide range of samples, it is equally desirable to locate the magnetic tip on the cantilever.

The work in this thesis centers on the development of nanomagnets on cantilevers that produce sufficiently large field gradients for nanometer-scale nuclear spin MRFM imaging and single electron spin detection. A new fabrication protocol is introduced to prepare nickel and cobalt nanomagnets on cantilevers. Custom attonewton-sensitivity cantilevers were batch fabricated. Nanomagnets were prepared separately on micrometer-scale silicon chips using electron beam lithography and electron beam deposition. Each magnet-tipped silicon chip was serially attached to a cantilever using focused ion beam manipulation. Frequency-shift cantilever magnetometry and superconducting quantum interference device magnetometry were used to assess the nanomagnet magnetization. X-ray photoelectron spectroscopy was used to determine the extent of oxidation damage.

A cobalt nanomagnet-tipped chip attached to an attonewton-sensitivity cantilever was used to detect statistical fluctuations in the proton magnetization of a polystyrene film. MRFM signal was studied versus rf irradiation frequency and tip-sample separation. The tip-field gradient $\partial B_z^{\mathrm{tip}}/\partial z$ of the nanomagnet was estimated to be between 4.4 and 5.4 $\mathrm{MT\,m^{-1}}$, which is comparable to the gradient used in recent 4 nm resolution ^{1}H imaging experiments

and nearly an order of magnitude larger than the gradients achieved in prior magnet-on-cantilever MRFM experiments. These magnet-tipped cantilevers are projected to achieve a proton imaging resolution of 5 to 10 nm.

The key design considerations and development of a new magnetic resonance force microscope are also discussed in this thesis. The microscope will use the newly-developed nanomagnet-tipped cantilevers to conduct high-resolution, three-dimensional MRFM imaging experiments at cryogenic temperatures, in high vacuum, and at magnetic fields up to 9 T.

Overall, the work in this thesis has significantly advanced the capabilities of MRFM and has poised the field to begin conducting high-resolution imaging experiments on a broad range of previously-inaccessible samples.

BIOGRAPHICAL SKETCH

Jonilyn Longenecker grew up in Lancaster, Pennsylvania. At an early age, she developed lasting interests in music, mathematics, and science. She gained her first appreciation for conducting scientific research through participation in high school science fair projects on designs for improved passive solar power Trombe walls.

Jonilyn attended Juniata College for her undergraduate education, where she earned a major in chemistry and a minor in mathematics. While taking chemistry courses at Juniata, she became fascinated by chemical characterization and explored a variety of physical chemistry independent research projects. She conducted simulations-based research on the binding affinity of novel drug targets for two summers. After her junior year, she participated in a Research Experience for Undergraduates (REU) program at the University of Hawaii at Manoa and completed an experimental astrochemistry project on the reaction dynamics after irradiation of diboranyl ices. Through this summer REU project and her senior thesis on diffusion NMR, Jonilyn learned that her passion lies in experimental research.

In graduate school at Cornell University, Jonilyn sought to combine her interest in experimental chemistry with interdisciplinary applications. By joining Professor John Marohn's research project on magnetic resonance force microscopy, she gained extensive experience in the nanofabrication of high-compliance force sensors and co-developed a third-generation magnetic resonance force microscope. During her graduate career Jonilyn presented at more than 15 conferences, including invited talks at a NanoMRI Conference in Ascona, Switzerland and at a Gordon Research Conference on Nanostructure Fabrication. She was selected to participate in the 2010 National Nanotechnology Infrastructure Network International Winter School for Graduate Students at the Indian Institute for Science in Bangalore, India. In 2011 she also received a Best Paper Award in the MEMS and NEMS division of the American Vacuum Society International Symposium and the Nellie Yeh-Poh Lin Whetten Memorial Award from the Cornell Center for NanoScale Science and Technology.

To my parents, Dave and Karen Longenecker,

for inspiring, guiding, and encouraging me to always pursue my dreams.

ACKNOWLEDGEMENTS

Thanks first goes to my advisor, John Marohn. Thank you for encouraging me, pushing me, and giving me room to grow into an independent researcher. Your enthusiasm and creativity have been a perpetual source of inspiration. By fostering a group culture that values collaboration, positive outlooks, and an awareness of the scientific community around us, you have given me a home within Cornell in which I could thrive and contribute. Thanks and gratitude also goes to my committee members, David Muller, Jiwoong Park, and Poul Petersen, for their guidance during my graduate career.

I have had a wonderful group of coworkers during my time at Cornell. Early on Steve Hickman taught me the ropes of Cornell's cleanroom and the fabrication techniques for integrated magnet-tipped cantilevers. Eric Moore mentored me on conducting magnetic resonance force microscopy (MRFM) experiments and collaborated on frequency-shift cantilever magnetometry experiments. Both Eric Moore and Lei Chen, who helped to co-design the third-generation magnetic resonance force microscope, taught me a great deal about designing, constructing, and testing a cryogenic system. Thanks to Alex Senko for his contributions to the characterization of thin-film magnetic materials. Thanks also to the rest of the Marohn group for being such a fun group of people to work alongside every day. Best of luck to the next generation of MRFM students, Paméla Nasr and Christine Gleave, as you further the development of the microscope and launch the applications-based phase of our team's MRFM studies.

I am also grateful to many others for collaboration and assistance. Thanks to Daniel Rugar and John Mamin at the IBM Almaden Research Center for conducting a joint NMR-MRFM experiment. Through interactions with you I grew as both a scientist and as a scientific writer. Thanks also to collaborators Doran Smith at the Army Research Laboratory and Lee Harrell at West Point Military Academy for sharing their expertise and creativity on the development of a new MRFM probe. Cornell's Research Services Shop and Laboratory

of Atomic and Solid State Physics Machine Shop were invaluable during the construction of the new magnetic resonance force microscope. My nanofabrication work was greatly aided by interactions with the staff at the Cornell NanoScale Science and Technology Facility; thanks specifically goes to Daron Westly, Rob Ilic, Vince Genova, Meredith Metzler, and Alan Bleier. Thanks also to Mick Thomas at the Cornell Center for Materials Research for teaching me how to use the focused ion beam microscope and for always being available to trouble-shoot the tool. Additional collaborators, and the specific contributions that each made to data presented in this thesis, are acknowledged at the end of each thesis chapter.

My family and friends have provided balance, support, and encouragement during my time in graduate school. Thanks to my parents for your unconditional love and support. You have given me an amazing foundation, and have instilled in me both a strong moral center and the gumption to follow through and complete what I pursue. Thanks to my fiancé, Jonathan Yoder, for being an incredible partner and listener. I am looking so forward to starting our life together. Thanks to Chin Subban for all of the awesome restaurant testing adventures, cooking experiments, and shopping excursions. It meant so much that you were always there to celebrate the good times and commiserate when things were stressful. Thanks also to Marie Krysak for all of our relaxing taco and game nights and to Michele Tague for making me laugh more times than I could ever count. Thanks to the first-year physical chemistry homework crew. I learned so much from all of you, and you even greatly improved my skills at ping-pong for a few months! And thanks to all of the friends I have made in the CNF — you made the cleanroom a warm, friendly, and fun place to work.

The work in this thesis was funded by the National Science Foundation through the Cornell Center for Nanoscale Systems (Grant Nos. EEC-0117770 and EEC-0646547), the National Institutes of Health (Grant No. 5R01GM-070012), and the Army Research Office MultiUniversity Research Initiative (Grant No. W911NF-05-1-0403). The research presented in this thesis made use of the facilities at the Cornell Center for Materials Research, which is

supported by the National Science Foundation Materials Research Science and Engineering Centers program (Grant No. DMR-0520404), and the Cornell NanoScale Science and Technology Facility (CNF), a member of the National Nanotechnology Infrastructure Network supported by the National Science Foundation (Grant No. ECS-0335765).

TABLE OF CONTENTS

LIST OF FIGURES

LIST OF TABLES

CHAPTER 1

INTRODUCTION TO MAGNETIC RESONANCE FORCE MICROSCOPY

Three-dimensional imaging techniques have continually revolutionized our understanding of the macroscopic and microscopic world around us. Magnetic resonance imaging, developed in the 1970's, has become a tool routinely used in medicine to non-invasively obtain full three-dimensional maps of soft tissue in the body at millimeter resolution. Techniques such as inductively detected nuclear magnetic resonance (NMR) and X-ray diffraction have been used to determine the atomic-resolution structures of thousands of proteins [1]. However, both NMR and X-ray diffraction require large quantities of purified sample; in addition, X-ray diffraction requires sample crystallization. Optical microscopy has recently become a serious contender in single molecule localization through the development of super-resolution imaging techniques [2–4]. Stochastic optical reconstruction microscopy (STORM) has achieved three-dimensional localization of photoswitchable dyes attached to proteins with 30 nm lateral resolution and 50 nm resolution in the axial dimension when imaging live cells at room temperature [5]. However, further advances will be needed before three-dimensional STORM can be used for structural determination of biological samples, including improving the resolution to better than 5 nm.

Cryogenic electron microscopy is a state-of-the-art method for determining the three-dimensional structure of non-crystalline biological macromolecules. Single particle cryoelectron microscopy (cryo-EM), in which many thousands of identical copies of the molecule of interest are imaged and averaged, often has achieved 2 nm resolution when applied to disordered asymmetric complexes and has reached nearly atomic resolution if stringent symmetry requirements when imaging highly symmetric samples, such as viruses [6]. Electron cryotomography (cryo-ET) is used to study single copies of biomacromolecules and can obtain three-dimensional images by rotating the sample stage between approximately $\pm 70°$. Al-

though the resolution of cryo-ET is slightly lower at 3-8 nm, the key benefit is that cryo-ET can be used to study a single copy of a molecule. Single copy analysis is essential when studying asymmetrical viruses and pleomorphic macromolecular assemblies that have variability in their size and shape [7, 8]. Single copies of biological samples have also been studied by cryo-ET to image the components of neuronal processes [9] and to assess single macromolecules in their native cellular context, which, for example, has enhanced the understanding of disease transmission by imaging the structures of viruses during the process of infection [10] and studying the organization of intact bacterial cells [11].

Magnetic resonance force microscopy (MRFM) is emerging as a cryogenic nanoscale imaging technique that could quickly become complementary to cryogenic electron microscopy. For three-dimensional reconstruction, the 4 to 10 nm resolution achieved by Degen *et al.* [12] in their NMR-MRFM [13–18] experiment is already competitive with the resolution achieved by cryo-ET when applied to single copies of biomacromolecules [19–22] and approaches the resolution often achieved by cryo-EM. MRFM is being developed to study systems that are similar to those analyzed by cryo-EM and cryo-ET, but MRFM has the distinct advantages of using isotopic labeling as a contrast agent and being able to work with many-micrometer thick samples, as long as the features of interest are located near or at the surface. Additionally, MRFM could play an important role in the determination of structures that are challenging to study by cryo-EM. Exosomes are a critical component in cell trafficking, but have rarely been studied by cryo-EM [23]. Proteins smaller than 100-200 kDa, such as membrane proteins, are also difficult to study by cryo-EM since the weak signals from these samples lead to poor contrast with embedded vitrified water and difficulties with orientation determination [7, 21, 24]. Unlike cryoelectron microscopy, which has firm resolution limits set by radiation damage, MRFM is a non-invasive technique with resolution continuing to be enhanced through improvements in sensitivity. With a modest factor of two enhancement in MRFM resolution compared to the experiment in Ref. 12, structural studies of the nuclear

spins in many exciting biomacromolecules and macromolecular complexes will be possible using NMR-MRFM.

In addition to using NMR-MRFM to determine biological structures by imaging their proton spin density, MRFM could also be used to detect and image unpaired electron spin labels on proteins. Imaging of individual electron spins has been demonstrated for E' centers in gamma-irradiated quartz [25]; however, the detection protocol used in the experiment required 13 hours of averaging per point and a sample with an extraordinarily long spin-lattice relaxation time. Although E' centers cannot be incorporated into biological samples, electron spin resonance (ESR) active nitroxide spin labels are commonly used to label cysteine residues in proteins. In conventional pulsed ESR, the tertiary structures of proteins have been determined by measuring the distances between pairs of the nitroxide-labeled residues [26–29]. Since the nitroxide free radical in tempamine (4-amino-2,2,6,6-tetramethyl-1-piperidinyloxy) has a spin-lattice relaxation time that is significantly shorter than what could be detected using the detection protocol of Ref. 25, a new MRFM protocol was developed to enable ESR-MRFM studies of biological samples labeled with tempamine spin probes [30]. The spin detection protocol of Ref. 30 can detect electrons with spin-lattice relaxation times consistent with those observed in tempamine-labeled biological samples ($T_1 > 0.2$ ms at a temperature T=4.2 K and external magnetic field B^{ext}=0.6 T) and has been used to detect ESR signal from a tempamine film with a sensitivity of 400 polarized electron spins. The next step will be to improve the sensitivity to detect, and subsequently image, single nitroxide spin labels.

With single-spin imaging capabilities, the key advantage of ESR-MRFM over conventional ESR is that significantly less sample preparation — and less total quantity of sample — would be required. In contrast with conventional ESR measurements, which are limited to the detection of pairwise coupling of nitroxide labels and thus require extensive

sample preparation with site-directed spin labels, ESR-MRFM with single-spin resolution could map the absolute positions of nitroxide labels that are uniformly tagged on just a single copy of the biomacromolecule. For a protein with even just five cysteine residues, 10 separate samples (each with a separate pair of nitroxide labels) would need to be prepared for conventional ESR, whereas only a single sample would be needed for ESR-MRFM. In addition to determining the tertiary structure of proteins, ESR-MRFM could be used, for example, to determine the mode of binding of a DNA- or RNA-protein complex by attaching nitroxide spin labels to either the nucleic acids [31–33] or the binding protein [34].

ESR-MRFM imaging could also contribute to the analysis of organic materials. For instance, it would be an exciting advance to use MRFM to obtain three-dimensional images of the phase morphology in bulk heterojunction (BHJ) solar cells [35], which are comprised of a blend of two semiconducting organic materials. In BHJ solar cells, the lateral morphology has been well-characterized using electron tomography, X-ray diffraction, and scanned probe techniques such as atomic force microscopy and electric force microscopy [36–41]; however, the vertical segregation has rarely been imaged at nanoscale resolution [42] and the three-dimensional morphology is still a field of active debate [43]. ESR-MRFM could be used to assess the full three-dimensional phase morphology at a resolution of a few nanometers by adding tempamine spin probes to either the electron-donor or electron-acceptor polymers that make up the photoactive layer. Since MRFM is non-invasive, a top metal electrode and electrical leads could be attached to enable imaging of sandwich-geometry solar cell devices during operation at cryogenic temperatures. Additionally, MRFM is expected to enable the quantification of the internal electric fields in halogen-containing organic electronic materials and the assessment of charge redistribution when light is applied to the solar cell [44–47].

To realize these exciting imaging applications, a key change to the experimental geometry previously used for high-resolution MRFM imaging [12] is required. MRFM is a scanned-

probe technique conducted at cryogenic temperatures that detects the spin density of a sample as a force or force gradient exerted on a high-compliance cantilever. The force is generated by the interaction between the net magnetic moment of the sample spins and the magnetic field gradient generated by a small ferromagnet. Either the sample or magnet is located on the cantilever, and the other is rigidly fixed in close proximity (see Section 1.1 and Figure 1.1). In the highest-resolution MRFM imaging experiment to date [12], a magnetic tip with a field gradient of 4.2 $\mathrm{MT\,m^{-1}}$ was achieved by fabricating a 200 nm diameter $Fe_{70}Co_{30}$ pillar on a flat surface.[1] The resultant high-resolution imaging experiments were conducted after individual copies of tobacco mosaic virus particles were adhered to the leading edge of a high-compliance silicon cantilever. The particles were prepared on the cantilever by dipping the cantilever leading edge in a dilute solution containing the virus and air-drying the sample.

The advance of Ref. 12 has not been extended to the study of more general samples, including the experiments proposed in this section, because few samples are robust enough to be prepared in the manner used by Degen *et al.* Frustratingly, the "sample-on-cantilever" nature of the experiment in Ref. 12 precludes the use of sample cryopreservation techniques widely used in electron microscopy [19–21, 49, 50]. The high-compliance cantilevers used in MRFM experiments also cannot support large samples, such as whole cells or organic semiconductor devices. Efforts have been made to switch to the "magnet-on-cantilever" geometry [25, 30, 51–57], in which the magnetic particle would be attached to the cantilever so that the sample could be prepared on a flat substrate. By moving the sample preparation off of the cantilever, standard preservation techniques used in cryoelectron microscopy could be implemented and the size of the sample would not be limited. However, the highest tip-field gradients produced using previous magnet-tipped cantilever fabrication protocols [25, 53, 54, 56, 57] were almost an order of magnitude lower than the gradient achieved in

[1] Here the revised gradient estimate reported in Ref. 48 is used.

Ref. 12 and were unsuitable for high-resolution imaging experiments.

The central challenge taken on in this thesis was the fabrication of ferromagnetic particles on cantilevers with sufficiently large magnetic field gradients to achieve the sensitivity needed for sub-5 nm resolution MRFM imaging of a broad range of samples. In the following sections of this chapter, details of the MRFM experimental setup, basics of the physics governing magnetic resonance, and factors that influence MRFM sensitivity are discussed. This chapter concludes with an outline of the key advances reported in the subsequent chapters of the thesis.

1.1 The MRFM Experiment

MRFM was first proposed by John Sidles in 1991 [13]. Since that time, extensive research has been conducted in the field, which has led to improvements in theory, experimental design, and sensitivity. The basic experimental setup and the physics making MRFM possible are described in this section for the magnet-on-cantilever geometry [16–18]. Although the spin physics is identical for the magnet-on-cantilever and sample-on-cantilever (also known as magnet-on-surface) geometries, the magnet-on-cantilever geometry is discussed here since it can be used with a much more diverse set of samples.

The MRFM experiment seeks to measure the magnetic moment of spins in a sample by observing the deflection or frequency change of a magnet-tipped cantilever brought to within nanometers of the sample surface. A cross-sectional illustration of the experimental setup is sketched in Figure 1.1. A magnet extending beyond the leading edge of a cantilever is brought close to a sample containing nuclear or electron spins. Here the magnet is shown as a rectangular cuboid and the cantilever is aligned perpendicular to the sample surface. The magnet is magnetized along the direction of an external field $\mathbf{B}^{\text{ext}}$. A nearby microwave (MW) or radiofrequency (rf) source is used to manipulate electron or nuclear spins, respectively.

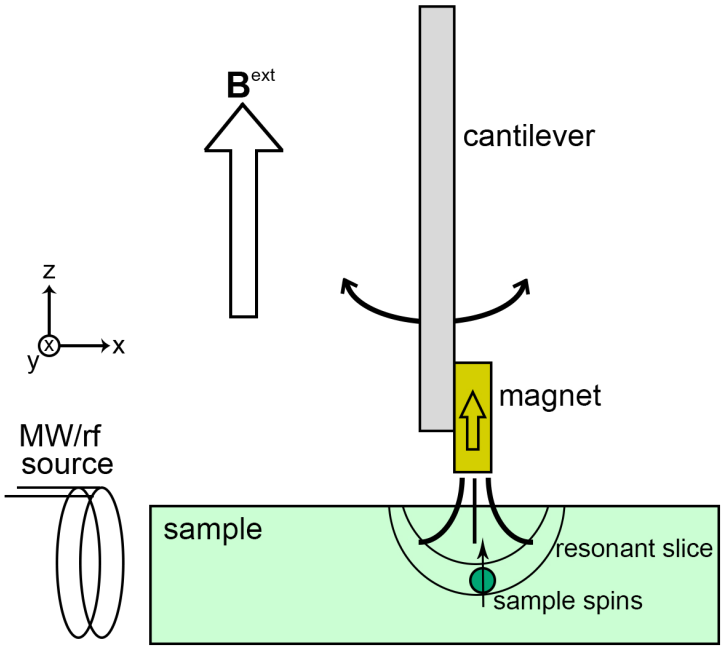

Figure 1.1: Schematic of a general MRFM experimental setup in the perpendicular or "pendulum" geometry. A rectangular cuboid magnet attached to a high-compliance cantilever is brought close to a sample surface. The magnet is magnetized in the direction of the external applied field $\mathbf{B}^{\text{ext}} = B_0\hat{\mathbf{z}}$. A microwave/radiofrequency (MW/rf) source supplies a transverse magnetic field. The transverse magnetic field is used in combination with the distance-dependent field gradient supplied by the magnetic particle to manipulate the sample spins. The magnetization of the spins in a thin, bowl-shaped slice, called a resonant slice, is modulated to create an observable shift in the cantilever amplitude (for instance, the COZMIC [58] and cyclic-CERMIT [30, 59] protocols) or cantilever frequency (for instance, the CERMIT [55] protocol).

The MW/rf source is shown as a coil, but microwires [12, 48, 60], microstripline halfwave resonators [30], and coplanar waveguides [61] have also been used.

The force $\mathbf{F}$ enacted between the magnetic moment of a spin $\boldsymbol{\mu}$ and the gradient of the magnetic field of a small magnetic particle $\mathbf{B}^{\mathrm{tip}}$ is

$$\mathbf{F} = (\boldsymbol{\mu} \cdot \nabla)\, \mathbf{B}^{\mathrm{tip}}. \tag{1.1}$$

The magnetic particle is magnetized in the direction parallel to the applied external field, which we have defined as the z direction. The sample spins are also polarized in the direction of the applied external field such that μ_z is the only non-zero component of the spin magnetic moment.

The gradient-dipole force between the polarized spin magnetic moment μ_z and the magnetic particle is read out through the motion of a singly-clamped cantilever. The length of the cantilever can be aligned with respect to the nearby surface in two ways. In the first MRFM experiments, the cantilever was aligned parallel to the surface in the typical atomic force microscopy (AFM) geometry [14, 15, 52, 57, 62–65]. In the AFM geometry, the relevant field gradient is the vertical field gradient $\partial B_z^{\mathrm{tip}}/\partial z$ and Eq. 1.1 can be simplified to

$$F_z = \mu_z \frac{\partial B_z^{\mathrm{tip}}}{\partial z}. \tag{1.2}$$

More recently, ultrasensitive cantilevers [66–68] have been employed in MRFM experiments to detect smaller forces [25, 30, 53, 55, 56, 69–71]. Due to the high compliance nature of these cantilevers, a perpendicular "pendulum" geometry must be used instead of the AFM geometry to prevent the cantilevers from snapping into contact with the surface due to van der Waals interactions. The cantilever in Figure 1.1 is shown in the pendulum geometry. The relevant field gradient in the pendulum geometry is instead the lateral field gradient $\partial B_z^{\mathrm{tip}}/\partial x$, which would lead to the gradient-dipole force being

$$F_x = \mu_z \frac{\partial B_z^{\mathrm{tip}}}{\partial x}. \tag{1.3}$$

In the pendulum geometry, the net time-averaged force for a homogenously dispersed sample are equivalent on both sides of the cantilever, which results in no net force acting on the cantilever. New protocols were created in order to detect MRFM signal in the pendulum geometry. Two of these protocols include OSCAR (OScillating Cantilever Adiabatic Rapid passages) [52] and CERMIT (Cantilever-Enabled Readout of Magnetization Inversion Transients) [55]. OSCAR is a force-based MRFM protocol that is used to detect statistical imbalances in spin polarization; the OSCAR protocol has been used to detect statistical polarization of small ensembles of spins [56]. CERMIT, on the other hand, is a force-gradient-based protocol that can measure statistical imbalances [59] or can instead measure the interaction between the Curie law magnetization of large ensembles of spins and the second derivative of $\mathbf{B}^{\mathrm{tip}}$ [55]. Spin signal in a force-based MRFM experiment is measured by lock-in detection of a shift in the cantilever amplitude, whereas signal in a force-gradient-based MRFM experiment is observed as the change in the cantilever frequency before and after the spin magnetization is inverted. Note that unlike Curie law polarization, the net polarization due to statistical fluctuations carries random sign; thus, only the signal power — not the raw signal — can be averaged in the force-based OSCAR and Ref. 12 experiments.

In Chapter 5, a new force-based MRFM protocol based on the detection scheme used in Ref. 12 is introduced and used to measure the statistical fluctuations of a small ensemble of proton spins in a polystyrene film [58]. In this protocol, which is termed COZMIC (COmpensated Zero Mean Inversion Cycles), a frequency-chirped radiofrequency waveform was used to cyclically invert the proton magnetization at twice the resonance frequency f_c of the cantilever using adiabatic rapid passage [72] sweeps. The proton magnetization of the polystyrene film, which had a coherence time during rf modulation of $\tau_m \approx 0.1$ s, interacted with the field gradient of a rectangular cuboid nanomagnet to induce force fluctuations acting on the cantilever. Force fluctuations were measured in the COZMIC experiment instead

of the Curie law average polarization since the magnitude of the Curie law polarization was too small to be observed. Additional experimental details are provided in Section 5.2.4.

In MRFM experiments, imaging is achieved by applying a distance-dependent resonance condition to independently select spins in thin, bowl-shaped resonant slices [62]. The rf frequency f_{rf} at which resonance occurs for a given spin is dependent on both $\mathbf{B}^{\mathrm{ext}}$ and the distance-dependent field $\mathbf{B}^{\mathrm{tip}}$ supplied by the magnetic particle on the cantilever tip. The resonance condition is given by

$$f_{\mathrm{rf}} = (\gamma/2\pi)|\mathbf{B}^{\mathrm{ext}} + \mathbf{B}^{\mathrm{tip}}(\mathbf{r})| \tag{1.4}$$

with γ the gyromagnetic ratio for the electron or nuclear spins and $\mathbf{B}^{\mathrm{tip}}(\mathbf{r})$ the magnetic field generated by the magnetic particle at location $\mathbf{r}$. The gyromagnetic ratio for a proton spin is $\gamma_{\mathrm{p}}/2\pi = 42.56\,\mathrm{MHz/T}$ and for an electron spin is $\gamma_{\mathrm{e}}/2\pi = 28\,\mathrm{GHz/T}$. When protocols are implemented to invert the spin magnetization, only spins in or near the resonant slice are affected. By sweeping either $\mathbf{B}^{\mathrm{ext}}$ or f_{rf}, the spin density along the z-axis of the sample can be mapped. The thickness of the resonant slice is set by the sweep width and the intensity of the magnetic field gradient supplied by the magnetic particle.

For direct three-dimensional imaging, the process of sweeping through the sample thickness is iterated while laterally scanning along the x- and y-axes [12, 51, 73–75]. Spin density maps are obtained that can be used to reconstruct a three-dimensional image. The 4 nm resolution images produced by Degen *et al.* used the Landweber reconstruction algorithm [12]. The limitation of the Landweber algorithm is that it requires that the sample be of a finite size and that the spin density at all boundaries is zero. The algorithm worked well for the small tobacco mosaic virus particles studied in Ref. 12, but would introduce artifacts if the sample is larger than the image boundaries, such as when working with whole cells or photovoltaic devices. An alternative method was proposed by Kempf and Marohn to use Fourier-transform (FT) imaging to reconstruct images without introducing edge artifacts

[76]; two-dimensional FT imaging has been demonstrated by Nichol and Budakian for a polystyrene sample [77].

1.2 Dependence of MRFM Sensitivity on the Magnetic-Field Gradient and Force Fluctuations

The figure of merit to assess MRFM sensitivity is the achievable signal-to-noise ratio (SNR). In this section, we will consider the SNR for the COZMIC protocol implemented in Chapter 5. For stochastically-polarized proton spins in a force-based NMR-MRFM experiment, the power signal-to-noise ratio ($\mathrm{SNR_p}$) is

$$\mathrm{SNR_p} = \frac{N_{\mathrm{spin}} {\mu_p}^2}{S_{\mathrm{F}}} {G_{zx}}^2 \sqrt{\mathrm{T_{avg}} \tau_m}, \tag{1.5}$$

with N_{spin} the number of spins in resonance, $\mu_p = 1.41 \times 10^{-26}$ N m T^{-1} the proton magnetic moment, $G_{zx} = \partial B_z^{\mathrm{tip}} / \partial x$ the lateral tip-field gradient, T_{avg} the signal averaging time, τ_m the spin correlation time, and S_{F} (in units of N^2 Hz^{-1}) the spectral density of force fluctuations experienced by the cantilever [78, 79]. Note that in Eq. 1.5, the "optimal reset-time theorem" introduced by Degen *et al.* to optimize the spin correlation time [70] was not taken into consideration.

Two parameters in Eq. 1.5 can be experimentally manipulated to improve the SNR per unit time for a given number of spins: the spin signal can be enhanced by achieving a high magnetic field gradient G_{zx}, and the noise can be minimized by working at low temperatures and having S_{F} approach the thermal limit. The parameters that influence S_{F} are considered in Section 1.2.1; optimizing the tip-field gradient is discussed in Section 1.2.2.

1.2.1 Minimizing Force Fluctuations for Magnet-Tipped Attonewton-Sensitivity MRFM Cantilevers

The noise in an MRFM experiment is set by the spectral density of force fluctuations $S_{\mathrm{F}} = (F_{\mathrm{min}}/b)^2$, with F_{min} the minimum detectable force and b the detection bandwidth. F_{min} is set by

$$F_{\mathrm{min}} = \sqrt{4k_{\mathrm{B}}T\left(\Gamma_{\mathrm{I}} + \Gamma_{\mathrm{S}}\right)b} \tag{1.6}$$

with $k_{\mathrm{B}} = 1.38 \times 10^{-23}$ N m K^{-1} as Boltzmann's constant, T the experimental temperature, Γ_{I} the thermally-limited internal dissipation experienced by the cantilever due to thermal fluctuations, and Γ_{S} the surface-induced dissipation attributed to non-contact dielectric fluctuations.

The cantilever's thermally-limited dissipation, also known as the cantilever's "thermal floor", can be expressed in terms of the cantilever quality factor Q:

$$\Gamma_{\mathrm{I}} = \frac{k}{2\pi Q f_c} = \frac{12.360}{14.064}\frac{wt^2}{Ql}(E\rho)^{1/2}, \tag{1.7}$$

with the cantilever spring constant $k = (1.030/4)\,E\,(wt^3/l^3)$ and the cantilever resonance frequency $f_c = (3.516/24\pi)\,t/l^2\,(E/\rho)^{1/2}$ [68]. In these equations, w, t, and l are the width, thickness, and length of the cantilever beam; E is Young's modulus; ρ is the density; and $Q = \pi f_c \tau$ is the quality factor of the cantilever dependent on the cantilever ringdown time τ [68]. It can be determined from Eq. 1.7 that to minimize Γ_{I}, the cantilevers should be long, thin, and narrow. They also should be made of a material with a low Young's modulus and density while maintaining a high quality factor. Parameters that determine the quality factor are not fully understood, but are at least in part influenced by surface effects [66, 80]; a further discussion on the cantilever quality factor is provided in Section 3.3. All cantilevers used in the work presented in this thesis are made from single-crystal silicon, and the parameters for the fabricated cantilevers are $w = 4$ µm, $t = 340$ nm, $l = 200$ µm,

$E = 1.3 \times 10^{11}$ N m^{-2}, and $\rho = 2.3 \times 10^{3}$ kg m^{-3}. The cantilevers are typically observed to have $k = 0.5$ to 1.0 mN m^{-1}, $f_c = 6$ to 9 kHz, and $Q = 40,000$ to 100,000 [58, 81, 82].

As a high-compliance cantilever approaches a surface in the pendulum geometry, the friction experienced by the cantilever is observed to increase [83]. In MRFM experiments that detect the amplitude of the cantilever motion, such as the COZMIC protocol used in Chapter 5, minimizing the surface-induced dissipation Γ_S is critical. The strength of $\mathbf{B}^{\text{tip}}$ is largest at small tip-sample separations, so Γ_S must be minimized for tip-sample separations as small as 5 nm. Over a polymer-coated surface, such as the polystyrene surface in Chapter 5, dielectric fluctuations in the polymer induce fluctuating electric fields that lead to damping interactions between the surface and the cantilever leading edge [84]. Mitigation of noncontact friction Γ_S for MRFM-style magnet-tipped cantilevers was studied extensively by Hickman *et al.* [81]. Surface-induced dissipation was minimized by reducing the cross-sectional area of the silicon near the cantilever leading edge and by extending a nanomagnet with a narrow cross-section past the leading edge of the silicon cantilever by at least 200 nm. It is important to note that the excellent Γ_S result of Ref. 81 was also due to the optimization of additional experimental parameters. In Ref. 81, the sample was chosen to be a thick layer of polystyrene that was coated with gold, and the potential of the cantilever was adjusted to null the contact potential difference between the gold-coated sample and the magnet-tipped cantilever. In a second experiment, no bias was placed on a similar overhanging magnet-tipped cantilever and an uncoated, 40 nm thick polystyrene sample was spin coated on a copper microwire [58]; additional experimental details are provided in Chapter 5. In the experiment in Ref. 58 and Chapter 5, significantly higher dissipation was observed than in the Ref. 81 experiment even though nearly identical overhanging magnet-tipped cantilevers were used. Instead of detecting the amplitude of cantilever motion, as in the COZMIC MRFM experiment, some MRFM protocols, such as OSCAR and CERMIT, detect shifts in the cantilever resonance frequency. The noise in frequency-based measurements is governed

by the power spectral density of cantilever frequency fluctuations $S_{\delta f_c}(f)$. The frequency fluctuations are set by

$$S_{\delta f_c} = 4k_{\mathrm{B}}T\Gamma \left(\frac{f_c}{2k_{\mathrm{c}}x_{\mathrm{rms}}} \right)^2, \tag{1.8}$$

with Γ the total dissipation experienced by the cantilever and x_{rms} the root mean square (rms) amplitude of the cantilever motion. At low modulation frequencies f, additional sample-induced fluctuations $S_{\delta f_c} \propto f^{-1}$ are observed over polymer samples [85, 86]. At high modulation frequencies, the frequency fluctuations are dominated by detector noise $S_{\delta f_c} \propto f^2$ [85]. Frequency fluctuations are also very sensitive to mechanical vibrations [87].

Although the overhanging magnet-tipped cantilevers developed by Hickman *et al.* were shown to mitigate surface-induced dissipation, the frequency fluctuations measured when using these cantilevers were still quite large [58, 81]. A parametric upconversion scheme was developed and implemented in an MRFM experiment to convert a frequency-shift MRFM signal to an amplitude-detection signal [88]. Using this protocol, it should be possible to evade surface frequency noise and detector noise, and to instead be limited by Γ_{S} at close tip-sample separations.

1.2.2 Optimizing the Magnetic Field Gradient of Magnet-Tipped MRFM Cantilevers

In addition to minimizing cantilever dissipation, achieving a high SNR in an MRFM experiment requires that the magnetic particle exhibit a large magnetic field gradient. MRFM signal is maximized by using a magnet comprised of a material with a high saturated magnetic moment; the material's coercivity [89] and resistance to degradation [48] should also be taken into consideration. The magnet should be patterned to have a narrow cross-section, since the tip-field gradient — and thus the signal per spin in an MRFM experiment — scales

inversely with the size of the magnet. However, the cross-sectional area of an MRFM magnet should not simply be as small as possible. Instead, the optimal magnet cross-sectional area is dependent on the distance between the sample spin and the leading edge of the magnetic particle, also called the tip-sample separation h_{mag}. For example, let us consider the optimal magnet radius $r_{\mathrm{mag}}^{\mathrm{opt}}$ for a magnet that is approximated as a uniformly magnetized spherical particle. Under the assumption that the MRFM signal is due to force detection of a single spin [17], the optimal magnet radius is

$$r_{\mathrm{mag}}^{\mathrm{opt}} = 3h_{\mathrm{mag}}. \tag{1.9}$$

Eq. 1.9 also holds true in a force-gradient experiment on a single spin when the cantilever amplitude is set to an optimal value [17]; optimizing the detection of multiple spins in a force-gradient experiment has been considered by Lee and coworkers [90].

A key implication of Eq. 1.9 is that there is not a single optimal magnetic particle width. The tip-sample separation is based on the sample spin's depth below the sample surface; therefore, $r_{\mathrm{mag}}^{\mathrm{opt}}$ also is dependent on the sample spin location. For instance, if the distance between the magnet leading edge and the sample surface is 5 nm and if spins are detected within the top 50 nm of the top of the sample, $r_{\mathrm{mag}}^{\mathrm{opt}}$ would range from 15 to 165 nm. Thus, Eq. 1.9 indicates that the fabrication of MRFM magnets should allow for the patterning of magnets with easily tunable dimensions.

Optimizing the tip-sample separation requires consideration of how both the signal and noise in an MRFM experiment are influenced by h_{mag}. MRFM signal increases as h_{mag} is reduced; however, MRFM measurement noise — which is set by the spectral density of force fluctuations S_{F}, and specifically by the surface-induced dissipation Γ_{S} — also increases as the distance between the cantilever leading edge and the sample surface is reduced. Thus, maximizing the SNR in an MRFM experiment requires setting h_{mag} as small as possible while still maintaining S_{F} within acceptable limits.

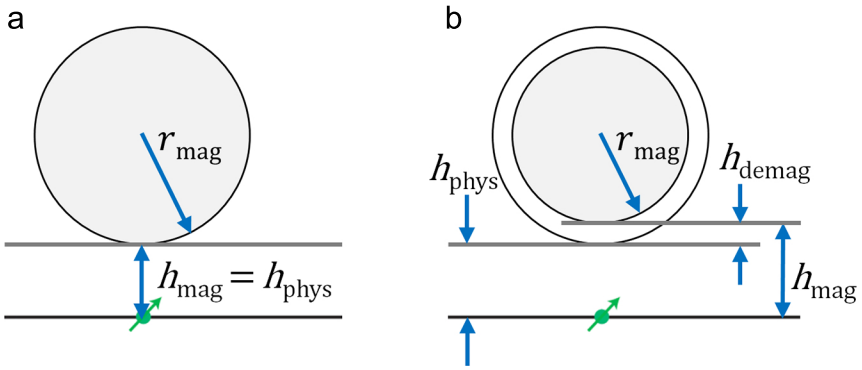

Figure 1.2: Cross-sectional schematics of spherical magnets demonstrate the influence of magnetically inactive "damage" layers on the tip-sample separation h_{mag}. (a) Fully-intact magnet (gray circle) with radius r_{mag}. The distance between the sample spin (green arrow) and the leading edge of the magnetic material h_{mag} is the same as the physical separation h_{phys}. (b) Magnet with a damage layer of thickness h_{demag}. For the damaged magnet, $h_{mag} = h_{phys} + h_{demag}$.

Two additional factors must be considered to achieve the highest MRFM signal. To minimize h_{mag} for a given separation between the cantilever leading edge and the sample surface, the leading edge of the magnet should be in line with, or overhanging, the leading edge of the cantilever. Once the optimal h_{mag} is determined, potential magnetic damage layers also must be considered. As shown in Figure 1.2, a "damage" layer of demagnetized material with thickness h_{demag} at the magnet edge would increase the spacing between the sample spin and the magnetic material in the nanomagnet. Instead of h_{mag} being equal to the physical spacing h_{phys} between the sample spin and the physical leading edge of the magnet, the introduction of a damage layer would increase the tip-sample separation to $h_{mag} = h_{phys} + h_{demag}$. Due to the increase in h_{mag}, magnets with a damage layer exhibit lower observable tip-field gradients.

The focus of Chapters 2 through 5 in this thesis is the preparation of high-gradient nanomagnet-tipped cantilevers. Nanomagnets with adjustable dimensions are defined using electron beam (e-beam) lithography and deposited using e-beam evaporation; this combination of techniques can produce nanomagnets with cross-sectional areas ranging from

200×200 nm^2 to less than 30×30 nm^2. The key constraint during nanomagnet fabrication is prevention of the formation of magnetically inactive layers at the nanomagnet leading edge. In this thesis, the minimization of damage layers is achieved by careful process integration and limiting degradation due to chemical and heat-induced damage.

1.3 Outline of the Dissertation

The work in this thesis centers on the the development of a method to fabricate high-gradient nanomagnets attached to cantilevers. As discussed in Sections 1.2.1 and 1.2.2, high-resolution imaging can only be achieved by combining (1) large per-spin signal resulting from high field gradients and (2) low $\Gamma_{\rm I}$ and $\Gamma_{\rm S}$ noise due to the thermal fluctuations in the cantilever and noncontact surface dissipation, respectively. To that end, a second design criteria for high sensitivity in MRFM is to overhang the nanomagnet past the leading edge of the cantilever, both to reduce the noncontact friction, as observed in Ref. 81, and to have the leading edge of the nanomagnet as close to the sample spins as possible. It is furthermore essential to minimize magnetic damage, particularly at the nanomagnet leading edge. Since previous efforts to fabricate nanomagnets on cantilevers [25, 53, 54, 56, 57] resulted in tip-field gradients that were almost an order of magnitude smaller than the tip-field gradients needed for nanometer-scale NMR-MRFM imaging [12], it is essential to develop a new protocol to fabricate high-gradient nanomagnets on cantilevers.

Chapter 2 begins with a summary of the prior approaches for the fabrication of magnets on cantilevers and a discussion of the record-low dissipation for a cantilever with an integrated nickel nanomagnet that was observed by Hickman *et al.* [81]. My attempts to reproduce the Hickman fabrication protocol indicated that the yield for the magnet-tipped cantilevers was extremely low. I report new findings that indicate that the low yield of the Hickman protocol

was due to a combination of exceeding the thermal budget for the nanomagnets and damage during deposition of plasma enhanced chemical vapor deposition of silicon dioxide. Attempts to improve the yield and magnetization of the magnet-tipped cantilevers, including the use of barrier layers, are described. The chapter concludes with a discussion of alternative methods to attach magnetic particles to cantilevers.

Chapter 3 introduces a new fabrication protocol that was designed to improve the process yield, decrease processing-induced damage, and retain the critical ability to use high-resolution electron beam lithography to define the nanomagnets. The protocol involves a combination of batch- and serial-fabrication processing. Magnets are defined on a silicon-on-insulator wafer using e-beam lithography and liftoff. The wafer is then batch-processed to yield nanomagnet tips protruding from the leading edge of suspended micron-scale silicon chips, which are attached serially to the ends of attonewton-sensitivity silicon cantilevers using focused ion beam (FIB) milling and attachment. Methods for fabricating nickel and cobalt nanomagnet-tipped chips, and for conducting the FIB lift-out procedure, are described. Optimization of the experimental parameters and alternative fabrication methods are discussed. The successful fabrication of cobalt nanomagnets, which has a saturation magnetization that is $3\times$ larger than nickel, is a particularly exciting advance since previous attempts to batch-fabricate cobalt nanomagnets had been unsuccessful [91].

Chapter 4 describes extensive characterization of the elemental composition and magnetization of nickel and cobalt thin films. Frequency-shift cantilever magnetometry was conducted to assess the saturated magnetic moment of individual nickel and cobalt nanomagnets. Large-area thin films of both nickel and cobalt were characterized by superconducting quantum interference device (SQUID) magnetometry. SQUID magnetometry conducted on both uncapped and platinum-capped films indicated that the magnetic material saturated near the theoretical values. X-ray photoelectron spectroscopy (XPS) with depth profiling

was conducted on both uncapped and platinum-capped thin films of nickel and cobalt to determine the extent of oxidation damage; XPS findings indicated that unprotected magnetic materials incurred less than 10 nm of oxidation, and that oxidation was prevented by capping with 10 nm of platinum.

Chapter 5 details the use of an attonewton-sensitivity cantilever with an integrated cobalt nanomagnet tip to detect NMR-MRFM signal with ≤ 500 proton magnetic moment sensitivity. Spin signal was obtained at tip-sample separations ranging from 13.1 nm to 42.3 nm. The observed tip-field gradient of 4.4 to 5.4MTm^{-1} is comparable to the 4.2MTm^{-1} field gradient produced by the $Fe_{70}Co_{30}$ pillar in the sample-on-cantilever experiment of Ref. 12 and is 8 to 10 times larger than the best tip-field gradient demonstrated to date in a magnet-on-cantilever MRFM experiment [53]. For the closest tip-sample separation of 13.1 nm and under the signal averaging conditions of Ref. 12, these magnet-tipped cantilevers are projected to achieve a resolution of 5 to 10 nm. The resolution could be further improved by minimizing the noncontact friction, which was significantly higher than what had been observed by Hickman *et al.* [81]. It is hypothesized that Γ was dominated by eddy current damping in this experiment, which could be mitigated by increasing the thickness of the sample or putting a bias on the cantilever to null the contact potential difference between the tip and the substrate.

Chapter 6 discusses the development of Cornell's third-generation magnetic resonance force microscope, which will be used to conduct high-resolution three-dimensional MRFM imaging experiments. The key enhancement is that this microscope has a stage with three dimensions of motion. Other improved features include superior vibrational isolation, a longer hold time for the liquid helium dewar containing the 9 T superconducting magnet, separate coaxial lines for radiowaves and microwaves, and enhanced heat sinking of the probe head.

Chapter 7 summarizes the key findings in this dissertation and comments on potential future directions for the fabrication of magnet-tipped cantilevers with further improved performance.

Work presented in this thesis includes findings that were previously published in three manuscripts (Refs. 81, 82, and 58), in addition to extensive newly-presented results. The publication status of the work in the chapters of this thesis is summarized in this paragraph; copyright information for previously-published figures is detailed in each chapter. Scanning transmission electron microscopy (STEM) and electron energy loss spectroscopy (EELS) data for an integrated nickel nanomagnet on cantilever (Section 2.3) were published in Ref. 81. The original nickel magnet-tipped chip fabrication protocol (Section 3.2), FIB lift-out procedure (Section 3.4), and details on process optimization (Sections 3.5, 3.7.2, and 3.8) were first reported in Ref. 82. The fabrication of cobalt magnet-tipped chips (Section 3.6) and improved FIB lift-out procedure (Section 3.7.1) were introduced in Ref. 58. For magnetic-material characterization, the nickel frequency-shift cantilever magnetometry data (Section 4.1) were published in Ref. 82, and the cobalt cantilever magnetometry (Section 4.4) and large-area thin-film cobalt SQUID magnetometry and XPS findings (Section 4.3) were presented in the manuscript and Supporting Information of Ref. 58. All data presented in Chapter 5 were published in Ref. 58. The work presented here for the first time includes the vast majority of Chapters 1, 6, and 7; all data in Chapter 2 aside from Figures 2.2(c,e), 2.5, and 2.7; additional figures and details to clarify the methods discussed in Chapter 3; and the SQUID and XPS findings for nickel thin films in Section 4.3. The work conducted in this thesis was carried out with collaborations and funding that are acknowledged separately at the end of each chapter.

CHAPTER 2

MAGNET-ON-CANTILEVER PRECEDENT AND INTEGRATED MAGNET-ON-CANTILEVER FABRICATION

2.1 Introduction

The development of attonewton-sensitivity cantilevers [66, 68] has opened up exciting new approaches for characterizing materials. Attonewton-sensitivity cantilevers have been used to detect electron spin resonance (ESR) [25, 30] and nuclear magnetic resonance (NMR) [12, 55], to observe near-surface dissipation due to dopants in semiconductors [92] and dielectric fluctuations in polymers [84, 86], to characterize switching and fluctuations of ferromagnetic domains in individual magnetic nanoparticles [68, 89, 93] and individual magnetic vortices in superconducting rings [94], and to measure persistent currents in normal metal rings [95, 96].

The application of studying ESR or NMR in an MRFM experiment requires that an attonewton-sensitivity cantilever be functionalized with either a sample [12, 48, 70, 71] or a magnetic particle [25, 30, 53, 55, 56, 68, 69, 89, 92, 93]. Although the interaction between the magnetic moment of the sample spins and the field gradient of the magnetic particle is independent of which component is adhered to the cantilever, other factors strongly influence the choice between the magnet-on-cantilever and sample-on-cantilever geometries. The key consideration for determining the MRFM geometry is the sample of interest. As discussed in Chapter 1, the preparation methods required for many exciting samples are incompatible with the limitations of working at the leading edge of an attonewton-sensitivity cantilever. Thus, to study the widest range of samples in MRFM experiments, it is critical to prepare the sample off-cantilever and instead attach the magnet to the cantilever.

In Chapter 3 a new combination batch- and serial-fabrication protocol for the fabrication

of magnet-tipped cantilevers will be introduced. Using the Chapter 3 approach, magnets are batch-fabricated on microscale silicon chips and are serially adhered to separately-prepared attonewton-sensitivity cantilevers. Cobalt nanomagnets fabricated using this combined batch-and-serial technique are ultimately shown to exhibit the highest tip-field gradients to date for the magnet-on-cantilever geometry.

In order to motivate the development of the magnet-on-cantilever fabrication protocol presented in Chapter 3, it is critical to understand the limitations of previous integrated magnet-on-cantilever methods. Section 2.2 includes a summary of the previous methods used in the MRFM community to fabricate integrated magnets on cantilevers. The protocol introduced by Hickman *et al.* [81] best met the criteria discussed in Section 1.2.2 for the optimal magnet design for magnet-tipped MRFM cantilevers. However, the yield of the Hickman protocol was not reported, and attempts to reproduce the procedure had extremely low yields of $< 1\%$. In Sections 2.3 and 2.4, characterization of the failure mechanism of the Hickman fabrication protocol is discussed and attempts to improve the process yield through the introduction of barrier layers to prevent oxidation and silicidation of the magnetic material, which proved to be unsuccessful, are described. The work presented in this chapter is summarized in Section 2.5, and in Section 2.6 is a discussion of the goals for the new high-yield fabrication protocol detailed in Chapter 3.

2.2 Prior Magnet-on-Cantilever Fabrication Methods and Results

The force of the interaction between the magnetic moment of a single electron spin and the magnetic field gradient of a small cobalt ferromagnet (approximated as a spherical particle of radius 50 nm) with $h_{\mathrm{mag}} = 10$ nm is on the order of 10^{-16} N $= 100$ aN; the force due to the interaction between a single proton and the same magnetic particle is three orders

of magnitude lower with a force of approximately 0.1 aN [66, 97]. In a joint experiment by Kenny's group at Stanford University and Rugar's team at IBM Almaden Research Center, Stowe *et al.* introduced the first protocol to fabricate cantilevers with sufficient sensitivity to detect attonewton-scale forces [66]. The cantilevers were prepared by thinning the device silicon layer of a silicon-on-insulator (SOI) wafer to as thin as 50 nm, followed by defining the cantilever bodies and sharp leading-edge tips using two overlapping optical lithography masks. After backside processing, cantilevers up to 400 µm long and as thin as 60 nm were released using critical point drying, with yields higher than 80%. The cantilevers exhibited a spring constant as low as 6.5×10^{-6} N m^{-1} and a minimum detectable force $F_{\rm min} = 5.6$ aN in a 1 Hz bandwidth at a temperature of 4.8 K. However, the cantilever quality factor Q at 4.8 K was only $Q = 6,700$. In comparison to $Q = 26,000$ for similarly-prepared 175 nm thick cantilevers, the relatively low Q for these 50 nm thick cantilevers indicated that surface effects induced significant cantilever energy losses. In Ref. 66, magnetic tips were prepared on individual attonewton-sensitivity cantilevers using shadow-masked evaporation of cobalt onto the sidewalls of post-released cantilevers. In order to evaporate metal on the sidewall of the cantilever leading edge, each cantilever was loaded into the evaporator at an angle with respect to the cobalt target, and the majority of the cantilever was masked off using a knife edge. The magnet-tipped cantilevers of Ref. 66 were not used in an MRFM experiment.

Chui *et al.* extended the Stowe fabrication protocol during a second collaboration between the Kenny and Rugar groups [98]. In the revised process, the cantilevers were mass-loaded at the leading edge to damp high-order modes of the cantilever and mitigate high-frequency vibrational noise [99, 100]. The thickness of the base of the cantilevers was also increased to minimize clamping losses from misalignment of the front and back sides of the cantilever handle chips. The bendable "hinge" portion of the cantilever was fabricated from the 100 nm thick single-crystal silicon device layer of SOI wafers, and the added thicknesses of the mass loaded cantilever leading edge and cantilever base were achieved by two separately-masked

undoped single-crystal silicon epitaxial growths. The thickness of the mass-loaded cantilever leading edge was 2 µm, and the base of the cantilever was grown to a thickness of 5 µm. The cantilevers were then fabricated in a manner similar to Ref. 66. The cantilever quality factor, spring constant, and resonance frequency were observed to be up to $Q = 80,000$ (at 20 K), $k = 3 \times 10^{-4}$ N m^{-1}, and $f_c = 7$ kHz, respectively; using Eqs. 1.6 and 1.7, Q, k, and f_c can be used to calculate that the corresponding $F_{\rm min} = 10$ aN in a 1 Hz bandwidth at $T = 20$ K. To use the magnet-on-cantilever geometry in subsequent MRFM experiments, samarium cobalt (SmCo) magnetic particles were serially attached to the leading edge of the mass-loaded cantilevers. To improve the tip-field gradient exhibited by SmCo magnets, the width of the particles was reduced to as small as 150 nm using focused ion beam (FIB) milling [25]; due to FIB-milling-induced magnetic damage, the particle width could not be further reduced. The largest vertical and lateral tip field gradients reported by FIB-milling of SmCo magnets employed in MRFM experiments were $\partial B_z^{\rm tip}/\partial z = 5.5 \times 10^5$ T m^{-1} and $\partial B_z^{\rm tip}/\partial x = 4.3 \times 10^5$ T m^{-1}, respectively [53]. For reference, the tip-field gradients used in the high-resolution MRFM imaging experiment of Ref. 12, which used the sample-on-cantilever geometry, were an order of magnitude larger. Although one of the SmCo-tipped cantilevers was used to detect ESR-MRFM signal from a single electron spin in the seminal experiment of Ref. 25, 13 hours of signal averaging were required per point. It thus was unfortunately determined that FIB-milled SmCo-tipped cantilevers produced insufficient tip-field gradients for high-resolution MRFM imaging experiments.

Methods to batch fabricate integrated nanomagnets directly on attonewton-sensitivity cantilevers were investigated by Marohn's group at Cornell University. In 2004, Jenkins *et al.* batch-fabricated nickel nanomagnets as small as 1.2 µm × 400 nm in area and 200 nm thick using electron-beam (e-beam) lithography and thermal evaporation [68]. Cantilevers were defined around the pre-deposited magnets such that the magnets were near the cantilever leading edge. The cantilevers were fabricated from the 340 nm thick device silicon layer of SOI

wafers. The cantilever fabrication and release process followed the methods of Ref. 66. The magnet-tipped cantilevers were not employed in a magnet-on-cantilever MRFM experiment, but frequency-shift cantilever magnetometry results indicated that the magnets were close to fully magnetized and had a damage layer of less than 28 nm. At a temperature of approximately 11 K, quality factors were observed to be as high as $Q = 200,000$, indicating that the surface effects observed by Stowe *et al.* in Ref. 66 had been minimized.

Although $F_{\min}$ is set by the intrinsic dissipation and experimental temperature at large tip-sample separations, as shown in Eq. 1.6, at small tip-sample separations $F_{\min}$ is often dominated by surface interactions. In an effort to maintain low $F_{\min}$ at close tip-sample separations, Hickman *et al.* revised the Jenkins magnet-on-cantilever batch-fabrication protocol to extend e-beam-defined nickel nanomagnets past the leading edge of attonewton-sensitivity cantilevers [81]. The observed cantilever spring constants for the magnet-tipped cantilevers were approximately 8×10^{-4} N m^{-1}. Q varied significantly between cantilevers, ranging from 85,000 to as high as 235,000. The key alteration in the Hickman protocol, the overhanging nature of the nanomagnet, was expected to minimize surface-induced dissipation by improving the spatial separation between trapped charge on the silicon cantilever and electric field fluctuations in the substrate. It was observed that the overhanging nickel-tipped cantilevers did in fact exhibit a record-small force sensitivity for a magnet-tipped cantilever near a surface. At a temperature of 4.2 K, $F_{\min} < 10$ aN ($b = 1$ Hz bandwidth) for tip-sample separations down to 3 nm [81]. For comparison, $F_{\min} = 10$ aN was observed at a tip-sample separation of 24 nm in the 4 to 10 nm resolution NMR-MRFM imaging experiment of Ref. 12. The nickel nanomagnets were characterized by cantilever magnetometry and found to have saturation magnetizations that were roughly 70% of the theoretical value. However, when the nickel magnet-tipped cantilevers were used in an MRFM experiment, the experimentally observed ESR-MRFM signal had poor agreement with theory. The same theory gave a predicted signal that agreed almost perfectly with the observed signal in an ESR-MRFM experiment

that used a 4 μm diameter spherical nickel magnet-tipped cantilever [30], indicating that the nickel nanomagnets fabricated using the Hickman protocol were not as well-magnetized as expected.

Out of these prior methods developed for magnet-tipped cantilevers in MRFM experiments, the fabrication protocol introduced by Hickman *et al.* best meets the criteria described in Section 1.2.2 for defining reproducible, adjustable, and small-scale magnets on cantilevers that experience minimal force sensitivity degradation as the tip-sample separation is reduced. Additionally, Hickman *et al.* demonstrated that overhanging the magnet past the cantilever leading edge produced cantilevers that could be brought to within less than 5 nm of the sample surface without significantly increasing the surface-induced dissipation. Unfortunately, the yield of the Hickman process was low and the magnets prepared by Hickman were not well-magnetized. In Sections 2.3 and 2.4, efforts to reproduce and improve the Hickman fabrication protocol are discussed.

2.3 Process Integration Challenges of the Overhanging Nanomagnet-on-Cantilever Fabrication Protocol

The key steps of the Hickman protocol are shown in Figure 2.1. The process is fully described in Refs. 81 and 91; an overview of the critical components of the process is provided here to facilitate subsequent discussion of the low yield and failure mechanism. SOI wafers with a 340 nm thick, $\langle 100 \rangle$ oriented device silicon layer and a 400 nm thick buried oxide (BOX) silicon dioxide (SiO_2) layer were used. Platinum alignment marks were used to align subsequent e-beam lithography and photolithography steps; the 100 nm thick marks were defined using e-beam lithography and evaporated using e-beam evaporation (with a 5 nm thick chromium adhesion layer). Nickel nanomagnets as narrow as 100 nm in width were de-

fined in bilayer resist [101] by e-beam lithography and were deposited by e-beam evaporation (Figure 2.1, Step 2). A 5 nm chromium layer was deposited under the nickel magnets to promote adhesion to the silicon substrate. U-shaped holes were defined by e-beam lithography and a calibrated isotropic SF_6:O_2 reactive ion etch (RIE) plasma etch was used to remove the silicon under the magnet leading edge to create a 100 to 300 nm overhang (Figure 2.1, Step 3 and Inset A). The cantilever bodies were patterned using photolithography and an identical SF_6:O_2 silicon plasma etch (Figure 2.1, Step 4 and Inset B). Prior to backside processing, the front and back of the wafer were coated with low-stress plasma enhanced chemical vapor deposition (PECVD) SiO_2 at 275°C (Figure 2.1, Step 5); the front of the wafer was coated first with 1.6 µm of PECVD SiO_2 to protect the magnets and cantilevers against damage, and the backside was coated afterwards with 2 µm of SiO_2 that was used as an etch mask during subsequent steps. Windows in the wafer substrate under the cantilevers were defined in photoresist on the back side of the wafer, and the pattern was transferred to the backside SiO_2 using a CHF_3:O_2 etch (Figure 2.1, Step 6). The 500 µm thick handle silicon layer was anisotropically etched using deep reactive silicon etching, commonly called Bosch etching (Figure 2.1, Step 7) [102]. The backside photoresist acted as the etch mask while etching the first 400 µm of the handle silicon layer; prior to etching the final 100 µm of handle silicon, the resist was stripped, leaving the backside SiO_2 as the only remaining etch mask. A "handler" wafer [91] also was attached to the device side of the wafer prior to etching the final 100 µm of handle silicon. Because the Bosch etching tool flows helium gas over the back of the wafer to keep the substrate cool during processing, an air-tight seal between the tool and the wafer must be retained at all times. When the windows in the device wafer become very thin membranes, they are subject to cracking; the handler wafer was attached to the helium-cooling side of the wafer to retain an air-tight seal in the Bosch tool even if the membranes cracked. Since adding the handler wafer reduced the cooling efficiency while the handle wafer was attached, the wafer was frequently removed from the

etch chamber to cool. To release the cantilevers, the PECVD and BOX SiO_2 layers were simultaneously etched using buffered oxide etch (BOE); the thickness of the PECVD SiO_2 had been set so that it would release at the same time as the BOX SiO_2 layer in order to limit exposure of the magnetic material to BOE. The cantilevers were critical point dried to prevent curling or stiction (Figure 2.1, Step 8). Overall, the Hickman fabrication protocol required 38 fabrication steps on 10 different fabrication tools and instruments; the process could be completed with approximately two weeks of processing time.

The yield of the original Hickman fabrication protocol was not reported, but magnetic material damage to a significant number of the nickel nanomagnets was discussed in Ref. 91. Tentative evidence indicated that the nickel magnets were converted to nickel silicide during the through-wafer Bosch etch — particularly while the handler wafer was attached — due to an increased temperature of the substrate; efforts were made to minimize the damage by removing the wafer from the etch chamber frequently to cool. However, conclusive evidence confirming the damage mechanism was not reported, and it remained unclear whether the damage was due to poor process control or a fundamental incompatibilities due to poor process control or chemical reactions between silicon, chromium, and nickel at the high temperatures present during backside etching.

New work was undertaken to determine the yield of the Hickman protocol and to better understand the sources of nanomagnet damage. Attempts to reproduce the Hickman protocol were conducted on four separate wafers. Scanning electron microscopy (SEM) images from three of these iterations are presented in Figure 2.2.[1] Images are shown for magnets at the completion of the front-side processing (Figure 2.2(a,b)) and at the end of the process after the cantilevers were released (Figure 2.2(c-h)). It was observed that although most magnets were still intact after the completion of the front-side processing, less than 1% of

[1]Figure 2.2(c,e) reprinted with permission from J. G. Longenecker *et al.*, J. Vac. Sci. Technol. B **29**, 032001 (2011). Copyright 2011, American Vacuum Society.

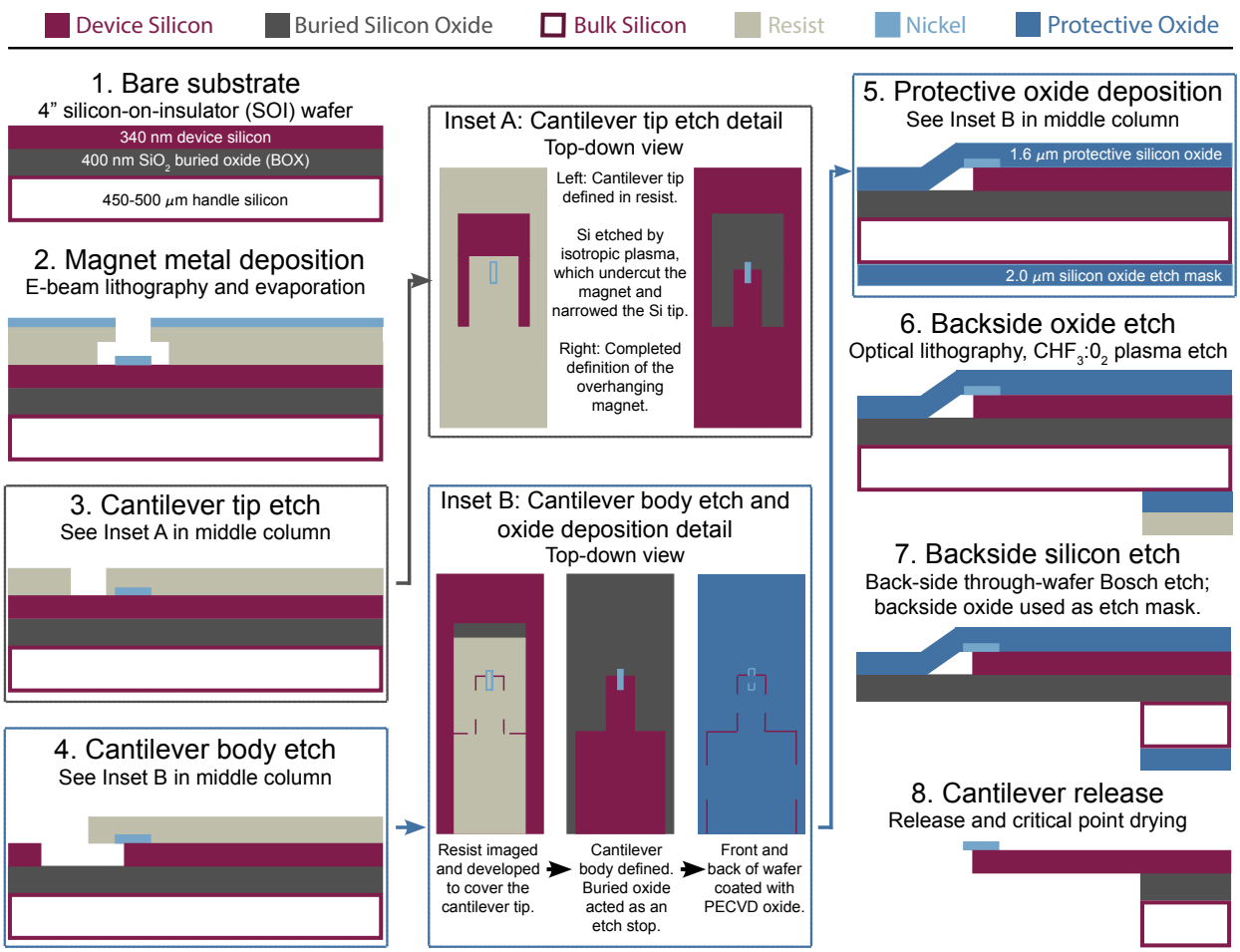

Figure 2.1: Schematics of the key steps of the integrated, overhanging magnet-tipped cantilever fabrication protocol introduced by Hickman *et al.* [81]. The color key is provided at the top of the image. (1) SOI wafers with a 340 nm thick device silicon layer and 400 nm thick buried oxide (BOX) layer were used. (2) 100 nm thick nickel nanomagnets, with a 5 nm chromium adhesion layer, were defined in bilayer resist by e-beam lithography and deposited by e-beam evaporation; the resist was lifted off after deposition. (3) U-shaped holes (top-down view schematic in Inset A, left side) directly above the nanomagnets were defined using e-beam lithography. The silicon device layer was isotropically etched using SF_6:O_2 plasma to achieve a magnet overhang of 300 nm and reduce the width of the silicon at the leading edge; a top-down view of the magnet overhang after the resist was stripped is shown in the right-hand image in Inset A. (4) The cantilever bodies were defined using photolithography and were etched using an SF_6:O_2 plasma (before and after top-down views of Step 4 are shown in the left and middle images of Inset B). (5) PECVD SiO_2 was deposited on the top and bottom sides of the wafer. (6) Windows in the wafer substrate under the cantilevers were defined in photoresist, and the exposed PECVD SiO_2 was etched using CHF_3:O_2 plasma. (7) The silicon handle wafer was anisotropically etched using through-wafer Bosch etching. (8) The cantilevers were released by using BOE to etch the BOX and PECVD SiO_2 layers, and the cantilevers were critical point dried to prevent stiction.

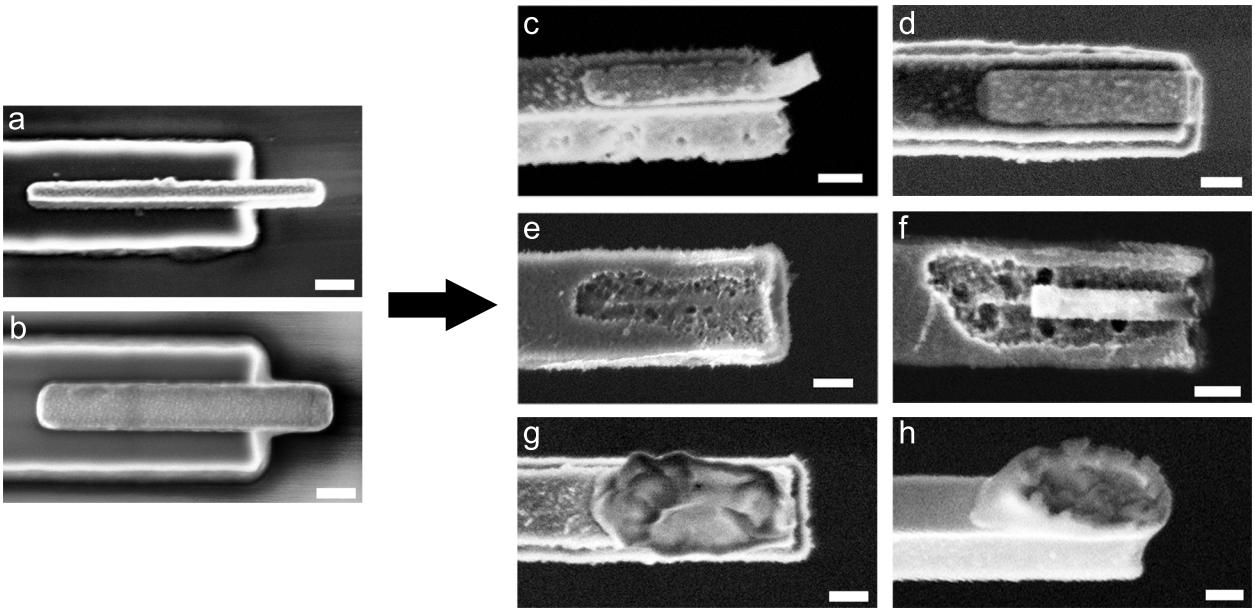

Figure 2.2: SEM images of nickel nanomagnets at the leading edge of attonewton-sensitivity cantilevers. (a,b) Nickel magnets remained intact after the completion of the front-side cantilever definition (Step 4 in Figure 2.1). (c-h) Nickel magnets were extensively damaged at the end of the process. Common damage scenarios consisted of partial or complete damage to the magnet leading edge (c,d), damage involving the removal of silicon near the nanomagnet (e,f), or the alteration of the nickel structure (g,h). All scale bars represent 200 nm.

magnets survived the remainder of the process. Multiple damage scenarios were observed: the magnetic material at the leading edge of the magnets was damaged (Figure 2.2(c)) or missing (Figure 2.2(d)); device layer silicon surrounding the nanomagnets was removed and the nickel nanomagnets were completely (Figure 2.2(a)) or partially (Figure 2.2(a)) missing; or, the nickel material reacted to form an unknown amorphous compound (Figure 2.2(g,h)). It was extremely difficult to explore the mechanism(s) leading to this extensive damage since, to avoid physical damage during backside processing, the magnets and cantilevers were encased in PECVD SiO_2 after the cantilever definition; after the protective PECVD SiO_2 was deposited, the magnets could not be visualized until the cantilevers were released.

The formation of nickel silicide can account for some of the observed damage in Figure 2.2. During deposition of the nickel magnetic material, the 1.5 nm thick native SiO_2 layer on the

silicon substrate [103], coupled with a chromium or titanium adhesion layer, is sufficient to prevent the formation of nickel silicide. However, nickel silicide readily forms on Si⟨100⟩ substrates at temperatures above 250°C [104, 105]; the nickel-rich Ni_2Si phase is formed at 250-350°C, and increasingly silicon-rich phases are observed above 350°C. There are two processing steps when the nickel nanomagnets were exposed to temperatures above 250°C in the Hickman fabrication protocol: (1) during the 275°C PECVD SiO_2 deposition on the front and back sides of the wafer, and (2) during the through-wafer Bosch etch. Although helium cooling should prevent temperature spikes during Bosch processing, the helium flow is insufficient to cool the wafer once the handler wafer is attached, and it is likely that the temperature exceeds 300° [106]. The damage observed in Figure 2.2(g,h) thus can be attributed to the formation of nickel silicide. However, it is unlikely that the formation of nickel silicide accounts for the damage to the nanomagnets that are partially or completely missing after the release in BOE, since nickel silicide is resistant to etching by hydrofluoric acid/BOE [107].

The remainder of the damage observed in Figure 2.2 required another mechanism. Other than the silicon substrate and the chromium adhesion layer, the only chemicals that the nickel was exposed to directly were the silane (SiH_4) and nitrous oxide (N_2O) precursors for the PECVD SiO_2 deposition. By concurrent exposure to a plasma and elevated temperatures of 275°C, it is likely that these PECVD SiO_2 precursors could react with the nickel nanomagnets. Silane has been shown to dissolve into nickel at temperatures above 125°C [108], and decomposed precursors that form reactive oxygen species could oxidize the nickel beyond the typical 3 nm NiO thickness [109–112] observed at temperatures up to 275°C.

Evidence that interactions between unprotected nickel nanomagnets and the PECVD SiO_2 precursors contributed to the damage observed in Figure 2.2 was obtained during the fourth iteration of reproducing the Hickman fabrication protocol. For this wafer, a film

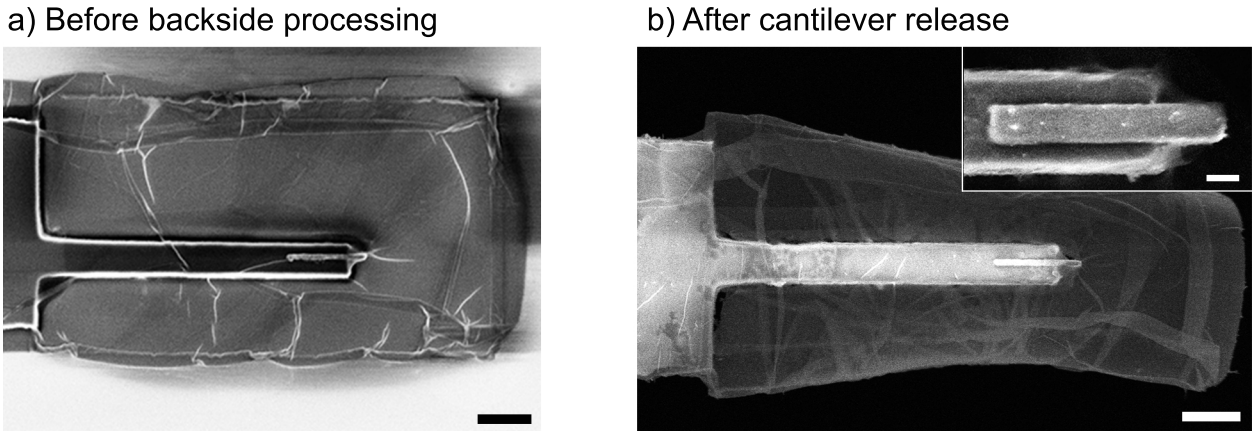

Figure 2.3: SEM images of the leading edges of magnet-tipped cantilevers that were coated with a thin film, likely residual photoresist. (a) Magnet-tipped cantilever after the cantilever bodies were etched (Step 4 in Figure 2.1) and the photoresist strip processing step had been conducted. However, the SEM image indicates that the resist had not lifted off properly. (b) The leading edge of a magnet-tipped cantilever after release. The thin film was still present on most cantilevers, with visually intact magnets underneath. The film had lifted off of a few of the magnets during the release; one of these film-free magnets is shown in the inset. The scale bars in (a) and (b) represent 1 µm, and the scale bar in the inset represents 200 nm.

remained over the cantilevers and magnets after the front-side photolithography step used to define the silicon cantilever bodies (Figure 2.3(a)); the film was likely residual photoresist. Although film-coated cantilevers would be unsuitable for MRFM experiments, the processing of the wafer was still completed. It was observed that unlike the other trials, most of the film-coated magnets remained intact after processing (Figure 2.3(b)); the residual film even lifted off of some magnets during release, leaving a few magnets that were film-free and largely intact (Figure 2.3(b) inset). The only known difference between the first three iterations of the Hickman protocol, in which almost all magnets were damaged, and the fourth trial, when many magnets remained intact, is that the magnets for the fourth trial were inadvertently protected during the PECVD deposition. This observation suggests that in addition to silicide damage, the magnets were also damaged by the PECVD SiO_2 processing step.

The integrity of one of the nickel nanomagnets that had remained intact during the fourth iteration of reproducing the Hickman protocol, and was not coated with resist after

the release of the cantilever, was assessed by scanning transmission electron microscopy (STEM) and electron energy loss spectroscopy (EELS). The magnet-tipped cantilever was prepared for TEM analysis by attaching the leading edge of the cantilever to a copper TEM grid using a dual-beam FEI Strata 400 STEM FIB system. The TEM grid was loaded in the flipstage (tilted 90°) so that the magnet would be viewed top-down in the transmission electron microscope and so the cantilever could be rigidly mounted as shown in Figure 2.4. All STEM and EELS experiments were conducted using a 200 kV FEI Tecnai F20-ST STEM. A top-down, bright-field STEM image of the overhanging portion of the nickel nanomagnet is shown in Figure 2.5.[2] Strong grain boundary contrast indicates that the bulk of the nanomagnet was polycrystalline with a grain size of 20-40 nm, whereas the leading and side edges of the nanomagnet appeared amorphous.

EELS analysis was conducted to assay the elemental composition of the nanomagnets with nanometer resolution. In all spectra, the only observed elements were chromium, nickel, and oxygen. An example EELS spectrum is shown in Figure 2.6, with each of the peaks of interest labeled. The inset in Figure 2.6 shows a dark-field image of the leading edge of the nanomagnet; the small cross indicates the position of the electron beam during the EELS measurement.

EELS linescans were obtained to determine the composition of the nanomagnet. To compare the relative atomic concentrations of each element, scattering cross sections were obtained from DigitalMicrograph using the Hartree-Slater approximation [113]. The energy ranges over which the chromium, oxygen, and nickel peaks were integrated were 575 to 595 eV, 532.2 to 575.7 eV, and 855.5 to 955.5 eV, respectively. The convergence angle was 9 mrad and the collection angle was 20 mrad. The calculated scattering cross sections for chromium, oxygen, and nickel were 1245 barns, 880 barns, and 2006 barns, respectively.

[2]Figures 2.5 and 2.7 adapted with permission from S. A Hickman, E. W. Moore, S.-G. Lee, J. G. Longenecker, S. J. Wright, L. E. Harrell, and J. A. Marohn, ACS Nano **4**, 7141 (2010). Copyright 2010, American Chemical Society.

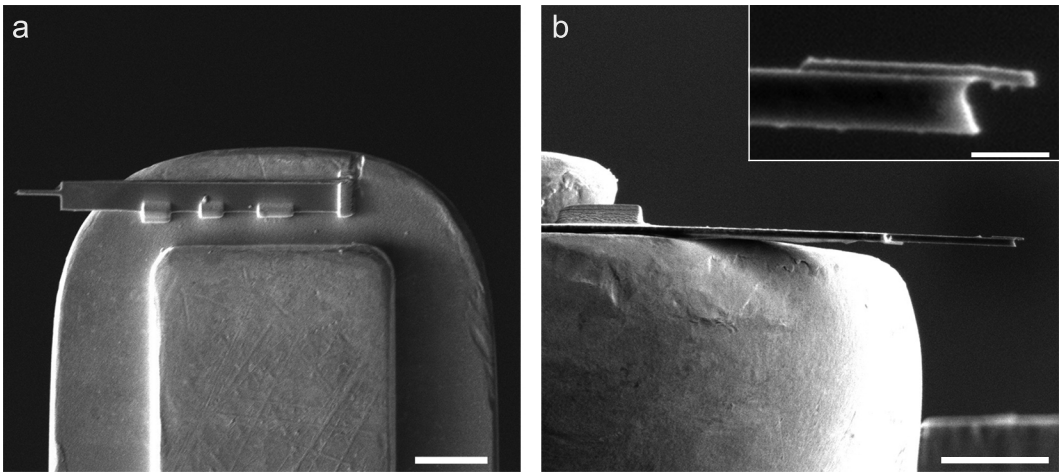

Figure 2.4: SEM images of the leading portion of a magnet-tipped cantilever attached to the center finger of a copper TEM grid. (a) Side-on view showing the cantilever mounted on the TEM grid. The TEM grid was mounted in the flipstage so that the cantilever could be positioned flush against the TEM grid finger and so that the magnet would be viewed top-down in the transmission electron microscope. Four rectangular patches of platinum were deposited to adhere the cantilever to the TEM grid. (b) View from the top of the TEM grid. A magnified side-on view of the magnet is shown in the inset. The scale bar in (a) represents 10 µm, the scale bar in (b) represents 5 µm, and the scale bar in the inset represents 500 nm.

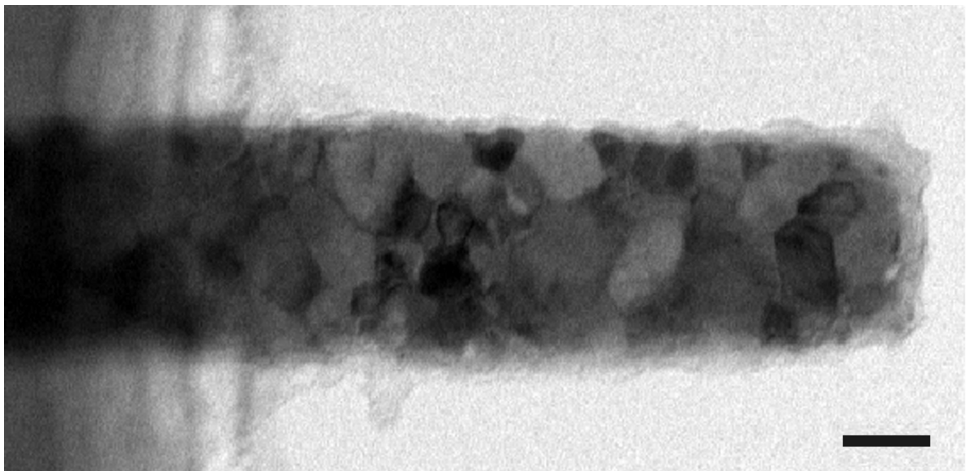

Figure 2.5: Bright-field STEM image of the overhanging portion of a 100 nm thick nickel nanomagnet with a 5 nm thick chromium adhesion layer underneath. The leading edge of the silicon cantilever is viewable on the left side of the image. The scale bar represents 50 nm.

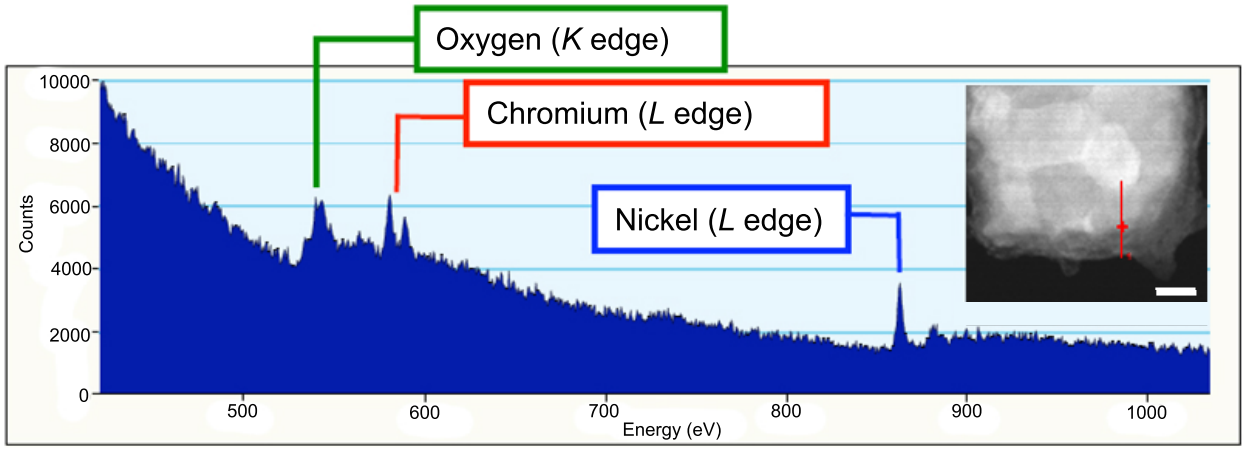

Figure 2.6: Example EELS spectrum showing the electron energy loss edges for oxygen, chromium, and nickel against the EELS background signal. The EELS measurement was one of many points taken along the red line shown in the dark-field STEM image of the magnet leading edge; the specific position of the electron beam during the measurement is indicated by the small red cross. The scale bar in the STEM image represents 20 nm.

EELS linescans were collected along the leading edge (Figure 2.7(a,b)) and side edge (Figure 2.7(c,d)) of the nickel nanomagnet. Near the center of the nanomagnet, the ratio of chromium to nickel was 0.05:1, which is in excellent agreement with the measured thicknesses for chromium and nickel of 5 nm and 100 nm, respectively. As both the leading and side edges were approached, the nickel concentration decreased and the oxygen concentration increased. In Figure 2.7(b), the concentration of nickel at the leading edge began to decrease 20 nm from the edge, implying that the leading 20 nm of magnetic material was damaged. In Figure 2.7(d), a 14 nm thick damage layer was observed. It should be noted that although the oxygen-to-nickel ratio of 1:1 for the damaged portion of the nanomagnet side edge could correspond to the formation of NiO, the anomalously high oxygen-to-nickel ratio at the leading edge cannot be explained solely by the formation of an oxide layer. It is likely that the additional oxygen content was due to oxygen-containing organic material on the magnet surface that was not measured in the EELS measurement.

In summary, SEM, STEM, and EELS analysis of four iterations of the Hickman protocol indicated that multiple factors contributed to nanomagnet damage during processing. As

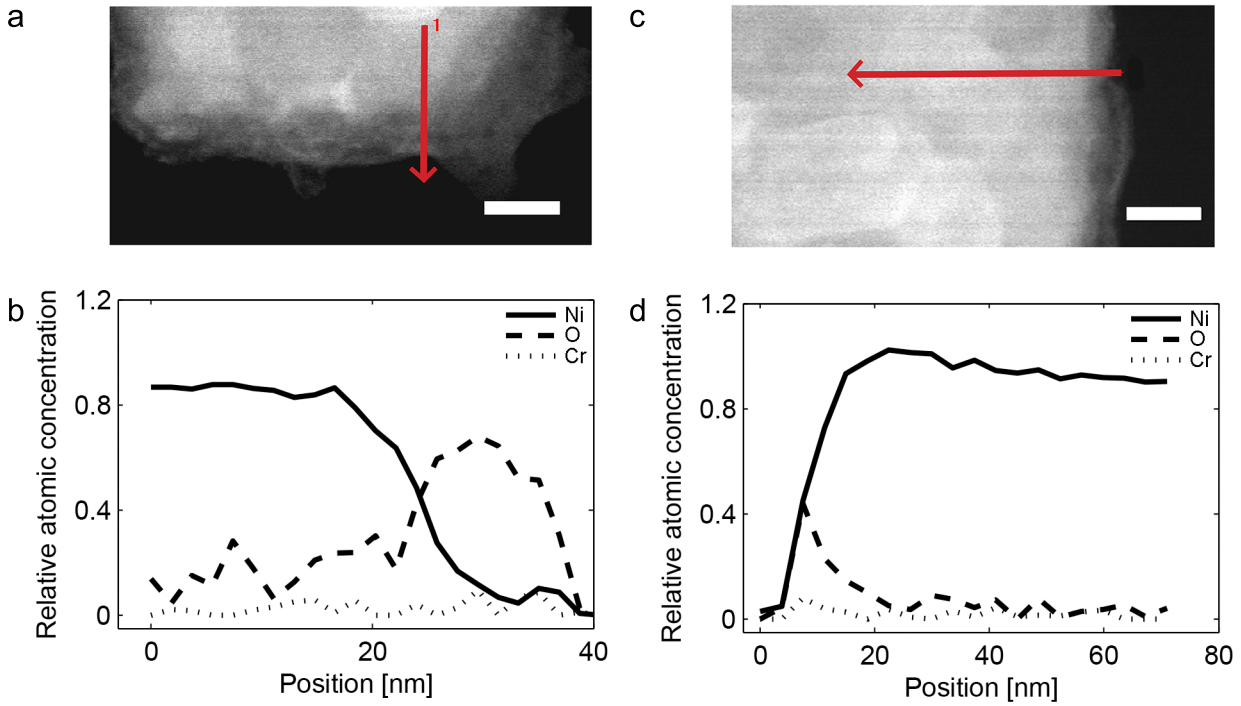

Figure 2.7: EELS linescans along the edges of the overhanging portion of a nickel nanomagnet. Dark-field STEM image (a) and relative EELS signal (b) for the leading edge of the nanomagnet are shown on the left-hand side. Dark-field STEM image (c) and relative EELS signal (d) for the side edge of the nanomagnet are shown on the right-hand side. The red arrows in the STEM images indicate the length and direction of the EELS linescans. The scale bars in (a) and (c) represent 20 nm. In the EELS scans, nickel, oxygen, and chromium are plotted using solid, dot-dashed, and dotted lines, respectively.

expected, silicide formation likely contributed to the damage mechanism. However, new findings indicated that damage also occurred during the PECVD SiO_2 processing step. When the nanomagnets were protected during the deposition of PECVD SiO_2, only 20 nm of damage was observed. These findings suggest that the use of barrier layers should be explored to make the Hickman protocol more robust against the formation of undesired nickel compounds, including nickel oxide and nickel silicide. The implementation of barrier layers in the Hickman protocol is discussed in the next section.

2.4 Barrier Layers Introduced to Prevent Nanomagnet Damage

The use of barrier layers to prevent silicidation of magnetic material was considered previously for the Hickman fabrication protocol, but only for cobalt magnetic material [91]. In Ref. 91, the use of a tantalum barrier layer was tested by evaporating 20 nm of tantalum under cobalt nanomagnets. To assess whether the barrier layer was effective, the magnets were coated with a thin layer of PECVD SiO_2 and annealed at 500°C for 5 min to mimic the heating conditions of the Bosch through-wafer silicon etch. The PECVD SiO_2 was then removed in BOE. The cobalt magnets appeared to be damaged after processing; however, it was inconclusive whether the damage was caused by the anneal or by other processing, since damage to cobalt nanomagnets was observed both for the annealed magnets and for control samples that were coated with PECVD SiO_2 but not annealed. In Ref. 91 the damage to the cobalt nanomagnets was attributed to the BOE etch that removed the PECVD SiO_2 after the anneal; data presented in Section 2.3 indicates that the damage instead may have occurred during the PECVD SiO_2 deposition.

The implementation of barrier layers to prevent damage to nickel magnetic material during the Hickman fabrication protocol had not been studied previously, nor had silicidation

or oxidation barriers been implemented in successful trials. The use of a magnet capping layer to prevent nickel oxidation and protect the magnets during the PECVD SiO_2 deposition step was of particular interest based on the findings of Section 2.3. Prevention of nickel silicide and nickel oxide have been demonstrated previously for other applications using tantalum and alumina (Al_2O_3) layers, respectively. Nickel silicide forms by the diffusion of nickel atoms into silicon above temperatures of 250°C [104, 105]. The introduction of a thin tantalum layer between a nickel film and a silicon substrate has been observed to inhibit the formation of nickel silicide until temperatures above 400°C [114]; 10 nm thick tantalum layers inhibited silicide growth of a Ni/Ta/Si sample for the full length of a 30 min anneal at 400°C, and a tantalum film that was just 2 nm thick prevented the formation of nickel silicide for the first 10 minutes of a 400°C anneal. Nickel oxidation occurs by the chemisorption of oxygen atoms onto the nickel surface. The oxidation of the nickel component of permalloy ($Ni_{81}Fe_{19}$) has been prevented by coating the permalloy surface with 1.5 nm of aluminum, which oxidized upon exposure to air to an alumina film that was less than 5 nm thick [115]. Conformal atomic layer deposition (ALD) alumina films have also been demonstrated to prevent oxidation; a sub-1 nm thick film (2 monolayers) deposited at 50°C successfully prevented the oxidation of silver film-over-nanosphere (AgFON) substrates, and remained stable for at least 9 months [116].

To determine whether tantalum and ALD alumina barrier layers would be effective at mitigating the formation of nickel silicide and nickel oxide during the integrated overhanging magnet-on-cantilever fabrication protocol of Ref. 81, a test sample was prepared and analyzed by EELS. The sample was deposited by e-beam evaporation of 100 nm of tantalum and 100 nm of nickel on a Si$\langle 100 \rangle$ wafer, followed by ALD deposition of approximately 9 nm of alumina (processing temperature 110°C). The sample was annealed for 2 hours at 350°C, which was the highest temperature expected during processing steps of the Hickman fabrication protocol. The sample was cross-sectioned using a dual-beam FIB and assessed by STEM

and EELS using the parameters that were described in Section 2.3. In Figure 2.8, a bright-field STEM image of the cross-section of the film is shown on the left-hand side. The EELS linescan shown on the right-hand side of Figure 2.8 was collected along the transition from the nickel layer to the tantalum layer, as indicated by the arrow in the STEM image. The tantalum EELS signal was insufficient to quantify, but the relative concentrations of nickel and silicon were assessed. The primary finding was that no silicon was observed in the nickel or tantalum layers, indicating that the tantalum barrier layer had successfully prevented the formation of nickel silicide. Additional EELS linescans along the nickel-alumina interface (data not shown) indicated that oxygen was only contained in the top few nanometers of the nickel film. Oxidation of a few nanometers of nickel was expected since the unprotected nickel film was exposed to air prior to the deposition of the ALD alumina film. The absence of further oxidation indicated that using an ALD alumina film as a barrier against oxidation damage had been successful.

Based on the success of the barrier layer test sample, tantalum and ALD alumina barrier layers were incorporated into the Hickman fabrication protocol to assess their effectiveness at preventing the silicidation and oxidation of nickel nanomagnets, respectively. A schematic detailing the implementation of the barrier layers is shown in Figure 2.9. A tantalum layer that was 10 nm thick was deposited between the 5 nm thick chromium adhesion layer and the 100 nm thick nickel film using e-beam evaporation. Note that the thickness of the tantalum barrier layer was reduced from 100 nm for the test sample tantalum layer to only 10 nm for the nickel nanomagnets because nickel nanomagnet layers were observed to delaminate from 100 nm thick tantalum underlayers. A 7.5 nm thick ALD alumina film (processing temperature 110°C) was deposited after definition of the cantilevers and before deposition of the PECVD SiO_2 layer. Integration of ALD alumina into the fabrication protocol worked exceptionally well because alumina is etched readily in BOE. Thus, the ALD alumina was removed during the cantilever release of the magnet-on-cantilever fabrication protocol and

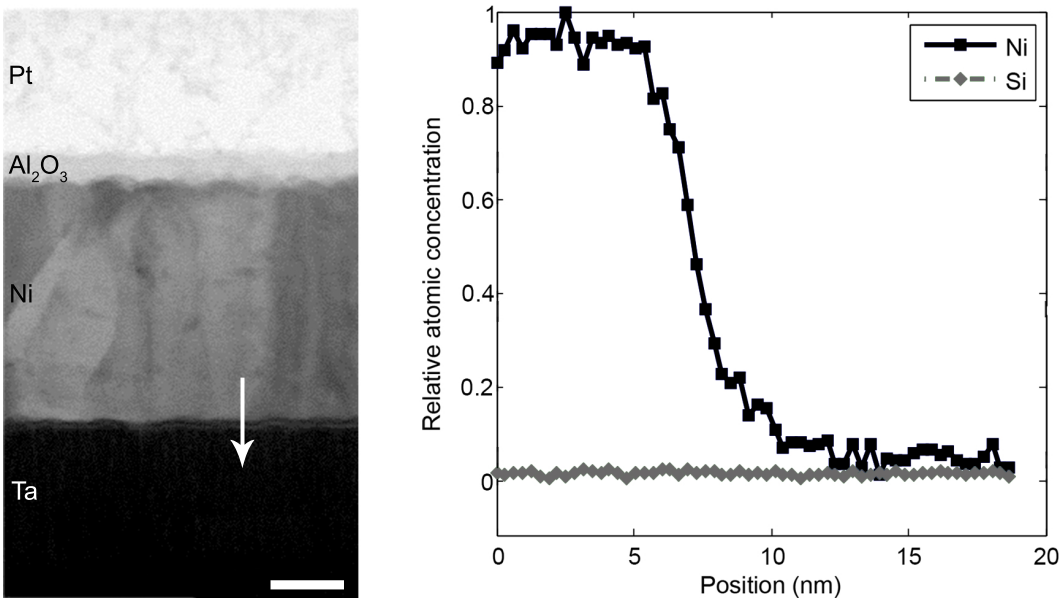

Figure 2.8: EELS analysis of a nickel film protected by tantalum and ALD alumina barrier layers to prevent the formation of nickel silicide and nickel oxide, respectively. The film was annealed at 350°C to mimic the conditions of the Bosch through-wafer silicon etch. A bright-field, cross-sectional STEM image is shown on the left-hand side. From top-to-bottom, the layers of the sample are a protective platinum coating deposited during the FIB sample preparation, ALD alumina (9 nm), nickel (100 nm), and tantalum (100 nm). The STEM scale bar represents 25 nm. The white arrow indicates the length and direction of the EELS linescan shown on the right-hand side of the image. The relative intensities of nickel (black squares) and silicon (gray diamonds) are shown. The EELS tantalum signal was too weak to measure.

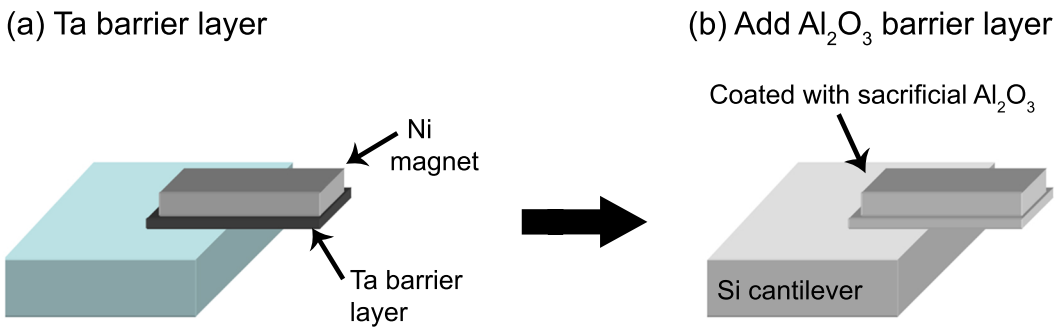

Figure 2.9: Schematic demonstrating how the tantalum and alumina barrier layers were incorporated into the revised overhanging magnet-tipped cantilever fabrication protocol. (a) The tantalum barrier layer was incorporated during the nickel nanomagnet evaporation. (b) After the front-side wafer processing was complete, the front side of the wafer was coated with conformal alumina before being coated with PECVD SiO_2. The alumina film remained in place until the release of the cantilevers. The alumina was etched by BOE during the release, leaving the magnets and cantilevers free from an alumina coating after processing.

the nickel nanomagnets were free from added material at the completion of the process. The absence of material extending past the nanomagnet leading edge was critically important since the nanomagnet leading edge could be brought as close as 5 nm from the surface during MRFM experiments. It was also essential that the cantilever not be coated with any material after processing, since the cantilever resonance frequency and quality factor could be adversely affected.

SEM images of nickel nanomagnets fabricated with the tantalum and ALD alumina barrier layers are shown in Figure 2.10. The images show that the nickel nanomagnets remained visually intact after the cantilevers were released — a very promising finding when compared to the sub-1% yield of the original fabrication protocol. However, the true test of the success of the fabrication protocol was whether the nanomagnets remained well-magnetized after processing. The magnetization of one of the nickel nanomagnet-tipped cantilevers that had been processed with barrier layers was assessed by frequency-shift cantilever magnetometry (Figure 2.11). In cantilever magnetometry experiments [89, 93, 117], shifts in the cantilever frequency are measured as a function of applied magnetic field; in Figure 2.11, the field was

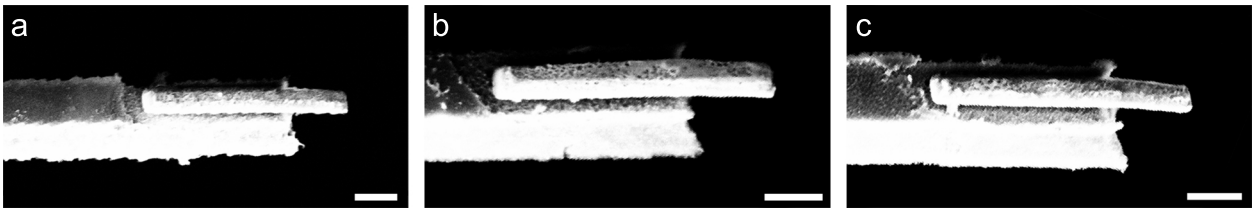

Figure 2.10: Side-view SEM images of released magnet-tipped cantilevers that were fabricated using tantalum and alumina barrier layers. The nanomagnets appeared to be visually intact. All scale bars represent 300 nm.

first swept from +5 T to −5 T, and then from −5 T to +5 T. Note that the divergence of the resonance frequency at positive fields in Figure 2.11 for the two directions of scanning was due to drift in the cantilever frequency during the $\sim$ 2 hour measurement. A typical shift in frequency for a well-magnetized nickel nanomagnet of similar volume would be at least $\Delta f = 0.36$ Hz [81]. In Figure 2.11, the shift in resonance frequency was approximately 0.01 Hz. Thus, surprisingly and unfortunately, the nickel nanomagnet was almost completely demagnetized in spite of appearing visually intact.

The reason for the poorly-magnetized nickel nanomagnet has remained puzzling. The magnetic material was not expected to be pinned by the tantalum barrier layer, but even if pinning of the magnetic domain walls had occurred, we would not expect the associated anisotropy to be large enough to prevent full alignment of the tip's magnetization with the high external field of 5 T. Since cantilever magnetometry was only conducted on one magnet-tipped cantilever, it is possible that the majority of the nanomagnet delaminated during transport or loading into the instrument. Due to the two weeks of processing time required for each iteration of the integrated overhanging magnet-tipped cantilever fabrication protocol, with or without the incorporation of barrier layers, further trials to determine the reason for the discrepancy between the visually intact nanomagnets and the non-magnetic cantilever magnetometry findings were not pursued.

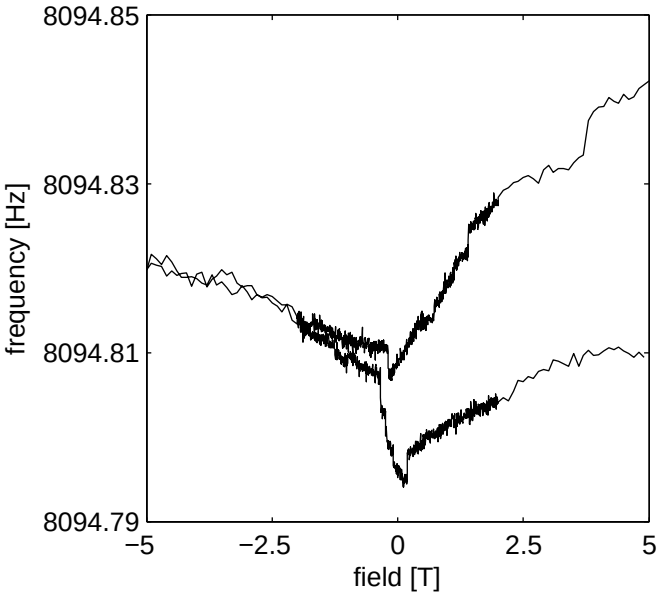

Figure 2.11: Frequency-shift cantilever magnetometry for a nickel nanomagnet fabricated using tantalum and alumina barrier layers. Data was collected by sweeping the applied magnetic field from +5 T to −5 T, and then from −5 T to +5 T. The divergence at positive fields for the two directions of scanning was due to thermal drift during the measurement.

2.5 Discussion

Out of the previously-developed techniques for the fabrication of attonewton-sensitivity cantilevers with integrated magnetic tips, the batch fabrication process introduced by Hickman *et al.* in Ref. 81 demonstrated the best promise for implementation in high resolution MRFM experiments. Yields were not reported by Hickman *et al.*, but damage to the nanomagnets was discussed at length [91]. For overhanging nickel magnets that did remain intact after the cantilevers were released, frequency-shift cantilever magnetometry indicated that the saturation magnetization $\mu_0 M_{\rm sat}$ was only approximately 67% of the theoretical value of $\mu_0 M_{\rm sat} = 0.6$ T. Attempts to switch to cobalt, which is a material with a factor of 3× larger saturation magnetization than nickel, were unsuccessful [91].

In this chapter, four attempts to reproduce the Hickman fabrication protocol for nickel nanomagnets were discussed. Three iterations of the process led to yields of less than 1%,

indicating that the process was either unreliable or contained processing steps that were incompatible with the stringent requirements for maintaining well-magnetized nickel magnetic material. During the fourth iteration of reproducing the Hickman protocol, a residual film did not lift off properly after the definition of the cantilevers. Surprisingly, the nanomagnets processed during this fourth iteration, most of which were still coated with the film after the cantilever release, remained visually intact underneath the residual film. EELS elemental analysis indicated that there was less than 20 nm of damage to the nickel leading edge of magnets that had been coated with a film during processing. These unexpected findings indicated that the use of barrier layers, and in particular a capping layer over the magnets to provide protection during PECVD SiO_2 deposition, could improve the yield of nanomagnet-tipped cantilevers.

The incorporation of barrier layers into the Hickman fabrication protocol were pursued in order to protect the magnets during PECVD SiO_2 deposition and to improve the robustness of the process against the formation of nickel silicide. When tantalum and ALD alumina barrier layers were added to the Hickman protocol, the overhanging magnets appeared to be visually intact after the release of the overhanging magnet-tipped cantilevers. However, frequency-shift cantilever magnetometry conducted on one of the magnets indicated that the nickel nanorods were nonmagnetic.

Even with the unexplained magnetometry data, it is clear that the implementation of barrier layers — and in particular the protection of the nanomagnets using ALD alumina — had a beneficial effect on the visual integrity of the nanomagnets. The results presented in this chapter thus indicate that the nanomagnets in the original Hickman fabrication protocol were damaged both by heating during the Bosch through-wafer etch and by interactions with the PECVD SiO_2 precursors. If the incorporation of barrier layers is considered further in future experiments, additional cantilever magnetometry and superconducting quantum

interference device (SQUID) measurements should be conducted to determine whether the cantilever magnetometry result in Figure 2.11 is correct.

If the nanomagnets are consistently demagnetized, then the use of other barrier layer materials could be considered, such as replacing the ALD alumina film with a metal film to encase the nanomagnets during the backside processing. However, a significant number of process integration challenges must be considered if the protective capping layer is changed. Nickel is damaged by BOE, so the capping layer must protect the nickel nanomagnets until 1-2 minutes before the end of the BOE cantilever release. However, if the film is still in place after the cantilever release, any stress in the capping layer film would instantly break the fragile cantilevers. Additionally, no barrier layer films could cover the cantilevers or extend more than 2-3 nm beyond the leading edge of the nanomagnets after the cantilevers are released, since the signal in MRFM experiments requires the close approach of the nanomagnets to the sample surface. Integration of alternative capping layers would likely require significant process development.

2.6 Moving Forward: A New Protocol is Needed to Improve Yield and Magnetization of Magnet-Tipped Cantilevers

With the 38 steps and 2 weeks of processing time required for each iteration of the Hickman protocol [81], conducting failure analysis was a slow and tedious process. The nanomagnets were deposited in one of the first processing steps, and all cantilever processing that followed the nanomagnet deposition had to be conducted within an acceptable heat budget and using compatible chemicals. The fabrication protocol also required that the nanomagnets be encased during multiple consecutive processing steps, which meant that they could not be imaged during the final half of the process. Thus, multiple factors contributing to the

damage mechanism were difficult to disentangle. Furthermore, if the magnetic material was switched to cobalt or to another material with a higher saturated magnetic moment than nickel, then new compatibility constraints would need to be considered and would again be difficult to assess.

These significant process integration challenges for the fabrication of integrated, overhanging magnet-on-cantilevers are precisely why many MRFM experiments are instead conducted using the sample-on-cantilever geometry [12, 48, 70, 71]. The highest-gradient magnetic particles employed in MRFM imaging experiments to date have all been fabricated off-cantilever [12, 48], where process integration is not required and the magnetic material can be analyzed immediately after deposition.

Chapters 3 through 5 of this thesis seek to answer the following question: Could the best of off-cantilever magnet fabrication methods be combined with the design of a high-gradient magnet-on-cantilever fabrication protocol? Continued progress towards the development of high-gradient magnetic tips on cantilevers — which requires higher magnet-on-cantilever yield, better-magnetized tips, and the use of new magnetic materials — would be greatly facilitated if there was a way to conduct rapid-prototyping fabrication trials with only a few days of processing time. Additionally, failure analysis could provide fast, conclusive results if the nanomagnets could be analyzed after each processing step. Unfortunately, both of these goals would be challenging, or impossible, to implement using the Hickman protocol.

Existing alternative techniques for the fabrication of magnets on cantilevers also do not meet the criteria for the rapid-prototyping development of cantilevers suitable for high-sensitivity magnet-on-cantilever MRFM experiments. FIB milling of magnetic material has been shown in MRFM experiments to not produce sufficiently high magnetic-field gradients [25, 53]. It is possible that FIB-induced damage could be minimized using low-energy ion beam polishing [118]; however, serial preparation and device-to-device variation would

still limit the desirability of FIB preparation. For magnet-tipped magnetic force microscopy (MFM) cantilevers, the magnetic material is oriented in the wrong direction [119]; a cone coated with magnetic material is oriented out of the plane of the cantilever instead of in-line with the cantilever, as required for high-sensitivity MRFM experiments. MFM tricks of adding magnetic coatings to narrow-diameter structures such as nanowires [120] or FIB-thinned silicon [121, 122], but with the tips oriented to extend inline past the cantilever leading edge, would (1) result in significant device-to-device variation and (2) have non-magnetic cores that would lower the total magnetic volume and the achievable MRFM signal strength. The electrodeposition of magnetic material on gold catalytic seeds at the ends of silicon nanowire cantilevers [123] would also lead to non-magnetic cores, as well as spherical magnetic particles with low tip-field gradients. The use of iron-filled multiwall carbon nanotubes (MWCNTs) [124] would result in 5 to 40 nm thick shells of carbon surrounding the magnetic material. Additionally, the 10-20 nm diameter magnetic material inside the MWCNTs could not be optimized for varying tip-sample separations (Eq. 1.9), and nanotubes have been found to be difficult to align precisely parallel to the cantilever length. And although directed assembly has been used in high yield to align silicon and rhodium nanowires [125], it is unclear how the necessary sacrificial electrodes could be incorporated into MRFM cantilever fabrication without incurring a different, but equally long, list of process integration challenges. One alternative batch-fabrication process that could be possible to implement would be to fabricate the cantilevers — including the backside processing — first [126], and to not pattern the nanomagnets until immediately before the cantilever release. However, the processing time required per trial would be equivalent whether the nanomagnets were fabricated before or after the definition of the cantilevers.

In Chapter 3, a novel approach is introduced to conduct rapid-prototyping fabrication trials of batch-fabricated nanomagnets that are attached to overhang attonewton-sensitivity cantilevers. In the protocol, batch-fabricated nanomagnets that overhang microscale, sus-

pended silicon chips are prepared separately from attonewton-sensitivity cantilevers; the nanomagnets are then serially attached to the leading edge of cantilevers. This fabrication protocol indeed meets the goals discussed in this section: (1) the protocol is designed so that the magnets, which are fabricated off-cantilever, can be analyzed after any processing step using cantilever magnetometry or elemental characterization techniques such as EELS; (2) the fabrication of the magnets does not need to be compatible with the cantilever fabrication protocol; and (3) the magnet-tipped chip fabrication protocol requires only a few days of processing time, which makes it amenable to rapid prototyping experiments. By fabricating the magnets off-cantilever, process integration challenges are greatly minimized and can be adjusted for a variety of magnetic materials with different fabrication constraints, and by attaching the magnet-tipped chips to attonewton-sensitivity cantilevers, all of the benefits of working in the magnet-on-cantilever geometry can be retained. In Chapter 5 the benefit of using this combination batch-and-serial approach is confirmed by using a cobalt nanomagnet-tipped chip-on-cantilever assembly to detect NMR-MRFM signal. The tip-field gradient produced by the cobalt nanomagnet is as high as the gradient used in the 4-10 nm resolution imaging experiment of Degen *et al.* [12].

In future experiments it may be desirable to reintegrate the magnets and cantilevers into one batch-fabrication protocol. If so, cantilever processing steps could be added one-at-a-time to the magnet-tipped chips process of Chapter 3 to conclusively determine all steps contributing to the damage mechanism; since the nanomagnet chips are suspended, the chips could be lifted out after any processing step to conduct cantilever magnetometry or EELS experiments. The impact of adding barrier layers on the magnetization of the nanomagnets could also be reassessed using the rapid-prototyping technique.

Acknowledgements

Thanks to Steve Hickman for invaluable conversations regarding the proper implementation of the fabrication techniques used in Ref. 81. Thanks to Mick Thomas for assistance with TEM sample preparation, and to Pinshane Huang, John Grazul, and David Muller for assistance with STEM and EELS experiments. Coworker Eric Moore assisted with cantilever magnetometry, and undergraduate student Eric VanWerven assisted with integration of the tantalum barrier layer into the fabrication protocol. Work in this chapter was conducted with the financial support of the National Institutes of Health (Grant No. 5R01GM-070012), the Army Research Office MultiUniversity Research Initiative (Grant No. W911NF-05-1-0403), and the National Science Foundation through the Cornell Center for Nanoscale Systems (Grant Nos. EEC-0117770 and EEC-0646547). The transmission electron microscopy facility within the Cornell Center for Materials Research, which is supported by the National Science Foundation Materials Research Science and Engineering Centers program (Grant No. DMR-0520404), was used for TEM sample preparation, STEM imaging, and EELS analysis. Fabrication was conducted in the Cornell NanoScale Science and Technology Facility, a member of the National Nanotechnology Infrastructure Network, which is supported by the National Science Foundation (Grant No. ECS-0335765).

CHAPTER 3

MAGNET-TIPPED CHIP FABRICATION AND ATTACHMENT TO ATTONEWTON-SENSITIVITY CANTILEVERS BY FOCUSED ION BEAM MANIPULATION

3.1 Introduction

As discussed in Chapter 2, although the tips fabricated using the integrated magnet-on-cantilever protocol developed by Hickman *et al.* exhibited record-small force sensitivity near a surface, their fabrication was problematic [81]. The nanomagnets were damaged extensively by processing incompatibilities during the thirty-eight steps of fabrication, resulting in extremely low yields. Scanning electron microscopy (SEM) imaging indicated that less than 1% of the magnets remained intact after processing; the rest of the magnets were either physically absent after processing or were damaged and unusable, as shown in Figure 2.2.

In order to conduct high resolution MRFM experiments, process yields had to be greatly improved and magnet damage had to be reduced, particularly at the leading edge where the force gradient acting on the sample spins is greatest. To this end, a high-yield method for fabricating overhanging nanomagnets on micrometer-scale silicon chips and serially attaching them to attonewton-sensitivity cantilevers has been developed. This approach made it possible to reduce the processing time for nanomagnet fabrication from approximately two weeks (see Section 2.3) to just four days, and it completely decoupled the fabrication of the nanomagnets, which are particularly susceptible to heating and chemical damage, from the fabrication of the cantilevers, which involves multiple high-temperature processing steps. The process was first successfully demonstrated for nickel nanomagnets; process modifications have also enabled the fabrication of cobalt nanomagnets, which have saturated magnetic moments that are three times higher than is observed for nickel.

The high-yield fabrication protocol involves a combination of batch- and serial-fabrication techniques. The overhanging nanomagnets were batch-fabricated on silicon microchips. These microchips were released prior to deposition of the nanomagnets so that the chips could be analyzed after any post-deposition processing step. To obtain nanomagnets on cantilevers, the magnet-tipped chips were serially attached to separately-fabricated attonewton-sensitivity silicon cantilevers using focused ion beam (FIB) manipulation. FIB lift-out and milling is routinely used to image sample cross-sections [127, 128] and to prepare transmission electron microscopy (TEM) samples [129–132]. Here we show that the ability of FIB to mill, transfer, and adhere samples with microscale precision makes it an ideal tool for lifting out the magnet-tipped chips and adhering them to the leading edges of cantilevers.

In addition to the fabrication details provided in the subsequent sections, thorough procedures for fabricating the magnet-tipped chips and for conducting the FIB attachment protocol are provided in Appendix A and Appendix B, respectively. A step-by-step procedure for fabricating blank cantilevers can be found in Appendix A of Ref. 91, starting with Section A.5.

3.2 Nickel Nanomagnet-Tipped Chip Fabrication Protocol

Overhanging nanomagnet-tipped silicon chips were fabricated from 100 mm diameter silicon-on-insulator (SOI) wafers having a device silicon thickness of 340 nm, a buried oxide (BOX) thickness of 400 nm, and a silicon handle wafer thickness of 500 µm. The device silicon resistivity was 14 to 22 Ω cm, corresponding to a boron dopant concentration of 6 to 9 × 10^{14} cm^{-3}.

Alignment Marks. Lift-off alignment marks for the three subsequent electron beam (e-beam) lithography steps were defined in a bilayer of 50 nm of 950,000 molecular weight

(MW) (poly)methylmethacrylate (PMMA) on top of 550 nm of 495,000 MW PMMA, and were patterned using either a JEOL JBX9300FS (at 2 nA) or a JEOL JBX6300FS 100 kV (at 1 nA) e-beam lithography system. The marks were deposited by e-beam evaporation (CVC products SC 4500 evaporator) and consisted of a 5 nm chromium or titanium adhesion layer with 100 nm of platinum. All materials were deposited at a rate of approximately 2.0 Å/sec. The resist and excess metal were removed by sonication in a 1:1 (v/v) solution of methylene chloride (CH_2Cl_2) and acetone. Separate sets of global alignment marks, which were used for global positioning and rotation of the wafer, and local marks, which were needed to determine the precise center of each die of magnet-tipped chips, were patterned for each of the three subsequent layers; a fourth set of marks was also patterned as a spare set. It was necessary to fabricate individual sets of alignment marks for each layer because the marks were often damaged while manually locating them in SEM mode prior to exposure. In SEM mode, all of the resist over the imaged region, was exposed. The exposed mark was then damaged by the subsequent processing steps. These processed areas, in which either the silicon was etched or magnetic material was deposited over the mark (Figure 3.1), often lost the contrast needed for e-beam alignment and were unusable for subsequent alignments.

Chip Design and Release. Slits to define rectangular chip bodies, along with support tethers halfway along the chip length to prevent post-release stiction, were defined in approximately 700 nm of 495,000 MW PMMA and patterned by e-beam lithography. These "etch slits" can be seen in Figure 3.2(a).[1] The device-layer silicon was etched in sulfur hexafluoride and oxygen (SF_6:O_2; Oxford Instruments Plasmalab 80), and the resist was subsequently stripped by sonication in a 1:1 (v/v) solution of methylene chloride and acetone. The chips were released by wet etching of the BOX layer in 6:1 buffered oxide etch (BOE), followed by soaking the wafer in a water bath and spin drying.

[1]Figures 3.2, 3.5, 3.6, and 3.12(c) reprinted with permission from J. G. Longenecker *et al.*, J. Vac. Sci. Technol. B **29**, 032001 (2011). Copyright 2011, American Vacuum Society.

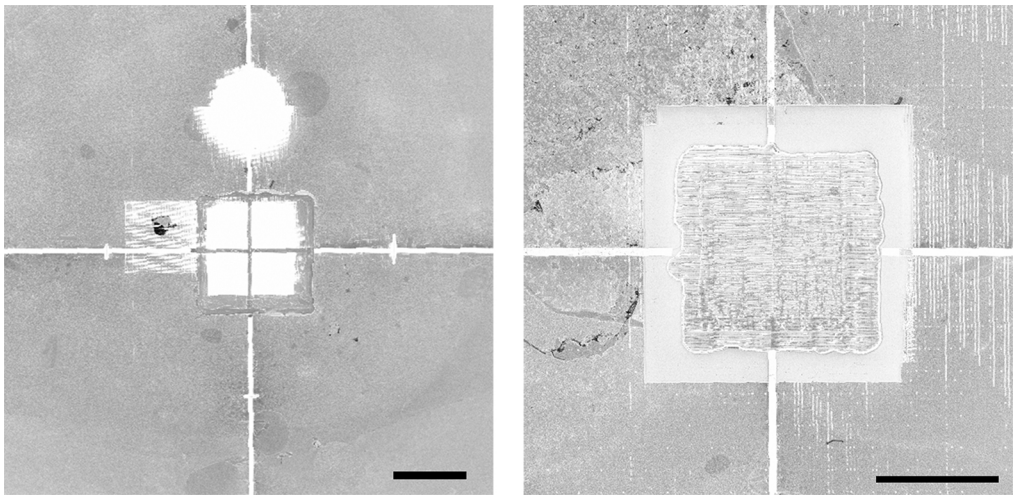

Figure 3.1: Damaged e-beam lithography alignment marks. When an alignment mark was located manually in SEM mode, the resist over the alignment mark was exposed, and the mark was damaged by the subsequent processing steps. The marks were damaged either by SF_6:O_2 plasma etching of the device silicon layer surrounding an exposed alignment mark or by the alignment mark being covered by magnetic material during the magnet definition processing step. Both scale bars represent 50 µm.

Nanomagnet Deposition. Nickel nanomagnets with widths of 70 nm, 110 nm, and 220 nm were patterned by e-beam lithography in a bilayer of 50 nm of 950,000 MW PMMA on 550 nm of 495,000 MW PMMA. The magnets were deposited by e-beam evaporation; a 5 nm thick chromium[2] adhesion layer was deposited prior to evaporating the 100 nm thick magnets. Chromium was deposited at a rate of 2.0 Å/s, and nickel was deposited at a rate of 2.5 Å/s. After a waiting period to allow the chamber to cool to room temperature, the wafer was unloaded and the resist and excess metal were removed by sonication in a 1:1 solution of methylene chloride and acetone, followed by spin drying. A nanomagnet deposited on a suspended silicon chip is shown in Figure 3.2(b). To protect against post-processing oxidation, some samples were coated with approximately 6 nm of alumina prior to resist removal. The alumina was prepared via atomic layer deposition (ALD; Oxford FlexAL) using trimethlyaluminum and plasma oxygen precursors at 110°C [115, 116].

[2]It has subsequently been determined that titanium is a better choice for an adhesion layer, since chromium is antiferromagnetic [133].

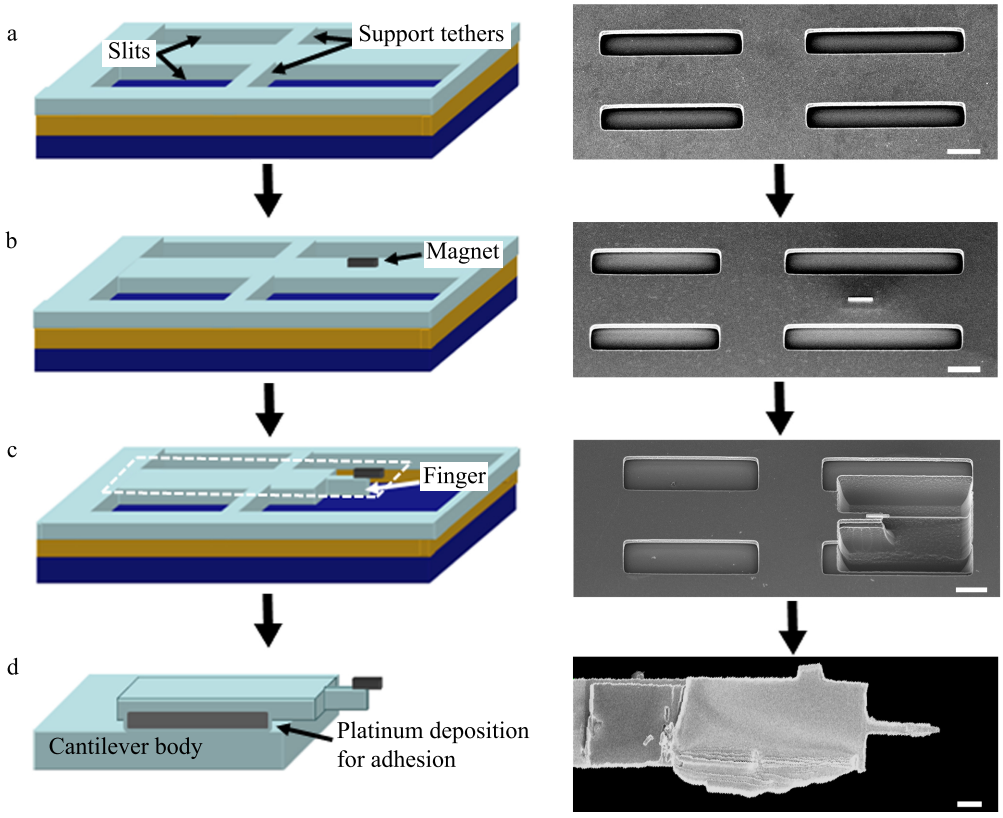

Figure 3.2: Process flow schematics (left) and corresponding SEM images (right) at key steps in the process used to fabricate overhanging magnet-tipped silicon chips and attach the chips to cantilevers. The layers in the schematics correspond to the nickel magnet (black), device silicon (light blue), buried silicon dioxide (yellow), handle silicon (dark blue), and ion-beam deposited platinum for adhesion of the chip to the cantilever (gray). The magnet-tipped chips were fabricated by (a) etch slit definition and chip release, (b) magnet deposition, and (c) definition of silicon leading-edge "fingers". Note that because the chips were released prior to the silicon finger definition, the handle-wafer silicon was also etched, creating deep U-shaped craters as shown in the SEM in panel (c). To attach the chip to a cantilever, the portion of the chip inside the dashed line in the schematic in panel (c) was lifted out and attached to the leading edge of the cantilever (see Figure 3.5), resulting in the magnet-tipped chip-on-cantilever shown in panel (d). All scale bars represent 2 µm.

Silicon Underetch of U-Shaped Etch Pits. In order to achieve overhanging magnets, as shown in Figure 3.2(c) and Figure 3.3, the silicon under the nanomagnets was removed by defining U-shaped "etch pits" in front of the nanomagnets. The etch pits were patterned by e-beam lithography in approximately 700 nm of 495,000 MW PMMA and were isotropically etched using SF_6:O_2 plasma. The position of the U-shaped pits and the etch time were carefully calibrated so that the nanomagnets extended past the silicon leading edge by 300 to 400 nm (Figure 3.3(c-f)). Because of the design of the U-shaped holes, silicon "fingers" were also defined at the leading edges of the chips that were 2 to 3 µm long and 1 µm wide. The resist was removed by sonication in a 1:1 solution of methylene chloride and acetone, followed by spin drying.

Overall, the magnet-tipped silicon chip fabrication protocol required 17 steps and could be completed within four days of processing time. The process is currently designed to produce four dies with 100 chips each per wafer, but could be redesigned to produce thousands of chips per wafer. The factor of three improvement in processing time, when compared to the integrated magnet-on-cantilever fabrication protocol of Ref. 81, enables the rapid prototyping of new chip designs, magnet dimensions, and magnetic materials.

3.3 Summary of Blank Cantilever Fabrication

Attonewton-sensitivity silicon cantilevers that were either intentionally magnet-free (also known as "blank" cantilevers) or were from failed magnet-on-cantilever trials (see Section 2.3), with the metal-tipped fingers milled away, have been used for magnet-tipped chip attachment (Figure 3.4). The scheme for the batch fabrication of these cantilevers is similar to previous protocols [66, 68, 81]. Currently 21 dies with 10 cantilevers each, totaling 210 cantilevers, are prepared per wafer.

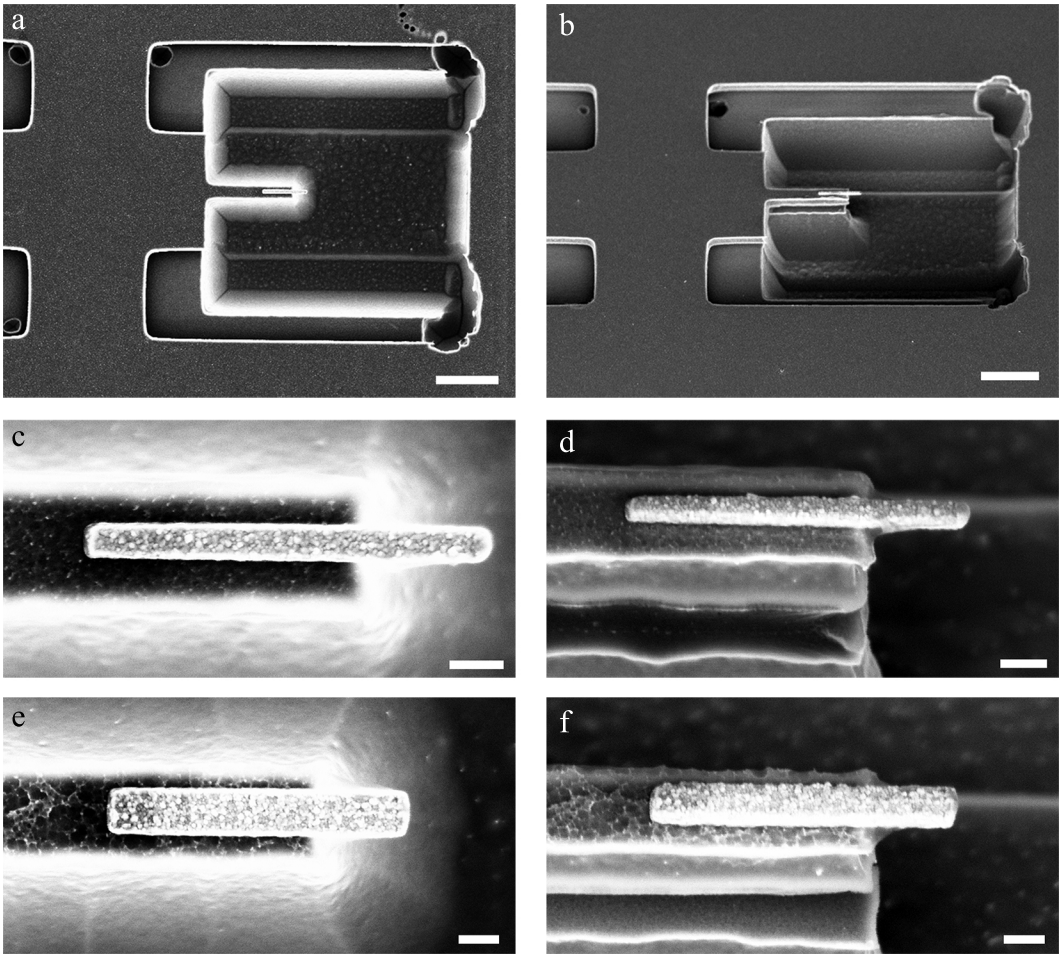

Figure 3.3: Top-down (left column) and side-on (right column) SEM images of the leading edges of magnet-tipped chips and magnified views of overhanging nickel nanomagnets. (a-b) Views of the leading edges of magnet-tipped chips. The deep pit etched into the silicon resulted from etching U-shaped holes into the suspended device silicon layer; since there was air instead of a BOX etch-stop layer between the device silicon and underlying handle silicon layers, a by-product of etching the device silicon layer to create the overhanging magnet and reduced-width silicon finger was that the observed pit was also etched into the handle silicon layer. (c-d) A 115 nm wide nickel nanomagnet that extended past the leading edge of the silicon chip by 380 nm. (e-f) A 225 nm wide nickel nanomagnet that extended past the leading edge of the chip by 400 nm. The scale bars in (a) and (b) represent 2 µm, and the scale bars in (c-f) represent 200 nm.

The cantilevers were fabricated from silicon-on-insulator (SOI) wafers identical to those used to prepare the nanomagnet-tipped silicon chips (Section 3.2). Cantilever bodies that were 195 µm long and 4 µm wide, as shown in Figure 3.4(b), were patterned in the single-crystal device silicon layer by photolithography using an Autostep 200 5× reduction wafer exposure tool, followed by an SF_6:O_2 isotropic plasma etch. In order to protect against scratching of the cantilevers during back side processing, the front of the wafer was coated with 1.6 µm of low-stress plasma enhanced chemical vapor deposition (PECVD) SiO_2 using a GSI PECVD system. The back of the wafer was coated with 2 µm of PECVD SiO_2 for an etch mask. Windows in the back side of the wafer were aligned underneath the cantilever bodies and patterned by contact photolithography; the alignment marks for this front-to-back alignment were patterned during the cantilever body definition step. The PECVD SiO_2 was etched using a CHF_3 reactive ion etch, and the underlying silicon handle wafer was etched by Bosch through-wafer processing using the procedure described in Appendix A.11 of Ref. 91. The Bosch etch both created windows in the silicon under the cantilevers and defined cantilever handle dies (Figure 3.4(a)), which are necessary for the transport and handling of the cantilevers. The resist on the back side of the wafer was removed partway through the Bosch etch, leaving the back side SiO_2 as the only etch mask during the etching of the final 100 µm of handle wafer silicon. The cantilevers were released in BOE, and critical point drying (CPD) was used to to prevent stiction or curling of the cantilevers.

The 195 µm long cantilevers fabricated using this method have had resonance frequencies $f_c \approx 9000$ Hz, spring constants of approximately $k = 0.75$ mN m^{-1}, and intrinsic quality factors ranging from $Q = 40,000$ to $Q = 100,000$ in high vacuum and at 4 K. Parameters that contribute to the cantilever quality factor are not fully understood, but studies have shown that Q can be strongly altered by surface effects [66, 80]. For our cantilevers, a second factor that can affect Q is a "shelf" of device layer silicon at the base of the cantilever that is caused by the back side through-wafer Bosch etching of the 500 µm thick silicon handle

wafer layer. Bosch etching is a process by which an isotropic plasma process is converted into an anisotropic method for etching deep into silicon by alternating between steps that (1) isotropically etch a shallow trench into the silicon layer, (2) deposit a protective fluorocarbon layer onto the side walls and base of the silicon trench, and (3) directionally etch the base of the trench to remove the fluorocarbon polymer and further etch the silicon [102]. Bosch etching results in mostly-directional etching of silicon, but the silicon trench does broaden with depth. In our case, this broadening led to tapering back of the silicon device layer as it was etched from the back side of the wafer, which exposed more than 50 µm of the device silicon layer of the cantilever handle die; this exposed shelf is highlighted by the arrow in Figure 3.4(a). Because this unsupported shelf is only 340 nm thick, the shelf bends when the cantilever oscillates. We have observed that the cantilever Q is greatly damped if there are any cracks in this shelf.

3.4 Focused Ion Beam Lift-Out and Attachment to Cantilevers

FIB processing was conducted using a dual-beam FEI Strata 400 STEM FIB system with ion beam and e-beam imaging, ion beam milling, and platinum deposition capabilities. The dual-beam FIB also was equipped with a probe needle with a 1 µm diameter tip for transferring samples. A schematic of the lift-out and attachment process is shown in Figure 3.5. In order to prevent gallium ion implantation, the magnets always remained out-of-view of the ion beam. All ion beam processing was done at 30 kV with a nominal ion beam current of 28 pA. Exposure of the magnets to the ion beam was limited to less than three seconds of total exposure, all at low resolution ($< 650\times$); the total ion dose experienced by the magnetic material was less than 0.22 µC cm^2.

To attach a magnet-tipped silicon chip to the probe needle, the tip of the needle was

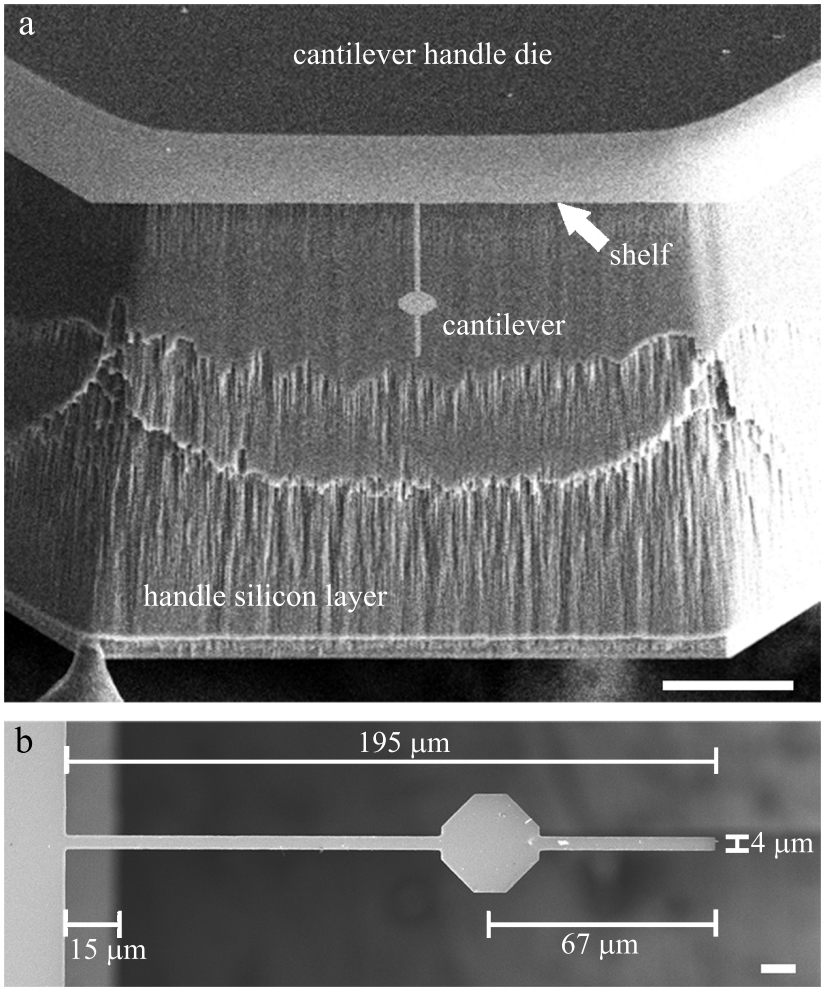

Figure 3.4: SEM images of 195 µm long cantilevers with the components and dimensions of the cantilever chips labeled. (a) Angled front-on image of a cantilever attached to its cantilever handle die. The tapering of the handle die side wall leads to a "shelf" of unsupported handle wafer at the cantilever leading edge; the portion of the handle die that is connected to the underlying handle silicon layer is shown as dark gray in the SEM image, and the unsupported shelf (indicated with the arrow) is much lighter in color. Additional nonuniformities caused by the Bosch etch can be seen in the handle silicon layer. (b) Image of a blank cantilever. The length and width of the cantilever, as well as the distance from the cantilever leading edge to the center of the cantilever pad used for interferometric detection of the cantilever motion, are labeled. The base of the cantilever handle die is observed to protrude past the front of the cantilever handle die shelf by 15 µm. The scale bar in (a) represents 100 µm and the scale bar in (b) represents 10 µm.

brought into light contact with the chip surface approximately 5 µm from the base of the chip. The needle was adhered to the silicon chip using platinum deposition to join the two components (Figure 3.5(a)). For all adhesions, approximately 1 µm of platinum was deposited by ion-beam-induced decomposition of methylcyclopentadienyl(trimethyl)platinum(IV) precursor gas. After adhesion of the chip to the needle, the chip base and support tethers were milled (Figure 3.5(b)) and the chip was gently raised from the substrate and moved near the cantilever's leading edge.

Before the chip was brought into contact with the cantilever, the chip and cantilever were aligned horizontally by rotating the stage (and mounted cantilever) as needed. The chip was softly brought into contact with the cantilever (Figure 3.5(c)). Since the cantilevers tend to bend downward at a slight angle, the probe was retracted slightly to pull the cantilever upwards and improve vertical alignment between the chip and the cantilever. Once the vertical alignment was confirmed, platinum was deposited on the sides of the chip and cantilever to facilitate adhesion (Figure 3.5(d)). The probe tip was milled, and the probe was lifted away from the cantilever (Figure 3.5(e)). Additional platinum-deposited contacts were added to the side and top of the cantilever. A completed chip mounted on a cantilever is shown in Figure 3.5(f).

3.5 Nanomagnet-Tipped Chip Process Yield

Yields were estimated for the fabrication of the magnet-tipped chip bodies, cantilevers, and FIB attachment procedure. By analyzing thirteen magnet-tipped silicon chip dies, with each die containing 100 individual magnet-tipped silicon chips, an average magnet-tipped chip body yield was estimated to be $94.2\% \pm 6.0\%$. It was determined that in order to achieve this high yield, the width of the slits, the width of the support tethers, and the length of the

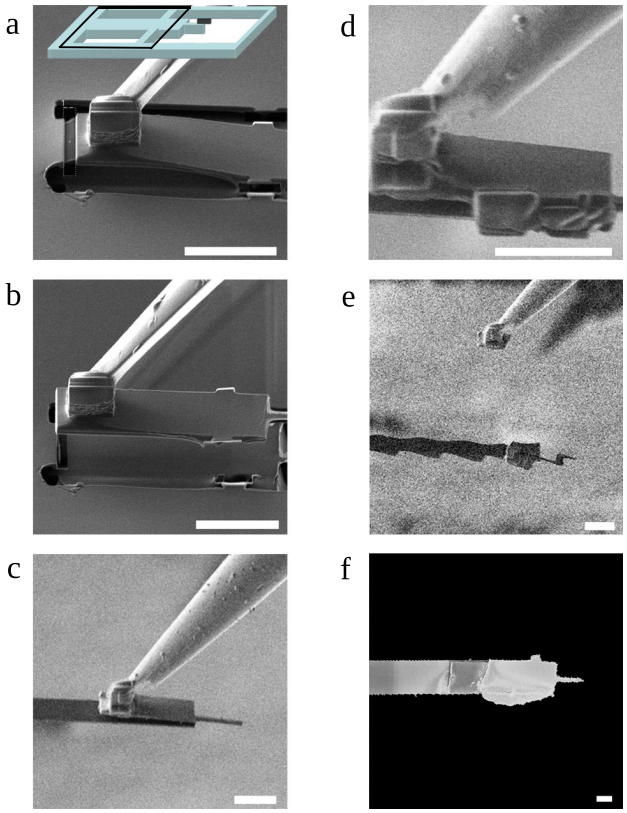

Figure 3.5: Ion-beam side-view (panels (a-e)) and SEM top-view (panel (f)) images detail the original magnet-tipped chip lift-out and cantilever attachment procedure using a dual beam FIB instrument. The inset in panel (a), which includes a schematic of the chip device layer from Figure 3.2(c), indicates the chip orientation, and the box details the visible region of the chip in the subsequent images. The process includes: (a) adhesion of the probe tip to the magnet-tipped chip by FIB deposition of platinum; (b) milling of the chip's support tethers and lift-out of the chip; (c) positioning of the chip over the cantilever's leading edge and bringing the chip into contact with the cantilever; (d) adhesion of the chip to the cantilever by FIB deposition of platinum deposition; (e) milling and removal of the probe tip; and (f) completion of the chip-on-cantilever process. The serial attachment process requires approximately 1.5 hours per fabricated chip-on-cantilever assembly, with an additional 0.5 hour for sample loading and unloading from the chamber. All scale bars represent 5 µm.

leading-edge silicon finger had to be carefully chosen in order to prevent stiction. The need for support tethers can be seen in Figure 3.6(a), which shows that 15 µm long chips without tethers snapped into contact with the underlying substrate. The silicon finger at the leading edge incurred stiction and curling if it was 5 µm long (Figure 3.6(b)), but was stiction-free even without critical point drying for short finger lengths of 2-3 µm (Figure 3.2(c)). Slits that were too wide resulted in stiction, whereas slits that were too narrow did not provide room for lateral motion during the FIB lift-out procedure. Since stiction occurred in approximately 50% of chips with slit widths of 4 µm and in all chips with slit widths wider than 6 µm, widths of 2 to 3 µm were chosen. Support tethers that were too narrow also resulted in stiction (Figure 3.6(c)), whereas support tethers that were at least 4 µm wide remained stiction-free (Figure 3.2(a-c)).

The nickel nanomagnet yield was estimated by visual inspection using an SEM (Zeiss Ultra 55 microscope); analysis of the nickel magnetization was conducted separately using cantilever frequency-shift cantilever magnetometry, and those results are included in Chapter 4. Visual analysis of the magnets was used to confirm whether (1) part or all of the magnets were missing after processing or (2) the metal had reacted to form either nickel silicide or nickel oxide. Damage would appear as either removal of the magnetic material or the transformation of crystalline nickel into "blob-like" amorphous balls, as seen for damaged nanomagnets integrated on cantilevers in Figure 2.2. It was observed that overhanging nanomagnets were present on nearly 100% of the magnet-tipped chips. Since the nickel grain structure was clearly visible (Figures 3.3(c-f)), it was concluded that the magnets had no appreciable damage due to silicidation or oxidation.

The cantilever yield for the wafer prepared for these experiments was 90.5%, with 190 out of 210 potential cantilevers remaining intact. Yields for similarly processed wafers have ranged from 50% to 90%. The FIB lift-out and attachment procedure yield was 91%, with

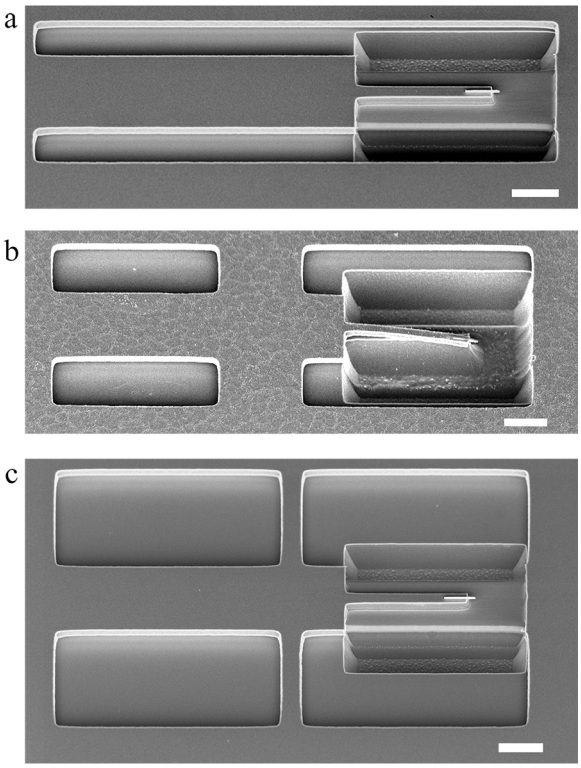

Figure 3.6: SEM images of unsuccessful alternative dimensions for the support tethers, silicon "finger" length, and slit width. Stiction was observed for magnet-tipped chips with (a) no support tethers, (b) long silicon fingers, and (c) wide slits and narrow support tethers. For comparison, free-standing chips have an observable gap between the finger and the substrate, as shown in Figure 3.3. All scale bars represent 2 µm.

only one failure out of eleven attempts (caused by a crack in the chip silicon that propagated during lift-out). After FIB manipulation, the cantilever quality factors remained high, implying that the cantilevers were not damaged by the FIB processing. Cantilever quality factors were measured for six magnet-on-cantilever assemblies and ranged from 41,000 to 94,000 at 4.2 K and 10^{-6} mbar (shown in Table 4.1 in Chapter 4); these Q's are consistent with previously reported values for non-FIB processed cantilevers [68, 81].

3.6 Switching to Cobalt Magnets

Although nickel nanomagnets have been used in MRFM experiments to detect electron spin resonance [81], switching to a magnetic material with a significantly higher saturation magnetization would increase the tip-field gradient produced by the nanomagnet and greatly enhance the signal-to-noise ratio in MRFM experiments [48]. For instance, it would be highly desirable to switch from nickel, which has a saturation magnetization of only $\mu_0 M_{sat} = 0.6$ T, to cobalt, which has a three-times-larger saturation magnetization of $\mu_0 M_{sat} = 1.8$ T. Previous efforts to fabricate cobalt nanomagnets by e-beam lithography were unsuccessful [81]. By modifying the nanomagnet-tipped chip fabrication protocol detailed in Section 3.2 to not exceed temperatures of 115°C, cobalt nanomagnets defined by e-beam lithography can be fabricated for the first time. The importance of reducing the processing temperature can be observed in Figure 3.7; it can be seen that cobalt nanomagnets that were exposed to temperatures of 170°C during resist baking were damaged significantly (Figure 3.7(a)), whereas cobalt exposed to reduced temperatures of only 115°C remained intact (Figure 3.7(b)).

Cobalt nanomagnet-tipped chips were fabricated using the same basic procedure outlined in Section 3.2, except that the temperature never exceeded 115°C once the nanomagnets were deposited. Etch slits were defined in the SOI wafer's device layer and the resulting chips

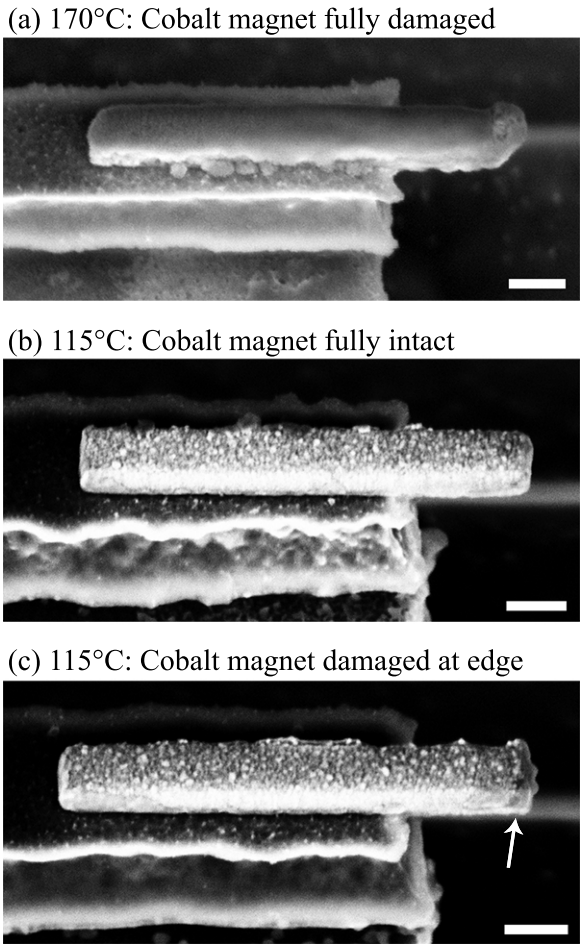

Figure 3.7: SEM images of overhanging cobalt nanomagnets. (a) An uncapped cobalt nanomagnet that was damaged by exposure to 170°C temperatures. (b) A fully intact, platinum-coated nanomagnet that was undamaged by processing at a reduced temperature of 115°C. (c) A cobalt nanomagnet from the same wafer as (b) that was damaged at the leading 20 nm of the nanomagnet, as denoted by the arrow. All scale bars represent 200 nm.

were released using 6:1 BOE prior to deposition of the nanomagnets. The magnets were defined using e-beam lithography in a bilayer resist of 50 nm of 950,000 MW PMMA on 550 nm of 495,000 MW PMMA, and the metal was deposited by e-beam evaporation. The nanomagnets were prepared by depositing a titanium adhesion layer (deposited at 1.5 Å/sec), cobalt (2.9 Å/sec), and a platinum capping layer (1.2 Å/sec). Relative metal thicknesses were measured during deposition by a quartz crystal microbalance, and the combined thickness of the Ti/Co/Pt film was measured after fabrication by atomic force microscopy (AFM). For the cobalt nanomagnet studied by frequency-shift cantilever magnetometry in Section 4.4 and used to detect NMR signal from a polystyrene film in Chapter 5, the layer thicknesses were 4.0 ± 0.2 nm of titanium, 79.2 ± 4.7 nm of cobalt, and 8.0 ± 0.5 nm of platinum. Silicon under the leading 300 nm of the magnets was removed by patterning U-shaped holes [81, 82] in a layer of 700 nm thick, 495,000 MW PMMA resist; cobalt oxidation was prevented at this step by baking the PMMA at only 115°C for 40 minutes (in Section 3.2, the resist was baked at 170°C for 20 minutes). The inside edge of the U-shaped hole was patterned to be offset from the nanomagnet leading edge by 50 nm. The silicon under the U-shaped hole was isotropically etched using SF_6:O_2 plasma.

Although yield as determined by SEM visual analysis was generally excellent for the cobalt nanomagnet-tipped chips, one problem was observed. For some overhanging nanomagnets, approximately 20 nm of cobalt at the leading edge was removed between the deposition of the nanomagnets and the end of the process. The damage was not consistent throughout a wafer; undamaged magnets ((Figure 3.7(b)) and damaged magnets ((Figure 3.7(c)) were interspersed on the same 1 mm wide die. It is interesting to note that although the leading edge of the nanomagnet was damaged, as indicated by the arrow in Figure 3.7(c), the back and side edges of the nanomagnet remained intact. Although quantitative yields were not recorded, estimates indicate that 10% to 50% of magnets per die incurred this leading-edge damage.

The source of the cobalt nanomagnet leading-edge damage is not fully understood. Since the damage occurred at only one edge of the magnet, it is not consistent with oxidation or silicide formation. Damage could have been due to an interaction with the SF_6:O_2 plasma, but then it is not understood why only some of the nanomagnets were effected. Since the magnets were capped with 10 nm of platinum and covered by PMMA resist, which left only the undamaged titanium adhesion layer exposed to the plasma, it is also difficult to see how the plasma could have reacted with the cobalt. The source of this damage will remain an open field of investigation. However, even magnets with this leading edge damage have been found to be suitable for high-sensitivity MRFM measurements. In fact, a nanomagnet with 10 to 20 nm of damage at the leading edge produced a tip-field gradient that is comparable to the tip employed in the 4 to 10 nm resolution imaging experiment of Ref. 12 (see Chapter 5 and Ref. 58).

3.7 Improvements to the Chip Design

3.7.1 Side Tabs Added to Magnet-Tipped Chips

During FIB lift-out of the original rectangular magnet-tipped chips (Figure 3.5), the FIB probe needle was adhered near the base of the chip and centered with respect to the chip's width. When the chip was positioned over a cantilever, the probe needle was thus also centered directly over the cantilever. After the attachment was complete, the probe needle could only be removed by milling through the adhesion point between the chip and the needle. Often the 1 µm-wide platinum adhesion point did not mill uniformly, causing some of the silicon under the needle to be milled during extraction. Milling a small hole into the cantilever could weaken the structure and increase the bending of the cantilever at

that position. Further milling could completely mill through the adhesion point between the magnet-tipped chip and the cantilever, and would result in the removal and loss of the magnet-tipped chip. Although this step was carefully monitored and chip-on-cantilever attachment yields were almost 100%, modified chips designs were sought out to mitigate this risk of milling into the cantilever body.

For the second generation of magnet-tipped chips, a key change in the design that improved the attachment process was the addition of a "side tab" to the shape of the chip. An image of this second-generation magnet-tipped chip design is shown in Figure 3.8(a);[3] the side tab is shown at the top of the chip. The probe needle could be attached to this side tab during FIB lift-out (Figure 3.8(b-c)). After the magnet-tipped chip was attached to a cantilever, the entire side tab was milled away to cleanly separate the probe needle from the magnet-on-cantilever assembly (Figure 3.8(d)). With this improved process, no milling ever was conducted over the body of the cantilever. The process of attaching the probe needle to the tab, lifting out the chip and attaching it to a cantilever, and particularly removing the probe needle from the chip-on-cantilever assembly was faster and more straight-forward using this enhanced design.

Since these second-generation chips were larger to accommodate the addition of the side tabs, the chip shape had to have rigid structural support so that it would not incur stiction during processing. The chips were designed to have four support tethers: two tethers were located at the bottom of the magnet-tipped chip, and two more were at the top of the chip between the side tab and the surrounding silicon substrate. The tab shape was designed to provide stability both during subsequent fabrication of the suspended chips and during the FIB lift-out process, when the chip body was suspended by the probe needle attached to the tab. The yield of fabricating these second-generation chips was nearly 100%.

[3]Figure 3.8 reprinted with permission from the Supporting Information for J. G. Longenecker *et al.*, ACS Nano **6**, 9637 (2012). Copyright 2012, American Chemical Society.

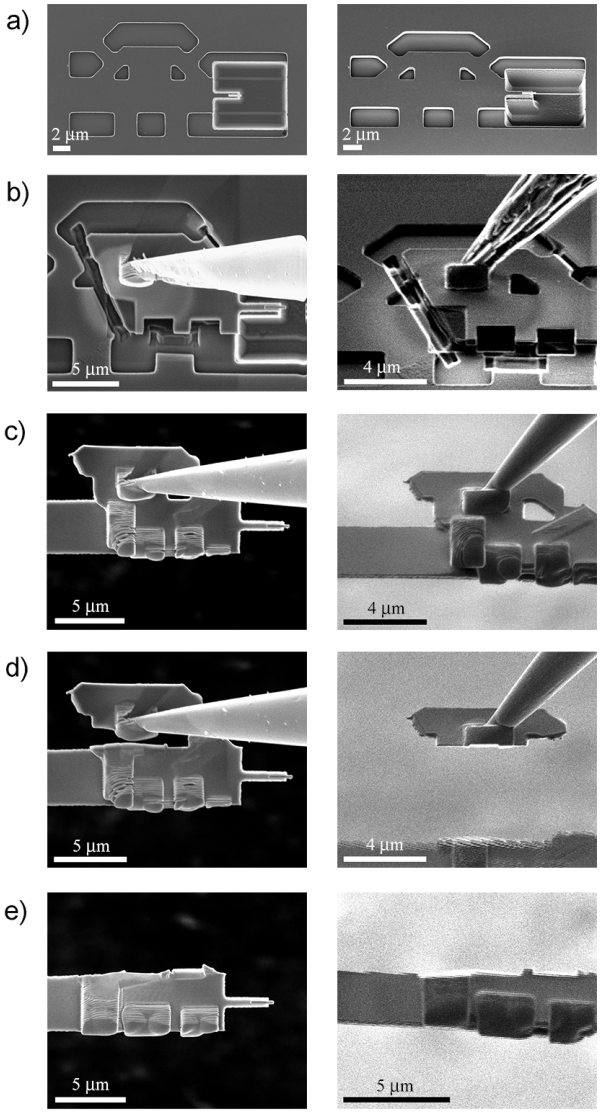

Figure 3.8: Second-generation magnet-tipped chip design and a revised FIB attachment procedure. Top-down SEM (left column) and side-on FIB images (right column) of the key steps used to remove the magnet-tipped silicon chip from the substrate [panels (a)-(b)] and attach it to the leading edge of a blank cantilever [panels (c)-(e)]. To remove the chip from the substrate, a probe needle was attached to the silicon tab connected to the chip, the support tabs were milled, and the shape of the chip was fine-tuned in order to promote superior adhesion to the cantilever by milling rectangular holes into the side of the chip and angling the back edge of the chip [panel (b)]. The chip was positioned over the leading edge of the cantilever and adhered to the cantilever by depositing FIB-assisted platinum in the rectangular holes and at the back edge of the chip [panel (c)]. The tab at the side of the chip was milled away [panel (d)] in order to cleanly separate the probe tip from the chip-cantilever assembly [panel (e)].

Concurrently with modifying the shape of the second-generation chips, steps during the FIB lift-out process to refine the chip shape in preparation for adhesion to the cantilever were introduced (Figure 3.8(b)). Specifically, two rectangular holes were added on the side of the chip and the back of the chip was tapered. Both of these adjustments provided increased surface area for the platinum to adhere the chip to the cantilever during attachment (Figure 3.8(c-e)).

A third-generation chip shape was also designed and fabricated, but has not yet been used in FIB attachment procedures. The third-generation chips were designed to be shorter, and therefore more structurally rigid, than the second-generation chips. As can be seen in Figure 3.8(b), the second-generation chips were diagonally milled during FIB lift-out so that only the rightmost two-thirds of the chips were lifted out from the substrate and attached to cantilevers. This was because it was found that the full-length, > 20 µm long second-generation chips could not be aligned vertically with the cantilevers. The chips always first touched down at the back edge of the cantilevers because the custom attonewton-sensitivity cantilevers had a slight downward bend. Since the chips were always perfectly straight, a gap was introduced between the chip and the cantilever at the chip leading edge. With short chips, this difference in angle did not lead to a significant gap at the leading edge; however, the gap became significantly wider as the chip length was increased. It was observed that chips that were less than approximately 15 µm long could regularly be vertically aligned to cantilevers with no observable gap. The third-generation chip, which is shown in Figure 3.9, was designed to meet this shortened length criterion while still retaining the side tab for easy FIB lift-out.

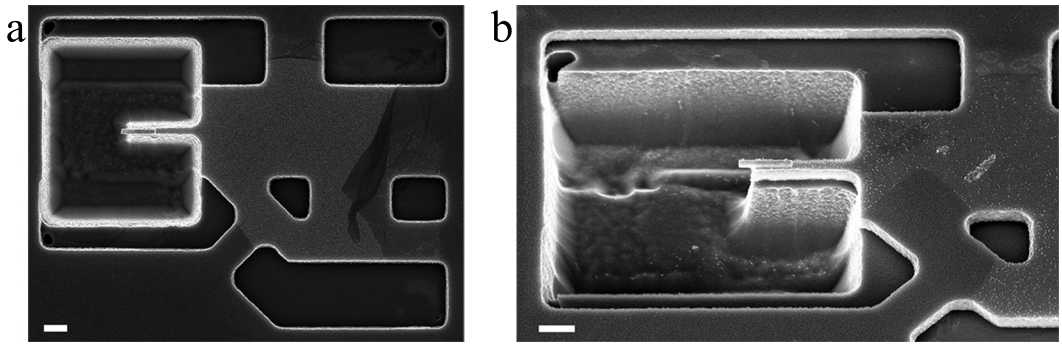

Figure 3.9: Third-generation magnet-tipped chip design. These chips were designed to be shorter than the second-generation chips, which provides extra stability and a superior shape for FIB lift-out. (a) Top-down SEM image of the full chip body. (b) Tilted and magnified SEM image of the leading edge of the magnet-tipped chip. Both scale bars represent 1 µm.

3.7.2 Fabrication of Non-Overhanging Magnet Chips

In order to assess the integrity of as-deposited nanomagnets, a simplified protocol for preparing *non*-overhanging magnets was developed. The main alteration and benefit of this process was that at the "etch slits" level of the procedure described in Section 3.2, silicon chips were defined such that one end was free-standing past the support tethers. The non-overhanging chips were pre-released in BOE so that after the magnetic material was deposited and the resist liftoff completed, the magnets could be immediately attached to cantilevers using the FIB lift-out technique. SEM images of the non-overhanging magnet chip design are shown in Figure 3.10. The fabrication of these non-overhanging magnet chips enabled the first frequency-shift cantilever magnetometry studies of nanomagnets with no post-deposition fabrication processing (Chapter 4), which was used to determine that no damage was incurred by nickel nanomagnets during the definition of the U-shaped etch pits or the etching of the silicon under the nanomagnet leading edges.

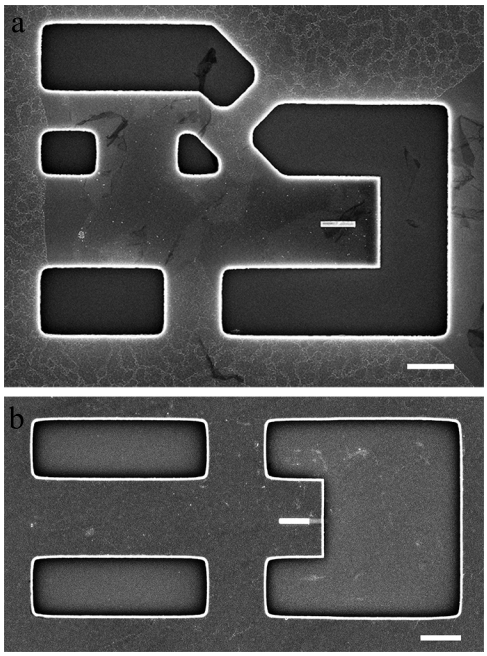

Figure 3.10: SEM images of two designs of non-overhanging magnet chips. (a) A magnet chip with a side tab and cobalt nanomagnet that was based on the third-generation magnet-tipped chip design. (b) A nickel nanomagnet on a non-overhanging chip based on the original chip design. Both scale bars represent 2 µm.

3.7.3 Incorporation of Release Chips

Release of the silicon chips from the underlying buried SiO_2 layer required an underetch of at least 2.5 µm of SiO_2. Since BOE etches SiO_2 isotropically, the SiO_2 under the silicon substrate surrounding the chips was etched back at the same rate as the SiO_2 under the chips. As the width of this suspended silicon substrate device increases, the chips become significantly more fragile. Thus, careful calibration of the BOE etch time was essential in order to make sure that the etch was stopped as soon as all chips were released.

As an easy way to identify whether the magnet-tipped chips were released, "release chips" were designed and added to each die of chips. These release chips were identical in shape to the magnet-tipped chips except that they had no tethers joining them to the surrounding silicon substrate; in other words, they were only adhered to the underlying SiO_2.

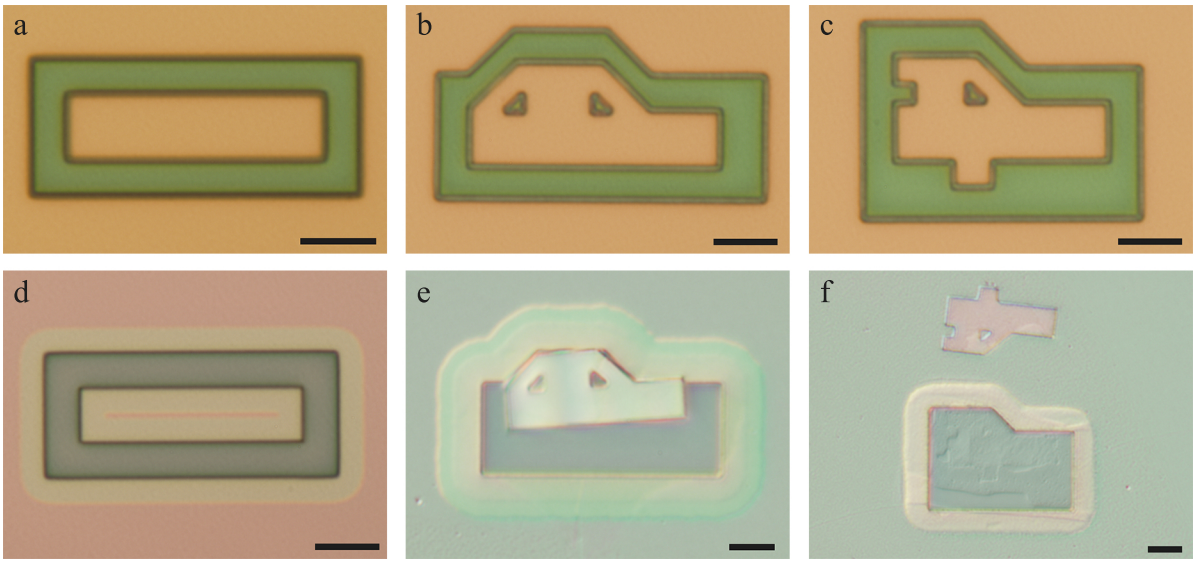

Figure 3.11: Release chips for the original design of magnet-tipped chip (left column), second-generation chip (middle), and third-generation chip (right column). Top row: Optical images of pre-released chips that were etched down to the BOX layer (green) and were still coated with resist (pink). Bottom row: Optical images at two stages of release. (d) A chip that had not been fully released – the BOX layer in the exposed regions had been etched down to the silicon (gray) and most of the SiO_2 under the rectangular chip has been etched (the freely-suspended silicon device layer appears white), but a thin strip of SiO_2 under the center of the rectangular chip had not yet been released (the device silicon layer with SiO_2 underneath appears pink). (e-f) Two examples of how the movement of the release chips after the BOX was completely underetched clearly indicates that they had been fully released. Note that the chip in panel (d) was etched by HF vapor (see Section 3.8); no images of partially-etched chips using BOE etchant were recorded. All scale bars represent 5 µm.

Therefore when the SiO_2 was completely underetched, the release chips were free to fall to the underlying handle silicon layer or to float away in the liquid BOE. When imaging a wafer to determine whether the chips were fully suspended, the release could be easily determined based on whether the release chips were still in position (not yet released) or if they had moved or were absent (fully released). Optical images of the release chips for the three different magnet-tipped chip designs before (top row) and after (bottom row) BOE etching are shown in Figure 3.11.

3.8 Chip Release by HF Vapor

In the magnet-tipped chip fabrication protocols described in Section 3.2 and Section 3.6, the silicon chips were released by BOE wet etching the BOX SiO_2 layer under the chips before the magnet deposition and silicon underetch fabrication steps. This pre-release was necessary because both nickel and cobalt are readily etched by BOE; the nanomagnets would have been completely destroyed during the 50 minute BOE wet etch required to release the chips. However, many metals, including nickel, have been reported to be resistant to hydrofluoric acid (HF) vapor etching [134]. HF vapor is a dry etchant that effectively and conformally etches SiO_2 by operating at reduced pressures with ethanol as a catalyst and nitrogen as a carrier gas. Since there is no water in the system, the corrosive anhydrous reagents that react with exposed metals, such as nickel, are avoided. Nickel in particular was found by Primaxx Inc., the manufacturer of the HF vapor etching tool used in this section, to be so unreactive to HF vapor that they coated the inside of their etching chamber with a few micrometers of nickel metal to protect against chamber corrosion [135].

The resistance of nickel to HF vapor at the nanoscale was tested by releasing nickel nanomagnet-tipped chips after the magnets were deposited. Releasing completed chips was of interest since no steps were performed on suspended chips and the chips were more stable during processing. Also, since the chips were released at the end of the process, the separate steps of defining and etching (1) the etch slits and (2) the U-shaped etch pits, as described in Section 3.2, were combined into one step conducted after the magnet definition, which eliminated six steps and one-fourth of the total processing time.

A magnet-tipped chip and magnified views of nickel nanomagnets that were released using HF vapor at the end of the process are shown in Figure 3.12. The BOX SiO_2 layer was etched at a rate of 500 Å/min for 60 minutes using HF vapor in nitrogen and ethanol carrier gases (Primaxx uEtch Single Wafer Process Module; the process was conducted at

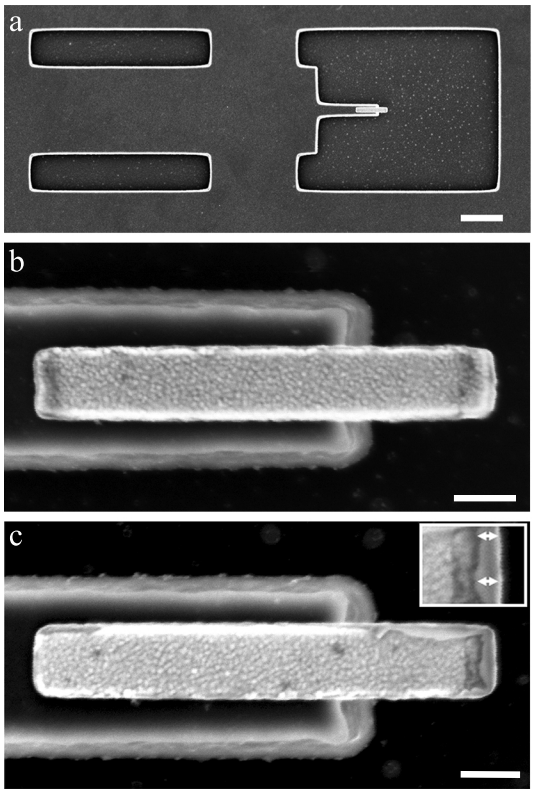

Figure 3.12: An uncapped nickel magnet-tipped chip that was released by HF vapor after magnet deposition. (a) SEM image of the released magnet-tipped chip. (b) Magnified view of a nickel nanomagnet that remained intact after HF vapor processing. (c) Magnified view of a nickel nanomagnet that was damaged during HF vapor processing. The damage to more than 20 nm of the nickel at the leading edge of the magnet is highlighted by the arrows in the inset. The scale bar in (a) represents 2 µm and the scale bars in (b) and (c) represent 200 nm.

Primaxx, Inc., in Allentown, PA, but the Cornell CNF now has an identical tool). Some of the nanomagnets remained mostly intact after processing (Figure 3.12(b)); however, it was observed that more than 20 nm of nickel at the leading edge of many of the nanomagnets was etched during the process, as indicated by the arrows in the inset in Figure 3.12(c). This result, which contradicts the findings of Ref. 134, was not well-understood. Further analysis of the damage mechanism was not conducted.

The effect of HF vapor exposure on cobalt metal was also tested using the Primaxx uEtch module (once it had arrived at the CNF). Arrays of cobalt nanomagnets (100 nm

thick) on chromium adhesion layers (5 nm thick) were defined by e-beam lithography and deposited by e-beam evaporation. After lift-off, the nanomagnets were exposed for 20 minutes to an HF vapor etch process that was calibrated to laterally etch thermal SiO_2 at a rate of 0.1 µm/min (recipe name on the CNF tool: "0.1uR7.5"). As shown in Figure 3.13, the cobalt nanomagnets were damaged significantly by the exposure to HF vapor. Large "blob-like" growths ballooned from the cobalt layers; these growths were sometimes more than 130 nm taller than the nanomagnets. Further characterization of the damaged nanomagnets was not conducted, but it was clear that HF vapor release of unprotected cobalt magnet-tipped chips after deposition was not possible.

Nickel and cobalt nanomagnets could potentially remain undamaged during HF vapor etching if they were fully encased by a material that is highly selective against HF vapor. Initial studies were undertaken to determine whether an ALD alumina (Al_2O_3) film would be a suitable protective layer; ALD tantalum oxide (Ta_2O_5) was also considered, but alumina was pursued because it could be easily removed using solvents that would not damage the nanomagnets, such as quick dips in in very dilute BOE or MIF 726 developer. Four samples of approximately 40 nm (450 loops) of alumina were prepared by ALD deposition at 110°C. The samples were exposed for 20 minutes to an HF vapor etch that was calibrated to etch thermal SiO_2 at 0.1 µm/min. As a control, one of the four samples was baked on a hot plate at 225°C for 60 seconds prior to the HF vapor exposure; this bake was recommended by Primaxx Inc. to drive off water vapor condensed on the surface of the film. The thickness of the ALD alumina was measured by ellipsometry before and after exposure to the HF vapor to determine the alumina etch rate. The etch rate for the control sample of alumina was -0.09 nm/min, and the etch rates for the other three films were -0.14 nm/min, -0.14 nm/min, and -0.04 nm/min, respectively. The negative etch rates indicate that instead of being etched, the films grew by 0.7 nm to 3 nm during the 20 minute exposure. Elemental analysis was not conducted to determine what new species were incorporated into the film, but since the

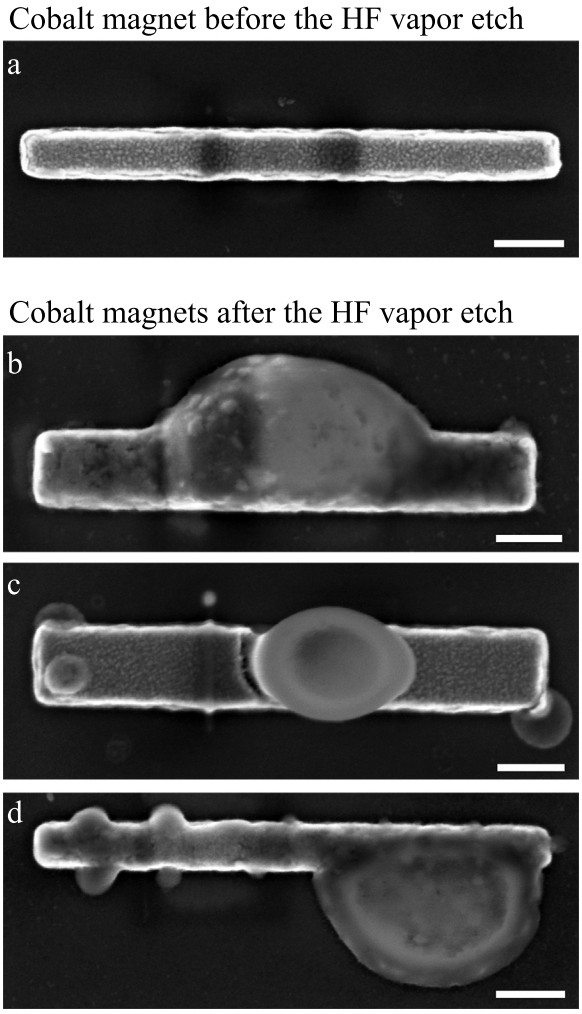

Figure 3.13: SEM images of uncapped cobalt nanomagnets that were exposed to HF vapor. (a) A cobalt nanomagnet prior to exposure to HF vapor. (b-d) Cobalt nanomagnets from the same chip as the magnet in panel (a) after they have been exposed to HF vapor for 20 minutes, which is approximately the length of exposure required for the release of magnet-tipped chips. The magnets were damaged extensively, as can be seen by the formation of growths on the nanomagnets; some of the growths were more than 130 nm taller than the cobalt nanomagnets. All scale bars represent 200 nm.

film thickness change was minimal, ALD alumina may be a suitable protective coating for the nanomagnets. If this method of capping the nanomagnets with ALD alumina would be pursued further, the challenge would be to pattern the alumina to coat the nanomagnets without covering areas of the magnet-tipped chip, including the etch slits and U-shaped holes, that need to be etched by the HF vapor. ALD alumina deposited at 110°C was observed to be removed by most liquids and could be difficult to pattern.

HF vapor etching was also considered as an alternative to BOE etching for the release of the silicon chips in the etch slit definition step, before the deposition of the nanomagnets. In the BOE release procedure of Section 3.2, it was observed that the corrosive anhydrous reagents in liquid BOE caused significantly increased surface roughness, called pitting, of the silicon device layer of some magnet-tipped chips during the 50 minute release; the extent of pitting was non-uniform over a wafer and varied extensively between wafers (Figure 3.14). Pitting of the silicon device layer led to comparable roughness of the nanomagnets deposited directly on top of the silicon. This larger-than-expected surface roughness could increase the exposed surface area of the nanomagnets, which could induce additional nickel oxidation and increase the thickness of the leading-edge damage layer.

In contrast to the effects of BOE etching, HF vapor etching of the etch slits was found to be highly selective against silicon and was not observed to alter the smooth surface of the device silicon layer. However, when this process was tested and a wafer with silicon chips that were released by HF vapor was put back into an e-beam lithography tool to align and expose the subsequent layers, it was observed that the alignment marks had disappeared; only remnant traces of metal were still present that indicated that the correct alignment mark positions had been located. It was not understood what could have caused the removal of 3 µm wide alignment marks made of 100 nm of platinum with a 5 nm thick chromium adhesion layer; chromium was not observed to be affected by HF vapor etching of nickel

nanomagnets (Figure 3.12), and platinum metal is resistant to hydrofluoric acid. Alignment marks made of different metals, such as palladium, or etched alignment marks (see Appendix C of Ref. 81) could be explored to replace the problematic platinum marks.

3.9 Discussion

The work presented in this chapter details the development of the first high-yield protocol for the fabrication of e-beam-defined nickel nanomagnets on attonewton-sensitivity cantilevers, which was achieved by fabricating the magnets *en batch* on silicon chips and attaching them serially to cantilevers by FIB manipulation. Moreover, the process for fabricating magnet-tipped chips only required a few days of processing time, compared to two weeks of processing time using the integrated magnet-on-cantilever protocol of Ref. 81.

The magnet-tipped chip protocol enabled fast prototyping of new chip designs and different magnetic materials. This rapid-prototyping capability was used to develop a revised process that eliminated high-temperature steps from the magnet-tipped chip fabrication process and led to the first successful fabrication of cobalt nanomagnets on cantilevers [58]. New chip designs were also prepared; magnet-tipped chips with side tabs made the FIB attachment process significantly more straight-forward, and the first studies of as-deposited magnets were made possible by preparing non-overhanging magnet chips.

The magnet-tipped chip fabrication process provides unprecedented flexibility for the fabrication of nanomagnets, since the cantilever processing is decoupled from the fabrication of the magnets. In future experiments, new magnetic materials, such as permalloy ($\mu_0 M_{sat}$ = 0.7 T) or sputter-deposited, amorphous CoFeB ($\mu_0 M_{sat}$ = 1.48 T) [136], could be patterned on magnet-tipped chips. The ion-beam milling that would be necessary to pattern these sputtered films would have damaged the quality factor of high-compliance cantilevers but

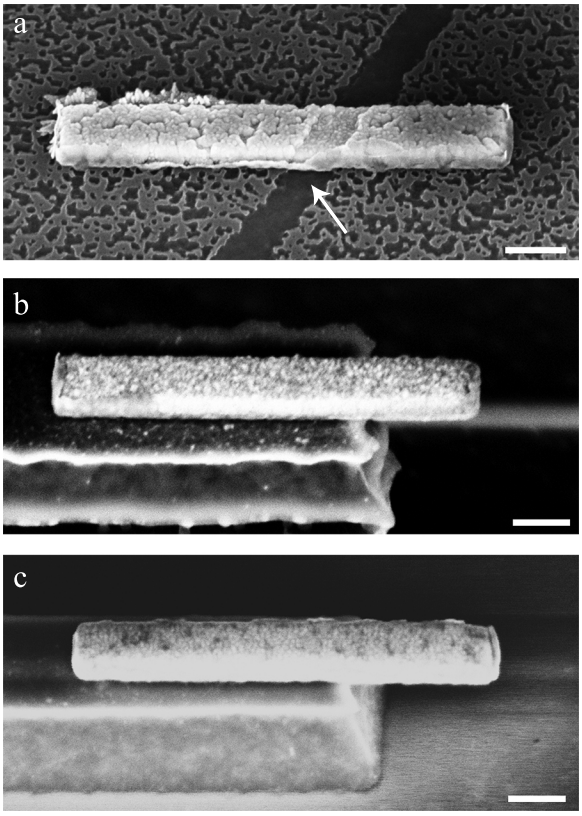

Figure 3.14: The influence of substrate roughness on the surface roughness of nanomagnets. (a) The surface roughness of a silicon substrate that was severely pitted by BOE during the chip release led to the deposition of a nanomagnet with high surface roughness. Note that the roughness of the nanomagnet corresponds to the roughness of the substrate; the nanomagnet surface roughness was large over the pitted silicon but was significantly less over the diagonal stripe of silicon that was not damaged (indicated by the arrow). (b) A cobalt nanomagnet on another wafer that was exposed to BOE. This silicon substrate was significantly less pitted than the substrate in panel (a), and the nanomagnet surface was correspondingly smoother. (c) A nickel nanomagnet deposited on a silicon wafer that had not been exposed to BOE. Note that the surface roughness of the nickel nanomagnet was minimal. All scale bars represent 200 nm.

could be integrated on magnet-tipped chips.

In addition to attaching nanomagnet-tipped chips to cantilevers, this chip-on-cantilever approach also represents a versatile route for affixing essentially any vacuum-compatible sample to the leading edge of a fragile, high-sensitivity cantilever. The combination batch- and serial-fabrication process could be used to attach a custom-fabricated magnetic tip onto the end of a commercial cantilever. Samples that require heat-intensive growing conditions such as carbon nanotubes [137] or samples that cannot tolerate the high-heat processing steps in cantilever fabrication such as superconducting rings [94] could also be adhered to cantilevers by this technique without needing to resolve process integration challenges.

Acknowledgements

I thank Daron Westly for helpful discussions and assistance with e-beam lithography and Mick Thomas for assistance with FIB processing. I also thank undergraduate student Alex Senko for assistance with HF vapor encasement material testing. Work in this chapter was conducted with the financial support of the National Institutes of Health (Grant No. 5R01GM-070012), the Army Research Office MultiUniversity Research Initiative (Grant No. W911NF-05-1-0403), and the National Science Foundation through the Cornell Center for Nanoscale Systems (Grant Nos. EEC-0117770 and EEC-0646547). The Transmission Electron Microscopy facility within the Cornell Center for Materials Research, which is supported by the National Science Foundation Materials Research Science and Engineering Centers program (Grant No. DMR-0520404), was used for FIB processing. Fabrication was conducted in the Cornell NanoScale Science and Technology Facility, a member of the National Nanotechnology Infrastructure Network, which is supported by the National Science Foundation (Grant No. ECS-0335765).

CHAPTER 4

NICKEL AND COBALT MAGNETIC MATERIAL CHARACTERIZATION

High-sensitivity magnet-on-cantilever MRFM requires that nanoscale magnetic tips at the leading edge of attonewton-sensitivity cantilevers be well-magnetized and have high saturated magnetic moments. A process to fabricate nanomagnet-tipped chips and attach them to cantilevers was presented in Chapter 3. Scanning electron microscopy (SEM) images indicated that the nanomagnets were fabricated with high yield.

This chapter summarizes work conducted to analyze the magnetization and elemental composition of nickel and cobalt nanomagnets, as well as large-area thin magnetic films. Frequency-shift cantilever magnetometry was conducted to provide estimates of the magnetization of individual nanomagnets with dimensions of approximately $100\text{nm} \times 100\text{nm} \times 1.5\mu\text{m}$. Initial cantilever magnetometry studies indicated that the nickel nanomagnets exhibited saturation magnetizations that were significantly lower than the theoretical value for nickel of $\mu_0 M_{\text{sat}} = 0.6$ T. To analyze potential sources of damage, superconducting quantum interference device (SQUID) magnetometry and X-ray photoelectron spectroscopy (XPS) with depth profiling were utilized. Key findings from this analysis led to adjustments of the nanomagnet fabrication process. Frequency-shift cantilever magnetometry conducted on a cobalt nanomagnet after the modifications were made indicated that the magnetization of the nanomagnet had a fully saturated magnetic moment.

4.1 Initial Frequency-Shift Cantilever Magnetometry Studies on Nickel Nanomagnets

Frequency-shift cantilever magnetometry is one of the few techniques that is capable of determining the average magnetization of individual sub-micrometer magnetic particles [81, 89,

93, 117]. Frequency-shift cantilever magnetometry was used to calculate the saturation magnetization of overhanging nickel nanomagnets on silicon chips that were prepared using the original magnet-tipped fabrication protocol detailed in Section 3.2. Six nickel nanomagnet-tipped chips were attached to cantilevers by the focused ion beam (FIB) lift-out method (Section 3.4) prior to cantilever magnetometry analysis.

These nickel nanomagnets had widths of either 120 nm or 220 nm and were either non-overhanging or had an overhang of approximately 300 nm (Table 4.1). Magnetometry experiments were conducted on a custom-built probe operating at $T = 4.2\,\mathrm{K}$ and $P = 10^{-6}\,\mathrm{mbar}$. Changes in cantilever frequency were measured as an external magnetic field applied along the long axis of the magnet was swept between $-4\,\mathrm{T}$ and $+4\,\mathrm{T}$. Cantilever motion was monitored using a fiber-optic interferometer (wavelength $\lambda = 1310\,\mathrm{nm}$ and power $P \approx 3\,\mu\mathrm{W}$). During the measurement, the cantilever was forced to self oscillate at a root mean square (RMS) amplitude of approximately 90 nm. Self oscillation was achieved by using the cantilever as the frequency determining element of a proportional-integral-controlled-gain positive feedback circuit that drove a piezoelectic element located under the cantilever base. The cantilever frequency was determined by digitizing the interferometer output and using a software frequency demodulator [85]. Spring constant changes Δk were computed from frequency shifts Δf using $\Delta k = 2k\Delta f/f_0$ with k and f_0 the cantilever spring constant and resonance frequency, respectively. The spring constant was determined from the mean square displacement of the undriven cantilever at a temperature $T = 4.2\,\mathrm{K}$ [138]. Cantilever dissipation was inferred from either the cantilever ringdown time or by following the gain control of the positive feedback loop. The magnetic moment of the nanomagnet was extracted by fitting the spring constant shift versus magnetic field data to [89, 93, 139]:

$$\frac{\Delta k}{k} = \frac{\mu_{\mathrm{sat}}}{k}\left(\frac{\alpha}{l}\right)^2 \frac{B\Delta B}{B + \Delta B}. \tag{4.1}$$

with μ_{sat} the saturated magnetic moment, $\alpha = 1.377$ a constant dependent on the cantilever mode shape, l the cantilever length, $B = \mu_0 H$ the applied magnetic field, and $\Delta B =$

$\mu_0\mu_{\rm sat}\Delta N/V$, where μ_0 is the permeability of free space and $\Delta N = N_t - N_l$ is the difference in demagnetization factor along the cantilever's thickness and length, respectively. The volume V of the nanomagnet was computed from estimates of the magnet's lateral dimensions (obtained from SEM images) and thickness (measured for one representative sample using atomic force microscopy). Fractional cantilever frequency shift as a function of applied magnetic field is shown in Fig. 4.1[1] for the magnet on cantilever C1, which had a 220 nm wide overhanging magnet. The parameters $\mu_{\rm sat}$ and ΔN were obtained from a non-linear least-squares fit of the frequency-shift data to Eq. 4.1, and the magnetization $\mu_0 M_{\rm sat}$ was computed using $\mu_0 M_{\rm sat} = \mu_0\mu_{\rm sat}/V$. Fit results are shown in Table 4.1, and the nominal saturated magnetic moment $\mu_{\rm sat}^{\rm nominal}$, which was calculated for fully-magnetized nickel particles of the same measured dimensions, is provided for comparison. For one magnet, indicated in the table, the fit was too poor to accurately obtain all three parameters from the frequency-shift data; in this case, ΔN was calculated from the estimated length and thickness using demagnetization factors obtained by Aharoni for a rectangular prism [140], and $\mu_{\rm sat}$ and V were obtained by fitting.

The data in Table 4.1 indicate that the net magnetization of each of the six nickel nanomagnets studied was lower than the theoretical value for bulk nickel. Two magnets with widths of 120 nm, C2 and C3, were studied. When compared to the saturation magnetization $\mu_0 M_{\rm sat} = 0.6$ T of bulk nickel [91], the saturation magnetization for C2 and C3 were 42% $\pm$ 5% and 59% $\pm$ 12% of the expected value, respectively. Four 220 nm wide nanomagnets were studied: C1, C4, C5, and C6. All of the 220 nm wide nanomagnets exhibited saturation magnetizations that were more than 50% of the value for bulk nickel; the average saturation magnetization was 63% $\pm$ 10%, and the best-magnetized magnet (on C6) was 79% $\pm$ 11% magnetized. Here the standard error in $\mu_0 M_{\rm sat}$ is reported as an indication of the goodness of fit; note that the true error in $\mu_0 M_{\rm sat}$ is dominated by the uncertainly in measuring k, which

[1]Figure 4.1 and Table 4.1 reprinted with permission from J. G. Longenecker *et al.*, J. Vac. Sci. Technol. B **29**, 032001 (2011). Copyright 2011, American Vacuum Society.

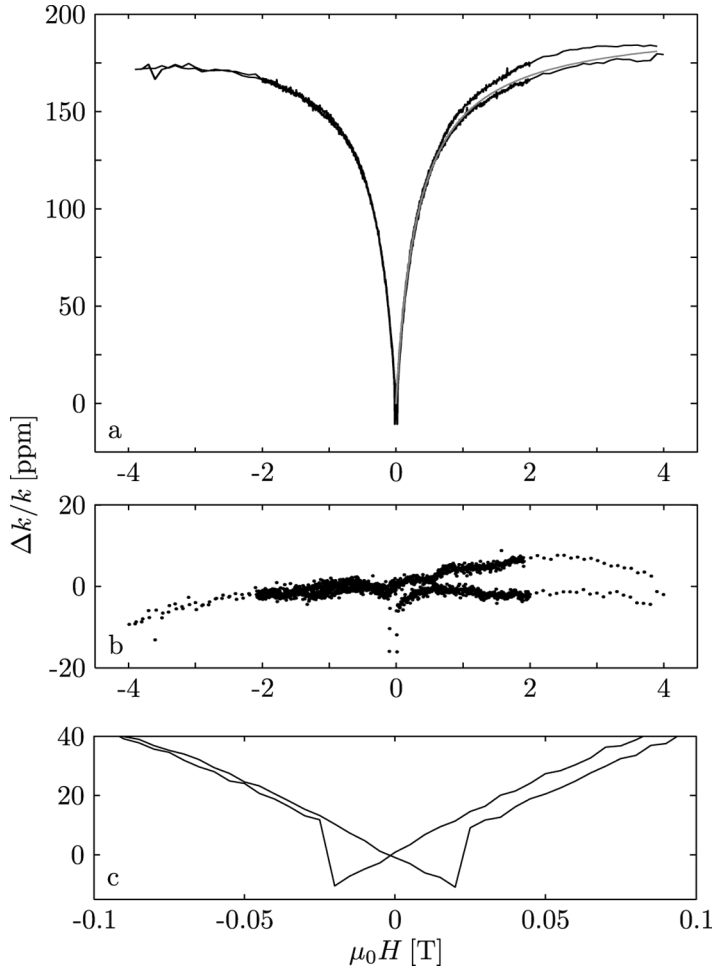

Figure 4.1: Frequency-shift cantilever magnetometry for the 220 nm wide nickel nanomagnet on cantilever C1. The applied external field was aligned parallel to the length of the nanomagnet. Upper: Data (solid; black) and best-fit to Eq. 4.1 (dotted; gray). Middle: Fit residuals, shown for an applied field ranging from -4 T to $+4$ T. Lower: Magnified view of the hysteresis present near zero field, indicating single-domain switching with a coercive field of $H_c \approx 0.05$ T.

Table 4.1: Summary of cantilever and magnet properties. All cantilever properties were measured at a field of 0 T unless otherwise indicated. All of the cantilevers studied had dimensions of 200µm × 4µm × 0.34µm. Cantilever resonance frequencies were $f_0 \approx 9000\,\mathrm{Hz}$ prior to adhesion of the magnet-tipped chips. The reported error bars represent a 95% confidence interval.

quantity	C1	C2	C3	C4	C5	C6	C7	unit
f_0	6631	6053	5054	6486	5351	4838	5695	Hz
Q (at 0 T)	67,900	74,400	41,000	86,700	43,200	94,000	49,800	(unitless)
Q (at 5 T)	68,600	75,500	39,600	84,200	41,600			(unitless)
k	780	500	563 ± 63	780	780	703 ± 52	764 ± 61	$\times 10^{-6}$ N m^{-1}
Γ	275	177	432	221	537	246	429	$\times 10^{-15}$ N s m^{-1}
F_{min}	8.0	6.4	10.0	7.2	11.2	7.6	10.0	$\times 10^{-18}$ N
l_{m}	1500	1500	1500	1500	1500	1500	1500	nm
l_{overhang}	~ 300	~ 300	~ 300	~ 300	0	0	0	nm
w_{m}	220	120	120	220	220	220	220	nm
t_{m}	90	90	90	90	90	90	90	nm
μ_{sat}	9.71 ± 0.98	4.50 ± 0.90	3.21 ± 0.30	9.08 ± 1.36	9.05 ± 1.43	11.72 ± 1.27	8.83 ± 0.72	$\times 10^{-15}$ A m^{-2}
$\mu_0 M_{\mathrm{sat}}$	0.41 ± 0.04	0.35 ± 0.07	0.25 ± 0.03	0.38 ± 0.06	0.38 ± 0.06	0.49 ± 0.08	0.37 ± 0.03	T
ΔN	0.81 ± 0.08	0.51[a]	0.93 ± 0.10	0.99 ± 0.15	0.86 ± 0.15	0.40 ± 0.10	0.70 ± 0.06	(unitless)
$\mu_{\mathrm{sat}}^{\mathrm{nominal}}$	14.18	7.73	7.73	14.18	14.18	14.18	14.18	$\times 10^{-15}$ A m^{-2}

[a] For this fit, ΔN was calculated from the magnet shape as described in the text.

could be 40% or larger. As discussed further in Section 4.5, this large experimental error is due to the inability to localize the position of the laser interferometer on the cantilever pad (see Figure 3.4) to better than within ±15 µm.

In summary, frequency-shift magnetometry conducted on 120 and 220 nm wide magnets indicated that the nanomagnets exhibited saturation magnetizations that were lower than the value for bulk nickel. Even considering the large 40% uncertainty in the spring constant, the magnetization of most of the tips is lower than the expected $\mu_0 M_{\mathrm{sat}} = 0.60$ T. The reduced-magnetization results presented in Table 4.1 would be consistent with the presence of a uniform-thickness damage shell of approximately 16 nm. By studying both overhanging (C1-C4) and non-overhanging (C5-C6) nanomagnets, it was determined that the saturation magnetization of the nanomagnets was unaffected by the fabrication steps required to produce overhanging magnets. The cantilever quality factor was not measured to have a strong dependence on applied magnetic field; representative shifts in an applied field of 5 T are reported in Table 4.1.

4.2 Hypotheses to Explain the Low Magnetization of the Nickel Nanomagnets

The low saturated magnetic moments of the nickel nanomagnets measured by frequency-shift cantilever magnetometry in Section 4.1 were a surprising finding because they could not be attributed to process incompatibilities. Nickel oxidation could not account for a 16 nm thick shell of damage since nickel is well-documented to not form an oxide that is thicker than 1 to 2 nm near room temperature and atmospheric pressure [110–112, 141]. Damage due to silicide formation during the evaporation of hot nickel onto the silicon substrate also was unlikely; electron energy loss spectroscopy (EELS) did not indicate the presence of any

silicon in the overhanging component of the nickel nanomagnet studied in Chapter 2, and it has been reported that the native SiO_2 layer on a silicon surface is sufficient to prevent nickel silicidation during deposition of the magnetic material [103]. Additionally, the FIB attachment procedure was not indicated to be a source of magnet damage. Frequency-shift cantilever magnetometry characterization was conducted on a seventh magnet-tipped cantilever (C7 in Table 4.1) that had a nickel nanomagnet coated with 10 nm of platinum. The saturation magnetization of C7 was comparable to other 220 nm wide magnets, indicating that coating with a protective layer did not change the magnetization. If the damage had been due to ion-beam exposure at 30 kV, significant gallium implantation damage should have damaged the top 10 nm of the film and a difference in magnetization would have been observed between the platinum-capped and uncapped nanomagnets.

It was also considered whether the low magnetization could have resulted from a faulty assumption about the planarity of the cantilevers. It has been observed that some of the custom-fabricated silicon cantilevers have a downward bend of a few degrees near the leading edge (Figure 4.2). In the frequency-shift cantilever magnetometry measurements in Section 4.1, it was assumed that the longest axis of the nanomagnet (the 1.5 µm length) was parallel to the applied external field. Since the long axis of the nanomagnet lies along the length of the cantilever, a bend in the cantilever would have introduced an offset angle between the nanomagnet and the applied external field. Frequency-shift magnetometry simulations were carried out for offset angles ranging from $\alpha = 0°$ to $\alpha = 45°$, as shown in Figure 4.3. It was determined that the cantilever would need to be bent by at least 30° to account for the reduction of magnetization observed in Section 4.1; the observed bending of less than 10° in Figure 4.2 would at most account for a 5% error in the saturation magnetization.

Since the error in the spring constant k could be as large as 40%, it is possible that almost

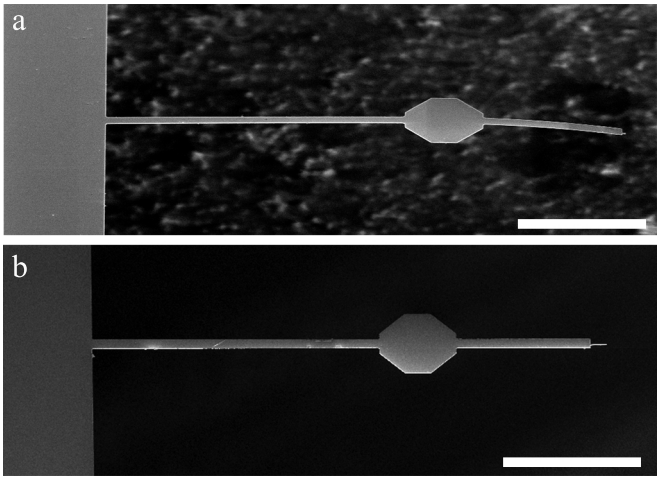

Figure 4.2: SEM images of attonewton-sensitivity cantilevers. (a) 52° tilted image of a cantilever that is bent by a few degrees. (b) 30° tilted image of a straight cantilever. Both scale bars represent 50 µm.

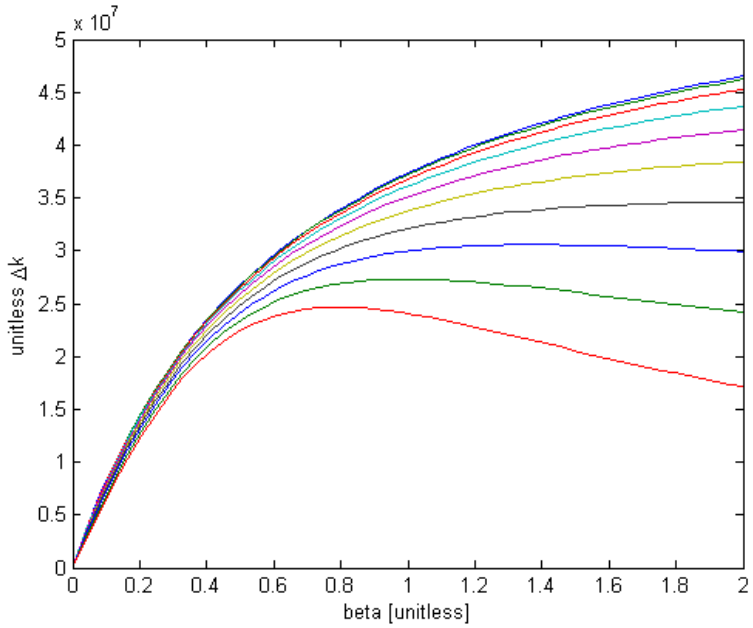

Figure 4.3: Frequency-shift cantilever magnetometry simulations to assess the effect of cantilever bending. Offset angles between the long axis of the nanomagnet/cantilever and the applied field were simulated between angles of 0° (top line) to 45° (bottom line) in increments of 5°. The simulations indicate that offset angles larger than 30° (black line) would be required to account for the loss of magnetization observed in Section 4.1.

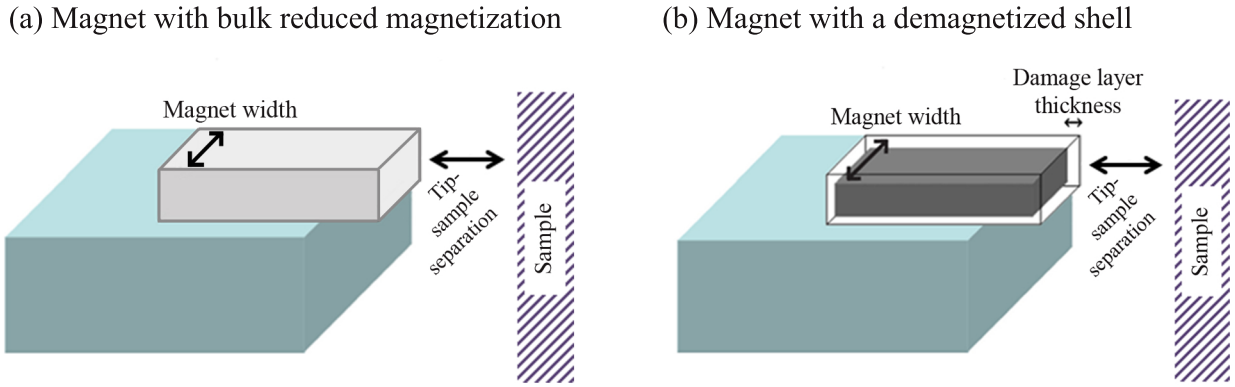

Figure 4.4: Illustrations of two proposed reduced-magnetization damage scenarios (hypotheses 1 and 2). (a) Bulk damage scenario in which the saturated magnetization of the nanomagnet is uniformly reduced; the reduced magnetization is represented as light gray. In this case, the tip-sample separation is the same as the spacing between the magnetic material and the sample surface. (b) Fully-magnetized nanomagnet core (dark gray) encased by a shell of non-magnetic material (white). In this case, the spacing between the magnetic material and the sample surface is equal to the sum of the tip-sample separation and the damage layer thickness.

all of the observed reduction of magnetization was due to poor measurement of k. However, two alternative fabrication-related explanations for the observed reduction in saturation magnetization were still possible and worthy of consideration: (1) the nickel films could have been contaminated by using the general-purpose evaporation chamber at the Cornell CNF nanofabrication facility, which possibly could have caused the formation of non-magnetic or antiferromagnetic regions and resulted in a roughly uniform reduction in magnetization, as illustrated in Figure 4.4(a); or (2) a damage layer of demagnetized material could have been formed as a shell around the nanomagnet, as illustrated in Figure 4.4(b).

4.3 Nickel and Cobalt Magnetic Material Analysis

SQUID and XPS data on nickel and cobalt films are presented to distinguish between hypotheses 1 and 2 from Section 4.2. Contamination of the bulk magnetic material (hypothesis 1) was tested by using SQUID magnetometry to study large-area thin films of nickel and

cobalt that were deposited using the same evaporation chamber that was used for the evaporation of the nickel nanomagnets in Section 4.1. Nickel and cobalt crucibles used for the evaporations were stored separately from the common-access crucibles in the cleanroom to avoid contamination of the metal targets. Surface contamination (hypothesis 2) was tested by performing elemental analysis of blanket-deposited thin films of nickel and cobalt using XPS in combination with depth profiling. Understanding the presence of any contamination at the leading edge of the nanomagnets was of particular importance since the nanomagnet leading edge is brought to within a few nanometers of a sample surface in MRFM experiments. At these small tip-sample separations, the experimental noise is dominated by non-contact friction interactions between the magnet-tipped cantilever and the surface [83, 84]. A non-magnetic layer at the leading edge of the nanomagnet would increase the distance between the nanomagnet and the sample spins, which would decrease the tip-field gradient and the signal-to-noise ratio of the MRFM signal.

4.3.1 SQUID Magnetometry Sample Preparation

Square and circular thin magnetic films were studied using SQUID magnetometry. Square films had lateral dimensions of 1.5 mm and circular films had a diameter of approximately 1.7 mm; all films covered an area of 2.25 mm^2. All samples were prepared on 500 µm thick fused silica wafers. Fused silica had a low observed diamagnetic susceptibility, whereas p-type silicon wafers with a resistivity of 10 to 25 Ω cm had a high magnetic susceptibility that overpowered the SQUID signal. A bilayer resist of LOR 10A below SPR 220-3 was spun on the wafer. The LOR 10A layer was spun at 500 rpm for 10 seconds, followed by spinning at 3000 rpm for an additional 45 seconds. Prior to depositing the second resist layer, the wafer was baked at 180°C for 5 minutes. The SPR 200-3 resist layer was spun at 3000 rpm for 30 seconds and the wafer was baked again at 115°C for 90 seconds. The

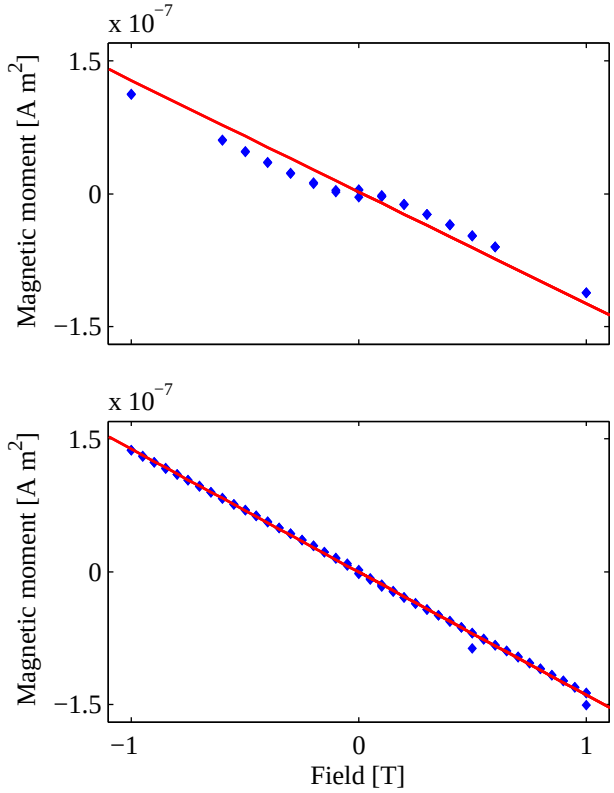

Figure 4.5: In-plane SQUID magnetization loops obtained at 4.0 K for blank fused silica chips that were handled with metal tweezers (top) or plastic tweezers (bottom). Metal tweezers were observed to induce ferrometric contamination of the fused silica substrate.

wafer was patterned on the ABM contact aligner; the exposure time was 12 seconds. The post exposure bake was at 115°C for 90 seconds. The patterned wafer was descummed for 60 seconds in an oxygen plasma using an Oxford PlasmaLab 80+ RIE System. The magnetic films were deposited using the same procedures as outlined in Sections 3.2 and 3.6. Nickel films (either 43 or 82 nm thick) or cobalt films (84 or 92 nm thick) were deposited on top of 5 nm thick chromium or titanium adhesion layers. In some cases, 10 nm of platinum was evaporated on top of the thin films. After lift-off, the wafers were diced into 6.5×6.5 mm pieces using a KS 7100 Dicing Saw such that each chip contained one magnetic circle or square. The resulting chips were handled with plastic tweezers to minimize ferromagnetic contamination (Figure 4.5).

4.3.2 SQUID Magnetometry Analysis and Results

SQUID magnetometry was conducted using a Quantum Design MPMS-XL SQUID Magnetometer. Each chip was centered in a plastic drinking straw sample holder; the chip width was optimized to fit snugly in the drinking straw. The drinking straw was adhered to the end of a sample rod using Kapton tape, and the sample was inserted into the magnetometer. The system was cooled to 4.0 K in the absence of a magnetic field and was allowed to equilibrate for 30 minutes prior to data collection. Measurements were typically taken between either ± 1.5 T or ± 3 T, first sweeping positive to negative and then back from negative to positive fields.

The magnetic moment of each film was calculated by subtracting the linear diamagnetic background of the fused silica chip from the total signal. To convert to saturation magnetization, the magnetic moment was averaged in the saturated regime and was divided by the volume of the thin film sample. The film diameter (circle) or width (square) was measured by optical microscopy, and the thickness of the magnetic material was determined by using an *in situ* quartz crystal microbalance and carrying out atomic force microscope (AFM) profilometry on the sample edge.

Background-subtracted SQUID magnetometry data for circular platinum-capped nickel (TiNiPt) and uncapped nickel (TiNi) films, both with titanium adhesion layers, are shown in Figure 4.6. The platinum-capped nickel film was 43 ± 2 nm thick and the uncapped film was 82 ± 4 nm thick; both error bars represent a 95% confidence interval. The saturation magnetization was determined to be 0.54 ± 0.03 T for the platinum-capped film and 0.61 ± 0.03 T for the uncapped film. The saturation magnetization error bars represent 95% confidence intervals and account for the error in the nickel thickness, the nickel lateral dimensions, and the SQUID measurement. The saturation magnetizations of both the protected and unprotected nickel films are within reasonable agreement of the expected value for nickel of 0.6 T,

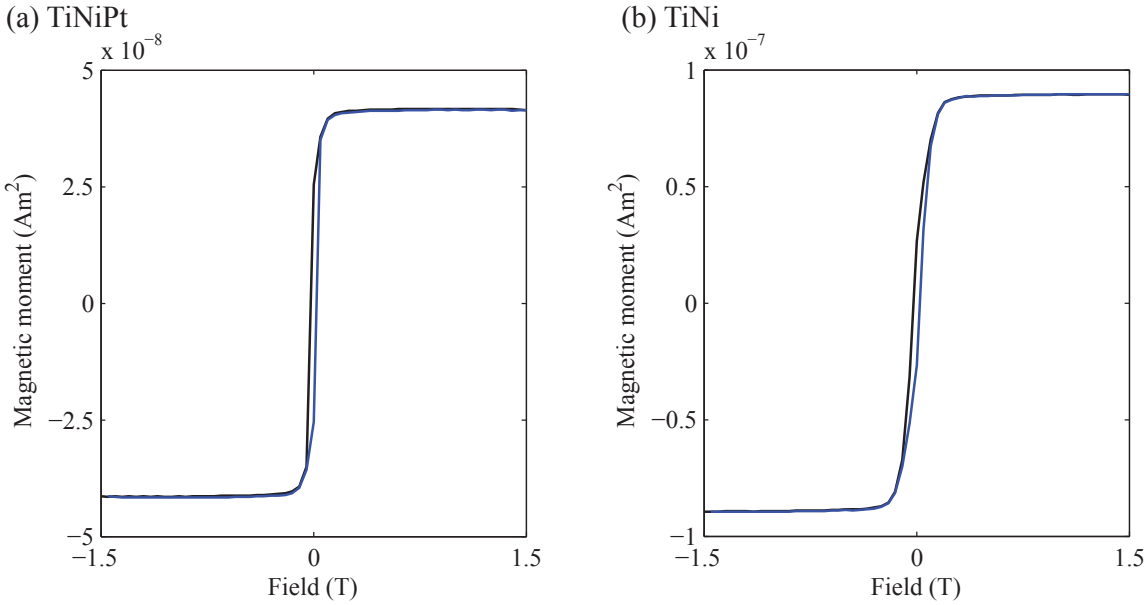

Figure 4.6: In-plane magnetization loops for two circular nickel films with titanium adhesion layers that were obtained at 4.0 K using SQUID magnetometry. The magnetization was swept from +1.5 T to −1.5 T (black) and then from −1.5 T to +1.5 T (blue). (a) Platinum-capped nickel film with an area of 2.25 mm^2 and a magnetic layer thickness of 43 nm. Given this volume, the observed saturated magnetic moment corresponds to a saturation magnetization $\mu_0 M_{sat} = 0.54 \pm 0.03$ T. (b) Uncapped 82 nm thick nickel circular film that also had an area of 2.25 mm; the corresponding saturation magnetization is 0.61 ± 0.03 T.

which indicates that there was minimal degradation or contamination of the nickel magnetic material.

It is important to note that the choice of adhesion layer material can play a critical role in the magnetization properties of the film. In Section 4.1 and in previous studies [68, 81, 89], 5 nm thick chromium adhesion layers were used and the magnetic contributions of the chromium layers were assumed to be negligible. In Figure 4.7, in-plane magnetization loops for two square nickel films with the same lateral dimensions and thicknesses are shown. The nickel film with the titanium adhesion layer (Figure 4.7(a)) displayed the expected saturation behavior. In contrast, the otherwise identical nickel film with a chromium adhesion layer (Figure 4.7(b)) exhibited anomalous behavior at high fields, which is attributed to interactions between the ferromagnetic cobalt and antiferromagnetic chromium or Cr_2O_3

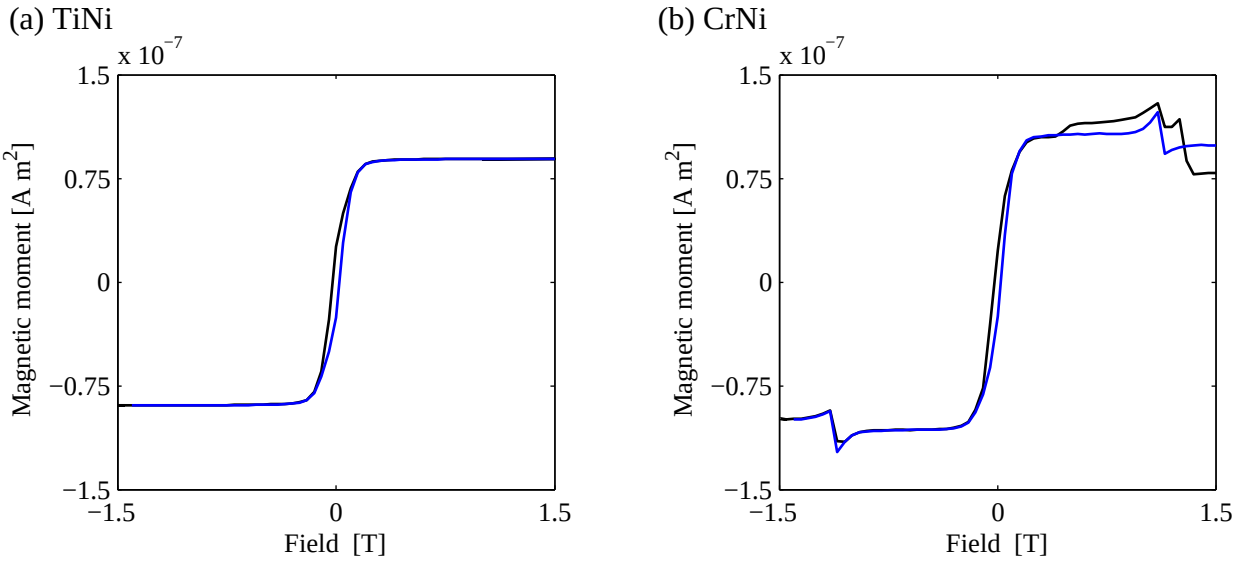

Figure 4.7: SQUID in-plane magnetization loops for nickel films with (a) titanium and (b) chromium adhesion layers. Measurements were conducted at 4.0 K. The magnetization was swept from +1.5 T to −1.5 T (black) and then from −1.5 T to +1.5 T (blue). Other than the choice of adhesion layer material, the films were nominally identical in area and thickness. The high-field magnetic behavior in panel (b) is attributed to the 5 nm thick chromium layer.

[133]. Because of these findings, all subsequent deposited magnetic films were evaporated with titanium adhesion layers.

Circular cobalt thin films with and without platinum capping layers were also studied by SQUID magnetometry. Both films were circular and had titanium adhesion layers. The platinum-capped cobalt film was 84 ± 5 nm thick, and the uncapped film was 92 ± 4 nm thick; both error bars represent a 95% confidence interval. The area of the platinum-capped film was straight-forward to calculate based on its thickness and area. The chip containing the uncapped film had residual magnetic material at the corners from dicing saw alignment marks that were not completely removed during dicing; the small combined area of these alignment marks (approximately 1% of the total area) was taken into account for the final volume of the uncapped sample.

After accounting for the volume of each film, the measured saturated magnetic moments

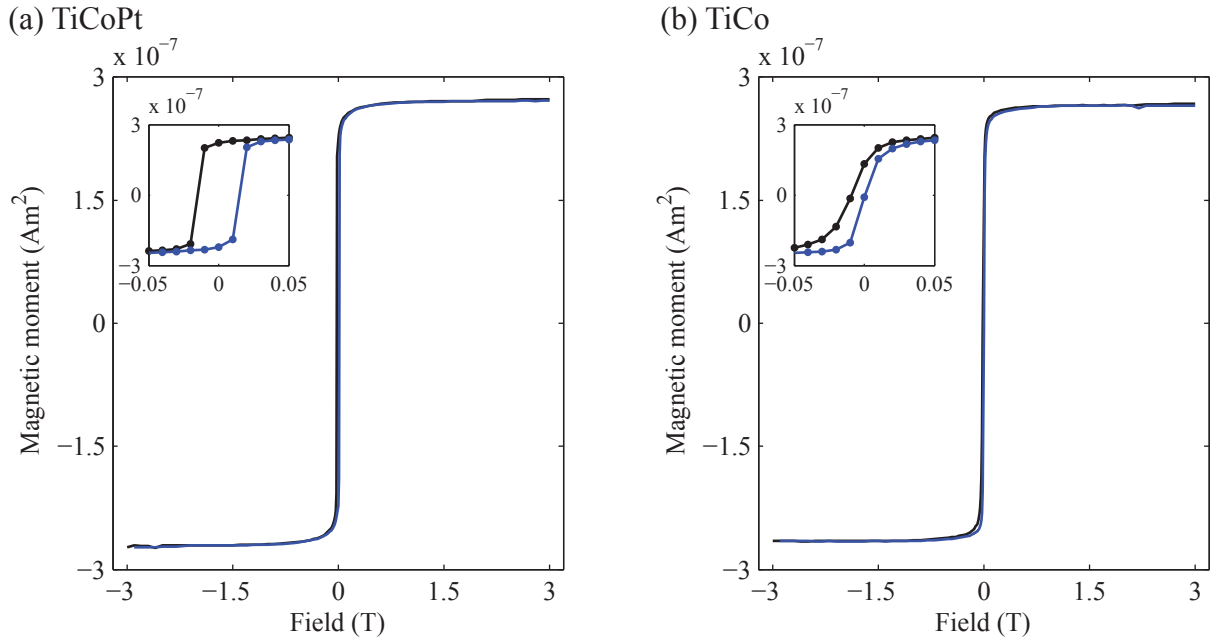

Figure 4.8: In-plane magnetization loops for platinum-capped and uncapped cobalt films obtained at 4.0 K using SQUID magnetometry and magnified views of the hysteresis near zero field. (a) Platinum-capped thin film with an 84 nm thick cobalt layer and a corresponding saturation magnetization of $\mu_0 M_{\text{sat}} = 1.8 \pm 0.1$ T. (b) Uncapped 93 nm thick cobalt film with $\mu_0 M_{\text{sat}} = 1.6 \pm 0.1$ T. For both films, the magnetization was swept from +3 T to −3 T (black) and then from −3 T to +3 T (blue).

were converted to saturation magnetizations of $\mu_0 M_{\text{sat}} = 1.8 \pm 0.1$ T for the platinum-capped film (Figure 4.8(a))[2] and 1.6 ± 0.1 T for the uncapped film (Figure 4.8(b)). The saturation magnetization error bars again represent 95% confidence intervals and account for the error in the cobalt thickness, the cobalt lateral dimensions, and the SQUID measurement. The saturation magnetization for the platinum-capped film corresponds well to the theoretical saturated magnetic moment for cobalt of 1.8 T [91]. The saturation magnetization for the uncapped film is lower than the value for bulk cobalt, indicating the possible presence of a cobalt oxide damage layer.

For the cobalt thin films, it is instructive to note the differences between the hysteresis

[2]Figures 4.8(a), 4.9, 4.12, and 4.13 reprinted with permission from the Supporting Information for J. G. Longenecker *et al.*, ACS Nano **6**, 9637 (2012). Copyright 2012, American Chemical Society.

observed for the platinum-capped and uncapped films, as shown in the insets in Figure 4.8(a) and 4.8(b), respectively. Specifically, the hysteresis for the unprotected film (Figure 4.8(b)) transitions slowly between positive to negative magnetic moments, whereas the transition for the platinum-capped film (Figure 4.8(a)) is abrupt. The slow transition for the unprotected film is consistent with cooling a surface-oxidized cobalt film to cryogenic temperatures in the absence of an external magnetic field[142]. If unprotected cobalt samples would be field-cooled in future experiments, an exchange bias might be observed that could confirm the presence of a cobalt oxide layer [142]. It is also possible that SQUID magnetometry could be used to determine the thickness of this damage layer; SQUID magnetometry has been used to determine that a stable oxidation layer with a thickness of 4.4 nm formed on unprotected, 100 nm thick cobalt films [143]. Even though the platinum-capped sample also was cooled in the absence of a magnetic field, the abrupt transition for the hysteresis of the protected film indicates that the platinum-capping layer may have successfully prevented the formation of nickel oxide.

4.3.3 XPS Sample Preparation

XPS samples were prepared on silicon substrates by blanket deposition of 80 to 100 nm thick films using a CVC SC4500 E-gun Evaporation System. To best assess the damage experienced by platinum-capped nanomagnets, which are coated with platinum on their top surface but remain unprotected on their leading edge and other side walls, XPS samples with and without platinum capping layers were prepared.

Both nickel and cobalt XPS samples were prepared. A platinum-capped nickel film was used as a calibration sample to confirm that the XPS depth profiling method for determining etch depth was consistent with the film thickness measured by AFM; additional calibration details are provided in Section 4.3.4 and Figure 4.9. Uncapped and platinum-capped nickel

films (Figures 4.10 and 4.11) were assessed within 48 hours of preparation. Uncapped and platinum-capped cobalt films were exposed to air for one week prior to analysis to assess the oxidation damage; these are labeled in Fig. 4.12 and 4.13 as the 'unbaked' samples. A second set of cobalt samples were exposed to air for the same period of time, but they were spin-coated with 2 µm of 495,000 molecular weight (poly)methylmethacrylate (PMMA) resist and baked at 115°C for 40 minutes prior to analysis in order to emulate the processing conditions of the nanomagnets; these are labeled as the 'baked' films.

4.3.4 XPS with Depth Profiling Analysis and Results

XPS in conjunction with argon ion milling was used to measure the elemental composition versus depth in nickel and cobalt films. XPS samples were analyzed using a Surface Science Instruments model SSX-100 spectrometer with monochromated aluminum K_α X-rays (1486.6 eV) and a beam diameter of 1 mm. Photoemitted electrons were collected at a 55 degree emission angle using a hemispherical analyzer with a 150 V pass energy. Depth profiling was performed using an argon ion source with an ion energy of 500 eV (Figure 4.12), 1000 eV (Figure 4.13(baked)), or 4000 eV (all other samples); the total beam current was 1 µA and the ion beam was rastered over a $1.5 \times 2.5\,\text{mm}$ area. Survey scans over 0 to 1000 eV were used to determine atomic composition versus depth using the following peaks: Ni $2p$, Co $2p$, Pt $4d$ (Figure 4.9) or Pt $4f$ (Figures 4.11 and 4.13), O $1s$, Ti $2p$, and Si $2s$. The spectroscopic data were used to calculate atomic percent composition of the films by using the Shirley background [144] and integrating under the appropriate peaks. The count rates for the representative peaks of each element present were scaled by their relative sensitivity factors to calculate the atomic percent composition for each spectrum.

Estimation of sample composition as a function of depth was enabled by measuring the total etch depth of each ion-milled recess *ex situ* by stylus profilometry and linearly con-

verting from etch time to etch depth. To confirm that a linear conversion was appropriate, the cobalt film in Fig. 4.9 was etched through to the silicon substrate. For comparison, the relative thicknesses of the layers were measured *in situ* during deposition by a quartz crystal microbalance, and the total film thickness was measured after deposition by AFM profilometry. The layer thicknesses were determined by AFM to be 4.1 ± 0.05 nm of titanium, 81.4 ± 1.0 nm of cobalt, and 8.1 ± 0.1 nm of platinum; the error bars for each component, which represent 95% confidence intervals, were calculated based on the error in the total film thickness and the relative thicknesses of the three layers. The thicknesses of the film layers agreed well with the depths calculated using XPS depth profiling with linear conversion from milling time to depth. Since the same process was used to convert all etch times to depth, the depth profiles for the remainder of the films should also be accurate. The etch time-to-depth conversion factors for each film were 1.8 nm/min for Fig. 4.9, 1.53 nm/min for Figure 4.10, 1.04 nm/min for Figure 4.11, 0.31 nm/min for Figure 4.12(unbaked), 0.81 nm/min for Figure 4.12(baked), 6.6 nm/min for Figure 4.13(unbaked), and 1.0 nm/min for Figure 4.13(baked).

XPS data for platinum-capped and uncapped nickel films are shown in Figures 4.10 and 4.11, respectively. For the uncapped nickel film, oxygen content was observed within 25 nm of the nickel surface and was primarily concentrated in the first 5 nm. Capping with 8 nm of platinum was observed to successfully prevent the formation of nickel oxide.

XPS data for platinum-capped and uncapped cobalt films are shown in Figures 4.12 and 4.13, respectively. To estimate the damage to cobalt nanomagnets on magnet-tipped chips, magnetic films were compared with and without exposure to the elevated temperatures of the resist bake step for the definition of the U-shaped etch pits (Section 3.6). Baked films were coated with resist and heated at 115°C for 40 min. Unbaked cobalt films without protective platinum coatings showed oxygen within the first 3 nm of the cobalt layers, and

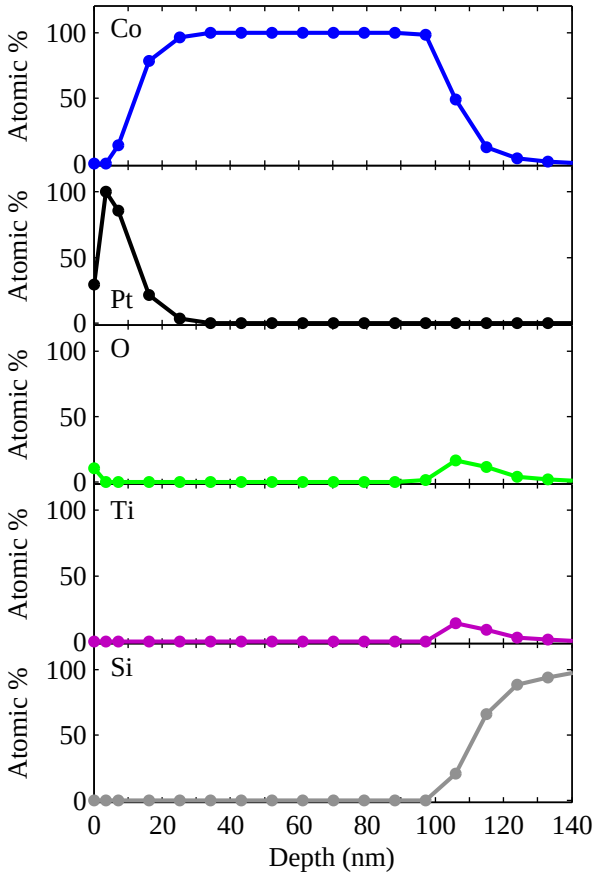

Figure 4.9: A cobalt film with a titanium adhesion layer and platinum capping layer that was evaporated onto a silicon substrate. The XPS depth profile details the atomic concentrations of cobalt (blue), platinum (black), oxygen (green), titanium (purple), and silicon (gray) as a function of depth in the film at approximately 9 nm/point spacing (data points indicated by filled circles). The depth at each point was calculated as a linear conversion of the percentage of the total time etched multiplied by the total etch depth that was measured by profilometry. The thicknesses calculated using XPS with depth profiling were compared to the thicknesses measured by the AFM-based approach discussed in the text to determine the validity of a linear conversion from etch time to depth. The thicknesses of the layers measured by the AFM-based approach were titanium (4.1 $\pm$ 0.05 nm), cobalt (81.4 $\pm$ 1.0 nm), and platinum (8.1 $\pm$ 0.1 nm), which roughly agree with the XPS thicknesses.

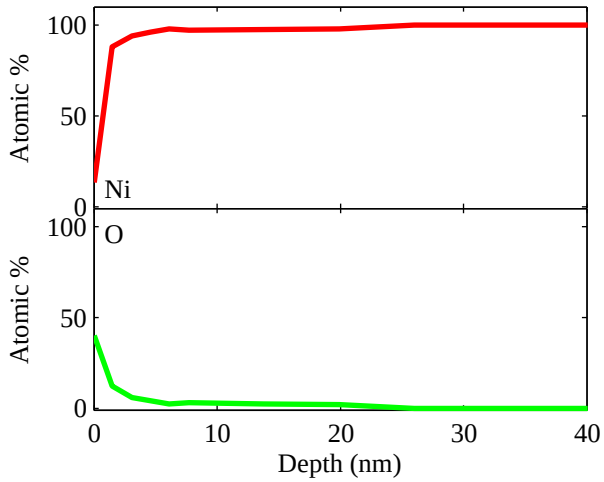

Figure 4.10: XPS depth profile of the top 40 nm of a blanket-deposited nickel film that was approximately 80 nm thick. Atomic concentrations as a function of depth are shown for nickel (red) and oxygen (green). The film was analyzed within 48 hours of deposition. Oxygen content was observed within the top 25 nm of the nickel film, with the majority of the oxygen concentrated in the top 2 to 5 nm of the film. The data indicate significant oxidation of the nickel film.

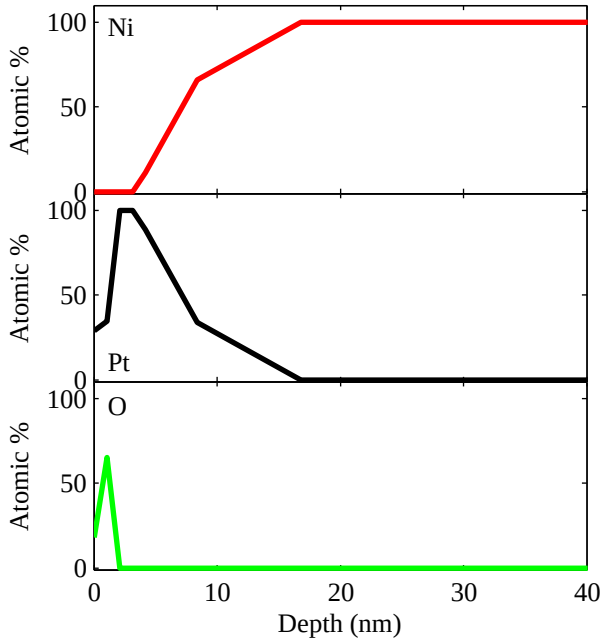

Figure 4.11: XPS depth profile of the top 40 nm of a platinum-capped, blanket-deposited nickel film. The nickel film was approximately 80 nm thick, and the platinum capping layer was approximately 10 nm thick. Atomic concentrations as a function of depth are shown for nickel (red), platinum (black), and oxygen (green). The film was analyzed within 48 hours of deposition. No oxygen was present in the nickel layer of the sample, indicating that the platinum film successfully prevented the formation of nickel oxide.

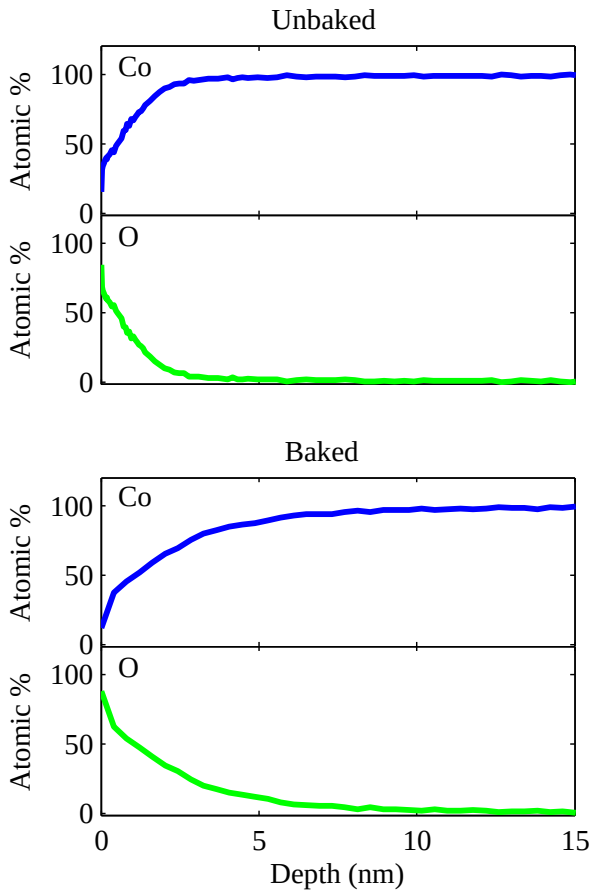

Figure 4.12: XPS depth profiles of unbaked (upper) and baked (lower) blanket-deposited cobalt films. Atomic concentrations as a function of depth are shown for cobalt (blue) and oxygen (green). The two samples were from the same wafer; both films were exposed to ambient conditions for one week prior to analysis, and the "Baked" film was coated with PMMA resist and baked at 115°C for 40 minutes in order to simulate processing damage to the leading edge of the nanomagnet studied in the manuscript.

baking the unprotected cobalt film caused an additional 2 to 9 nm of oxidation for a total oxidation depth of 5 to 12 nm (Figure 4.12). For the platinum-capped, unbaked film, a small oxygen peak was observed at the platinum-cobalt interface (Figure 4.13(a)). For the platinum-capped, baked sample, the platinum layer successfully prevented oxidation of the cobalt surface (Figure 4.13(b)).

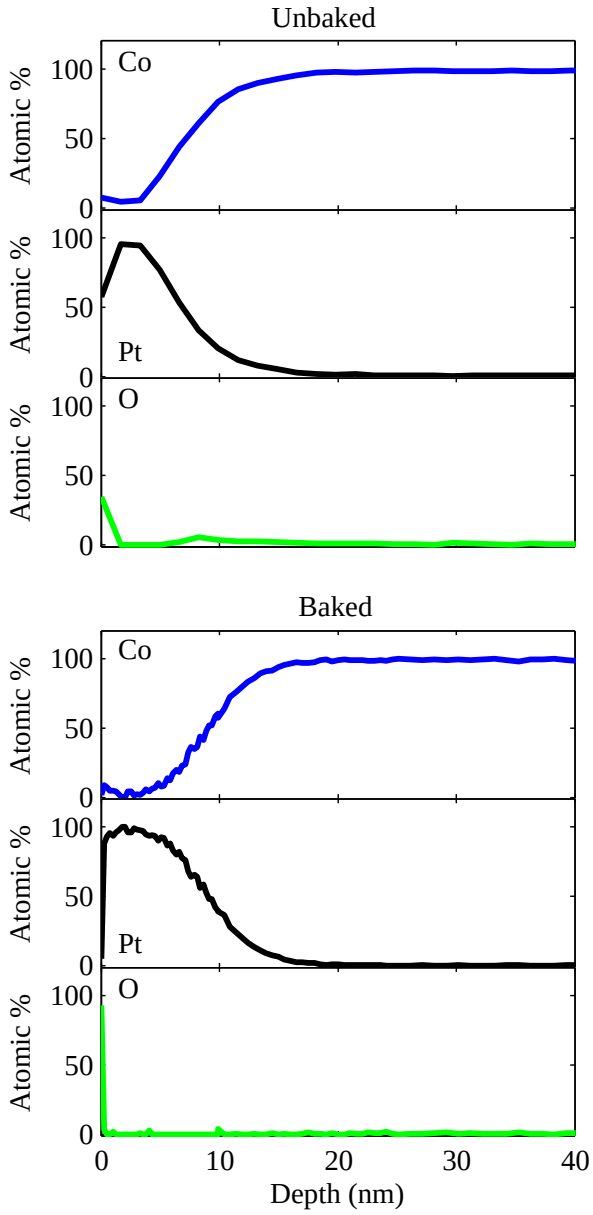

Figure 4.13: XPS depth profiles of unbaked (upper) and baked (lower) blanket-deposited cobalt films that were capped with 8 nm of platinum to mitigate surface oxidation. Atomic concentrations as a function of depth are shown for cobalt (blue), platinum (black), and oxygen (green). The two films were from the same wafer; both films were exposed to air for one week prior to analysis, and the "Baked" film was coated with PMMA resist and baked at 115°C for 40 minutes. The presence of oxygen is indicated in the cobalt layer near the cobalt-platinum interface of the unbaked film. No oxygen was observed in the cobalt layer of the baked film.

4.4 Reassessing Frequency-Shift Cantilever Magnetometry: Studying a Cobalt Nanomagnet

Since all magnetic and elemental analysis of the thin films indicated that the evaporated material was well-magnetized, the use of frequency-shift cantilever magnetometry was revisited, this time for a cobalt nanomagnet. The cobalt magnet — which had dimensions of $79\text{nm} \times 225\text{nm} \times 1494\text{nm}$ and was capped with 8 nm of platinum — was attached to a 200 µm long cantilever; additional details of the magnet-tipped cantilever preparation and storage conditions prior to the measurement are provided in Section 5.2.1. Frequency-shift cantilever magnetometry measurements on the cobalt nanomagnet were conducted using a custom magnetic resonance force microscope at the IBM Almaden Research Center; the details of the microscope are provided in Refs. 12 and 60. The observed cantilever frequency shift Δf was converted to an equivalent magnet-induced spring constant shift using $k_{\mathrm{m}} = 2k\Delta f/f_{\mathrm{c}}$, with $k = 1.0\ \mathrm{mN\ m^{-1}}$ and $f_{\mathrm{c}} = 6644\ \mathrm{Hz}$ measured as described in Section 5.2.1. The resulting data between -5.0 T to -0.05 T and 0.05 T to 5.0 T were fit to [93, 139]

$$k_{\mathrm{m}}(B) = \mu_{\mathrm{sat}} \left(\frac{\alpha}{l}\right)^2 \frac{B\,\Delta B}{B + \Delta B} + c\,|B|, \tag{4.2}$$

with $B = \mu_0 H$ the applied magnetic field, $\alpha = 1.377$ a constant for the fundamental cantilever mode, $l = 200$ µm the cantilever length, and μ_{sat} the saturated magnetic moment. $\Delta B = \mu_0 \mu_{\mathrm{sat}} \Delta N/V$ is the shape-anisotropy field, with V the tip volume and $\Delta N = N_t - N_l$ the difference in demagnetization factor along the cantilever's thickness and length, respectively. The only difference between Eq. 4.1 and Eq. 4.2 is that here the field-dependent spring constant shift of the bare cantilever at high field [89, 93] was accounted for by the term $c\,|B|$. The measured magnetic moment was converted to saturation magnetization using $\mu_0 M_{\mathrm{sat}} = \mu_0 \mu_{\mathrm{sat}}/V$ with $V = 225\ \mathrm{nm} \times 1494\ \mathrm{nm} \times 79\ \mathrm{nm}$.

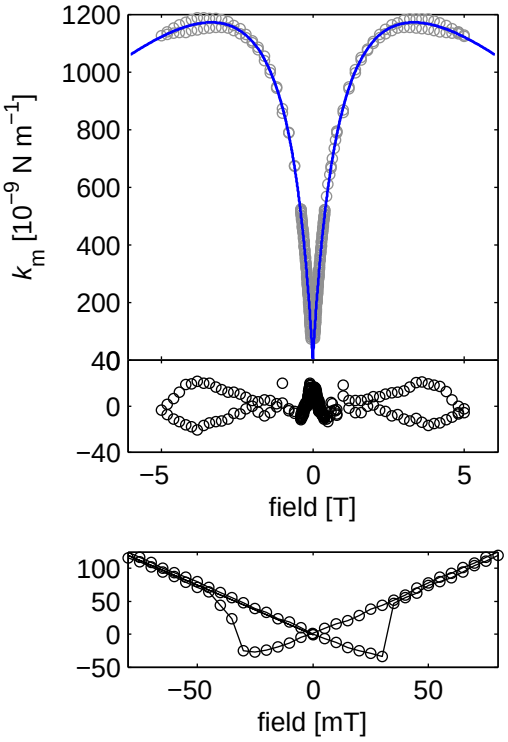

Figure 4.14: A frequency-shift cantilever magnetometry study of a cobalt nanomagnet with the applied field aligned parallel to the long axis of the nanomagnet. The external field was swept from +5 to −5 T and then back from −5 to +5 T. Upper: Magnetic spring constant shift k_{m} versus field (gray open circles) and a best fit to Eq. 4.2 (blue solid line). Middle: Fit residuals. Lower: Magnified view of the spring-constant hysteresis observed at low field.

The measured $k_{\mathrm{m}}(B)$ data shown in Figure 4.14[3] were well described by Eq. 4.2. The observed $\Delta N = 0.56 \pm 0.01$ was in reasonable agreement with 0.50 expected for a high-aspect-ratio prolate ellipsoid. The observed saturation magnetization $\mu_0 M_{\mathrm{sat}} = 1.91 \pm 0.03$ T agreed well with 1.80 T expected for cobalt. Note that the standard error in $\mu_0 M_{\mathrm{sat}}$ is again reported as an indication of the goodness of fit and that the true error in $\mu_0 M_{\mathrm{sat}}$ is dominated by the uncertainly in k.

[3]Figure 4.14 reprinted with permission from J. G. Longenecker *et al.*, ACS Nano **6**, 9637 (2012). Copyright 2012, American Chemical Society.

4.5 Discussion

SQUID magnetometry measurements on large-area thin films of nickel and cobalt indicated that the evaporated material saturated at the expected value. These SQUID magnetometry findings refute hypothesis 1 in Section 4.2 that questioned whether the general-purpose evaporator used in the CNF cleanroom had induced bulk contamination of the magnetic films that reduced the saturation magnetization. XPS with depth profiling indicated that the majority of the damage to the uncapped nickel and cobalt nanomagnets was within 5 nm of the surface, and that capping with 10 nm of platinum successfully mitigated the formation of magnetic oxides. Furthermore, platinum-capped cobalt films remained intact after exposure to the elevated temperatures experienced by the nanomagnets during post-deposition processing. No elements were found to be present other than those indicated in Figures 4.9 to 4.13, indicating that the only "shell" of damage to the nanomagnets, as proposed in hypothesis 2 in Section 4.2, would be the formation of oxides. The findings presented in Section 4.3 thus indicate that the nanomagnets were damaged primarily by surface oxidation, and that the "shell" of damage was no more than 5 nm thick.

Frequency-shift cantilever magnetometry conducted on a cobalt nanomagnet showed that the saturation magnetization of $\mu_0 M_{\text{sat}} = 1.91 \pm 0.03$ T agreed well with the value for bulk cobalt of 1.80 T. Taken together with the XPS and SQUID data on large-area thin films, these findings strongly support the conclusion that the tip exhibited a saturation magnetization close to the expected value for a fully intact cobalt nanomagnet. In contrast, frequency-shift magnetometry conducted on 120 and 220 nm wide nickel nanomagnets — even when the 40% uncertainty in the determination of the spring constant was accounted for — indicated that the magnetization of most of the tips was lower than the expected $\mu_0 M_{\text{sat}} = 0.60$ T. The nickel magnetization had not been affected by platinum capping or by the post-deposition processing steps of overhanging the nanomagnets. Based on the comparison between the

cobalt and nickel nanomagnets, it is expected that two factors contributed to the observed low magnetization of the nickel nanomagnets. First, the nickel nanomagnets were deposited with chromium adhesion layers whereas the cobalt nanomagnet had a titanium adhesion layer. After the nickel nanomagnet study was conducted, chromium adhesion layers were found to exhibit undesired high-field magnetic behavior (Figure 4.7). The chromium high-field behavior could have impacted the saturated magnetization of the nanomagnets.

A second difference between the cobalt and nickel cantilever magnetometry measurements — and likely the primary contribution to the difference in magnetization — was that the measurements were conducted on different instruments. Frequency-shift cantilever magnetometry measurements on cobalt and nickel nanomagnets were conducted using custom-built MRFM instruments at the IBM Almaden Research Center and Cornell University, respectively. Variations between the experimental setups at IBM Almaden and Cornell may have impacted the accuracy of the measurements; specifically, the spring constant may have been more accurately measured using the instrument at the IBM Almaden Research Center. The constant α in Eqs. 4.1 and 4.2 is set by the precise position of the laser interferometer reflectance off of the 30 µm long paddle on the cantilever that is centered 67 µm from the leading edge of the cantilever (see Figure 3.4). The large error in the determination of the spring constant is predominantly set by the difference between the laser being centered at the leading edge or far edge of this paddle. At the IBM Almaden Research Center, the position of the laser was set precisely using set screws, and thermal contraction was accounted for when adjusting the position at room temperature so that the laser was expected to be in the center of the paddle on cool down to liquid helium temperatures. The Cornell instrument used for the nickel magnetometry measurements did not have high-precision laser alignment capabilities, and no attempt was made in the Cornell measurements to account for thermal drift when aligning the fiber with the cantilever at room temperature. Additionally, low vibrational noise experienced by the IBM Almaden instrument allowed for the

measurement and comparison of the cantilever spring constant at 300 K, 77 K, and 5.5 K, whereas the spring constant was only measured in the Cornell instrument after stabilization in liquid helium at 4.2 K. The development of a new MRFM instrument with significantly improved vibration isolation is underway at Cornell University and should enable more accurate spring constant and magnetometry measurements. Details of the development of this third-generation Cornell magnetic resonance force microscope are provided in Chapter 6. For future cantilever magnetometry experiments, the additional construction of a dedicated cantilever magnetometry apparatus in which the optical fiber can be scanned at 4 K could completely eliminate errors in α.

In conclusion, the nanomagnet-tipped chip on cantilever process described in Chapter 3 has been demonstrated to produce well-magnetized nanomagnets. Magnetization damage for unprotected films has been estimated to be confined primarily to within 5 nm of the surface, and oxygen contamination is mitigated by capping the magnetic material with 10 nm of platinum. Although the top surface of nanomagnets is now routinely coated with platinum because of these findings, the leading edge and other nanomagnet side walls cannot be protected using the current line-of-site evaporation technique. In MRFM experiments, the strength of the interaction between the sample spins and the nanomagnet is based on the tip-field gradient produced by the nanomagnet. The saturation magnetization of the whole nanomagnet contributes to the tip-field gradient, but the gradient is dominated by the shape of the magnet and the magnetization at the nanomagnet's leading edge. To achieve sub-nanometer MRFM imaging resolution, it will be important to reduce nanomagnet damage and/or restrict the capping layer at the leading edge to a thickness of less than 2 nm. A possible strategy to decrease the damage at the magnet leading edge would be to develop a method to encase the nanomagnet side walls with a protective coating that is less than 5 nm thick; this is discussed further in Chapter 7.

Acknowledgements

I thank Alex Senko for his contributions to the SQUID magnetometry and XPS depth profiling data collection and analysis. I thank Eric Moore for his involvement in the nickel frequency-shift cantilever magnetometry experiments, as well as for generating code to simulate the effect of cantilever offset angle on observed magnetization. I also thank Dan Rugar and John Mamin for assistance with cobalt frequency-shift magnetometry experiments, and Jonathan Shu for assistance with the collection and interpretation of XPS data. Work in this chapter was conducted with the financial support of the National Institutes of Health (Grant No. 5R01GM-070012), the Army Research Office MultiUniversity Research Initiative (Grant No. W911NF-05-1-0403), and the National Science Foundation through the Cornell Center for Nanoscale Systems (Grant Nos. EEC-0117770 and EEC-0646547). The XPS, SQIUD, and dual-beam FIB instruments used in this work are part of the Cornell Center for Materials Research, which is supported by the National Science Foundation Materials Research Science and Engineering Centers program (Grant No. DMR-0520404). Fabrication was conducted in the Cornell NanoScale Science and Technology Facility, a member of the National Nanotechnology Infrastructure Network, which is supported by the National Science Foundation (Grant No. ECS-0335765).

CHAPTER 5

HIGH-GRADIENT COBALT NANOMAGNETS ON CANTILEVERS USED TO SENSITIVELY DETECT NUCLEAR MAGNETIC RESONANCE

5.1 Introduction

In the most sensitive MRFM experiments to date, signal has been detected as a force variance generated by interactions between the magnetic field gradient produced by a nanomagnet and magnetic dipole fluctuations in a small ensemble of nuclear spins [12]. An attonewton-sensitivity cantilever is used as the force sensor to detect this interaction. In this limit where the force variance is measured, for a given cantilever sensitivity and imaging resolution, the signal acquisition time is dependent on the magnetic tip-field gradient such that the acquisition time is proportional to the inverse of the field gradient to the fourth power [48]. To achieve high-sensitivity MRFM detection, it is thus critical to use a high gradient magnetic tip.

The highest-gradient nanomagnets used in MRFM experiments to date have been fabricated on flat substrates [12, 48] and the samples that were studied were adhered to the leading edges of the high-compliance cantilevers. As we transition from robust, small samples, such as the tobacco mosaic virus studied by high-resolution nuclear magnetic resonance (NMR) MRFM imaging in Ref. 12, to instead working with large-area samples or delicate biomacromolecules that require vitrification to be studied at cryogenic temperatures, it will be critical to have the flat substrate available for sample preparation.

Prior MRFM studies that have used the "magnet-on-cantilever" geometry [25, 30, 51–56] have either used micrometer-scale magnetic particles or have reduced the dimensions of large magnetic particles by ion beam milling, which incurred damage due to ion implanta-

tion. In practice these tips produced a gradient nearly an order of magnitude smaller than that achieved by Degen and co-workers. Thus nearly 10^4 longer imaging times would be required to achieve the 4 to 10 nm resolution of Ref. 12 using the best ion-beam milled tip demonstrated to date.

In this chapter, magnet-on-cantilever detection of NMR was achieved using an attonewton-sensitivity cantilever with an integrated cobalt nanomagnet-tipped silicon chip (Section 3.6). The observed magnetic tip-field gradient exceeds previous gradients produced by magnets on cantilevers by at least a factor of eight [25, 53, 54, 56, 57]. Remarkably, the tip gradient is comparable to the tip employed in the high-resolution imaging experiment of Ref. 12. These results thus demonstrate the potential for achieving 4 to 10 nm resolution proton magnetic resonance imaging with reasonable three-dimensional acquisition times for a wide range of thin-film organic samples.

NMR-MRFM signal was measured by using the cobalt nanomagnet-tipped cantilever to detect stochastic proton magnetization from a polystyrene film spun-cast over a microwire [60]. Artifact-free detection of NMR in this magnet-on-cantilever experiment required substantial modification of the spin-modulation protocols of Refs. 56 and 12. The spin signal was studied as a function of radiofrequency (rf) irradiation frequency at multiple tip-sample separations. By modeling this data numerically, the tip field and tip-field gradient were determined. The magnetic integrity of the tip at the nanoscale was assessed by comparing the spin signal to simulations carried out using different damage models. Measurements of force noise as a function of tip-sample separation over a copper microwire and over silicon indicate a larger-than-expected surface noise [81]; methods are suggested for mitigating this surface noise in future experiments.

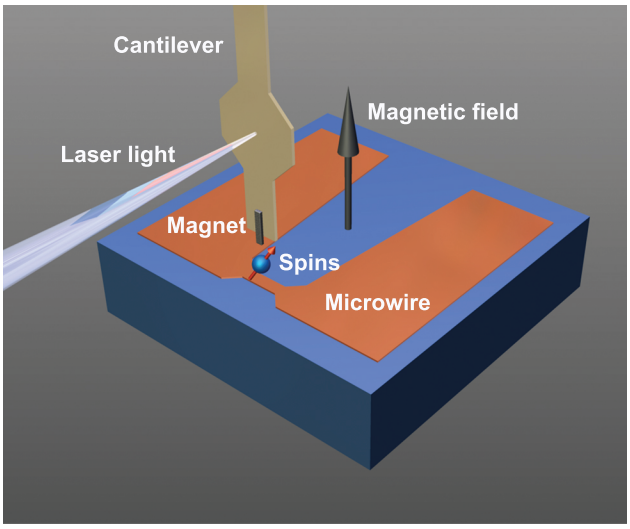

Figure 5.1: Schematic of the experiment. A cobalt magnet with cross section 225 nm × 79 nm was extended past the leading edge of an attonewton-sensitivity cantilever. The cantilever was centered over a 1 µm wide microwire coated with 40 nm of polystyrene. An external 2.63 T magnetic field was applied in the direction of the long axis of the cantilever as shown. A laser interferometer was centered on a 30 µm wide pad to measure cantilever vibrations.

5.2 Experimental Methods

The experiment is illustrated in Figure 5.1.[1] The IBM Almaden Research Center magnetic resonance force microscope used here has been described in detail elsewhere [12, 60]. Measurements were conducted in high vacuum ($P < 10^{-6}$mbar) with the temperature maintained at $T = 5.5$ K. In all experiments reported here, both the sample and the cantilever were electrically grounded.

5.2.1 Magnet-Tipped Cantilever Characterization

Cobalt nanomagnet-tipped cantilevers (Figure 5.2) were prepared by using the nanomagnet-tipped chip procedure described in Section 3.6 and serially attaching the magnet-tipped

[1]Figures 5.1, 5.2, 5.3, 5.4, and 5.5 reprinted with permission from J. G. Longenecker *et al.*, ACS Nano **6**, 9637 (2012). Copyright 2012, American Chemical Society.

chips to attonewton-sensitivity cantilevers using focused ion beam (FIB) manipulation (Section 3.7). The attonewton-sensitivity cantilevers were 4 µm wide, 200 µm long, and had a 30 µm wide reflective pad centered 70 µm from the leading edge (Figure 5.2(c)). The nanomagnets, which were deposited by electron beam (e-beam) evaporation, consisted of a 4.0 ± 0.2 nm thick titanium adhesion layer, 79.2 ± 4.7 nm cobalt layer, and 8.0 ± 0.5 nm platinum capping layer. In order to prevent oxidation of the cobalt magnets, it was critical to not exceed processing temperatures of 115°C once the nanomagnets were evaporated. Scanning electron microscope (SEM) images of the magnet-tipped chip and overhanging magnet are shown in Figure 5.2(a) and Figure 5.2(b), respectively. As seen in Figure 5.2(b), the cobalt nanomagnet extended past the leading edge of the magnet-tipped chip by ~ 300 nm. Magnet-tipped cantilevers were prepared at Cornell University four weeks before they were transferred to the MRFM apparatus at IBM Almaden Research Center. They were exposed to ambient air for approximately five days, were stored under nitrogen for three days, and were otherwise stored under a vacuum of 10^{-4} mbar.

The magnet-tipped cantilever used in this study had a resonance frequency $f_c = 6644\,\mathrm{Hz}$, an intrinsic quality factor $Q = 8.4 \times 10^4$, and a spring constant $k = 1.0\,\mathrm{mN\,m^{-1}}$. Cantilever displacement was monitored with a low-power [67], temperature-tuned [145] fiber optic interferometer ($\lambda = 1550\,\mathrm{nm}$, $P \sim 25\,\mathrm{nW}$). The interferometer output was sent to a field programmable gate array (FPGA), which was used to either control the cantilever Q *via* negative feedback [146] or self-oscillate the cantilever to a set amplitude *via* positive feedback [147]. The output of the FPGA drove a piezeoelectric disk at the base of the cantilever holder. The cantilever spring constant was determined from the mean square displacement of the undriven cantilever at a temperature $T = 5.5\,\mathrm{K}$ [138]; a correction factor was used to account for the distance from the reflective pad to the end of the cantilever. Based on the ±15 µm uncertainty in the position of the laser, the error in k could be as large as ±40%. To study cantilever dissipation, the cantilever ringdown time τ was measured and a cantilever quality

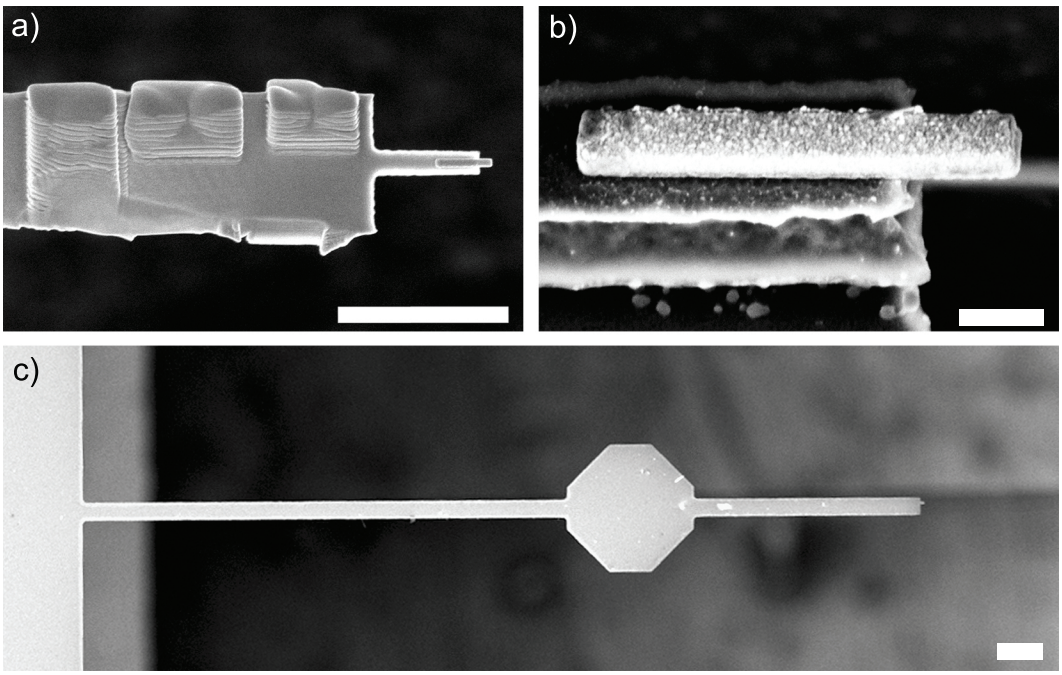

Figure 5.2: SEM images of the magnet-tipped cantilever used in the MRFM experiment. (a) Top-view image of the magnet-tipped chip attached to an underlying cantilever by ion-assisted platinum deposition; three rectangular platinum patches can be seen on the bottom side of the chip. The cobalt magnet is seen to overhang a 3 µm long finger at the leading edge of the chip. Scale bar = 5 µm. (b) Angled image of the overhanging cobalt nanomagnet, acquired before it was attached to a cantilever. The magnet was 225 ± 15 nm wide, 1494 ± 15 nm long, and 79 ± 4 nm thick. There was a 4 nm titanium layer under the magnet to promote adhesion to the silicon substrate, as well as an 8 nm platinum capping layer to mitigate oxidation. Scale bar = 200 nm. (c) Top-view image of a custom-fabricated 200 µm long cantilever drawn from the same batch as the cantilever used in this experiment. Scale bar = 20 µm.

factor and dissipation constant calculated using $Q = \tau\pi f_c$ and $\Gamma = k/(2\pi f_c Q)$, respectively. The cantilever amplitude was set to 15 nm when measuring dissipation during approach. To study cantilever frequency noise, the instantaneous frequency of the self-oscillated cantilever was determined by fitting short 4 ms segments of the digitized cantilever oscillation to a sine wave; the power spectral density of cantilever frequency fluctuations was computed from the resulting frequency versus time data. For these studies a cantilever peak-to-peak amplitude of 60 nm was chosen because it approximated the ideal amplitude for detecting a single spin at a tip-sample separation of 23 nm in a force-gradient experiment, assuming a spherical tip radius of 41 nm [17]. To determine the location of the sample surface, the tip-sample separation h was decreased until a dc deflection of the cantilever was observed. The displacement per volt of the vertical piezoelectric actuator was calibrated *via* fiber optic interferometry and the distance above this "touch point" was computed from the piezo voltage taking into account this (temperature-dependent) piezo calibration. The estimated error in h is ± 3 nm.

5.2.2 Magnetic Material Characterization

The integrity of the cantilever's cobalt nanomagnet was analyzed *in situ* using frequency-shift cantilever magnetometry [81, 82, 89, 93, 139]; the results are shown in Section 4.4. Additional magnetic and elemental analysis of cobalt films using superconducting quantum interference device magnetometry (SQUID) and X-ray photoelectron spectroscopy (XPS) are detailed in Section 4.3. The cantilever magnetometry, SQUID magnetometry, and XPS findings indicate that the cobalt nanomagnet exhibited a saturation magnetization close to the expected value for a fully intact cobalt nanomagnet and that the unprotected nanomagnet leading edge incurred < 10 nm of oxidation.

5.2.3 Sample and Microwire Preparation

A lithographically-defined copper microwire was used to generate magnetic radiofrequency fields [12, 60]. The microwire was prepared on a silicon substrate as described in Ref. 60, but with the magnetic pillar omitted. The sample consisted of a thin film of polystyrene prepared from solution *via* spin coating. Polystyrene powder (Pressure Chemical, $M_w = 2.0 \times 10^5$, $M_w/M_n = 1.06$) was dissolved into toluene to a final concentration of 0.3 weight percent and the resulting solution was spun onto a $4\,\text{mm} \times 4\,\text{mm}$ silicon-plus-microwire substrate rotating at 6000 rpm. The high rotation speed and low viscosity resulted in a reasonably uniform film in spite of edge effects and the substrate's topographic features. The film's solvent was removed *via* air drying. Using FIB milling and SEM, the final film thickness was estimated to be 40 nm.

5.2.4 Spin Detection Protocol

Statistical fluctuations in proton magnetization were observed following the general approach of Degen *et al.* [70]. Cyclic inversions of the sample magnetization were induced by triangle-wave rf sweeps with peak-to-peak frequency modulation (FM) deviation $\Delta f_{\text{FM}} = 2\,\text{MHz}$. The resulting cantilever motion was detected with a two-channel lock-in amplifier. The strength of the applied rf field was $B_1 \cong 5\,\text{mT}$. The proton magnetization fluctuated with a correlation time of $\tau_m = 100$ to 150 ms; to accurately capture the induced cantilever position fluctuations, the cantilever response time was adjusted *via* feedback to be approximately 15 ms. The lock-in outputs were converted to units of force, and a spin signal was computed from the variance of the outputs using $\sigma^2_{\text{spin}} = \sigma^2_x - \sigma^2_y$, where σ^2_x and σ^2_y represent the variances of the in-phase and quadrature lock-in signals, respectively. For most data points in Figure 5.3, the spin variance signal was computed from 12.5 minutes of lock-in data per rf

frequency step. For the 117 to 126 MHz data at the three smallest tip-sample separations, $h \leq 25$ nm, the spin variance signal was computed from 16.7 minutes of lock-in data per rf frequency step.

In prior sample-on-cantilever experiments [12], optimized spin inversions were obtained using rf that was both frequency modulated (swept unidirectionally twice per cantilever cycle) and amplitude modulated (ramped to zero when the rf frequency was maximally off resonance). In this magnet-on-cantilever experiment, however, it was observed that this modulation scheme caused a parametric amplification of thermomechanical noise in one lock-in channel, yielding a false spin signal. This false variance imbalance was eliminated by operating the rf continuously and using triangle-wave frequency modulation. The triangle-wave frequency modulation, however, produced a spurious oscillation of the cantilever which in practice exhibited variations that obscured the spin signal.

Using a new spin modulation protocol COZMIC (COmpensated Zero Mean Inversion Cycles), this problem was solved by adding a small amount of amplitude modulation back into the rf so as to just cancel any spurious cantilever excitation caused by the frequency modulation. This cancelation was accomplished by measuring the mean cantilever amplitude with the lock-in amplifier and applying a sinusoidal amplitude modulation (AM) to exactly cancel the mean cantilever excitation. The frequency-modulated rf waveform was multiplied by $1 + A\cos(2\pi f_c t) + B\sin(2\pi f_c t)$, where A and B are small numbers that control the amplitude compensation. The in-phase and quadrature lock-in outputs X and Y were measured for two trials of amplitude compensation and a complex-number transfer function computed from $\chi \approx (\Delta X + i\Delta Y)/(\Delta A + i\Delta B)$. Knowing the transfer function, one can precisely predict how much amplitude modulation to apply to cancel the mean signal. After every 50 s of MRFM data collection and every time the cantilever was moved to a new location, we (1) measured the cantilever frequency, (2) computed a triangle FM waveform using

the old values of A and B for AM compensation, (3) remeasured the lock-in mean for 5 s to determine the average X and Y, (4) calculated new values for A and B using the transfer function and the measured values for X and Y, (5) updated the triangle FM waveform using the new A and B values, (6) measured the mean lock-in outputs for 5 s and calculated an updated transfer function for future use, (7) measured the MRFM signal for 50 s, and (8) repeated. This compensation scheme worked precisely and automatically.

5.3 Magnet-on-Cantilever Detection of Nuclear Magnetic Resonance

To detect nuclear magnetic resonance, the magnet-tipped cantilever was centered over the microwire and brought into close proximity with the polystyrene film coating the microwire surface (Figure 5.1). The amplitude and frequency of the rf delivered to the microwire were modulated to induce cyclic inversions of the proton spins. To avoid spurious signal, the new spin modulation protocol COZMIC was implemented, as described in Section 5.2.4. A spin variance signal was inferred by subtracting in-phase and out-of-phase force fluctuations acting on the cantilever.

In Figure 5.3 the measured spin variance signal $\sigma^2_{\rm spin}$ (open circles) is displayed as a function of the rf center frequency $f_{\rm rf}$ at five tip-sample separations h ranging from 42.3 nm to 13.1 nm. For each tip-sample separation the low-frequency edge of the signal is constant at a frequency of 112 MHz, whereas the high-frequency edges increase in rf frequency as the tip is brought closer to the sample. Both of these observations are well-understood. The spin variance signal arises from protons in the sample that meet the resonance condition $f_{\rm rf} = (\gamma_{\rm p}/2\pi)|\mathbf{B}^{\rm ext} + \mathbf{B}^{\rm tip}(\mathbf{r})|$, with $\gamma_{\rm p}/2\pi = 42.56\,{\rm MHz/T}$ the gyromagnetic ratio for protons, $\mathbf{B}^{\rm ext}$ the applied magnetic field, and $\mathbf{B}^{\rm tip}(\mathbf{r})$ the magnetic field generated by the cobalt

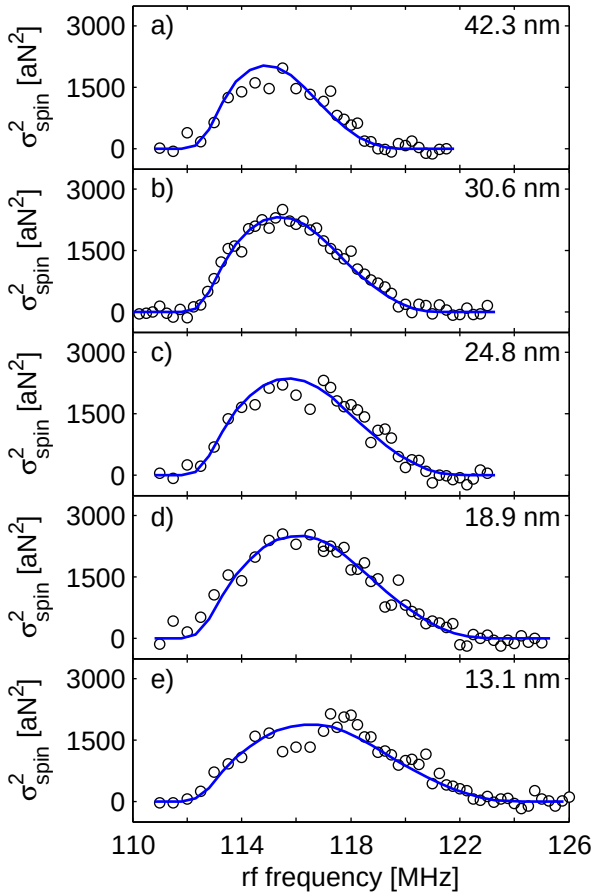

Figure 5.3: Magnetic resonance signal of protons in a 40 nm thick polystyrene film. The experimental spin variance signal σ^2_{spin} (open circles) was obtained by measuring the spin-induced force fluctuations experienced by a cobalt nanomagnet affixed to an attonewton-sensitivity cantilever that was brought into close proximity with the film. Signal was obtained at tip-sample separations of (a) 42.3 nm, (b) 30.6 nm, (c) 24.8 nm, (d) 18.9 nm, and (e) 13.1 nm. The static field was 2.63 T and the peak-to-peak rf frequency deviation Δf_{FM} was 2 MHz. Simulated spin variance signals (blue lines) were calculated at each tip-sample separation assuming a rectangular cuboid magnet with an extraneous spacing of 51 nm (Method 1).

nanomagnet at location $\mathbf{r}$. The low-frequency edge of each signal shown in Figure 5.3 arises from spins far away from the tip, where the magnetic field contribution from the tip is nearly zero. For $|\mathbf{B}^{\text{ext}}| = 2.63$ T, such "bulk" spins should meet the magnetic resonance condition at a frequency $f_{\text{l}} = 2.63\text{ T} \times 42.56\text{ MHz/T} = 112$ MHz, as was observed. The high-frequency edge of the signal arises from spins close to the cantilever experiencing an additional magnetic field from the cobalt nanomagnet. Due to the cobalt tip's field gradient, the field experienced by the spins at the surface increases as the tip-sample separation is reduced.

5.4 Calculating the Tip-Field Gradient of the Cobalt Nanomagnet

The tip field and vertical tip-field gradient of the cobalt nanomagnet were estimated as a function of tip-sample separation by matching the shape of the experimental data in Figure 5.3(a-e) to simulated spin variances. In the simulations, the sample was assumed to be a 40 nm thick polystyrene film and the magnet had dimensions identical to the nanomagnet shown in Figure 5.2(b). Details of the simulation parameters are provided in the Supporting Information of Ref. 58.

Agreement between the simulations and the experimental data was obtained after considering several tip models. When simulations were conducted for a fully saturated cobalt nanomagnet, the tip field was overestimated by more than a factor of two (Figure S6 in the Supporting Information of Ref. 58). Thus, damage models had to be considered. Magnet parameters using two models were optimized to match the shape of the spin variance signal and accurately estimate the tip field. In the first model (Method 1), the magnet was assumed to have a magnetic spacing that was 51 nm larger than the measured tip-sample separation. The spin variance signals calculated using this extraneous spacing of 51 nm are overlayed

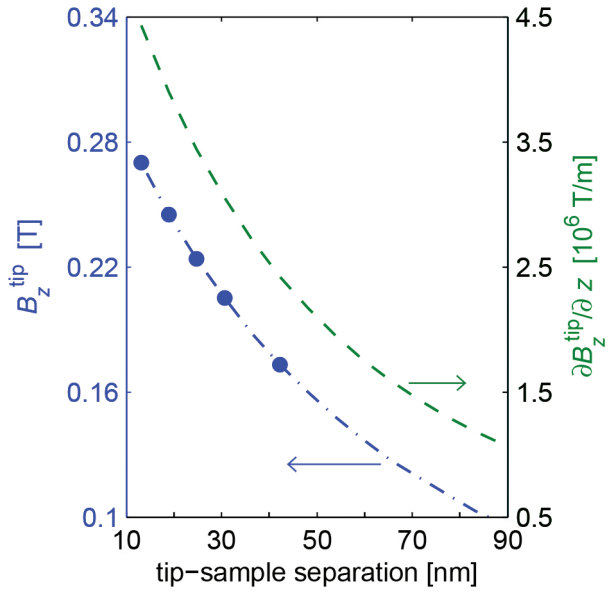

Figure 5.4: The tip field B_z^{tip} (left axis; blue) and tip-field gradient $\partial B_z^{\text{tip}}/\partial z$ (right axis; green) of the cobalt nanomagnet. As shown in Figure 5.3, a damage model for a tip with an extraneous spacing of 51 nm was used to calculate spin variance signal as a function of rf frequency. This model was used to determine B_z^{tip} as a function of tip-sample separation (blue dot-dashed line) by calculating the difference between the high-frequency and low-frequency edges of the simulated signal at 15 different spacings. The five calculated tip fields that correspond to the tip-sample separations in Figure 5.3 are shown as blue filled circles. The tip-field gradient for the cobalt nanomagnet at the same 15 tip-sample separations (green dashed line) was determined by numerically differentiating the tip fields.

with the experimental data in Figure 5.3 as the blue lines. Using Method 1, the nanomagnet's tip field B_z^{tip} was calculated as a function of tip-sample separation (Figure 5.4; blue dot-dashed line) and numerical differentiation was used to calculate the tip-field gradient $\partial B_z^{\mathrm{tip}}/\partial z$ (Figure 5.4; green dashed line). From the tip-field gradient plot in Figure 5.4, it can be seen that at the smallest tip-sample separation of 13.1 nm the vertical tip-field gradient was calculated to be $4.4\,\mathrm{MT\,m^{-1}}$ for spins directly below the cobalt nanomagnet. In the second damage model (Method 2), the extraneous spacing was set to zero, but the saturated magnetic moment for the nanomagnet was reduced from 1.8 T to 0.69 T. Method 2 provided a quality of fit that was almost as good as for Method 1. Using Method 2, the vertical tip-field gradient was estimated as $5.4\ \mathrm{MT\,m^{-1}}$ for a tip-sample separation of 13.1 nm.

A comparison of the results obtained using Method 1 and Method 2 indicates to us that a number of tip damage scenarios could reproduce the data within experimental error but estimate somewhat different tip-field gradients. As a check, a model-free method (Method 3) for estimating the tip field and tip-field gradient was also tested as follows. The downward-sloping peak data in each curve was fit to a line, and the frequency f_{h} of the high-frequency edge was obtained from the x-intercept of the line. The z-component of the tip field was calculated as $B_z^{\mathrm{tip}} = (f_{\mathrm{h}} - f_{\mathrm{l}})/(\gamma_{\mathrm{p}}/2\pi)$. The tip-field gradient was obtained by computing the derivative of the tip field data numerically; computing the tip-field gradient using the $h = 13.1$ nm and 18.9 nm data points gave the estimate $\partial B_z^{\mathrm{tip}}/\partial z = 5.1\ \mathrm{MT\,m^{-1}}$. Because of the curvature of the slope of the simulated signal, Method 3 is expected to underestimate the tip field.

In addition to the vertical tip-field gradients, the lateral gradients $\partial B_x/\partial z$ were also calculated for the nanomagnet. The lateral gradient was calculated to be $2.7\,\mathrm{MT\,m^{-1}}$ using the Method 1 tip model or $8.3\,\mathrm{MT\,m^{-1}}$ using the Method 2 tip model.

The vertical and lateral tip-field gradients shown here can be compared to the highest

reported gradients to date employed in NMR- and ESR-MRFM measurements in Table 5.1.[2] The cobalt nanomagnet used here has both vertical and lateral gradients that are almost an order of magnitude larger than any prior gradient achieved by affixing a magnet to the leading edge of an attonewton-sensitivity cantilever.

5.5 Dissipation and Frequency Fluctuations

The friction coefficient Γ experienced by the magnet-tipped cantilever was studied over both the (polystyrene-coated) copper microwire and the (polystyrene-coated) silicon substrate at tip-sample separations ranging from 5 to 300 nm. Measurements were conducted at 2.63 T and at zero field over both surfaces. The corresponding spectral density of force fluctuations at the cantilever frequency was calculated from the measured friction coefficient using $S_{\delta F} = 4k_{\mathrm{B}}T\,\Gamma$ with k_{B} as Boltzmann's constant and $T = 5.5$ K the temperature. The resulting data are displayed in Figure 5.5. For reference, the cantilever's calculated internal friction coefficient is also shown; the cantilever's parameters far away from the surface were used to calculate the intrinsic dissipation coefficient $\Gamma = k/(2\pi f_c Q) = 2.85 \times 10^{-13}$ Ns m^{-1}, which corresponds to a thermally-limited force noise spectral density of $S_{\delta F} = 9.3$ aN Hz$^{-1/2}$. The dissipation over the silicon substrate remained close to the thermal limit until a separation of approximately 100 nm. In contrast, the dissipation over the microwire became surface limited at tip-sample separations below 280 nm. The dissipation over both locations was essentially independent of applied magnetic field.

The power spectral density of cantilever frequency fluctuations $S_{\delta f_c}(f)$ over both the polystyrene-coated silicon substrate and the polystyrene-coated copper microwire are plotted in Fig. 5.6. Below $f \leq 10$ Hz, $S_{\delta f_c} \propto f^{-1}$, indicative of frequency noise arising from dielectric

[2]Table 5.1 and Figure 5.6 reprinted with permission from the Supporting Information for J. G. Longenecker *et al.*, ACS Nano **6**, 9637 (2012). Copyright 2012, American Chemical Society.

reference	magnet location	magnet material	h [nm]	$\partial B_z^{\mathrm{tip}}/\partial z$ [MT m^{-1}]	$\partial B_z^{\mathrm{tip}}/\partial x$ [MT m^{-1}]	measurement
Method 1[a]	on cantilever	Co	13	4.4	2.7	NMR
Method 2[b]	on cantilever	Co	13	5.4	8.3	NMR
Ref. 53	on cantilever	$SmCo_5$		0.55	0.43	ESR
Ref. 25	on cantilever	$SmCo_5$		—	0.2	ESR
Ref. 54	on cantilever	$SmCo_5$		0.13	—	ESR
Ref. 56	on cantilever	$SmCo_5$		0.1	—	NMR
Ref. 57	on cantilever	$SmCo_5$		0.25	—	ESR
Ref. 48	off cantilever	Dy	21	7.4	4.6	NMR
Ref. 12	off cantilever	$Fe_{70}Co_{30}$	24	4.2[c]	3.4[d]	NMR

Table 5.1: Vertical ($\partial B_z^{\mathrm{tip}}/\partial z$) and lateral ($\partial B_z^{\mathrm{tip}}/\partial x$) magnetic field gradients achieved in high sensitivity magnetic resonance force microscope experiments. Tip-sample separation h is listed when available. Note that 1 G nm^{-1} = 1 × 10^5 T m^{-1} = 0.1 MT m^{-1}.

[a] Nanomagnet modeled with an extraneous spacing of 51 nm.
[b] Nanomagnet modeled with a uniformly reduced magnetization of 0.69 T.
[c] Here the revised vertical gradient estimate reported in Ref. 48 is used.
[d] Here the revised lateral gradient estimate reported in Ref. 48 is used.

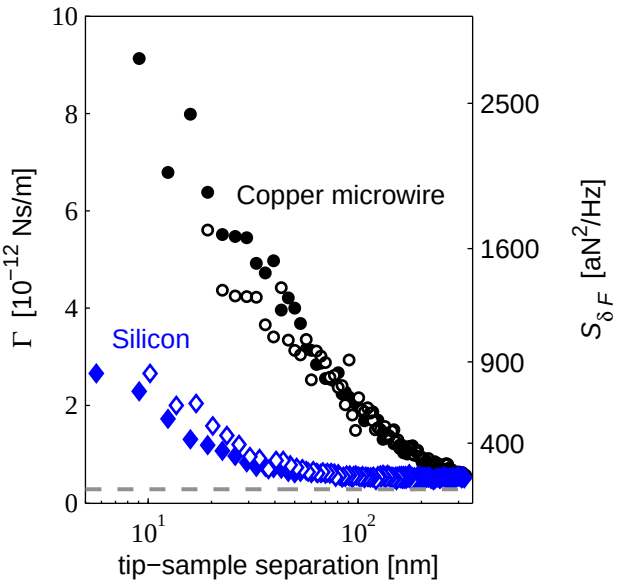

Figure 5.5: Cantilever dissipation Γ (left axis) versus tip-sample separation, and the corresponding spectral density of force fluctuations $S_{\delta F}$ at $T = 5.5\,\mathrm{K}$ (right axis). Dissipation is shown for the tip centered over the copper microwire (black circles) and over the silicon substrate (blue diamonds). Measurements were conducted at $B^{\mathrm{ext}} = 2.63\,\mathrm{T}$ (closed circles and diamonds) and at zero field (open circles and diamonds). The dotted gray line is the cantilever's internal dissipation, calculated from the cantilever f_{c}, k, and Q measured far away from the surface.

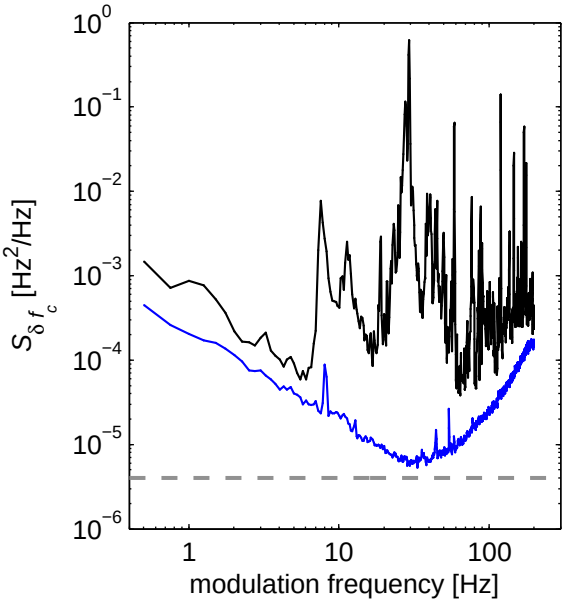

Figure 5.6: The power spectral density of the cantilever frequency fluctuations $S_{\delta f_c}$ versus modulation frequency measured over the copper microwire at 2.63 T (upper line, black) and over the silicon substrate at 0 T (lower line, blue). In both cases the surface was coated with 40 nm of polystyrene. The leading edge of the nanomagnet tip was 90 nm from the surface, and the peak-to-peak amplitude was 60 nm. The thermal noise, which was calculated to be 4.0×10^{-6} Hz^2/Hz, is shown as the gray dashed line.

fluctuations coupling to tip charge [85, 86]. At high frequencies $f \geq 50$ Hz, $S_{\delta f_c} \propto f^2$ as expected due to detector noise [85, 147]. Over the polystyrene-coated silicon substrate, $S_{\delta f_c}$ approaches the thermal limit at intermediate frequencies. Over the polystyrene-coated copper microwire at intermediate frequencies, in contrast, the power spectral density of cantilever frequency fluctuations is up to 10^6 larger than the thermal limit. The discreteness of the $S_{\delta f_c}$ spectrum over the microwire suggests frequency noise arising from coupling to mechanical vibrations [87].

5.6 Discussion

The data presented in Figure 5.3 and Figure 5.4 are the main results of this chapter. The successful detection of spin variance signal from protons was demonstrated in a magnet-on-cantilever MRFM experiment, and the vertical tip-field gradient of the cobalt nanomagnet was calculated to be on the order of 5 MT m^{-1}.

Method 1 and Method 2 (described in Section 5.3) provide relevant lower and upper bounds for the vertical tip-field gradient of the cobalt nanomagnet. In Method 1 the damage is modeled for the worst-case scenario, in which all damage is concentrated at the magnet-sample interface. This extraneous spacing effectively increases the tip-sample separation and would most strongly reduce the tip-field gradient experienced by spins closest to the magnet's physical leading edge. Alternately, the damage is spread evenly throughout the entire magnet in Method 2, which allows for the retention of interactions between sample spins and magnetic material as close as the measured tip-sample separation of 13.1 nm. For a tip-sample separation of 13.1 nm, Method 1 and Method 2 were used to calculate vertical tip-field gradients of 4.4 MT m^{-1} and 5.4 MT m^{-1}, respectively. As expected, the gradient estimated using Method 1 is the lower value.

To understand which, if either, of these simulated models correctly predicts the damage that led to the experimentally observed reduction in the tip field, the integrity of the cobalt material was characterized using XPS depth profiling, SQUID magnetometry, and *in situ* cantilever magnetometry. Results indicated that unprotected cobalt surfaces oxidized to a thickness of less than 10 nm, and that the rest of the cobalt remained fully intact. A simulation-free method for estimating the tip-field gradient was also used to compare to the results of Method 1 and Method 2; this method estimated that $\partial B_z^{\mathrm{tip}}/\partial z \geq 5.1$ MT m^{-1}. The gradient predicted by Method 1 is thus lower than expected. However, the assumption in Method 2 that the damage is uniformly spread throughout the nanomagnet is in stark

contrast with the less than 10 nm of damage expected based on the characterization measurements. Based on these findings, both of the simulation methods are likely oversimplifications of the true damage scenario. The simulation results taken together with the cobalt material characterization indicate that the discrepancy between the expected and observed tip fields may be due to a combination of (1) oxidation of all unprotected cobalt surfaces to a depth of 10 nm, (2) surface roughness on the magnet leading edge and sample film, and (3) a protrusion of the titanium underlayer past the cobalt leading edge.

While the nanomagnet's gradient is outstanding, the dissipation experienced by the magnet-tipped cantilever is disappointingly high, particularly near the microwire. At tip-sample separations of $h \leq 20$ nm, the intrinsic force sensitivity of 9 aN $\mathrm{Hz}^{-1/2}$ degraded to 40 aN $\mathrm{Hz}^{-1/2}$ over the polymer-coated microwire and to 20 aN $\mathrm{Hz}^{-1/2}$ over the polymer-coated silicon substrate. This behavior is in striking contrast with Hickman *et al.*, whose cantilever with a similarly sized nickel tip maintained a force sensitivity of 10 aN $\mathrm{Hz}^{-1/2}$ down to $h \leq 3$ nm over a gold-coated polymer film [81]. Comparing the two experiments is instructive. In the Hickman *et al.* experiment, Γ was measured at zero field over a gold-coated polystyrene film spun on top of an ac-coupled gold halfwave microwave resonator, and the tip potential was adjusted to minimize Γ. Here, in contrast, the tip was brought over a dc-coupled copper microwire at high magnetic field, the sample covering the microwire was not metal coated, and it was not possible to adjust the tip potential to null the contact potential difference between the tip and the substrate.

There are two general dissipation mechanisms to consider: (1) tip magnetization coupling to fluctuating magnetic field gradients in the substrate, equivalent *via* the fluctuation-dissipation theorem to eddy current damping [52, 148, 149], and (2) tip charge coupling to fluctuating electric field gradients in the substrate [83, 84, 150, 151]. One might expect the eddy current damping to be stronger in a high external field where the tip is fully magnetized,

whereas Γ was instead observed to be largely field independent. However, SQUID measurements revealed the magnetic film to have significant remanence (Figure 4.8(a)), which would lead to eddy current damping even at zero field. Now consider damping arising from fluctuating electric field gradients. There are certainly stray electrostatic fields between the tip and substrate at small separations due to both differences in the overall work functions and work function inhomogeneities. Previous room-temperature dissipation measurements [17, 83, 84] have shown sizeable differences between dissipation over metal layers and over polymer films due to electrostatic/dielectric effects; these same effects may be partly responsible for the roughly four times difference between the dissipation on and off the microwire. Still, since both the silicon and the microwire were covered with the same polymer, the dominant dissipation source is suspected to be magnetic.

For a tip-sample separation of 13.1 nm and under the signal averaging conditions of Ref. 12, these magnet-tipped cantilevers are projected to achieve a resolution of 5 to 10 nm. Assuming that we are dominated by eddy current damping, a simple solution to improve the dissipation and further enhance the achievable resolution could be to increase the sample thickness or introduce a dielectric spacer between the microwire and the sample.

Acknowledgements

The data presented in this chapter was collected at the IBM Almaden Research Center in collaboration with Daniel Rugar and John Mamin. I thank both Dan and John for providing their magnetic resonance force microscope for these experiments and for their invaluable contributions to data collection and interpretation. I also thank Dan for developing the COZMIC protocol and for conducting the MRFM simulations. Additionally, I thank Charles Rettner and Mark Sherwood for assistance with polymer sample preparation. This research

was funded by the National Science Foundation through the Cornell Center for Nanoscale Systems (Grant Nos. EEC-0117770 and EEC-0646547), the National Institutes of Health (Grant No. 5R01GM-070012), the Army Research Office (Grant No. W911NF-09-C-0073), and the Army Research Office MultiUniversity Research Initiative (Grant No. W911NF-05-1-0403). This work made use of facilities in the Cornell Center for Materials Research, which is supported by the National Science Foundation Materials Research Science and Engineering Centers program (Grant No. DMR-0520404). This work also was performed in part at the Cornell NanoScale Facility, a member of the National Nanotechnology Infrastructure Network, which is supported by the National Science Foundation (Grant No. ECS-0335765).

CHAPTER 6

BUILDING THE THIRD-GENERATION CORNELL MAGNETIC RESONANCE FORCE MICROSCOPE

6.1 Introduction

At the time of writing this thesis, a third-generation magnetic resonance force microscope (Figure 6.1) is in the final stages of construction and testing at Cornell University. The previous-generation microscope [79] enabled a number of exciting advances in spin detection protocols [30, 61, 88] and cantilever fabrication [81, 82]. However, multiple serious limitations prevent its continued use as we pursue three-dimensional imaging experiments and study sensitivity-enhancement techniques, such as dynamic nuclear polarization (DNP) [152] and Fourier-transform MRFM (FT-MRFM) imaging [76].

The largest motivating factor for building the new microscope was to change from only being able to scan the cantilever in one (vertical) dimension to instead having full three-dimensional scanning capabilities. In addition to needing three dimensions of motion to obtain three-dimensional images [12], lateral stage motion also is required to position magnet-tipped cantilevers over low-power, 1-10 μm wide radiofrequency (rf) field sources [60]; micrometer-wide transmission lines generate large transverse fields, which are essential to generate sufficiently large transverse magnetic fields for high-sensitivity MRFM experiments. A second goal was to increase the hold time of the liquid helium dewar from 2.5 days to at least 5 days, which would provide significantly more time for uninterrupted measurements between helium fills. Additionally, definitive studies of the transfer of polarization from electron spins to nuclear spins by DNP in an MRFM experiment will require a double-resonance apparatus that can simultaneously apply microwaves (to polarize electron spins) and radiowaves (to read out the transfer to nuclear spins). The previous-generation micro-

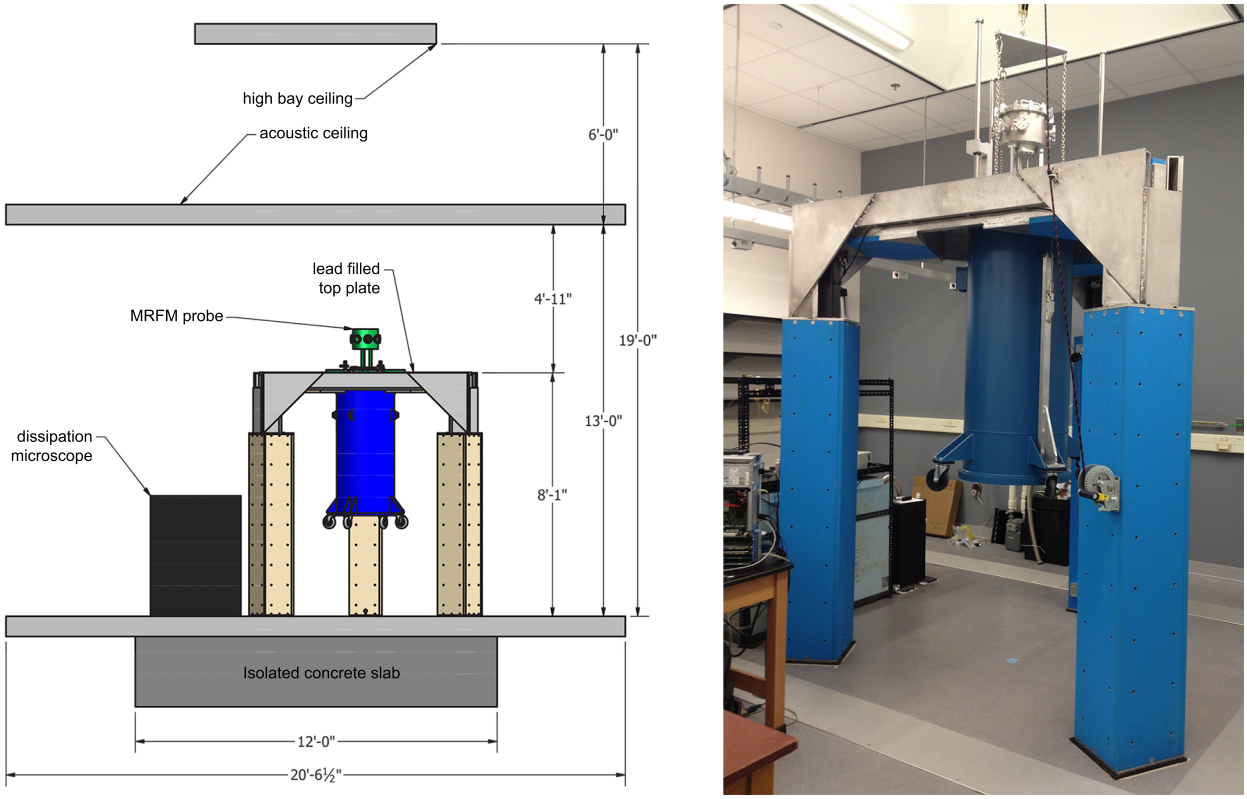

Figure 6.1: Third-generation MRFM microscope superstructure. The microscope is designed to operate in a vacuum of 10^{-6} mbar, at a temperature of 4.2 K, and in magnetic fields up to 9 T. Left: Schematic of the microscope inside the PSB B19 laboratory at Cornell University. The MRFM microscope was positioned over a concrete slab that is isolated from the building foundation. The room's ceiling is 19 ft tall, and the false ceiling surrounding the perimeter of the room is 13 ft. The superstructure consists of a lead-filled top plate that is suspended by air springs attached to three wooden legs filled with sand. The MRFM probe bolts to the top side of the top plate and inserts into a 9 T cold-bore magnet housed inside of a liquid helium dewar (blue). The dewar is bolted to the underside of the top plate. The probe is connected to a high-vacuum chamber (green), and pump lines run from this chamber to a turbomolecular pump located in an adjacent service chase. Right: Image of the probe superstructure with the dewar and microscope bolted to the top plate.

scope had room for only one coaxial cable to be fed through to the probe head, which did not allow for the simultaneous irradiation of electrons and nuclei through separate lines, and the use of a power splitter to feed radiowaves and microwaves through the same line caused significant electrical cross-talk. Improvements to heat-sinking were also desired; the previous microscope required a 50 Ω termination within the probe head and had no heat sinking to the center line of the coaxial cable, both of which caused significant heating. Furthermore, we hoped to improve the vibrational isolation of the microscope by building the new microscope in a new, ground-floor laboratory. The second-generation microscope rested on a light aluminum plate supported by three air-hydraulic legs and was in a room with significant acoustic noise that was located two levels above the building foundation. This configuration did not provide sufficient vibrational isolation to prevent environmental vibrations from exciting the commercial Attocube nanopositioner used for vertical cantilever motion (Attocube Systems AG, ANPx51/HV/LT). The third-generation microscope has been constructed in an rf-shielded laboratory on an isolated concrete slab on the ground floor of the newly-constructed Cornell Physical Sciences Building (PSB), which has been shown to provide far superior vibrational isolation (see Section 6.2.1).

The third-generation microscope is designed to operate at a temperature of 4.2 K, in a vacuum of 10^{-6} mbar, and in magnetic fields up to 9 T. These specifications have placed stringent constraints on the microscope design. The subsequent sections of this chapter include a discussion of the key features of the microscope superstructure, MRFM probe body, and the probe head. Note that the "probe head" refers to the portion of the microscope contained within the vacuum can, and primarily includes the sample platform, cantilever mount, and 3D scanning stage; the MRFM "probe body" refers to the vacuum-compatible support system for the probe head; and the "microscope superstructure" refers to all of the large-scale features of the microscope that are not under vacuum, such as the vibrational isolation platform, the liquid helium dewar, and the hoist system. Note also that throughout

this chapter, the unit of inches is denoted with a double prime; for example, 3 inches = 3".

6.2 MRFM Microscope Superstructure

The superstructure of the third-generation MRFM microscope can be seen in Figure 6.1. The microscope frame consists of a lead-filled top plate that is suspended by air springs on sand-filled legs. 1,000 lb of sand was divided evenly between the three legs. Very similar designs have been successfully used to decouple the microscope from environmental vibrations in scanning tunneling microscopes (STMs) [153, 154]. A liquid helium dewar containing a 9 T superconducting magnet, which supplies the external field in our MRFM experiments, is bolted to the underside of this floating, lead-filled top plate. The MRFM probe bolts to the top of the floating plate and inserts into the dewar so that the probe head, and specifically the cantilever and sample, are centered in the bore of the 9 T magnet. This section details the vibrational isolation of the MRFM microscope, the design specifications of the low-loss dewar, and a dual hoist system for the MRFM probe and the dewar.

6.2.1 Vibrational Isolation of the MRFM Microscope

Vibrational isolation of the sample and cantilever from the surrounding environment is essential to achieve a reasonable signal-to-noise ratio (SNR) in an MRFM experiment. Multiple levels of vibrational isolation were used in this third-generation microscope. The microscope was built in a room in the newly-completed Physical Sciences Building at Cornell University. Unlike our previous laboratory, which was located two floors above ground level, the new room is on the ground floor of PSB. The microscope is located on a concrete slab that is separate from the foundation of the building. The room is also rf-shielded, and acoustic

noise is minimized by having the vacuum pump located in an adjacent service chase.

To assess the improvement in vibrational isolation in the new laboratory, a geophone (Geospace Technologies) was used to compile vibrational data both for the second-generation microscope (in Baker 146) and for the new microscope (in PSB B19). Details on the calibration and use of a geophone are detailed in Appendix B of Ref. 155. In Baker 146, data were recorded on the floor of the room and on the floating aluminum plate that was used for vibrational isolation of the magnetic resonance force microscope. In PSB B19, data were recorded on the floor of the main portion of the room that is connected to the building foundation and on the isolated concrete slab. The collected data, shown in Figure 6.2, indicate that even just the building foundation in PSB B19 experienced significantly fewer vibrations compared to the floating aluminum plate in the previous laboratory. Vibrations were further reduced on the isolated concrete slab in PSB B19. These measurements can be compared to the vibrational profiles observed in six STM laboratories around the United States in Figure B.9 of Ref. 155; our laboratory's ambient vibration noise is observed to be comparable to, or slightly better than, the vibrations seen in many of these state-of-the-art STM laboratories.

The microscope frame consists of three 6 ft tall wooden legs that were braced with aluminum angle and each filled with sand. Hydraulic air springs were bolted to the tops of the legs, and the air springs support a top plate consisting of an aluminum frame with three triangular-shaped wells that each contain ten 25 lb bags of lead shot (totaling 750 lb of lead in the top plate). During MRFM measurements, the MRFM probe and liquid helium dewar are bolted to the top side and underside of the suspended top plate, respectively.

Decoupling vibrations that could pass through tubing and wires was also essential. All fiber optic cables and electrical wires were damped with weighted-down foam on the top plate before they were connected to the MRFM probe. Vibrations through the pumping

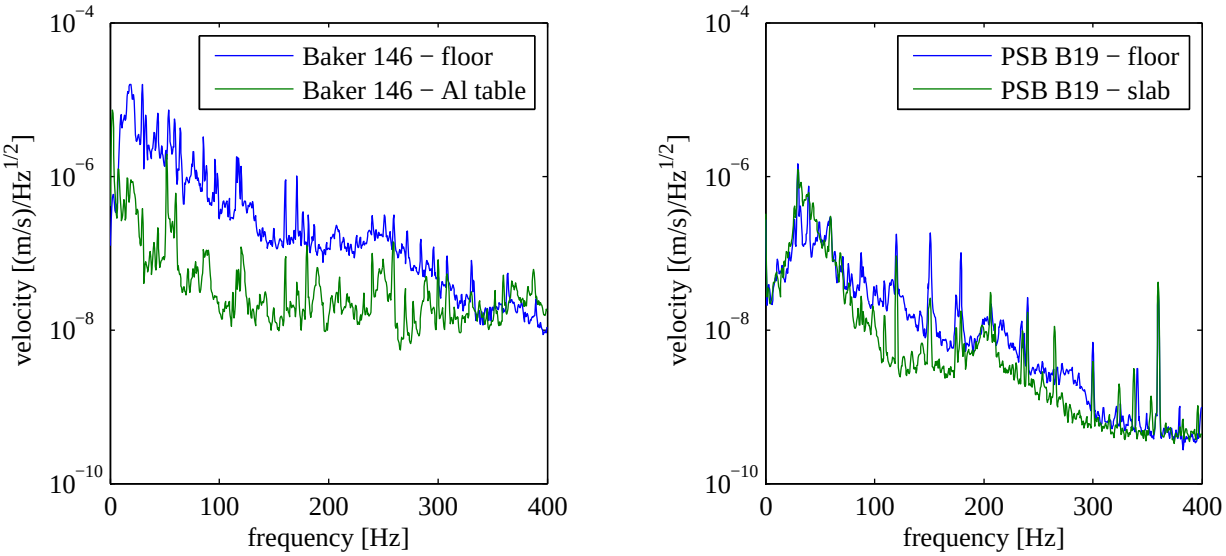

Figure 6.2: Vibrational measurements from the room that housed the second-generation MRFM microscope (Baker 146) and the room that now houses the third-generation microscope (PSB B19); both laboratories are at Cornell University. Left: Vibrational data on the floor (blue) and on the floating aluminum vibrational-isolation plate (green) in Baker 146. Baker 146 was two stories above the ground level of the building. Right: Vibrational data on the floor connected to the building foundation (blue) and on the floor of the isolated concrete slab (green) in PSB B19. The data indicate that the new laboratory in PSB has superior vibrational isolation from the environment.

line connected to the turbomolecular pump, which could induce significant vibrations, were decoupled using a multi-step approach. To mitigate acoustic vibrations the vacuum line was passed from the pump, which was stored in an adjacent service chase, into the laboratory by running 1.5" outer diameter (OD) stainless steel tubing through a 1 ft thick concrete wall. The vibrations were further damped by passing the line through additional solid stainless steel tubing in a concrete box and by bolting tubing to the side of the sand-filled wooden leg and the top plate using vibration-damping clamps. Between each bolted portion of solid tubing, flexible bellows of various lengths with NW-40 connectors on either side were used (Kurt J. Lesker Company; example part that was 36" long is MH-QF-C36). All pieces of solid tubing (1.5" outer diameter) were made of stainless steel and had stainless-steel-bored NW-40 flanges (Kurt J. Lesker Company, part QF40-150-SBB) welded to either end.

6.2.2 Narrow-Neck Liquid Helium Dewar

A new liquid helium dewar was purchased for this microscope to house the cold-bore 9 T superconducting magnet that supplies the external magnetic field in the MRFM experiments. The magnet has a 4" wide bore. For the new system the helium loss rate, with the MRFM probe inserted, was sought to be decreased from 20 L/day (the rate for the previous dewar) to less than 10 L/day. Since the new dewar has a liquid helium reservoir of 50 L, a loss rate of 10 L/day would correspond to a 5 day hold time. Five days between helium fills would provide sufficient uninterrupted measurement time to enable data collection for three-dimensional MRFM image reconstruction.

The high helium boil-off rate in the previous dewar was attributed primarily to the top loading design of the dewar, which required a 10" wide neck so that the superconducting magnet could be lowered to the base of the dewar from the top. Although the magnet insert included baffles to minimize blackbody radiation, it was expected that narrowing the width

of the neck would significantly improve the hold time.

The new dewar, which was purchased from American Magnetics Inc. (AMI) and manufactured by Kadel Engineering Corp, has a narrow 4" diameter neck that matches the 4" diameter bore of the superconducting magnet. The neck diameter could not be further reduced since the vacuum can at the base of the MRFM probe, which inserts into the dewar, has a 3.5" outer diameter. Schematics of the narrow-neck dewar are shown in Figure 6.3. The dewar is vapor shielded with multilayer superinsulation. A vapor-shielded dewar was chosen instead of a nitrogen jacket to prevent vibrations induced by boiling nitrogen; however, other MRFM labs have used dewars with nitrogen jackets without noticeably increased vibrational noise [156]. The neck of the dewar, which is the region between the top flange and the liquid helium reservoir, is made of low thermal conductivity fiberglass G-10 to promote thermal isolation. High temperature superconductor (HTS) current leads were installed to minimize the thermal loads of the leads; since the magnetic field is often swept in the MRFM experiments, HTS fixed leads were preferred over break-away leads. A custom centering puck with a 45° taper was fabricated at the base of the dewar. During measurements the base of the can, which has a matching 45° taper, is set down into the centering puck to prevent pendulum motion of the probe head. Casters and lifting lugs were required for movement of the dewar into position under the superstructure top plate. Note that since the lifting lugs were fabricated out of specification (at the wrong vertical position), custom stainless steel bars with lifting lugs lowered to the correct vertical position were retrofitted on the dewar. A helium level monitor was built into the dewar. The dewar has a 0.5" diameter helium fill port, which also is used to pre-cool with liquid nitrogen. The dewar has two NW-25 ports; one port is connected to a 5 psi relief valve, and the second is connected to Cornell University's helium recovery system.

The helium loss rate without the MRFM probe insert was quoted by AMI to be 0.187 L/hr,

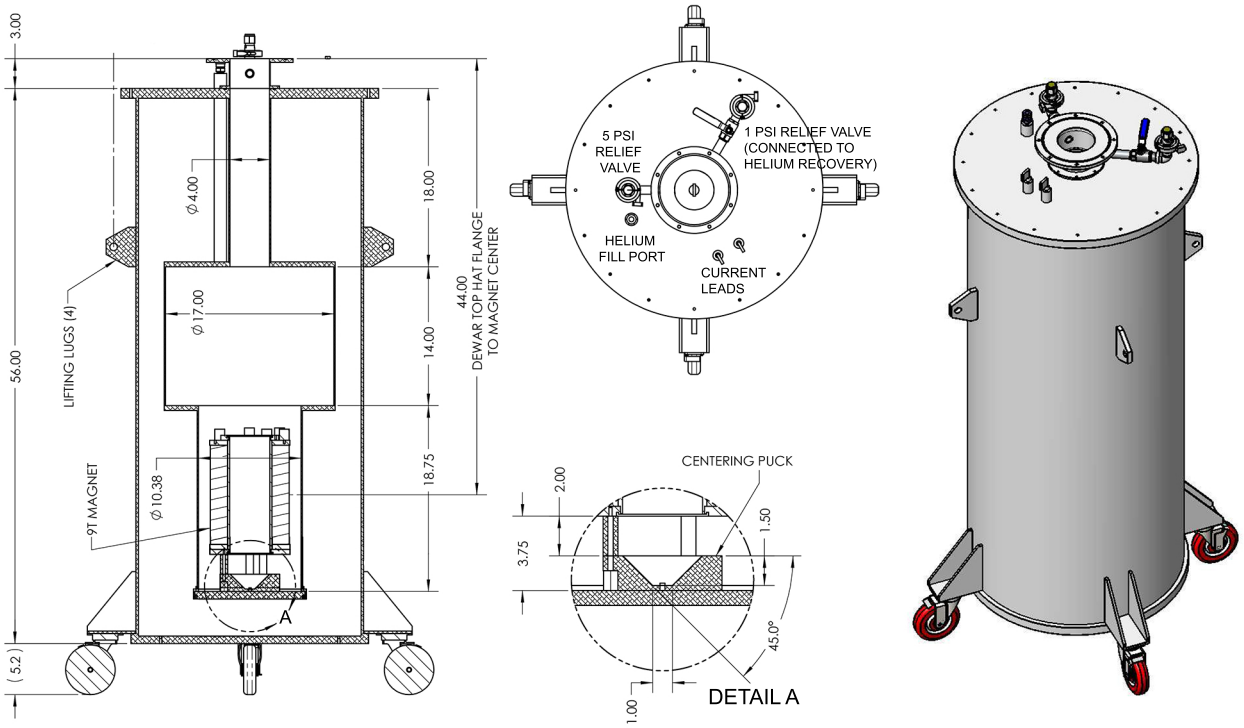

Figure 6.3: Schematics of the bottom-loading liquid helium dewar that contains a 9 T superconducting magnet. Left: Cross-section of the dewar detailing the relevant dimensions for the neck of the dewar, 50 L liquid helium reservoir, and cold-bore magnet. Top center: Top-down view of the dewar, which shows the top hat that mates to the MRFM probe (center), relief valves, liquid helium fill port, and current leads. Bottom center (Detail A): Details for the centering puck at the base of the dewar, which was designed to mate to the base of the MRFM probe vacuum can to mitigate pendulum motion of the probe head. Right: Three-dimensional schematic of the dewar.

which corresponds to 4.5 L/day. After inserting the MRFM probe, the loss rate immediately after the first helium fill was measured to be approximately 20 L/day. However, after the system had reached the base temperature of 4.2 K and after the second fill, the loss rate was measured to be approximately 7 L/day (without running the superconducting magnet). Once the MRFM probe is operational, additional data will need to be collected to approximate the losses while running the magnet. However, these initial results, which indicate a hold time of 7 days, are very encouraging.

6.2.3 Dual Hoist System

A hybrid movable/fixed probe setup was designed to provide the best combination of system performance and ease of access to the probe head between thermal cycles, given the constraint that a pit could not be installed in the laboratory. When the probe is bolted to the top plate, the dewar is too tall to be moved underneath the probe. Since the construction of a taller frame could introduce low-frequency vibrational modes into the microscope superstructure, the probe was designed to be lifted, but only to a controlled height and while always remaining rigidly supported. Prior to positioning the dewar, the probe is controllably hoisted 2.5 ft, which provides 6" of clearance between the dewar and the base of the vacuum can on the probe. The probe, which is bolted to a three-armed plate, is raised and lowered by gliding linear bearings in C-shaped clamps attached to the ends of the arms along stainless steel shafts. The shafts are rigidly fixed, so the probe can be smoothly hoisted vertically without any lateral displacement. Electrical and vacuum connections remain attached to the probe when it is being raised and lowered. Details of this guide system are shown in Figure 6.4.

To assemble and bolt the dewar and the MRFM probe to the top plate prior to filling with liquid helium, two hoists are used. The probe (with the vacuum can in place) is first

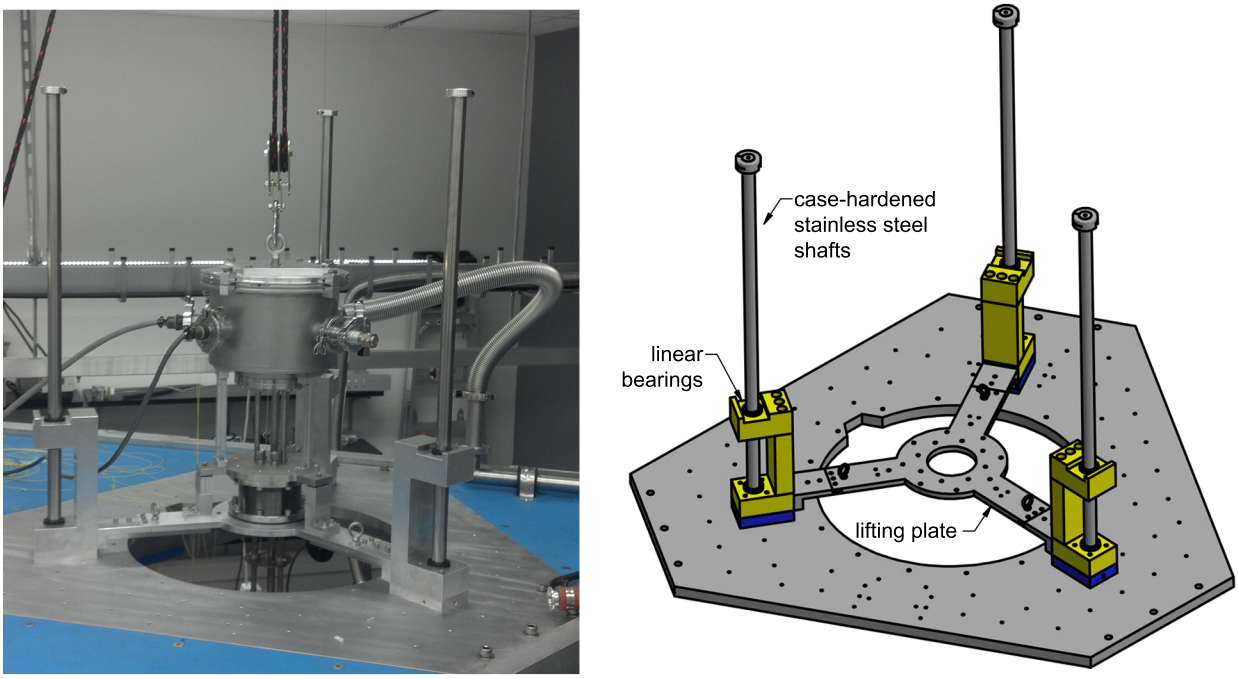

Figure 6.4: Hoist system for the MRFM probe. A hybrid movable/fixed probe hoist design was achieved by gliding the probe along case-hardened stainless steel shafts. A three-armed lifting plate was designed with C-shaped clamps at the end of each arm; the MRFM probe is bolted to this lifting plate. Two sets of linear bearings were placed in each C-shaped clamp, which are used to rigidly fix the lateral position of the MRFM probe. A single hoist point was affixed to the top of the MRFM probe vacuum chamber to lift the probe. When the hoist point is pulled, the linear bearings glide along the shafts and the probe is smoothly raised 2.5 ft, which provides sufficient clearance between the dewar and the bottom of the probe. Left: Image of the hoist plates that shows the hoist point connected to the center of the vacuum chamber lid. Right: Schematic of the lifting components, including the lifting plate, C-shaped clamps (yellow), linear bearings, and stainless steel shafts.

raised by a hoist point centered on the lid of the vacuum chamber at the top of the MRFM probe. A nylon rope connected to the hoist point goes through a block-and-tackle pulley system with a mechanical advantage of 4:1 in the ceiling of the room and then is routed to a winch located on one of the legs of the superstructure frame. Once the probe is raised, the dewar is brought into position under the probe. The dewar is raised by two lift points (lifting lugs) on the sides of the dewar. One stainless steel rope connects to both lifting lugs, and the center of this rope is hauled by a pulley that is connected to a second, larger winch with a mechanical advantage of 10×. After the dewar is raised and bolted to the underside of the top plate, the probe is lowered until the base of the vacuum can is centered in the centering puck at the base of the dewar. The probe is then also bolted into place.

The nylon rope connected to the MRFM probe vacuum chamber is removed during experiments; however, the wire rope is expected to remain connected to the dewar during measurements, with slack in the line to minimize the transmission of vibrations from the probe superstructure to the dewar. The wire rope and connectors to the lifting lugs therefore must be non-magnetic. Type 305 stainless steel wire rope with a 0.25" diameter (breaking strength of 4,900 lb) was purchased from McMaster Carr for this purpose. The wire rope fittings are Electroline Machined Series Clevis Socket Fittings (part IS-125; breaking strength 6,800 lb) purchased from Metro Industrial Supply, LLC.

6.3 Third-Generation MRFM Probe Body

The primary purpose of the long, thin MRFM probe body is to position the sample and cantilever for the MRFM experiment in the center of the bore of the 9 T superconducting magnet. The probe must be compatible with the constraints of the experiment, including working in high magnetic fields, at cryogenic temperatures down to 4.2 K, and in high

vacuum between the temperature range of 293 K and 4.2 K. High magnetic fields require the use of non-magnetic components. Choosing appropriate materials to account for thermal contraction and to mitigate thermal losses was essential. Maintaining high vacuum required the prevention of outgassing or virtual leaks, as well as the use of cryo-compatible welds and solder joints. A second function of the MRFM probe body is to transition all wires, fiber optic cables, and coaxial cables needed for the MRFM experiment into vacuum and to heat-sink them before they reach the cryogenically cooled experimental components in the probe head. In this section, details are provided for the vacuum-compatible probe body design, vacuum feedthroughs, and the use of baffles to mitigate blackbody radiation.

6.3.1 Vacuum-Compatible MRFM Probe Body Design

The MRFM probe body is shown in Figure 6.5. The "probe plate" is used to make an air-tight seal between the probe and the liquid helium dewar; everything above the probe plate is at room temperature, whereas the underside of the probe plate and everything beneath are sealed in the liquid helium dewar. Above the probe plate is a 10" OD cylindrical vacuum chamber with seven NW-40 vacuum ports (6" tall; approximate volume $V = 490\ \text{in}^3$; manufactured by Kurt J. Lesker Company). The chamber was designed to store spare fiber optic cables and electrical wires; for easy access to the inside of the chamber, an ISO-K 250 flange was installed as the lid to the chamber. Feedthroughs for the fibers and wires were attached to NW-40 blank flanges and connected to the ports on the vacuum chamber. One of the NW-40 ports is also used as the connection point for the turbomolecular vacuum pump. Three thin-walled type 304 stainless steel vacuum tubes connect this chamber to the vacuum can at the bottom of the MRFM probe. Two of the tubes have an OD of 7/16" and the third tube has an OD of 5/8"; all tubes have wall thicknesses of 0.035" and are 47.5" long. The vacuum tubes were welded to a 6" OD conflat (CF) flange at the base of the vacuum

chamber, to the probe plate (to transition to the inside of the liquid helium dewar), and to the top of the vacuum can.

Once inside the liquid helium dewar, blackbody radiation is mitigated using copper baffles [157]; further details on the baffles are provided in Section 6.3.3. At the base of the MRFM probe is the vacuum can. The vacuum can has a grease seal with a 10° taper and an overlap length of approximately 0.625" between the inner and outer halves of the seal. This angle was designed to be slightly shallower than the 14° taper for the second-generation probe to make it easier to disassemble the vacuum can; the overlap length was consistent between the two probes. The top of the can (the inside half of the grease seal) was made of stainless steel; the outer half of the grease seal was made of brass. The main body of the vacuum can was made from 3.5" diameter copper tubing (wall thickness 0.064") and the base of the vacuum can, which was made of brass, was tapered at a 45° angle to align with the centering puck at the base of the dewar. The 16.25" long vacuum can (when empty) has an approximately volume $V = 150$ in^3. The brass and copper components of the can were soldered together with silver solder.

Extra tolerance in the length of the probe, so that the base of the vacuum can could properly align with the dewar centering puck, was achieved by positioning an edge-welded bellows between the probe plate and the dewar. Airtight seals between the probe components and the bellows were maintained using ISO-100 (4" inner diameter) vacuum flange connections. The bellows was custom manufactured by Bellows Tech, LLC.

To facilitate disassembly of the vacuum can after it has been sealed to the probe body, a removal assembly was designed, as shown in Figure 6.6. Three rods bolt to the stainless steel top of the can and approach a ring that is attached to the base of the vacuum can. Set screws in the top rods are slowly pushed against the ring to release the vacuum can. Note that it is essential to hold the base of the vacuum can when releasing it, since it releases

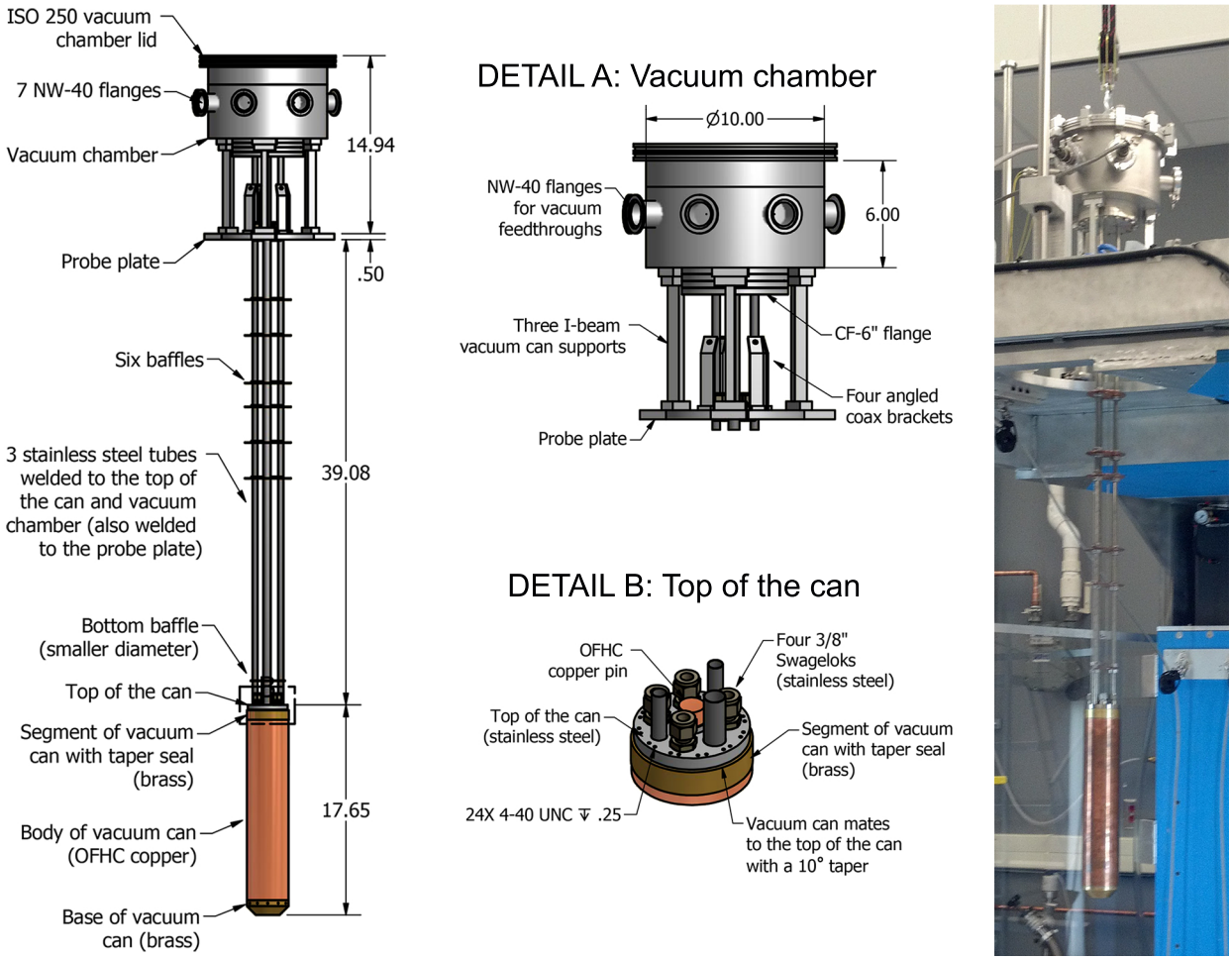

Figure 6.5: Third-generation MRFM probe body. Left: Schematic of the probe body, detailing critical dimensions and describing the key components. Note that three thin-walled stainless steel tubes were welded to the CF-6" flange at the base of the vacuum chamber, to the probe plate, and to the top of the can. Six copper baffles were installed between the probe plate and the top of the can, with an additional bottom baffle located near the vacuum can to guide the coaxial cables into the Swagelok feedthroughs. Detail A: Detail of the vacuum chamber (manufactured by Kurt J. Lesker Company). The chamber has an ISO-250 flange for a lid, CF-6" flange at the base, and seven NW-40 flange ports for vacuum feedthroughs and to connect to a turbomolecular pump. Detail B: Magnified view of the stainless steel top of the can, which shows the OFHC copper pin for heat sinking inside the probe head, four Swageloks for feeding the coaxial cables through to vacuum, and the three stainless steel tubes. A grease seal with a 10° taper mates the brass vacuum can to the stainless steel top of the can. Right: Image of the MRFM probe body mounted in the microscope superstructure.

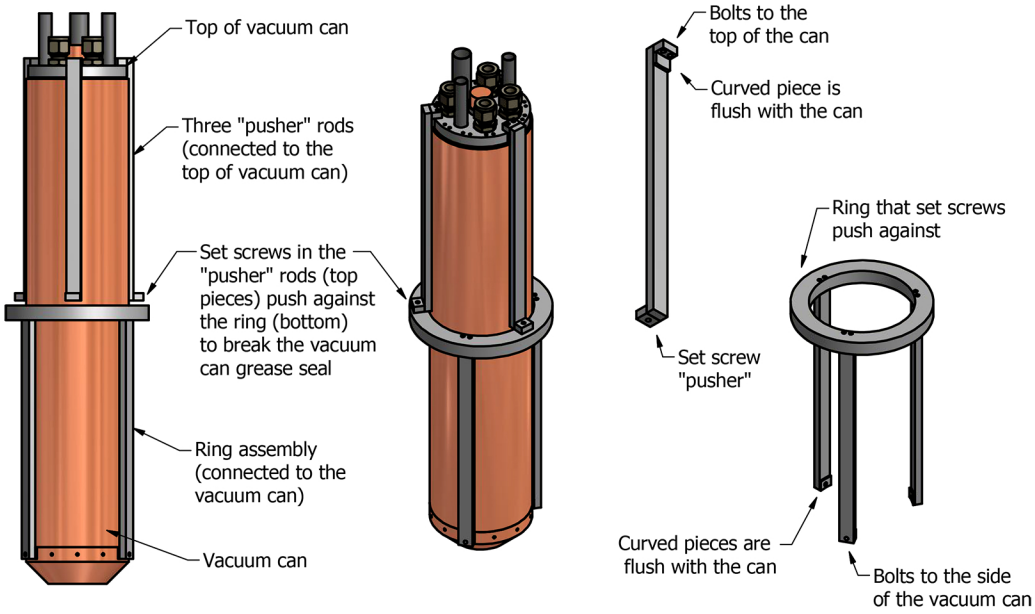

Figure 6.6: Schematics of the assembly used to dismantle the vacuum can. Left: Side-on view of the vacuum can with the assembly attached. The assembly consists of three "pusher" rods connected to the top of the can and a ring assembly with three rods connected to the base of the can. Set screws insert into the pusher rods to push against the ring and release the vacuum seal. Note that the can releases suddenly, so it is critical to support the can from the bottom during disassembly. Center: Angled view of the removal assembly. Right: Angled views of the pusher rod (top) and ring assembly (bottom).

suddenly.

In addition to the three vacuum tubes, a copper pin and four stainless steel ultra-torr vacuum fittings purchased from Swagelok (part SS-600-1-6WBT) also were welded (tubes and Swageloks) or soldered (copper pin) to the top of the can. The 0.75" OD oxygen-free high thermal conductivity (OFHC) copper pin is used to heat-sink the inside of the vacuum can to the liquid helium bath. The Swagelok fittings were designed to be combined with custom ferrules as vacuum feedthroughs for the coaxial cables. By feeding the coaxial cables through to vacuum at the top of the can, instead of with the fiber optic cables and electrical wires at the top of the probe, the heat-generating cables can be directly cooled in the liquid helium bath. The custom ferrules are discussed further in Section 6.3.2.

6.3.2 Vacuum Feedthroughs

Electrical wires and fiber optic cables were fed into vacuum *via* attachments to NW-40 ports on the MRFM probe vacuum chamber. Electrical wires were passed through standard, hermetically sealed 19-pin (Detoronics part DTIH-14-19PN) and 26-pin connectors (Detoronics part DTIH-16-26PN). Each connector was soldered with silver solder to the center of a blank NW-40 flange. Note that it was critical to slowly and uniformly heat the connectors prior to soldering in order to not crack the hermetic seals. The connectors were heated in an oven until they reached the temperature needed to make the solder connection (approximately 400°C). Fiber optic cables were used to watch the cantilever and the three dimensions of motion of the stage. Four 15 m lengths of 9/125 single mode fiber optic cable, purchased from Metrotek under the name "900 micron single mode" fiber with one end bare and the other end connectorized with an FC/APC connector, were fed into vacuum using 0.25" Ultra-Torr Swageloks (part SS-4-UT-A-4) fitted with custom teflon ferrules. A hole in the center of each teflon ferrule was drilled with a #67 drill bit (0.032" $\approx$ 813 µm) [158], and a light film of Apiezon N grease was applied inside the hole and around the surfaces of the teflon ferrule that mated with the Swagelok. Two Swageloks were welded to each NW-40 flange, totaling two flanges needed for the fiber feedthroughs.

New feedthrough methods for the coaxial cables were pursued with this probe design. Coaxial cables supply the transverse magnetic field at microwave (for electron spins) or radiowave (for nuclear spins) frequencies that is necessary to manipulate the sample spins in MRFM experiments. In the previous-generation probe, a single coaxial cable was fed through to vacuum at the top of the probe using a hermetically sealed SMA coaxial connector. 50 Ω impedance was maintained by terminating the line inside the probe head, which caused significant heating and raised the sample temperature from 4.2 K to often above 12 K when approximately 100 mW of microwaves were passed into the coaxial cable. For the third-

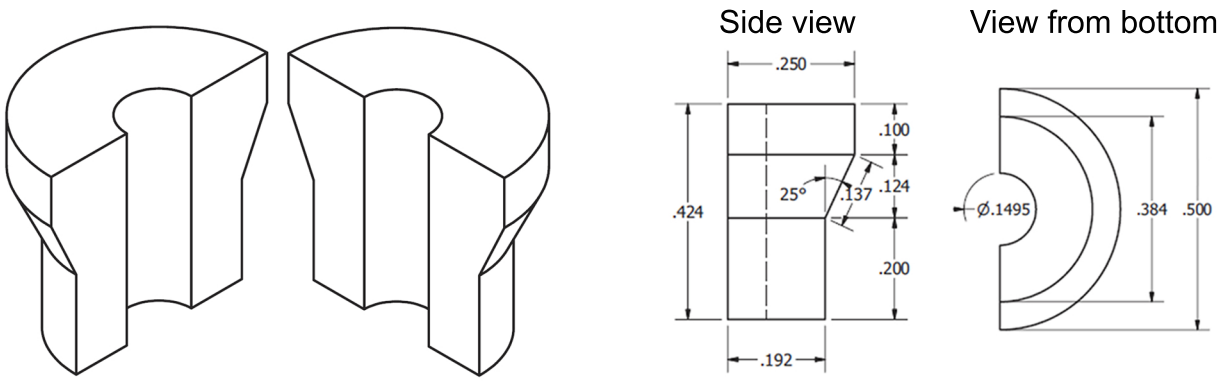

Figure 6.7: Schematics detailing the split ferrule used to feed a coaxial cable from liquid helium into vacuum. Left: Each split ferrule consisted of two identical aluminum halves. Right: Side and bottom-up schematics that indicate the dimensions of one of the split ferrule halves. Note that the provided measurements only should be used as a guide; dimensions should be adjusted based on the precise diameter of the coaxial cable and the dimensions of the obtained Swagelok. For example, the core of the ferrule should be bored to a radius equal to that of the coaxial cable, and the taper on the OD of the ferrule should mate flush with the taper of the Swagelok. To obtain liquid-helium-tight seals in initial tests (see text), strips of indium wire were pressed (1) along the inside width of each of the split ferrule halves (with the coaxial cable inserted between the two indium strips) and (2) around the perimeter of the split ferrule at the base of the taper. The split ferrule was inserted into a Swagelok to crush the indium.

generation probe, two design changes were made to mitigate microwave heating effects. Two sets of coaxial cables (four total cables) were designed to be fed into the probe, one set for microwaves up to 20 GHz and one set for radiowaves; the separate lines for microwaves and radiowaves have been installed for upcoming DNP experiments, as discussed in Section 6.1. For each set, one cable supplies the microwaves/radiowaves, and the second cable passes the microwaves/radiowaves back out of the probe to be terminated elsewhere.

The second design change pursued for the coaxial cable feedthroughs was to provide superior heat sinking by feeding the cables through the liquid helium bath and passing them into vacuum at the top of the vacuum can. 0.375" Swagelok tube fittings (part SS-600-1-6WBT) were purchased and welded to the top of the vacuum can (Figure 6.5, Detail B); the inner diameter of the Swageloks was wide enough to pass through preconnectorized cables.

Resealable, custom aluminum split ferrules were designed to fit around the coaxial cable (Figure 6.7). To seal each ferrule — which requires liquid-helium-tight seals between the coaxial cable and the ferrule, between the halves of the split ferrule, and around the outside of the ferrule — the use of indium wire (1.0 mm or 1.5 mm diameter; Alfa Aesar) or teflon tape was considered. Although a single split ferrule with a coaxial cable wrapped in indium wire successfully held vacuum both at room temperature and in liquid helium in a test setup (a long stainless steel rod with a single Swagelok at the base and an NW-40 vacuum fitting at the top), the split ferrules did not hold vacuum even at room temperature in the MRFM probe. The reason for this disappointing performance is unclear, but it is believed that the configuration of the top of the can, which has seven separate components in very close proximity, does not provide the clearance needed for sufficient tightening of the Swageloks. The probe has held vacuum at room temperature and in liquid helium by wrapping solid aluminum ferrules (the same design as the split ferrules, but one piece with no hole in the center) with 10 layers of teflon tape. Subsequent trials will involve switching to stainless steel ferrules to match the thermal contraction of the stainless steel Swageloks and coaxial cables, working to better match the taper between the Swageloks and the ferrules, and sealing the coaxial-filled split ferrules with an epoxy that can be thermally cycled, such as Stycast (Lake Shore Cryotronics, Inc.).

6.3.3 Mitigating Blackbody Radiation

Baffles were used to mitigate thermal losses due to blackbody radiation from the liquid helium reservoir to the close-to-room-temperature flange at the top of the dewar [157]. AMI recommended a 1/16" radial clearance between the 4.0" diameter neck of the dewar and the outer diameter of the baffles, meaning that the baffles should have a diameter of no more than 3.875". Because the bellows (located between the probe plate and the dewar top

hat) was made narrower than specification, and because the baffles must clear the bellows to assemble/diassemble the probe, the outer diameter of the baffles was further reduced to 3.8125". Six 1/16" thick copper baffles were installed along the stainless steel vacuum tubes between the probe plate and the top of the vacuum can. The baffles were clamped into place using two-piece clamp-on aluminum shaft collars with a 7/16" bore (McMaster-Carr, part 6436K134). Eight evenly-spaced half-baffles were also designed to feed down each of the three thin-walled stainless steel vacuum tubes to further mitigate the effects of blackbody radiation.

6.4 Third-Generation MRFM Probe Head

6.4.1 Probe Head Design

A schematic of the probe head, which consists of all of the microscope components inside of the vacuum can, is shown in Figure 6.8. The probe head houses the cantilever, the sample mounted on a coplanar waveguide that supplies the transverse magnetic field, and the three-dimensional stage. The cantilever motion is monitored using Fabry-Perot fiber-optic interferometers operating at 1310 nm [97, 159]. Three additional fiber optic cables were positioned to watch the motion of the three axes of the stage. Two OFHC copper plates were installed for heat-sinking. Currently copper posts connect the two copper plates; the posts will eventually be replaced by damped springs. Flexible coaxial cables were coiled between the top and bottom copper plates to supply the transverse field without disrupting the damping effects of the springs when installed. The sample and coplanar waveguide platform is bolted to the underside of the bottom copper plate. The cantilever is mounted on the three-dimension Pan-walker stage; the cantilever points up towards the sample. A rigid-

sample, moving-cantilever configuration was chosen so that the relatively-inflexible coaxial cables could be fed directly to the coplanar waveguide under the sample. The Pan-walker stage has 1 mm of coarse motion in each dimension and contains a piezoceramic tube for fine, nanometer-scale motion over a range of a few micrometers.

6.4.2 Heat Sinking of the Probe Head

Some of the features of the probe head that are used for heat sinking can be seen in Figure 6.8. As stated above, two OFHC copper plates were installed to heat-sink the probe head. A copper pin threaded against the top copper plate extends outside of the vacuum can to couple to the liquid helium bath. Glass beads (Delta electronics, part 41-10046-01-AU) were used to heat sink the center line of the coaxial cables on the top copper plate; the outer ground lines of the coaxial cables were passed through the liquid helium bath to be cooled to 4 K. To reduce the heat load passed from the room-temperature coaxial line to the low-temperature liquid helium bath and probe head, coaxial cable with a stainless steel outer shielding jacket was installed down the length of the probe body (AstroLab astro-cobra-flex cable, part 31000S-29043-29043-41.5). A stainless steel jacket incurs slightly higher microwave transmission losses than regular coaxial cable, but also exhibits lower thermal transmission. Before entering the probe head, the coaxial cable was transitioned to a cable with a standard tin-plated copper shielding jacket (RF COAX Inc. RF cable assembly part S086MM-47R, 0.086" OD tin-plated copper semi-rigid cable with SMA male to SMA male connectors rated for use up to 27 GHz).

Copper foil was used to heat sink critical components of the probe to the copper plates. Only one piece of copper foil, which is located between the bottom copper plate and the cantilever mount, was installed when the images in Figure 6.8 were collected. The copper foil is 0.001" thick (99.999% metals basis; Alfa Aesar, part 10950) and was cut into approximately

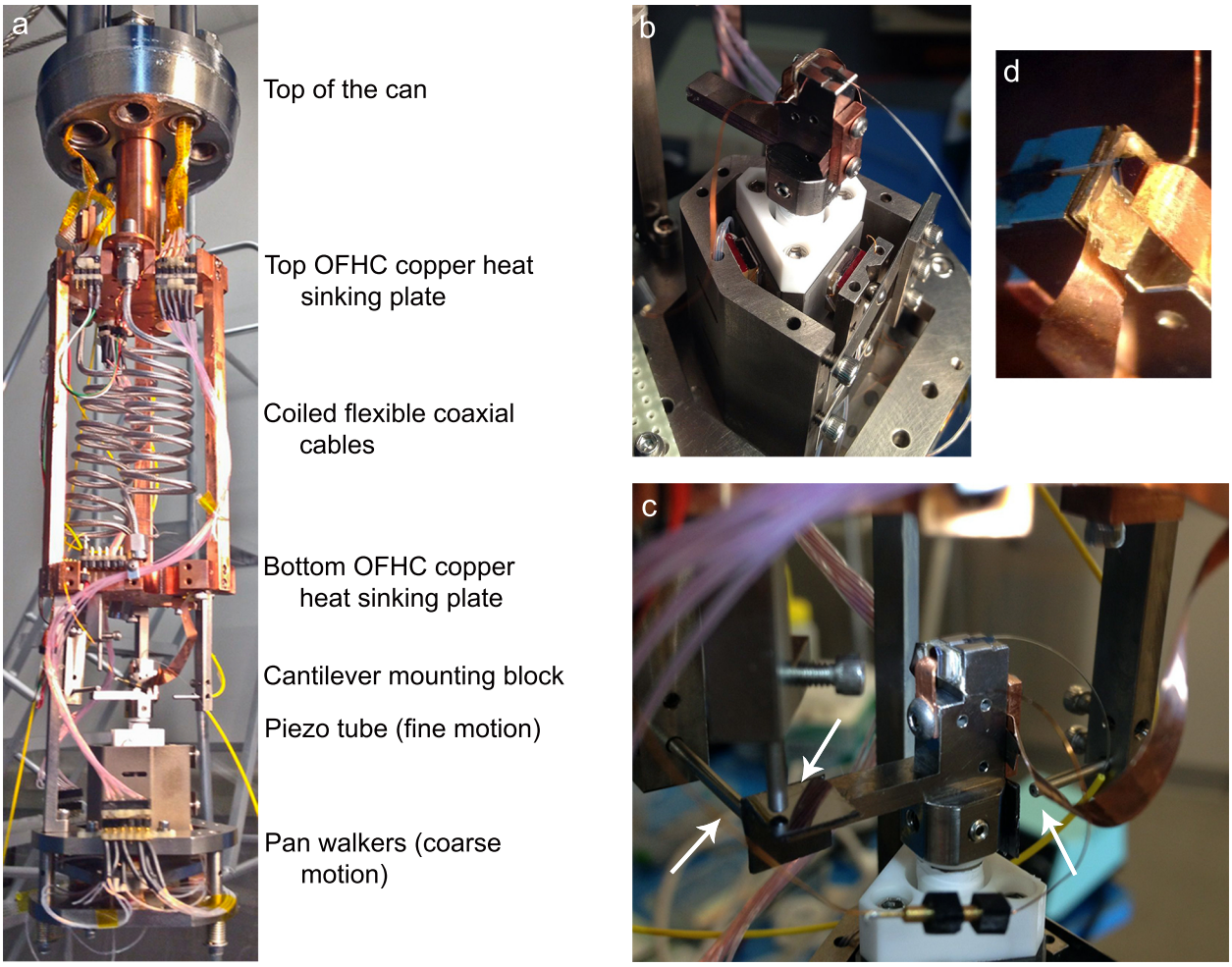

Figure 6.8: Images of the third-generation MRFM probe head. (a) Image of the full length of the probe head. The copper pin soldered to the outside of the top of the can passes into the probe head and heat sinks the top and bottom copper plates. Coaxial cables inserted from the top of the can (not shown) are heat-sinked to the top copper plate using glass beads and routed *via* coiled flexible coaxial cables to the sample platform bolted to the underside of the bottom heat-sinking plate (not shown). The cantilever is mounted on a piezo tube contained within a three-dimensional custom-built Pan-style nanopositioner. The fine-motion piezo tube achieves 2 µm motion in each direction at 4.2 K; the Pan-style walkers are used for coarse motion and have a range of 1 mm in x, y, and z. (b) Magnified, angled view of the Pan z-walker prism (white triangle) housed in its titanium casing. (c) Magnified view of the cantilever mount and the three fiber optic cables (encased in stainless steel sheaths) which are used to watch the motion of the stage. The fibers, which are pointed at three silicon mirrors, are highlighted by the white arrows. (d) Further magnified view of the fiber optic cable watching the cantilever motion. The fiber is glued to the cantilever mounting block (black Stycast epoxy, left-hand side of the frame), and the cantilever paddle is positioned so that the paddle is directly over the core of the fiber. The cantilever handle die (silicon chip in the center of the frame) is mounted on a drive piezo and is held in place with a copper clip.

1 mm wide strips. Very thin foil was used to minimize the propagation of vibrations to the cantilever and sample. In order to improve the thermal conductivity, the copper foil was annealed for 3 hours at 600-650°C in forming gas with 95% argon and 5% hydrogen. Note that the foil should not be touched with metal tweezers or scissors prior to the anneal to avoid contamination. The annealing was conducted at the Army Research Laboratory by Doran Smith's group; Smith *et al.* have measured the thermal conductivity of this type of foil to be in line with what is expected for 99.999% pure copper [160]. Before the copper foil was bolted in place, a thin film of Apiezon N grease was applied to the ends of the foil to enhance thermal conductance at cryogenic temperatures [161].

6.4.3 Hang-Down Geometry

There are two commonly-used experimental geometries for MRFM experiments. For the third-generation microscope, the hang-down geometry [53], in which the length of the cantilever is parallel to the external field, was chosen over the SPAM (Springiness Preservation *via* Aligning Magnetization) geometry [139], where the width of the cantilever is parallel to the external field. Schematics of both geometries are shown in Figure 6.9. In the SPAM geometry there is no observed field-damping of the magnetic tip [30, 55, 162]. Magnetic damping has been observed in the hang-down geometry [56, 93] for micrometer-diameter magnetic particles; however, magnetic damping is not expected to be an issue for small nanomagnets.

MRFM signal is significantly increased by working in the hang-down geometry; the relative magnetic field gradient is three times larger in the hang-down geometry than in the SPAM geometry [163]. Additionally, *in situ* magnetic tip characterization using frequency-shift cantilever magnetometry (Sections 4.1 and 4.4) can only be conducted in the hang-down geometry [58, 82].

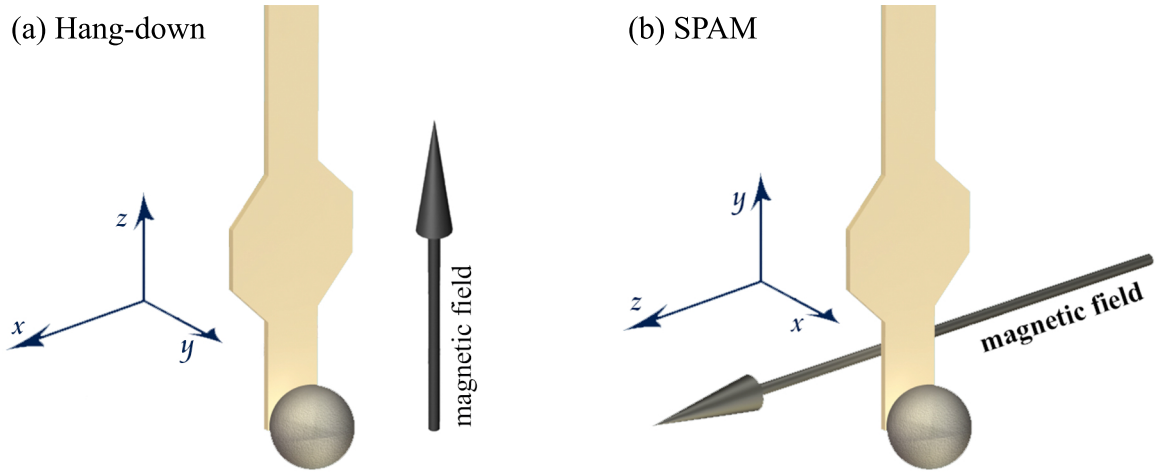

Figure 6.9: Schematics of the hang-down and SPAM geometries used in MRFM experiments. (a) The hang-down geometry, in which the applied magnetic field is parallel to the length of the cantilever, has been chosen for the third-generation MRFM microscope. (b) The SPAM geometry, in which the magnetic field is instead parallel to the width of the cantilever, was used in the previous-generation microscope.

Cantilever damping was assessed as a function of applied magnetic field for an attonewton-sensitivity cantilever with an integrated 4 µm diameter (nominally spherical) nickel magnetic particle (Novamet, CNS-10). The data shown in Figure 6.10 were collected at $T = 4.2$ K for a cantilever with a spring constant k_c=1 mN m^{-1}. The dissipation $\Gamma = k_c/(2\pi f Q)$ and minimum detectable force $F_{\mathrm{min}} = \sqrt{4k_{\mathrm{B}}T\Gamma}$ were determined. At zero field, $\Gamma = 1.2 \times 10^{-12}$ Ns/m and $F_{\mathrm{min}} = 17$ aN. At a field of 0.6 T, which is the approximate field used in electron spin resonance (ESR) MRFM experiments, $\Gamma = 6.3 \times 10^{-12}$ Ns/m and $F_{\mathrm{min}} = 38$ aN. These results indicate that by working in the hang-down geometry, the dissipation experienced by the nominally spherical 4 µm magnet-tipped cantilever at high applied magnetic field is increased by a factor of five. However, the SNR for this experimental setup should still be sufficient to conduct ESR measurements using the spin detection protocol in Ref. 30.

A new spin detection protocol COZMIC has been successfully used with nanomagnet-tipped cantilevers in the hang-down geometry for a nuclear magnetic resonance MRFM experiment. This protocol was introduced in Ref. 58 and is discussed in Section 5.2.4.

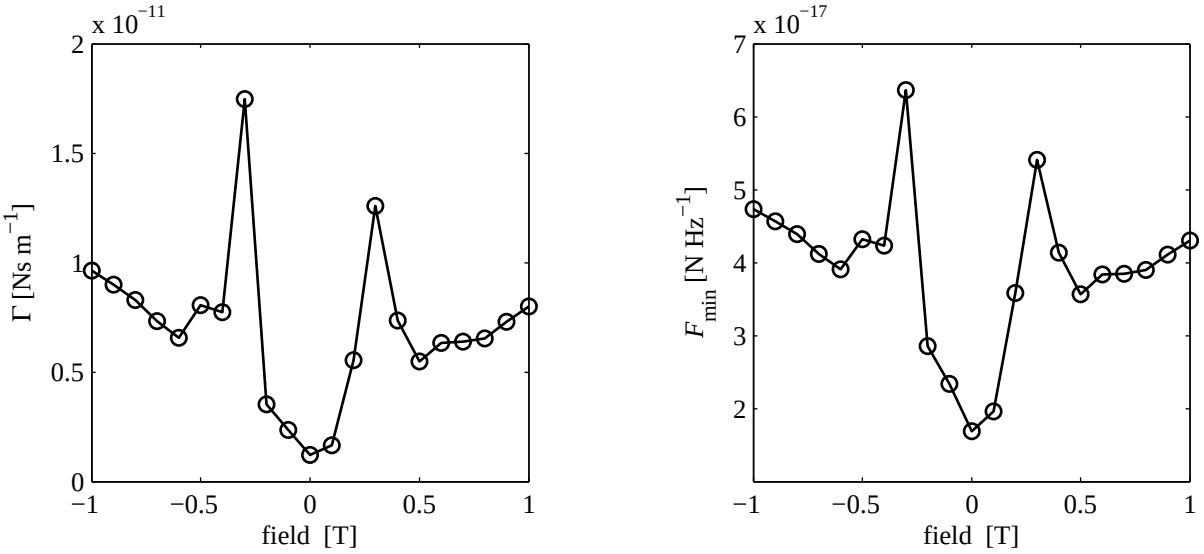

Figure 6.10: Magnetic damping in the hang-down MRFM geometry as a function of applied magnetic field for a 4 µm nickel magnet attached to an attonewton-sensitivity silicon cantilever. Dissipation Γ and the minimum detectable force F_{min} were calculated for a temperature $T = 4.2$ K and a cantilever spring constant of $k_{\mathrm{c}} = 1$ mN m^{-1}.

6.4.4 Pan-Walker Stage with Three-Dimensional Motion

Three-dimensional motion was achieved using a custom-built Pan-style nanopositioner (Figure 6.8(a-b)) [164–166], which is known to maintain performance at cryogenic temperatures and, due to its rigid design, is less susceptible to excitation by ambient vibrations than commercial Attocube positioners. Due to slow and steady stepping, the Pan-walker stage moves without any backlash, in contrast with commercial slip-stick positioners. The Pan-walker stage allows more than 1 mm of coarse motion in each x, y, and z direction. A piezo tube was positioned inside the core of the Pan walker to enable nanometer-precision motion over a 2 µm range in each direction. The piezo tube, which was custom-manufactured by EBL Products Inc. (made from material EBL #3), had a 0.250" outer diameter, a 0.190" inner diameter, and was 1.850" long. The tube contained four 90° quadrants, was grounded in the center, and had gold electrodes on the outer diameter. No gold was coated on the final 0.1" of the piezo tube at each end so that parts that were glued to the piezo tube were

not exposed to high voltages. The cantilever mount (Figure 6.8(c-d)) — which holds the cantilever, a drive piezo to excite cantilever motion, and a fiber optic cable to watch the cantilever motion — was mounted to the top of the piezo tube.

The Pan-walker stage was fabricated primarily from titanium and consisted of two parts: a prism for z-motion (see Figure 6.8(b)) and a plate for motion in the x and y directions (see Figure 6.8(a)). Low-friction sapphire plates were glued using Stycast epoxy to the surfaces of the z-walker prism and the x-y plate. Each shear piezo stack was comprised of two shear piezos that were glued together with silver paste to increase the range of motion. The piezoceramic plates with shear polarization were custom-fabricated by EBL Products Inc. (made from material EBL #4). They had an area of 0.275" $\times$ 0.275", and were 0.050" thick. One corner of each piezo was removed (0.07" $\times$ 0.07") to facilitate adhesion of electrical wires to the gold electrodes on the piezos. The piezos were glued with silver paste to the outer frame of the walker, and alumina plates were adhered with Torr Seal epoxy to the side of the piezo pressed against the sapphire sheets. The alumina-sapphire interface has relatively low friction, so the alumina sheets glide across the sapphire plates when moved slowly. A schematic of one piezo stack is shown on the right-hand side of Figure 6.11.

Six shear piezo stacks were used for each direction of motion of the Pan-walker stage. The stepping mechanism is illustrated on the left-hand side of Figure 6.11. The x and y piezo stacks were glued together; three stacks were positioned under the x-y stage plate, and the other three stacks were placed at the same positions above the plate. The tension to the x and y piezos was set by adjusting the force of three springs on a tensioning plate located underneath the bottom set of x-y piezos Three pairs of z piezo stacks move the z-prism; two piezo stacks are located on each of the three triangular surfaces of the z-stage. Tension to the z stage is supplied by tensioning a beryllium copper leaf spring on the front face of the z stage; a sapphire ball bearing transfers the tension to the stage.

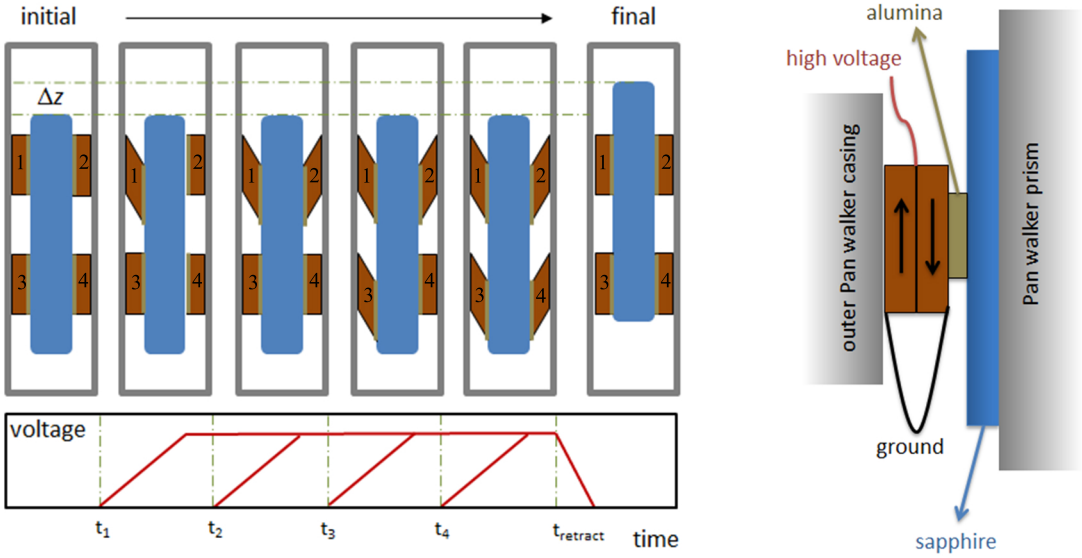

Figure 6.11: The stepping mechanism of the z-prism of the Pan-style nanopositioner. The mechanism for the motion of the x-y stage is almost identical. Left: Cartoon of how shear piezos (brown) are used to step the central prism (blue) of the third-generation MRFM probe head Pan-walker stage. For simplicity only four of the six piezo stacks are displayed. In the initial state, the central prism is held by all the piezo stacks. At time t_1, piezo stack 1 is charged and shears. Since the prism is still held by the other three piezos, it does not move. One-by-one the other piezo stacks are charged and shear. At time t_{retract}, the charges on all the piezo stacks are simultaneously dropped, and the prism is pushed forward a distance Δz in one smooth step. Right: Detailed schematic of one piezo stack between the central prism and the titanium outer casing. Each piezo stack is comprised of two shear piezos that move in opposite directions (as indicated by the arrows) to increase the range of motion. The high voltage sides of both piezos are in the center, and the outsides are grounded. The piezo stack was glued to the outer Pan-walker stage casing and to an alumina sheet. A sapphire plate was glued to the surface of the z-walker prism. Motion occurs along the alumina-sapphire interface.

6.4.5 Coplanar Waveguides

In MRFM experiments, a transverse magnetic field B_1 is necessary is used to saturate nearby sample spins. We have studied the strength of transverse fields generated using multiple types of transmission lines. Microstripline halfwave resonators have been used to generate modest fields of 3.9 mG, with 100 mW passed into the top of the second generation probe [30]. Recently, two coplanar waveguide designs have been considered to increase the B_1 field strength. Both types of waveguides were lithographically patterned on ultra-high-resistivity silicon substrates (purchased from University Wafer, intrinsic silicon with resistivity $> 20,000\ \Omega\,\mathrm{cm}$, dielectric constant $\epsilon_r = 11.7$, $\langle 100 \rangle$ oriented, 100 mm diameter, 500 µm thick, single side polished).

In the first design, coplanar waveguides with finite-width ground planes were fabricated [61]. The waveguides had a 321 µm wide middle conductive line and two 342 µm wide outer conductive lines that were separated by 290 µm wide interline gaps [158] to achieve 50 Ω impedance. In order to avoid problems associated with standing waves arising from imperfect termination, the waveguides were designed with a short at one end. In MRFM experiments, the cantilever approached the sample surface above the middle of one of the shorted segments. The short that terminated the three conductive lines was 300 μm wide. All of the conductive lines were made by patterning 100 nm thick gold on top of a 5 nm titanium adhesion layer. To pass microwave frequencies in to the center line of the waveguide, the waveguide silicon chips were inserted into high-dielectric-constant circuit boards equipped with end launch SMA connectors. The gap between the circuit board and the chip was designed to fit snugly and had a gap of less than 0.5 mm on all sides. The conductive lines were connected between the circuit board and the silicon chip by using three gold wire bonds per conductive line. The waveguide board was made of 0.015" thick Arlon ($\epsilon_r = 10.0$), with 1 oz/ft^2 copper cladding with a soft gold finish on the front side of the board [158]. The

board was patterned to match the dimensions of the center line and gaps in the waveguide silicon chips. From measurements of the mechanically-detected ESR signal versus power in the second generation probe, the coil constant at the short of the coplanar waveguide was estimated to be 45 mG $W^{-1/2}$, with the power measured for convenience at the input to the probe. At a typical power into the probe head of $P_1 = 15\,\mathrm{dBm} = 32\,\mathrm{mW}$, the rotating frame microwave field amplitude at the sample was estimated to be $B_1 \approx 8\,\mathrm{mG}$. This is a factor of two improvement over the field strength in Ref. 30.

Most recently, coplanar waveguides with infinite ground planes have been prepared. The large-area ground planes ensure a better connection to the ground. These waveguides were fabricated on silicon chips that are 9.8 mm long and 4.75 mm wide. They had a 1016 µm wide middle conductive line and two outer conductive lines that extended to the edges of the chip. To achieve a 50 Ω impedance, the interline gaps between the center line and the ground planes were 432 µm. The conductive lines were comprised of a 5 nm titanium adhesion layer (deposited at a rate of 1.67 Å/sec), approximately 800 nm of copper (5.56 Å/sec), and a 30 nm thick gold top layer for wire bonding (0.8 Å/sec). The titanium and copper layers were deposited by sputtering (AJA sputtering tool), and the gold was subsequently deposited by thermal evaporation (CVC SC4500 Evaporation System). The chips were again designed to insert into square gaps in the center of circuit boards with a high dielectric constant and to be electrically connected using gold wire bonds. This generation of circuit boards was made of 0.1" thick TMM10i ($\epsilon_r = 9.8$; purchased from PCBFabExpress). It was anticipated that the low B_1 generated by the previous coplanar waveguide design may have been due in part to the field lines being pulled down toward the copper sample mounting block below the thin Arlon boards, which would act as a ground plane. The significantly thicker TMM10i boards used here are expected to provide a thicker buffer layer of high-dielectric-constant material and push more of the field into the sample above the coplanar waveguide. The TMM10i boards were again coated with 1 oz/ft^2 copper cladding with a soft gold finish that

was patterned to match the design of the silicon chip. The field generated from these new chips will be tested in upcoming MRFM experiments in the third-generation MRFM probe.

6.5 Discussion

When fully operational, the third-generation magnetic resonance force microscope will have three-dimensional scanning capabilities with nanometer-scale precision over a 2 µm fine scanning range and coarse motion up to 1 mm in each direction. The microscope has been designed for the cantilever to be positioned on the nanopositioner stage, which leaves the rigid, large-area transmission line substrate free to accept a wide range of as-fabricated samples and devices. Enhanced vibration isolation has been achieved by designing a new microscope superstructure with a floating, lead-filled top plate. Better heat-sinking has been implemented to improve temperature stability within the probe, and a new bottom-loading dewar was introduced to improve the liquid helium hold time. At the time of writing, the probe has been cold tested and vacuum tested, and magnet operation and hold time have been verified. The Pan-walker stage has been tested at room temperature and is being optimized for operation at liquid helium temperatures.

The new microscope will enable many new and exciting MRFM experiments. Three-dimensional motion will be possible for the first time in our laboratory, which is essential for three-dimensional imaging and is needed in order to use either high-sensitivity microwires for NMR-MRFM experiments [60] or microscale versions of the coplanar waveguides for high-sensitivity ESR-MRFM measurements. In Chapter 5, methods were discussed for the fabrication of high-gradient cobalt nanomagnet-tipped cantilevers and their use to detect nuclear magnetic resonance with better than 500 proton magnetic moment sensitivity demonstrated. For a tip-sample separation of 13.1 nm and under the signal averaging conditions of Ref. 12,

this sensitivity corresponds to a proton imaging resolution of 5 to 10 nm in each dimension. These nanomagnet-tipped cantilevers are ready to be used in the third-generation MRFM microscope as soon as the optimization of the three-dimensional stage for operation at liquid helium temperatures is completed. It also may be possible to further enhance the resolution of NMR-MRFM experiments using DNP; however, definitive studies of DNP in an MRFM experiment have not yet been conducted by any MRFM group because no microscope exists with the ability to simultaneously apply both microwaves and radiowaves. We believe that the third generation Cornell MRFM microscope described in this chapter will be the first microscope capable of these double resonance experiments. When fully operational, we expect the microscope to be used to investigate the mechanism of DNP in the high magnetic field gradients experienced by spins close to nanomagnet tips [167], as well as to explore enhancements of SNR in NMR-MRFM experiments by using DNP to polarize nuclear spins.

Acknowledgements

The development of this microscope has been a joint effort over a two-year period, and I am grateful for the contributions of many collaborators. I thank my colleagues Eric Moore and Lei Chen for co-developing the microscope; Eric collaborated with me on the design of the microscope superstructure, and the probe head was largely designed by Lei. I also thank Eric for collecting the vibrational data in the Baker and PSB laboratories, and Lei and Christine Gleave both for collecting the MRFM data on the magnetic damping of a large magnetic tip in the hang-down MRFM geometry and for supplying information on the fabrication methods for our coplanar waveguides. Daniel Rugar and John Mamin at the IBM Almaden Research Center and Doran Smith at the Army Research Laboratory provided invaluable advice on microscope design during laboratory tours. Thanks to Doran also for annealing the copper foil and for giving a wealth of advice on heat sinking and overall probe construction.

Raffi Budakian and John Nichol at University of Illinois at Urbana-Champaign graciously shared their unpublished Pan-walker designs. Seamus Davis, Tien-Ming Chuang, and Milan Allan at Cornell University shared their STM superstructure CAD and provided excellent advice for maximizing vibrational isolation. Thanks to Lee Harrell at the West Point Military Academy for helpful discussions on the hybrid hoist system. Thanks to Cornell's Research Services Shop, and particularly Jason Russell and Daniel Sheerer, for assistance with redesigning PSB B19. And special thanks goes to the Cornell Laboratory of Atomic and Solid State Physics Machine Shop, especially Rodney Bowman, Chris Cowulich, and Jeffrey Koski, for fabricating the probe, collaborating on design adjustments, and for countless helpful conversations. Work in this chapter was conducted with the financial support of the National Institutes of Health (Grant No. 5R01GM-070012), the Army Research Office MultiUniversity Research Initiative (Grant No. W911NF-05-1-0403), and the National Science Foundation through the Cornell Center for Nanoscale Systems (Grant Nos. EEC-0117770 and EEC-0646547). This work was performed in part at the Cornell NanoScale Facility, a member of the National Nanotechnology Infrastructure Network, which is supported by the National Science Foundation (Grant No. ECS-0335765). Wire bonding was accomplished using resources available in the Cornell Center for Materials Research, which is supported by the National Science Foundation Materials Research Science and Engineering Centers program (Grant No. DMR-0520404).

CHAPTER 7

OVERALL CONCLUSIONS AND OUTLOOKS FOR THE NEXT GENERATION OF CORNELL MRFM FABRICATION

In the work presented in this thesis, the critical need within the magnetic resonance force microscopy community for the development of a fabrication protocol to prepare high-gradient nanomagnets on cantilevers has been achieved. The primary objective of this work was to fabricate overhanging nanomagnet-tipped cantilevers with sufficiently large magnetic field gradients to conduct high-resolution MfRFM imaging experiments.

To reach this goal, a new magnet-on-cantilever fabrication protocol was developed that decoupled the preparation of the nanomagnets from the fabrication of attonewton-sensitivity cantilevers. Nanomagnets were batch-fabricated on suspended silicon micrometer-scale chips and were attached to separately-fabricated cantilevers using focused ion beam manipulation. Using this new approach, nanomagnets were not exposed to high-temperature processing steps and could be patterned using the non-damage-inducing techniques of electron beam lithography and electron beam evaporation. These advantages allowed for the high-yield fabrication of both robust nickel nanomagnets and temperature-susceptible cobalt nanomagnets. The magnet-tipped chip process required only a few days of processing time, which facilitated rapid optimization of processing conditions. Additionally, both spectroscopic and microscopic analysis of as-deposited nanomagnets were possible for the first time. Cantilever magnetometry indicated that cobalt nanomagnets exhibited saturation magnetizations consistent with the theoretical value for fully-saturated cobalt. Characterization of similarly-processed cobalt magnetic films using X-ray photoelectron spectroscopy (XPS) with depth profiling indicated that unprotected cobalt films incurred less than 10 nm of oxidation damage, and that oxygen contamination was prevented by capping the cobalt layer with 10 nm of platinum.

A cobalt magnet-tipped cantilever fabricated using the new magnet-tipped chip protocol was successfully used to detect spin variance signal from protons in a polystyrene film with better than 500 proton magnetic moment sensitivity in a 1 Hz detection bandwidth. The observed vertical tip-field gradient of 4.4 to 5.4 $\mathrm{MT\,m^{-1}}$ is comparable to the 4.2 $\mathrm{MT\,m^{-1}}$ field gradient produced by the $Fe_{70}Co_{30}$ pillar in the sample-on-cantilever experiment of Ref. 12 that achieved 4 to 10 nm resolution MRFM imaging. Moreover, this gradient is 8 to 10 times larger than the best tip gradient demonstrated previously in a magnet-on-cantilever MRFM experiment [53].

That such a large gradient has been achieved in a magnet-on-cantilever MRFM experiment is an exciting advance. The tip-field gradient produced by these cobalt nanomagnets has been calculated to be sufficient to detect single electron spins by ESR-MRFM with only a few minutes of signal averaging per point, which would enable three-dimensional mapping of the positions of multiple nitroxide spin radicals on uniformly-labeled proteins to determine their tertiary structure [30]. The field gradients produced by the cobalt-tipped cantilevers also are large enough to enable the characterization of as-fabricated semiconductor devices where, for example, Stark shifts of magnetic resonance transitions [45, 168, 169] allow the measurement of internal electric fields in semiconductor devices containing quadrupolar nuclei [47, 170, 171]. Additionally, moving the sample off-cantilever is anticipated to allow the full battery of cryoelectron microscopy (cryo-EM) sample preparation techniques [49, 50] to be applied in an MRFM experiment to prepare fragile biomolecules, macromolecular complexes, and thin sections of biological material. In contrast with cryo-EM, MRFM can accommodate micrometer-thick samples, and image contrast can be achieved by isotopic labeling, which is non-perturbative. MRFM's present resolution of 4 to 10 nm is competitive with what has been demonstrated in electron cryo-tomography (cryo-ET) studies of subcellular structures [11], organelles [172], neuronal synapses [9], and viral synapses [10] where studying a single copy of the structure is essential. When multiple precisely identical copies of

a highly symmetric and large macromolecule or macromolecular complex are available, cryo-EM with single particle analysis can achieve near-atomic resolution. Frustratingly, broad classes of trafficking agents such as exosomes [23] and membrane proteins remain difficult to study by cryo-EM because the associated macromolecules or macromolecular complexes are disordered, have molecular weights less than 100 kDa [24], or simply do not retain their native structure in aqueous solution. With only slightly improved resolution, we anticipate that the type of magnet-on-tip magnetic resonance force microscope demonstrated here can begin to contribute to understanding such important biological nanostructures.

To continue to improve sensitivity in MRFM experiments, it will be critical to reduce the nanomagnet leading edge damage layer. Simulations based on the experimental MRFM data presented in Chapter 5 indicated that if all nanomagnet damage is localized at the magnet leading edge, there could be up to 51 nm of leading edge damage. These simulation results contrast with the less than 10 nm of damage estimated using XPS with depth profiling. It is expected that the damage to the cobalt nanomagnet studied in Chapter 5 was due to a combination of oxidation of all unprotected cobalt surfaces to a depth of 10 nm, surface roughness on the magnet leading edge, roughness of the sample surface, and a protrusion of the titanium underlayer past the cobalt leading edge. To decrease the spacing between the magnetic material in the nanomagnet and the sample surface — and thus increase the achievable tip-field gradient — it will be essential to determine the precise extent and sources of leading edge damage of individual nanomagnets in future experiments.

Characterization techniques are available to assess elemental degradation of nanoscale magnetic particles. The use of scanning transmission electron microscopy (STEM) and electron energy loss spectroscopy (EELS) to visualize and determine the elemental composition of the nanomagnets with nanometer-scale resolution was demonstrated in Chapter 2. STEM could be used in future work to determine the extent of leading-edge roughness and assess

whether titanium extended past the leading edge of the magnetic material. EELS is capable of obtaining side-on or top-down two-dimensional maps of the elemental composition of the nanomagnets. Energy-dispersive X-ray spectroscopy (EDS) could rapidly determine contaminant surface elements of sub-100 nm wide nanomagnets [91]. Additionally, Auger electron spectroscopy combined with depth profiling could be used to reconstruct a full three-dimensional map of the elemental composition of a nanomagnet with nanometer-scale resolution [173].

Once sources of damage contributing to increased tip-sample separation are understood, the magnet-tipped chip fabrication protocol can be improved to maximize the magnetization at the nanomagnet leading edge. Surface roughness of the nanomagnet could be reduced by depositing the magnetic material at a faster rate to decrease the grain size [174]. If damage is attributed to oxidation, the introduction of barrier layers could be reconsidered. A capping layer coating the leading edge side wall of the nanomagnet could be used to protect the nanomagnet leading edge against oxidation or other degradation of the magnetic material. Since the nanomagnets are fabricated off-cantilever, protective encasement layer processing does not need to be compatible with the constraints of cantilever processing; the magnet-tipped chips could be fully coated with the films used to encase the nanomagnets, as long as the protective layers only extend 2-5 nm past the leading edge of the nanomagnet.

In order to avoid oxidation of the leading edge of the nanomagnet, the magnet side walls must be protected prior to exposure to an atmospheric environment. The ideal process would involve electron beam evaporation of nanomagnets and ALD deposition of a capping layer material in tandem without breaking vacuum. However, the availability of such a system is not known. A potentially viable alternative would be to deposit magnetic material in a trench that is encased with a protective coating. A proposed protocol involves: (1) creating a nanomagnet-sized trench in an easily-etchable sacrificial material such as silicon dioxide

or silicon nitride; (2) coating the trench with a thin layer (2-5 nm thick) of an etch-resistant material that also acts as an oxidation barrier, possibly ALD tantalum oxide or a bilayer of an ALD alumina oxidation barrier with an etch-resistant ALD tantalum nitride outer shell; (3) conformally depositing the magnetic material inside the trench, likely using sputtering; (4) using chemical mechanical polishing (CMP) to remove the excess magnetic material on the wafer; and (5) etching the sacrificial material. This procedure could fabricate thinly-encased nanomagnets with leading edges that are fully protected against oxidation damage. Although a few nanometers of the unprotected top surface of the nanomagnets would oxidize, the thickness of magnetically inactive material at the nanomagnet leading edge would only be the 2-5 nm thick protective film. Thus, the leading-edge magnetically inactive layer could be reduced and the achievable tip-field gradient could be significantly improved. Extensive process development would be required to implement this protocol, including the fabrication of nanoscale trenches with highly vertical side walls and the employment of a CMP slurry that does not damage the magnetic material.

An alternative method to create a nanomagnet with limited leading edge damage would be to revisit the use of serial focused ion beam (FIB) milling to selectively remove the damaged portion of the nanomagnet leading edge. Fabricating the nanomagnets on magnet-tipped chips would be advantageous since the magnets could be rigidly fixed on the silicon chips during FIB milling. Conventional FIB milling causes damaging gallium ion implantation; however, new low-energy polishing techniques have been used with less than 2 nm of damage to the side wall [118]. Damage to the remainder of the nanomagnet could be minimized by protecting the top surface with platinum. FIB milling with alternative ion sources, such as helium, could also be considered [175]. Since helium ions are lighter than gallium ions, helium ions channel through some materials without disrupting the crystal structure or inducing damage; the extent of magnetization damage induced by helium ion beam (HIM) milling of polycrystalline nickel is not known and would need to be assessed, but the results

presented in Ref. 175 on high-resolution HIM milling of nickel are promising. Although this method would lead to device-to-device variations and would require additional processing time per nanomagnet, minimizing the nanomagnet leading edge damage layers using HIM milling could provide valuable proof-of-concept information about the upper bound for the achievable tip-field gradient.

In conclusion, the work in this thesis has significantly advanced the capabilities of magnet-on-cantilever MRFM and has positioned the field of MRFM to study exciting new classes of biological and materials-based samples. The newly-developed magnet-tipped chip protocol allows for the high-yield fabrication of high-gradient cobalt nanomagnets. It is projected that these cobalt nanomagnets can be used in magnet-on-cantilever MRFM experiments to detect single electron spins and achieve few-nanometer resolution imaging of nuclear spins. Additionally, the magnet-tipped chip protocol will enable rapid prototyping of new fabrication methods to protect nanomagnet side walls, minimize leading edge damage, and facilitate further enhancement of the magnetic tip-field gradient.

APPENDIX A

PROTOCOL FOR THE FABRICATION OF NANOMAGNET-TIPPED SILICON CHIPS

In this Appendix, details are provided for the fabrication of nanomagnet-tipped chips. All work was conducted at the Cornell NanoScale Science and Technology Facility (CNF).

Soitec silicon-on-insulator (SOI) wafers (Soitec product number G4P-005-02) were used for fabricating the magnet-tipped chips. The wafers had a device silicon thickness of 340 nm, a buried oxide (BOX) thickness of 400 nm, and a silicon handle wafer thickness of 500 µm. The device silicon resistivity was 14 to 22 Ω cm, corresponding to a boron dopant concentration of 6 to 9×10^{14} cm^{-3}.

Solvents were obtained from Fisher Scientific or J. T. Baker and used as received; all solvents met either ACS grade or electronic grade requirements. Electron beam (e-beam) lithography resists were supplied by Microchem. All metals were from Kurt J. Lesker Company. The crucibles of magnetic materials were stored separately from the common-access crucibles to ensure against contamination.

When spinning all e-beam resists, the ramp rate was 1000 rpm. All e-beam lithography steps were conducted using either a JEOL JBX-6300FS or JEOL JBX-9300FS 100 kV Electron Beam Lithography System. The systems could be used interchangeably, but alignment was most straight-forward if the same slot on the same tool was used consistently for a given wafer. On the JEOL 9300, a current of 2 nA was used. On the JEOL 6300, the fourth lens mode was used with a current of 1 nA. In the following sections, the names of the CAD files used on the CNF JEOL 6300 in the directory \job\user\longenecker\201106_mag_chips are listed; these files can be accessed by any CNF user and can be used as references for the creation of the appropriate files for alignment marks and the magnet-tipped chip layers.

Assessment of the yield of individual steps and the overall fabrication process was conducted using either the Zeiss Supra or Zeiss Ultra High Resolution Field Emission scanning electron microscopes with beam voltages of 2 kV or 5 kV.

A.1 Wafer Layout

Four sets of e-beam alignment marks were fabricated on each wafer; three sets were for the three aligned e-beam lithography layers of the magnet-tipped chip process, and the fourth set of alignment marks was spare. Each set of alignment marks consisted of both global and local marks. All alignment marks consisted of 100 nm of platinum, were "+"-shaped, and had a line width of 3 µm. Global marks, which were 2 mm long, were used to locate the center of the wafer and adjust the rotational alignment. Local marks, which were 60 µm long, were used to find the center of each die of magnet-tipped chips. An example of the wafer layout, including one set of global marks, blue squares to designate the magnet-tipped chip dies, and one set of local marks, is shown in Figure A.1.

Global P and Q marks were centered vertically on the wafer and placed laterally on the far left and right sides. The sets of four global marks were spaced in a 2×2 grid with 2 mm separations in each direction. The P and Q marks were approximately 70 mm apart. Sets of local marks were set at the corners of each chip, totaling 16 local marks per set. The marks were spaced 8.0 mm, 7.5 mm, or 7.0 mm from the center of the die for the first, second, or third layers of the process, respectively. The four dies of magnet-tipped chips were arranged in a 2×2 grid centered with the center of the wafer and spaced apart from each other in x and y by 30 mm.

The precise locations of all marks are detailed in Table A.1. Note that the positions are denoted based on the calibration sequence they are used with on the JEOL systems; the AGCRG locations are listed in the stage coordinate system, where the top-left corner

Calibration		Etch slit layer	Magnet layer	Etch pit layer	Extra layer
AGCRG (JEOL 9300) [a]	x	(A) 154; (B) 64	(A) 154; (B) 64	(A) 156; (B) 66	(A) 156; (B) 66
	y	(A) 64; (B) 174	(A) 66; (B) 176	(A) 64; (B) 174	(A) 66; (B) 176
AGCRG (JEOL 6300)	x	69,000	69,000	71,000	71,000
	y	84,000	86,000	84,000	86,000
SETWFR					
Material center offset	x	stage - AGCRG x	stage - AGCRG x	stage - AGCRG x	stage - AGCRG x
	y	AGCRG y - stage	AGCRG y - stage	AGCRG y - stage	AGCRG y - stage
P-point	x	-36,000	-36,000	-34,000	-34,000
	y	1,000	-1,000	1,000	-1,000
Q-point	x	36,000	36,000	34,000	34,000
	y	1,000	-1,000	1,000	-1,000
CHIPAL					
Center	x	15,000	15,000	15,000	15,000
	y	15,000	15,000	15,000	15,000
Marks	x/y	±8,000	±7,500	±7,000	±6,500

Table A.1: Positions of the e-beam lithography global and local alignment marks written during the alignment mark step and used for the subsequent aligned magnet-tipped chip fabrication layers. The numbers are organized based on the calibration sequence for which they are used. The AGCRG calibration, which sets the gain by measuring the P-point global mark, uses the stage coordinate system and thus has different values based on which slot in the JEOL 9300 or JEOL 6300 systems is used. The SETWFR calibration, which is used to set the center and rotation of the wafer, and the CHIPAL calibration, which is used to locate the local marks and find the center of each die, use the material coordinate system and are the same regardless of which tool or slot is used. Within the SETWFR calibration, the term "stage" refers to the stage position of the mark as viewed in the JEOL software and the terms "AGCRG x" and "AGCRG y" refer to the appropriate AGCRG values listed in the corresponding section of this table. All values have units of micrometers.

[a] Numbers in these rows must be multiplied by 1000 when input into the tool software.

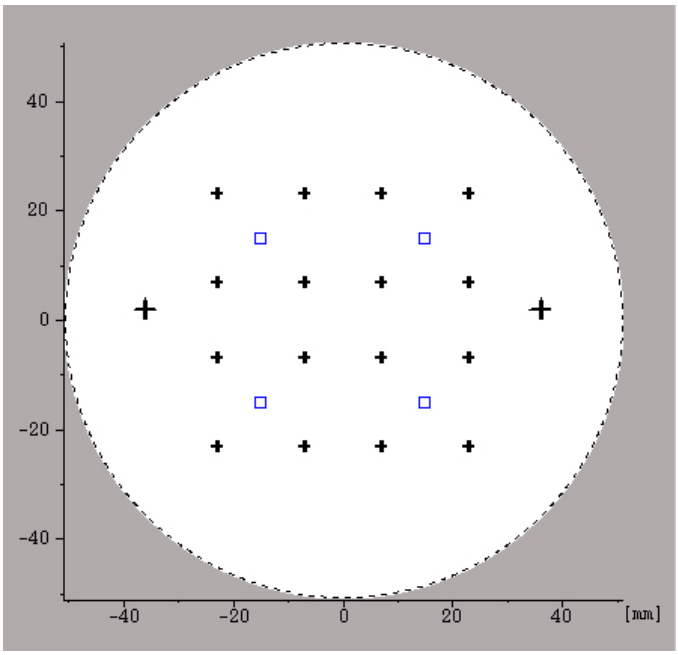

Figure A.1: Magnet-tipped chip example wafer layout, as rendered by the ACHK program in the JEOL software, for the chip design and release (etch slits) layer. The P-mark and Q-mark for this layer are the large crosses shown near the left and right edges of the wafer, respectively; the P-mark is located at (x,y) coordinates (-36 mm, 1 mm) and the Q-mark is located at (+36 mm, 1 mm). The four blue squares designate the four magnet-tipped chip dies, which are centered at ($\pm$15 mm, $\pm$15 mm). The small crosses designate the chip marks. For this layer, the local marks are 8 mm in each x and y from the center of each magnet-tipped chip die.

of the wafer is (0,0) and the positive directions move to the right and downward, whereas the SETWFR (for global marks) and CHIPAL (for local marks) locations are listed in the material coordinate system, in which the center of the wafer is (0,0) and the positive directions are to the right and upward. Note also that on the JEOL 9300 system, the 4" chuck has two slots, "A" (stage-coordinate center is $x = 190,000\,\mu$m and $y = 65,000\,\mu$m) and "B" (stage-coordinate center is $x = 100,000\,\mu$m and $y = 175,000\,\mu$m), whereas the JEOL 6300 system has two identical single-slot 4" chucks, each with their stage-coordinate center at $x = 105,000\,\mu$m and $y = 85,000\,\mu$m. In Table A.1, the AGCRG positions are calculated by $x =$ (x center position) + (P-point value) and $y =$ (y center position) $-$ (Q-point value).

A.2 Alignment Marks

1. Resist bilayer

   In the e-beam lithography hood:

   (a) 8% 495,000 MW PMMA in anisole, spin 70 seconds at 3000 rpm, bake at 170°C for 20 minutes

   (b) 2% 950,000 MW PMMA in methyl isobutyl ketone (MIBK), spin 60 seconds at 4000 rpm, bake at 170°C for 15 minutes

2. E-beam lithography patterning

   (a) Use the appropriate alignment mark file in the JEOL; Longenecker's file was called "jl_marks.sdf". The global and local marks were stored permanently in the JEOL pattern files.

   (b) Run the basic calibration sequence, including CURRNT, INITBE (3×), INITAE (3×), SFOCUS, PDEFBE, SUBDEFBE, and DISTBE. Running HEIMAP is not necessary if virtual marks are used.

   (c) Expose the wafer at an electron dose of 1800 μC cm^{-2}.

3. Developing the wafer

   Soak the exposed wafer in premixed 1:3 (v/v) MIBK:IPA for 75 seconds. Spray with IPA and dry with the nitrogen gun.

4. Descuming the wafer

   In the Glen 1000 Resist Strip system, center the wafer on shelf B. Use Program 3, 100 W for 60 seconds.

5. Electron gun evaporation: Ti/Pt (5/100 nm)

(a) Check the life of the quartz crystal and replace if the conditions specified in the instrument's manual are exceeded. Load titanium (adhesion layer) and platinum (contrast material for e-beam lithography marks) targets.

(b) For titanium: Ramp the power to 5% and wait a few minutes for the crucible to warm up. Continue to ramp at approximately 1% per minute until the rate is 2 Å/s (approximately 10% power). Open the shutter and deposit the 50 Å adhesion layer. Close the shutter and ramp the power back down at approximately 1% per minute.

(c) For platinum: Ramp the power to 5% and wait for the system to warm up the new target. Continue to ramp at approximately 1% per minute until a rate of 2 to 2.5 Å/s is reached (anywhere from 15% to 25% power, depending on the amount of dephasing of the electron beam). Continuously check the lateral and longitudinal sweep, especially as the power exceeds 15%. Open the shutter and deposit 100 nm of platinum. Close the shutter and ramp the power down at 5% per minute.

(d) Allow the chamber to cool for 10 minutes before venting the system and removing the wafer.

6. Resist liftoff

(a) Mix a 1:1 (v/v) solution of methylene chloride and acetone.

(b) Sonicate the wafer in the methylene chloride and acetone solution for at least 10 minutes, and for at least 1 minute after all platinum has detached from the wafer surface.

(c) Rinse the wafer with IPA as you remove the wafer from the solution, making sure that all excess metal specks are removed.

(d) Quickly dry the wafer with the nitrogen gun.

(e) Pour waste in the appropriate waste bottle. Rinse the container 3× with IPA (pour into waste container) before rinsing 3× with water (pour down drain).

A.3 Chip Design and Release

1. Resist layer

   8% 495,000 MW PMMA in anisole, spin 75 seconds at 2000 rpm, bake at 170°C for 20 minutes.

   Note that if 8% 495,000 MW PMMA in anisole is not available, a suitable replacement is:

   11% 495,000 MW PMMA in anisole, spin 70 seconds at 4000 rpm, bake at 170°C for 20 minutes.

2. E-beam lithography patterning

   (a) Use the appropriate alignment mark file in the JEOL; Longenecker's file was called "etchslits_201106.sdf".

   (b) Run the basic calibration sequence, including CURRNT, INITBE (3×), INITAE (3×), SFOCUS, PDEFBE, SUBDEFBE, and DISTBE. Running HEIMAP is not necessary if virtual marks are used.

   (c) Run AGCRG, SETWFR, and CHIPAL using the appropriate values in Table A.1. For SETWFR, all sweep positions and sweep widths were set to 100 µm. For CHIPAL, the sweep position was set to 15 µm and the sweep width was set to 10 µm.

   (d) If the global marks cannot be found automatically using AGCRG, locate the marks manually and enter the offset between the expected position and actual position in the "material center offset" positions in SETWFR (using the offset

calculation guide in Table A.1). Also enter the offset values in the appropriate jdf file. Offsets do not affect the CHIPAL calibration. On the JEOL 6300, offsets of up to 1 mm were observed and manual alignment was routinely needed. On the JEOL 9300, offsets were minimal and the global marks were almost always found automatically.

(e) Expose the wafer at an electron dose of 1600 µC cm^{-2}.

3. Developing the wafer

   Soak the exposed wafer in premixed 1:3 (v/v) MIBK:IPA for 75 seconds. Spray with IPA and dry with the nitrogen gun.

4. Descuming the wafer

   In the Glen 1000 Resist Strip system, center the wafer on shelf B. Use Program 3, 100 W for 60 seconds.

5. Etching the etch slits to define the chip bodies

   (a) Use the Oxford PlasmaLab 80+ RIE System # 2 (commonly called the Oxford 82).

   (b) Clean the chamber for 10 minutes using the standard oxygen clean recipe (50 sccm O_2, 150 W, 60 mTorr).

   (c) Stop the automatic vent cycle, evacuate the chamber to base pressure, and season the chamber for five minutes using the sulfur hexafluoride and oxygen (SF_6:O_2) recipe (30 sccm SF_6, 10 sccm O_2, 200 W, 200 mTorr).

   (d) Vent the chamber and load the wafer. Center the wafer on the substrate electrode and fix it in place using clean quartz pieces.

   (e) Etch the device layer silicon on the wafer for 40 seconds using the same SF_6:O_2 recipe as Step 5(c).

6. Visual inspection of etch completion

   After the slits have been etched, the underlying green BOX SiO_2 layer is visible. The complete removal of the silicon can be confirmed using an optical microscope by checking for a color change from gray to green in these exposed regions.

7. Resist liftoff

   (a) Mix a 1:1 (v/v) solution of methylene chloride and acetone.

   (b) Sonicate the wafer in the methylene chloride and acetone solution for 10 minutes.

   (c) Rinse the wafer with IPA as it is removed from the solution and quickly dry the wafer with the nitrogen gun.

8. Suspension of the chips by BOE etching

   (a) Fill one plastic tub 1/3 full with 6:1 buffered oxide etch (BOE). Fill two additional plastic tubs 3/4 full with deionized water.

   (b) Soak the wafer in BOE for 50 minutes.[1]

   (c) Quickly transfer the wafer to the first water bath and soak for 30 minutes to flush the BOE from the suspended region under the chips.

   (d) Transfer the wafer to the second water bath and carry the tub to an IPA-compatible spinner.

   (e) Transfer the wafer to an IPA bath.

   (f) Spin-dry the wafer for 75 seconds at 2000 rpm. Spin drying successfully dries the wafer while preventing stiction of the chips.

9. Visual inspection of suspension

   Release chips (Section 3.7.3) were added to the dies so that it would be easy to confirm

[1]The etch has been calibrated for a BOE bath without a stir bar; adding a stir bar may decrease the required etch time.

completion of the suspension etch. If the chips are fully suspended, the similarly-designed release chips become free-standing and are absent or moved on the silicon surface. Optical microscopy can be used to assess the status of the release chips.

A.4 Nickel or Cobalt Nanomagnet Deposition

1. Resist bilayer

   For nanomagnets up to 200 nm thick:

   (a) 8% 495,000 MW PMMA in anisole, spin 70 seconds at 3000 rpm, bake at 170°C for 20 minutes

   (b) 2% 950,000 MW PMMA in MIBK, spin 60 seconds at 4000 rpm, bake at 170°C for 15 minutes

2. E-beam lithography patterning

   (a) Use the appropriate alignment mark file in the JEOL; Longenecker's file was called "mags_201106.sdf". The guide boxes — which were centered on the dies, were 2 mm in length, and had line widths of 2 µm — were used to more easily locate and focus the magnet-tipped chips during SEM analysis.

   (b) Run the basic calibration sequence, including CURRNT, INITBE (3×), INITAE (3×), SFOCUS, PDEFBE, SUBDEFBE, and DISTBE. Running HEIMAP is not necessary if virtual marks are used.

   (c) Run AGCRG, SETWFR, and CHIPAL using the appropriate values in Table A.1. For SETWFR, all sweep positions and sweep widths were set to 100 µm. For CHIPAL, the sweep position was set to 15 µm and the sweep width was set to 10 µm.

(d) If the global marks cannot be found automatically using AGCRG, locate the marks manually and enter the offset between the expected position and actual position in the "material center offset" positions in SETWFR (using the offset calculation guide in Table A.1). Also enter the offset values in the appropriate jdf file.

(e) Expose the wafer at an electron dose of 1600 µC cm^{-2}.

3. Developing the wafer

(a) Soak the exposed wafer in premixed 1:3 (v/v) MIBK:IPA for 75 seconds.

(b) Use a squirt bottle to gently spray the wafer with IPA. Avoid spraying liquid directly over the suspended chips; instead spray only in the center and along the edges of the wafer.

(c) Spin-dry the wafer for 75 seconds at 2000 rpm. Since the wafer now has suspended chips, it must be handled delicately and drying the wafer with the nitrogen gun is not recommended. This alternate spin-drying procedure is used to gently dry the wafer.

4. Descuming the wafer

In the Glen 1000 Resist Strip system, center the wafer on shelf B. Use Program 3, 100 W for 60 seconds.

5. Electron gun evaporation: Ti/Ni/Pt (5/100/10 nm) or Ti/Co/Pt (5/100/10 nm)

(a) Check the life of the quartz crystal and replace if the conditions specified in the instrument's manual are exceeded. Loading a witness sample is recommended; witness samples can be used to confirm the total film thickness after deposition. The witness samples used in this work, which were freely available in the CNF, were small silicon chips with $\sim$ 1 mm wide lines (with a pitch of $\sim$ 2 mm) that were

patterned in photolithography resist. Load titanium (adhesion layer), platinum (capping layer), and nickel or cobalt (magnetic layer) targets. It is recommended that crucibles containing magnetic material be stored separately from common-access crucibles to prevent any chance of contamination.

(b) For titanium: Ramp the power to 5% and wait a few minutes for the crucible to warm up. Continue to ramp at approximately 1% per minute until the rate is 2 Å/s (approximately 10% power). Open the shutter and deposit the 50 Å adhesion layer. Close the shutter and ramp the power back down at approximately 1% per minute.

(c) For nickel: Ramp the power to 5% and wait for the system to warm up the new crucible. Continue to ramp 0.5% per minute until a rate of 2.5 Å/s (approximately 12% power). Prevent spitting of the material by reducing the power 0.5% and soaking the material for at least 3 minutes if spitting is observed. Consistently monitor the lateral and longitudinal sweep, especially since nickel deflects the beam differently as it becomes molten. Open the shutter and deposit 100 nm of material. Close the shutter and ramp the power down at 1% per minute.

(d) For cobalt: Ramp the power to 5% and wait for the system to warm up the new crucible. Continue to ramp 0.5% per minute until a rate of 2.5 Å/s (approximately 11% power). Prevent spitting of the material by reducing the power 0.5% and soaking the material for at least 3 minutes if spitting is observed. Consistently monitor the lateral and longitudinal sweep, especially since cobalt deflects the beam differently as it becomes molten. Open the shutter and deposit 100 nm of material. Close the shutter and ramp the power down at 1% per minute.

(e) For platinum: Ramp the power to 5% and wait for the system to warm up the new target. Continue to ramp at approximately 1% per minute until a rate of 2 to 2.5 Å/s is reached (anywhere from 15% to 25% power, depending on the

amount of dephasing of the electron beam). Continuously check the lateral and longitudinal sweep, especially as the power exceeds 15%. Open the shutter and deposit 10 nm of platinum. Close the shutter and ramp the power down at 5% per minute.

(f) Allow the chamber to cool for at least 10 minutes and until the chamber temperature is at or below room temperature of 68°F prior to venting and removing the wafer.

6. Resist liftoff

(a) Mix a 1:1 (v/v) solution of methylene chloride and acetone.

(b) Sonicate the wafer in the methylene chloride and acetone solution for at least 10 minutes, and for at least 1 minute after all material has been stripped off of the wafer surface. Sonication has been shown to minimize rough edges around the nanomagnets that are likely due to magnetic material propagating up the resist side walls during deposition.

(c) Rinse the wafer using a squirt bottle containing IPA as the wafer is removed from the solution, making sure that all excess metal specks are removed. Avoid spraying liquid directly over the suspended chips; instead spray only in the center and along the edges of the wafer.

(d) Spin-dry the wafer for 75 seconds at 2000 rpm.

A.5 Silicon Underetch of U-Shaped Etch Pits

1. Resist layer

8% 495,000 MW PMMA in anisole, spin 75 seconds at 2000 rpm, bake at 115°C for 40

minutes.

Note that if 8% 495,000 MW PMMA in anisole is not available, a suitable replacement is:

11% 495,000 MW PMMA in anisole, spin 70 seconds at 4000 rpm, bake at 115°C for 40 minutes.

2. E-beam lithography patterning

   (a) Use the appropriate alignment mark file in the JEOL; Longenecker's file was called "pits_201106.sdf".

   (b) Run the basic calibration sequence, including CURRNT, INITBE (3×), INITAE (3×), SFOCUS, PDEFBE, SUBDEFBE, and DISTBE. Running HEIMAP is not necessary if virtual marks are used.

   (c) Run AGCRG, SETWFR, and CHIPAL using the appropriate values in Table A.1. For SETWFR, all sweep positions and sweep widths were set to 100 µm. For CHIPAL, the sweep position was set to 15 µm and the sweep width was set to 10 µm.

   (d) If the global marks cannot be found automatically using AGCRG, locate the marks manually and enter the offset between the expected position and actual position in the "material center offset" positions in SETWFR (using the offset calculation guide in Table A.1). Also enter the offset values in the appropriate jdf file.

   (e) Expose the wafer at an electron dose of 1600 µC cm^{-2}.

3. Developing the wafer

   (a) Soak the exposed wafer in premixed 1:3 (v/v) MIBK:IPA for 75 seconds.

   (b) Use a squirt bottle to gently spray the wafer with IPA. Avoid spraying liquid

directly over the suspended chips; instead spray only in the center and along the edges of the wafer.

(c) Spin-dry the wafer for 75 seconds at 2000 rpm.

4. Descuming the wafer

   In the Glen 1000 Resist Strip system, center the wafer on shelf B. Use Program 3, 100 W for 60 seconds.

5. Etching the etch slits to define the chip bodies

   (a) Use the Oxford PlasmaLab 80+ RIE System # 2 (commonly called the Oxford 82).

   (b) Clean the chamber for 10 minutes using the standard oxygen clean recipe (50 sccm O_2, 150 W, 60 mTorr).

   (c) Stop the automatic vent cycle, evacuate the chamber again, and season the chamber for five minutes using the sulfur hexafluoride and oxygen (SF_6:O_2) recipe (30 sccm SF_6, 10 sccm O_2, 200 W, 200 mTorr).

   (d) Vent the chamber and load the wafer. Center the wafer on the substrate electrode and fix in place using clean quartz pieces.

   (e) Etch the device layer silicon on the wafer for 40 seconds using the same SF_6:O_2 recipe as Step 5(c). The etch time has been calibrated to create a 300 nm overhang of the nanomagnets.

6. Visual inspection of etch completion

   During the U-shaped pit etching, pits are also dug into the top few micrometers of the handle silicon layer. Visual inspection with an optical microscope can provide tentative confirmation that the etch has been completed, but thorough characterization of the overhang can only be achieved by SEM analysis.

7. Resist liftoff

   (a) Mix a 1:1 (v/v) solution of methylene chloride and acetone.

   (b) Sonicate the wafer in the methylene chloride and acetone solution for 10 minutes.

   (c) Rinse the wafer with a squirt bottle containing IPA as the wafer is removed from the solution. Avoid spraying liquid directly over the suspended chips; instead spray only in the center and along the edges of the wafer.

   (d) Spin-dry the wafer for 75 seconds at 2000 rpm.

APPENDIX B

FOCUSED ION BEAM PROCESS FOR LIFT-OUT OF MAGNET-TIPPED CHIPS AND ATTACHMENT TO CANTILEVERS

In this Appendix, details are provided for the protocol used to remove completed magnet-tipped chips from their substrate and attach them to separately-fabricated attonewton-sensitivity cantilevers. The development of the magnet-tipped chips is discussed in Chapter 3 and the fabrication protocol is detailed in Appendix A. A detailed description of an integrated magnet-on-cantilever fabrication protocol is provided in Appendix A of Ref. 91; to fabricate blank cantilevers, start with Section A.5.

The focused ion beam (FIB) lift-out and attachment process was conducted using an FEI Strata 400 STEM FIB DualBeam system with both an electron beam and a gallium-ion beam. Images of the original and revised FIB process flows discussed in Chapter 3 are shown in Figures 3.5 and 3.8, respectively; note that in both figures, the electron beam images were rotated by 180° so that all images were viewed with the magnet-tipped chips oriented in the same direction. The dual-beam FIB instrument used for this work is located in the Cornell Center for Materials Research transmission electron microscopy facility. The ion beam is oriented at a 52° angle with respect to the electron beam. The stage can be tilted between 0° and 52° degrees to allow one beam or the other to be aligned perpendicular to the sample surface. In the procedure described in this Appendix, all work (other than setting the eucentric height) is done with the stage at 0°, such that the sample is viewed top-down with the electron beam and side-on with the ion beam.

It should be noted that this set of directions is meant to be used in conjunction with the tool's manual. The following directions include all sample-specific details and are meant to

be as complete as possible, but they are not exhaustive.

B.1 Loading in Samples and Setting Up for the Magnet-Tipped Chip Release

1. Start the FIB software and unload the shuttle.
2. Load a magnet-tipped chip onto carbon tape on one FIB mounting holder and blank cantilevers onto a second carbon-tape-coated FIB mounting holder. It is helpful to load all cantilevers parallel to each other, and to load a sacrificial cantilever in the center for setup work. Mount the holders in the shuttle, insert the shuttle into the FIB loadlock, and load the shuttle onto the FIB stage.
3. Often the Omniprobe probe needle, which is used to lift out magnet-tipped chips and attach them to cantilevers, has been dulled by previous use and needs to be replaced. If the probe needle needs to be exchanged, the main FIB chamber must be vented. A detailed procedure can be obtained from the tool manager — changing the probe needle requires special training.
4. Once the samples are loaded and the chamber is pumped down, check that the electron beam is set to:
   (a) a voltage of 5 kV, and
   (b) a current of 1.6 nA.
5. Turn on the electron beam and locate the magnet-tipped chip die. Rotate the sample so that the side tabs are at the bottom of the screen in the scanning electron microscopy (SEM) image (for the second-generation and third-generation chips in Section 3.7.1, this means that the magnets/fingers on the chips are pointed towards the left).

6. Locate a chip that is a few chips away from the first region of interest (close enough to be accurate for the desired chip, but far enough away to not damage the critical nanomagnet). Raise the stage to a working distance of 5 mm, adjust the focus and stigmation, and "link the z axis" over the device silicon.

7. Set the eucentric height by confirming that the edge of a feature remains in the same position for tilts $T = 0°$ and $T = 52°$.

8. Check that the ion beam is set to:

   (a) a voltage of 30 kV,

   (b) and a current of 28 pA.

   Note that it is critical to not turn the beam on until the voltage and current have been confirmed; if the values are too high, the region of interest could be completely milled away in under a second. Also, when practicing to focus, stigmate, and find the eucentric height with the ion beam, the ion beam current can be set lower to 9.7 pA; the rate of carbon contamination is slower when using a lower current. However, once the current is set to 28 pA for platinum deposition and milling, it should not be changed since changing the aperture shakes the system and could damage overconstrained systems when the needle is in contact with a sample.

9. Adjust the scan rotation of the ion beam to 180° (the side tab should now be at the top of the ion beam screen and at the bottom of the SEM screen).

10. Once the settings are confirmed, increase magnification (while the beam is still inactive). Note that the magnet-tipped chip being viewed during this step should still be one that is near a chip of interest but should itself not be used. Briefly turn on the beam, decreasing the magnification just enough to confirm that the same region of the chip can be viewed simultaneously by both the electron and ion beams. Quickly adjust the focus and stigmation of the ion beam. Turn the ion beam off.

11. Move to the magnet-tipped chip of interest and repeat Steps 6-8. From here on out, it is essential that the nanomagnet not be viewed by the ion beam to prevent gallium implantation into the magnet.

B.2 Releasing the Magnet-Tipped Chip from the Substrate

1. Confirm that the tilt is set to 0°. Insert the probe needle. Heat and insert the platinum deposition gun. Note that FIB-assisted chemical vapor deposition is used to convert the platinum precursor methylcyclopentadienyl(trimethyl)platinum(IV) into (carbon-containing) platinum metal.
2. Using the SEM mode, center the probe needle laterally over the side tab on the magnet-tipped chip. Lower the needle vertically until it is within a few micrometers of the tab. The steps of raising/lowering the probe needle when in close proximity to the nanomagnet are the most challenging of the entire lift-out and attachment process because the nanomagnet cannot be imaged while moving the probe needle. It is recommended that multiple test trials be conducted to determine the best method for each new user. It is also recommended that one trial test over an unimportant portion of the substrate be conducted each day and that the user watch the z-coordinate stage positions at the start and end of bringing the probe needle into position. These positions should be consistent throughout the day. It is critical to not overshoot how far the needle should be lowered; the needle will immediately bend or break, and excessive driving of the needle into the substrate could cause further damage to the sample and/or tool. Once the mock trials have been conducted, one method for successfully bringing the needle into position without imaging the magnet is to image the chip next to the chip of interest (in the direction opposite than the nanomagnet-tipped end of the chip) at high enough magnification to not view any other chips. Lower the probe needle in the z

direction while leaving the ion beam image on. As soon as the top of the needle comes into view, move the stage to the correct chip (and increase the magnification so that the nanomagnet is never viewed), and finish lowering the chip into position.

One additional word of caution with lowering the probe needle is that the x-y lateral motion of the probe needle is coupled to the z motion. As the probe needle is moved towards the top of the SEM screen, the probe moves downward in z; when the probe needle is moved towards the bottom of the screen in the SEM pane, the probe needle moves up in z. Consistently check both screens to monitor the three-dimensional position of the probe needle.

3. Reduce the speed of the probe needle motion and gently bring the probe needle into contact with the side tab of the magnet-tipped chip. Deposit a rectangular patch of platinum to adhere the probe needle to the magnet-tipped chip. When depositing platinum, the rectangular box should have an area corresponding to 6 pA/µm^2; since the current is set to 28 pA, the total area should be approximately 4.5 µm. The thickness of the platinum should be approximately 1 µm.

4. To release the suspended chip from the substrate, mill away the back and side support tethers. The back tether should be milled at an angle, as shown in Figure 3.8. Note that in this figure, the electron beam images have been rotated by 180° for easier viewing.

5. Slowly lift the chip vertically away from the substrate at least 10 µm.

6. To refine the chip shape to promote increased surface area for platinum adhesion once the chip is attached to a cantilever, mill two rectangles into the bottom side of the chip (opposite the side tab) and taper the thickness of the back edge of the chip by approximately 50%, as shown in Figure 3.8(b).

7. The probe needle and platinum deposition gun must be retracted before moving over to the cantilever. First the probe needle must be raised to the starting height (the z

height should be at the top of the ion-beam screen when at the lowest magnification) and then to the load/unload horizontal position (the x-y position should be near the bottom-left corner of the SEM screen when at a magnification of 100×). Once the probe needle has been moved to the proper load/unload position, first retract the probe needle and second retract the platinum deposition gun.

B.3 Adhering the Magnet-Tipped Chip to a Blank Cantilever and Removing the Probe Needle

1. Using the SEM mode, move to the location of the cantilevers and find the desired cantilever on which to mount the magnet-tipped chip. Rotate the stage so that the cantilever is pointing in the same direction as the magnet/finger on the magnet-tipped chip (for the second- and third-generation tips, this means the cantilever should point to the left). Focus and stigmate on the leading edge of the tip and check the eucentric height. When using the ion beam, only image the portion of the cantilever in front of the paddle. Confirm that the cantilever is mostly straight (see Figure 4.2 for images of straight and bent cantilevers), since bent cantilevers are undesired for magnetic resonance force microscopy experiments.
2. Confirm that the tilt is set to $T = 0°$. Insert the probe needle and the platinum deposition gun.
3. Move the probe needle (as done in Section B.2, Step 2) so that the magnet-tipped chip is centered laterally over the cantilever leading edge and hovering vertically a few micrometers above the cantilever surface. Note that it is now critical that the probe needle itself not be imaged by the ion beam any more than necessary while moving it down to the leading edge of the cantilever, since the magnet-tipped cantilever is

attached to the probe needle. In other words, the ion beam should be left off while lowering the needle except for a few low-magnification screen shots. Note also that since the cantilever is suspended 500 µm above the surrounding area, there is less of a chance of crashing the tip. The recommended procedure is to move the tip laterally (in SEM mode) to the region of the screen to the top of the cantilever. Then lower the probe (choose the same speed as for Section B.2, Step 2 and pay close attention to the time it takes to lower it to the appropriate height), capturing a few quick, low-magnification screen shots to confirm the position. As a higher comfort level is gained with this step, fewer screen shots will be needed; three or less screen shots were needed when conducting the work in Chapters 3-5.

4. Lower the speed of the probe needle movement. Confirm that the horizontal alignment is as-desired right before the chip and cantilever come into contact. Gently lower the magnet-tipped chip into contact with the cantilever. If the cantilever is bent slightly down from the chip at the leading edge (the chip and cantilever will always be in contact at the base of the chip), slowly pull up on the probe needle. Surface forces will keep the chip and cantilever "stuck" together for a small vertical window; retracting the probe needle slightly has been shown to improve chip and cantilever alignment.

5. Once the alignment is set, the chip and cantilever can be adhered together. Confirm that the magnet is out-of-range of the ion beam. Check the ion beam focus and stigmation. Define three platinum welding boxes: one angled box used to join the base of the chip with the back of the cantilever, and two additional boxes that are slightly larger than each of the rectangles that were FIB milled into the magnet-tipped chip body in Section B.2, Step 6. Deposit approximately 1 µm of platinum at each position. Note that the platinum adhesion points can be seen in the side-on image in Figure 3.8(c); again, the electron beam images in this figure were rotated by 180° for simplicity.

6. Once the chip is adhered to the cantilever, the chip-on-cantilever system is overconstrained, and the probe needle should be removed as quickly as possible. First define a small, angled silicon etch box to mill the narrow silicon support tether closest to the leading edge of the chip. The milling should only take a few seconds, so monitor it closely. Second, define a straight, relatively thin silicon etch box to mill the remaining portion of the side tab. Again, the milling should be quite quickly. As soon as the chip-on-cantilever is milled free from the side tab and probe needle, the cantilever will likely move downward (see the side-on image in Figure 3.8(d)). This is because the probe needle has been observed to drift upward with time.

7. At this point, the magnet-tipped chip has been mounted onto the cantilever. Slowly move the probe needle so that it is at least 20 µm above the cantilever. Move the ion beam image and/or stage so that the cantilever is well out of view of the beam at reduced magnification.

8. If the same probe needle will be used again for a subsequent sample, clean up the probe needle by increasing the ion beam current above 1 nA. Note that at this current the cantilever must be well out of view of the beam because it would be milled away in seconds even in imaging mode. Focus and stigmate the beam at this new current, mill the chip and platinum adhesion point, and resharpen the tip.

9. Regardless of whether the probe needle will be replaced before being used again, the needle must be moved to the load/unload position before being retracted, as was done in Section B.2, Step 7. The probe needle should first be raised vertically to be at the top of the ion-beam screen when at the lowest magnification, and then the probe needle should be moved laterally to be near the bottom-left corner of the SEM screen when at a magnification of 100×. Once the probe needle has been moved to the proper load/unload position, first retract the probe needle and second retract the platinum deposition gun.

10. If additional samples will be lifted out, return to Section B.1, Step 5. If all FIB work is complete, move on to Section B.4.

B.4 Unloading the Completed Magnet-Tipped Cantilevers

1. Confirm that the probe needle and platinum deposition gun have been retracted. Turn off the platinum deposition gun heater.
2. Turn off the electron beam and ion beam.
3. Unload the shuttle into the loadlock.
4. Vent the loadlock and remove the shuttle.
5. The cantilevers are firmly adhered to the carbon tape on the mounting grid, so removal of the cantilever is a delicate process. Narrow tweezers with rounded ends are recommended. Gently take hold of the cantilever on the sides of the cantilever die. Rotate the cantilever and gently lift up, tilting to one side if necessary to loosen the tape on one side first. Maintain tension on the tweezers as the cantilever begins to release. Once the cantilever is released, it can be stored in a Gel-Pak.
6. It is recommended that the magnet-tipped chip die remain attached to the FIB mounting holder once it is attached; removal would likely break the chip. Store the mounting holder in a dust-proof container.
7. Return the empty shuttle to the loadlock and pump down the loadlock. Follow the remaining shut down procedures for the tool.

"And that's all I have to say about that."

- Forrest Gump

BIBLIOGRAPHY

[1] http://www.rcsb.org/. 1

[2] M. J. Rust, M. Bates, and X. Zhuang, Sub-diffraction-limit imaging by stochastic optical reconstruction microscopy (STORM), Nat. Methods **3**, 793 (2006). 1

[3] E. Betzig et al., Imaging intracellular fluorescent proteins at nanometer resolution, Science **313**, 1642 (2006).

[4] S. T. Hess, T. P. Girirajan, and M. D. Mason, Ultra-high resolution imaging by fluorescence photoactivation localization microscopy, Biophys. J. **91**, 4258 (2006). 1

[5] S. A. Jones, S.-H. Shim, J. He, and X. Zhuang, Fast, three-dimensional super-resolution imaging of live cells, Nat. Methods **8**, 499 (2011). 1

[6] Z. H. Zhou, Atomic resolution cryo electron microscopy of macromolecular complexes, Adv. Protein Chem. Struct. Biol. **82**, 1 (2011). 1

[7] A. Bartesaghi and S. Subramaniam, Membrane protein structure determination using cryo-electron tomography and 3D image averaging, Curr. Opin. Struct. Biol. **19**, 402 (2009). 1

[8] R. I. Koning and A. J. Koster, Cryo-electron tomography in biology and medicine, Ann. Anat. **191**, 427 (2009). 1

[9] R. Fernandez-Busnadiego et al., Insights into the molecular organization of the neuron by cryo-electron tomography, J. Electron Microscopy **60**, S137 (2011). 1, 7

[10] R. L. Felts et al., 3D visualization of HIV transfer at the virological synapse between dendritic cells and T cells, Proc. Natl. Acad. Sci. U.S.A. **107**, 13336 (2010). 1, 7

[11] J. L. S. Milne and S. Subramaniam, Cryo-electron tomography of bacteria: Progress, challenges and future prospects, Nat. Rev. Microbiol. **7**, 666 (2009). 1, 7

[12] C. L. Degen, M. Poggio, H. J. Mamin, C. T. Rettner, and D. Rugar, Nanoscale magnetic resonance imaging, Proc. Natl. Acad. Sci. U.S.A. **106**, 1313 (2009). 1, 1.1, 1.1, 1.1, 1.3, 2.1, 2.2, 2.6, 3.6, 4.4, 5.1, 5.2, 5.2.3, 5.2.4, 5.4, 5.6, 6.1, 6.5, 7

[13] J. A. Sidles, Noninductive detection of single-proton magnetic resonance, Appl. Phys. Lett. **58**, 2854 (1991). 1, 1.1

[14] D. Rugar, C. S. Yannoni, and J. A. Sidles, Mechanical detection of magnetic resonance, Nature **360**, 563 (1992). 1.1

[15] D. Rugar et al., Force detection of nuclear magnetic resonance, Science **264**, 1560 (1994). 1.1

[16] J. A. Sidles et al., Magnetic resonance force microscopy, Rev. Mod. Phys. **67**, 249 (1995). 1.1

[17] S. Kuehn, S. A. Hickman, and J. A. Marohn, Advances in mechanical detection of magnetic resonance, J. Chem. Phys. **128**, 052208 (2008). 1.2.2, 1.2.2, 5.2.1, 5.6

[18] M. Poggio and C. L. Degen, Force-detected nuclear magnetic resonance: Recent advances and future challenges, Nanotechnology **21**, 342001 (2010). 1, 1.1

[19] Z. H. Zhou, Towards atomic resolution structural determination by single-particle cryo-electron microscopy, Curr. Opin. Struct. Biol. **18**, 218 (2008). 1

[20] E. I. Tocheva, Z. Li, and G. J. Jensen, Electron cryotomography, Cold Spring Harbor Perspect. Biol. **2**, a003442 (2010).

[21] E. V. Orlova and H. R. Saibil, Structural analysis of macromolecular assemblies by electron microscopy, Chem. Rev. **111**, 7710 (2011). 1

[22] L. Zhang and G. Ren, IPET and FETR: Experimental approach for studying molecular structure dynamics by cryo-electron tomography of a single-molecule structure, PLoS ONE **7**, e30249 (2012). 1

[23] S. Mathivanan, C. J. Fahner, G. E. Reid, and R. J. Simpson, Exocarta 2012: Database of exosomal proteins, RNA and lipids, Nucl. Acids Res. **40**, D1241 (2011). 1, 7

[24] S. Wu et al., Fabs enable single particle cryoEM studies of small proteins, Structure **20**, 582 (2012). 1, 7

[25] D. Rugar, R. Budakian, H. J. Mamin, and B. W. Chui, Single spin detection by magnetic resonance force microscopy, Nature **430**, 329 (2004). 1, 1.1, 1.3, 2.1, 2.2, 2.6, 5.1, 5.4

[26] P. P. Borbat, A. J. Costa-Filho, K. A. Earle, J. K. Moscicki, and J. H. Freed, Electron spin resonance in studies of membranes and proteins, Science **291**, 266 (2001). 1

[27] O. Schiemann et al., A PELDOR-based nanometer distance ruler for oligonucleotides, J. Amer. Chem. Soc. **126**, 5722 (2004).

[28] P. P. Borbat, J. H. Davis, S. E. Butcher, and J. H. Freed, Measurement of large distances in biomolecules using double-quantum filtered refocused electron spin-echoes, J. Am. Chem. Soc. **126**, 7746 (2004).

[29] S. Y. Park et al., Reconstruction of the chemotaxis receptor-kinase assembly, Nat. Struct. Mol. Biol. **13**, 400 (2006). 1

[30] E. W. Moore et al., Scanned-probe detection of electron spin resonance from a nitroxide spin probe, Proc. Natl. Acad. Sci. U.S.A. **106**, 22251 (2009). 1, 1.1, 1.1, 2.1, 2.2, 5.1, 6.1, 6.4.3, 6.4.3, 6.4.5, 7

[31] Q. Cai et al., Site-directed spin labeling measurements of nanometer distances in nucleic acids using a sequence-independent nitroxide probe, Nucl. Acids Res. **34**, 4722 (2006). 1

[32] P. Z. Qin, K. Hideg, J. Feigon, and W. L. Hubbell, Monitoring RNA base structure and dynamics using site-directed spin labeling, Biochemistry **42**, 67726783 (2003).

[33] Q. Cai et al., Nanometer distance measurements in RNA using site-directed spin labeling, Biophys. J. **93**, 2110 (2007). 1

[34] J. H. Zhang, G. Xiao, R. P. Gunsalus, and W. L. Hubbell, Phosphorylation triggers domain separation in the DNA binding response regulator NarL, Biochemistry **42**, 2552 (2003). 1

[35] C. J. Brabec, M. Heeney, I. McCulloch, and J. Nelson, Influence of blend microstructure on bulk heterojunction organic photovoltaic performance, Chem. Soc. Reviews **40**, 1185 (2011). 1

[36] R. Giridharagopal and D. S. Ginger, Characterizing morphology in bulk heterojunction organic photovoltaic systems, J. Phys. Chem. Lett. **1**, 1160 (2010). 1

[37] M. Chiesa et al., Correlation between surface photovoltage and blend morphology in polyfluorene-based photodiodes, Nano Lett. **5**, 559 (2005).

[38] D. C. Coffey and D. S. Ginger, Time-resolved electrostatic force microscopy of polymer solar cells, Nat. Mater. **5**, 735 (2006).

[39] V. Palermo et al., The relationship between nanoscale architecture and function in photovoltaic multichromophoric arrays as visualized by Kelvin probe force microscopy, J. Am. Chem. Soc. **130**, 14605 (2008).

[40] E. J. Spadafora, R. Demadrille, B. Ratier, and B. Grevin, Imaging the carrier photogeneration in nanoscale phase segregated organic heterojunctions by Kelvin probe force microscopy, Nano Lett. **10**, 3337 (2010).

[41] J. L. Luria et al., Spectroscopic imaging of photopotentials and photoinduced potential fluctuations in a bulk heterojunction solar cell film, ACS Nano **6**, 9392 (2012). 1

[42] S. S. van Bavel and J. Loos, Volume organization of polymer and hybrid solar cells as revealed by electron tomography, Adv. Funct. Mater. **20**, 3217 (2010). 1

[43] B. Xue et al., Vertical stratification and interfacial structure in P3HT:PCBM organic solar cells, J. Phys. Chem. C **114**, 15797 (2010). 1

[44] N. Bloembergen, Theory of the variation of the nuclear quadrupole interaction in covalent bonds with applied electric field, J. Chem. Phys. **35**, 1131 (1961). 1

[45] R. W. Dixon and N. Bloembergen, Electrically induced perturbations of halogen nuclear quadrupole interactions in polycrystalline compounds. I. Phenomenological theory and experimental results, J. Chem. Phys. **41**, 1720 (1964). 7

[46] T. Kushida and K. Saiki, Shift of nuclear quadrupole resonance frequency by electric fields, Phys. Rev. Lett. **7**, 9 (1961).

[47] J. G. Kempf and D. P. Weitekamp, Method for atomic-layer-resolved measurement of polarization fields by nuclear magnetic resonance, J. Vac. Sci. Technol. B **18**, 2255 (2000). 1, 7

[48] H. J. Mamin, C. T. Rettner, M. H. Sherwood, L. Gao, and D. Rugar, High field-gradient dysprosium tips for magnetic resonance force microscopy, Appl. Phys. Lett. **100**, 013102 (2012). 1, 1.1, 1.2.2, 2.1, 2.6, 3.6, 5.1, 5.4, *c*, *d*

[49] R. A. Grassucci, D. J. Taylor, and J. Frank, Preparation of macromolecular complexes for cryo-electron microscopy, Nat. Protoc. **2**, 3239 (2007). 1, 7

[50] M. Marko, C. Hsieh, R. Schalek, J. Frank, and C. Mannella, Focused-ion-beam thinning of frozen-hydrated biological specimens for cryo-electron microscopy, Nat. Meth. **4**, 215 (2007). 1, 7

[51] K. Wago, D. Botkin, C. S. Yannoni, and D. Rugar, Paramagnetic and ferromagnetic resonance imaging with a tip-on-cantilever magnetic resonance force microscope, Appl. Phys. Lett. **72**, 2757 (1998). 1, 1.1, 5.1

[52] B. C. Stipe et al., Electron spin relaxation near a micron-size ferromagnet, Phys. Rev. Lett. **87**, 277602 (2001). 1.1, 1.1, 5.6

[53] H. J. Mamin, R. Budakian, B. W. Chui, and D. Rugar, Detection and manipulation of statistical polarization in small spin ensembles, Phys. Rev. Lett. **91**, 207604 (2003). 1, 1.1, 1.3, 2.1, 2.2, 2.6, 5.1, 5.4, 6.4.3, 7

[54] K. C. Fong, M. R. Herman, P. Banerjee, D. V. Pelekhov, and P. C. Hammel, Spin lifetime in small ensembles of electron spins measured by magnetic resonance force microscopy, Phys. Rev. B **84**, 220405 (2011). 1, 1.3, 5.1, 5.4

[55] S. R. Garner, S. Kuehn, J. M. Dawlaty, N. E. Jenkins, and J. A. Marohn, Force-gradient detected nuclear magnetic resonance, Appl. Phys. Lett. **84**, 5091 (2004). 1.1, 1.1, 1.1, 2.1, 6.4.3

[56] H. J. Mamin, R. Budakian, B. W. Chui, and D. Rugar, Magnetic resonance force microscopy of nuclear spins: Detection and manipulation of statistical polarization, Phys. Rev. B **72**, 024413 (2005). 1, 1.1, 1.1, 1.3, 2.1, 5.1, 5.4, 6.4.3

[57] K. J. Bruland, W. M. Dougherty, J. L. Garbini, J. A. Sidles, and S. H. Chao, Force-detected magnetic resonance in a field gradient of 250000 Tesla per meter, Appl. Phys. Lett. **73**, 3159 (1998). 1, 1.1, 1.3, 5.1, 5.4

[58] J. G. Longenecker et al., High-gradient nanomagnets on cantilevers for sensitivite detection of nuclear magnetic resonance, ACS Nano **6**, 9637 (2012). 1.1, 1.1, 1.2.1, 1.2.1, 1.3, 3.6, 3.9, 5.4, 5.4, 6.4.3, 6.4.3

[59] H. J. Mamin, M. Poggio, C. L. Degen, and D. Rugar, Nuclear magnetic resonance imaging with 90-nm resolution, Nat. Nanotechnol. **2**, 301 (2007). 1.1, 1.1

[60] M. Poggio, C. L. Degen, C. T. Rettner, H. J. Mamin, and D. Rugar, Nuclear magnetic resonance force microscopy with a microwire RF source, Appl. Phys. Lett. **90**, 263111 (2007). 1.1, 4.4, 5.1, 5.2, 5.2.3, 6.1, 6.5

[61] L. Chen, J. G. Longenecker, E. W. Moore, and J. A. Marohn, Long-lived frequency shifts observed in a magnetic resonance force microscope experiment following microwave irradiation of a nitroxide spin probe, in preparation (2012). 1.1, 6.1, 6.4.5

[62] O. Züger and D. Rugar, Magnetic resonance detection and imaging using force microscope techniques, J. Appl. Phys. **75**, 6211 (1994). 1.1, 1.1

[63] K. Wago, O. Züger, R. Kendrick, C. S. Yannoni, and D. Rugar, Low-temperature magnetic resonance force detection, J. Vac. Sci. Technol. B **14**, 1197 (1996).

[64] Z. Zhang, M. L. Roukes, and P. C. Hammel, Sensitivity and spatial resolution for electron-spin-resonance detection by magnetic resonance force microscopy, J. Appl. Phys. **80**, 6931 (1996).

[65] K. Wago et al., Magnetic resonance force detection and spectroscopy of electron spins in phosphorus-doped silicon, Rev. Sci. Instrum. **68**, 1823 (1997). 1.1

[66] T. D. Stowe et al., Attonewton force detection using ultrathin silicon cantilevers, Appl. Phys. Lett. **71**, 288 (1997). 1.1, 1.2.1, 2.1, 2.2, 3.3

[67] H. Mamin and D. Rugar, Sub-attonewton force detection at millikelvin temperatures, Appl. Phys. Lett. **79**, 3358 (2001). 5.2.1

[68] N. E. Jenkins et al., Batch fabrication and characterization of ultrasensitive cantilevers with submicron magnetic tips, J. Vac. Sci. Technol. B **22**, 909 (2004). 1.1, 1.2.1, 2.1, 2.2, 3.3, 3.5, 4.3.2

[69] R. Budakian, H. Mamin, B. Chui, and D. Rugar, Creating order from random fluctuations in small spin ensembles, Science **307**, 408 (2005). 1.1, 2.1

[70] C. L. Degen, M. Poggio, H. J. Mamin, and D. Rugar, Role of spin noise in the detection of nanoscale ensembles of nuclear spins, Phys. Rev. Lett. **99**, 250601 (2007). 1.2, 2.1, 2.6, 5.2.4

[71] F. Xue, D. Weber, P. Peddibhotla, and M. Poggio, Measurement of statistical nuclear spin polarization in a nanoscale GaAs samples, Phys. Rev. B **84**, 205328 (2011). 1.1, 2.1, 2.6

[72] C. P. Slichter, *Principles of Magnetic Resonance, 3rd Ed.*, Springer, New York, 1990. 1.1

[73] O. Züger, S. T. Hoen, C. S. Yannoni, and D. Rugar, Three-dimensional imaging with a nuclear magnetic resonance force microscope, J. Appl. Phys. **79**, 1881 (1996). 1.1

[74] S. H. Chao, W. M. Dougherty, J. L. Garbini, and J. A. Sidles, Nanometer-scale magnetic resonance imaging, Rev. Sci. Instrum. **75**, 1175 (2004).

[75] S. Tsuji, Y. Yoshinari, H. Park, and D. Shindo, Three dimensional magnetic resonance

imaging by magnetic resonance force microscopy with a sharp magnetic needle, J. Magn. Res. **178**, 325 (2006). 1.1

[76] J. G. Kempf and J. A. Marohn, Nanoscale Fourier-transform imaging with magnetic resonance force microscopy, Phys. Rev. Lett. **90**, 087601 (2003). 1.1, 6.1

[77] R. Budakian, NanoMRI using nanowire mechanical resonators, NanoMRI Conference 2012; Ascona, Switzerland, July 22 - 27, 2012. 1.1

[78] N. E. Jenkins, *Expanding the Limits of Magnetic Resonance Force Microscopy*, PhD thesis, Cornell University, 2007. 1.2

[79] S. Kuehn, *Force-Gradient Detected Nuclear Magnetic Resonance and the Origins of Noncontact Friction*, PhD thesis, Cornell University, 2007. 1.2, 6.1

[80] Y. Wang, J. Henry, A. Zehnder, and M. Hines, Surface chemical control of mechanical energy losses in micromachined silicon structures, J. Phys. Chem. B **107**, 14270 (2003). 1.2.1, 3.3

[81] S. A. Hickman et al., Batch-fabrication of cantilevered magnets on attonewton-sensitivity mechanical oscillators for scanned-probe nanoscale magnetic resonance imaging, ACS Nano **4**, 7141 (2010). 1.2.1, 1.2.1, 1.3, 2.1, 2.2, 2.3, 2.1, 2.4, 2.4, 2.5, 2.6, 2.6, 3.1, 3.2, 3.3, 3.5, 3.6, 3.6, 3.8, 3.9, 4.1, 4.3.2, 5.1, 5.2.2, 5.6, 6.1

[82] J. G. Longenecker, E. W. Moore, and J. A. Marohn, Rapid serial prototyping of magnet-tipped attonewton-sensitivity cantilevers by focused ion beam manipulation, J. Vac. Sci. Technol. B **29**, 032001 (2011). 1.2.1, 1.3, 3.6, 5.2.2, 6.1, 6.4.3

[83] B. C. Stipe, H. J. Mamin, T. D. Stowe, T. W. Kenny, and D. Rugar, Noncontact friction and force fluctuations between closely spaced bodies, Phys. Rev. Lett. **87**, 096801 (2001). 1.2.1, 4.3, 5.6

[84] S. Kuehn, R. F. Loring, and J. A. Marohn, Dielectric fluctuations and the origins of noncontact friction, Phys. Rev. Lett. **96**, 156103 (2006). 1.2.1, 2.1, 4.3, 5.6

[85] S. M. Yazdanian, J. A. Marohn, and R. F. Loring, Dielectric fluctuations in force microscopy: Noncontact friction and frequency jitter, J. Chem. Phys. **128**, 224706 (2008). 1.2.1, 4.1, 5.5

[86] S. M. Yazdanian, N. Hoepker, S. Kuehn, R. F. Loring, and J. A. Marohn, Quantifying electric field gradient fluctuations over polymers using ultrasensitive cantilevers, Nano Lett. **9**, 2273 (2009). 1.2.1, 2.1, 5.5

[87] N. Hoepker, S. Lekkala, R. F. Loring, and J. A. Marohn, Quantifying dielectric fluctuations over polymer films using an atomic force microscope, J. Phys. Chem. B **115**, 14493 (2011). 1.2.1, 5.5

[88] E. W. Moore, S.-G. Lee, S. A. Hickman, L. E. Harrell, and J. A. Marohn, Evading surface and detector frequency noise in harmonic oscillator measurements of force gradients, Appl. Phys. Lett. **97**, 044105 (2010). 1.2.1, 6.1

[89] T. N. Ng, N. E. Jenkins, and J. A. Marohn, Thermomagnetic fluctuations and hysteresis loops of magnetic cantilevers for magnetic resonance force microscopy, IEEE Trans. Mag. **42**, 378 (2006). 1.2.2, 2.1, 2.4, 4.1, 4.3.2, 4.4, 5.2.2

[90] S.-G. Lee, E. W. Moore, and J. A. Marohn, A unified picture of cantilever frequency-shift measurements of magnetic resonance, Phys. Rev. B **85**, 165447 (2012). 1.2.2

[91] S. A. Hickman, *Batch Fabrication of Cantilevered Magnetic Nanorods on Attonewton-Sensitivity Silicon Oscillators for Magnetic Resonance Force Microscopy*, PhD thesis, Cornell University, 2010. 1.3, 2.3, 2.3, 2.4, 2.5, 3.1, 3.3, 4.1, 4.3.2, 7, B

[92] T. D. Stowe, T. W. Kenny, D. J. Thomson, and D. Rugar, Silicon dopant imaging by dissipation force microscopy, Appl. Phys. Lett. **75**, 2785 (1999). 2.1

[93] B. C. Stipe, H. J. Mamin, T. D. Stowe, T. W. Kenny, and D. Rugar, Magnetic dissipation and fluctuations in individual nanomagnets measured by ultrasensitive cantilever magnetometry, Phys. Rev. Lett. **86**, 2874 (2001). 2.1, 2.4, 4.1, 4.4, 4.4, 5.2.2, 6.4.3

[94] J. Jang et al., Observation of half-height magnetization steps in Sr_2RuO_4, Science **331**, 186 (2011). 2.1, 3.9

[95] A. C. Bleszynski-Jayich, W. E. Shanks, B. R. Ilic, and J. G. E. Harris, High sensitivity cantilevers for measuring persistent currents in normal metal rings, J. Vac. Sci. Technol. B **26**, 1412 (2008). 2.1

[96] A. C. Bleszynski-Jayich et al., Persistent currents in normal metal rings, Science **326**, 272 (2009). 2.1

[97] S. R. Garner, *Force-Gradient Detection of Nuclear Magnetic Resonance*, PhD thesis, Cornell University, 2005. 2.2, 6.4.1

[98] B. W. Chui et al., Mass-loaded cantilevers with suppressed higher-order modes for magnetic resonance force microscopy, 12th International Conference on Solid-State Sensors and Actuators (Transducers 2003) **2**, 1120 (2003). 2.2

[99] D. Mozyrsky, I. Martin, D. Pelekhov, and P. C. Hammel, Theory of spin relaxation in magnetic resonance force microscopy, Appl. Phys. Lett. **82**, 1278 (2003). 2.2

[100] G. P. Berman, V. N. Gorshkov, D. Rugar, and V. I. Tsifrinovich, Spin relaxation caused by thermal excitations of high-frequency modes of cantilever vibrations, Phys. Rev. B **68**, 094402 (2003). 2.2

[101] M. J. Rooks, S. Wind, P. McEuen, and D. E. Prober, Fabrication of 30-nm-scale structures for electron transport studies using a polymethylmethacrylate bilayer resist, J. Vac. Sci. Technol. B **5**, 318 (1987). 2.3

[102] F. Laermer and A. Schilp, Method of anisotropic etching of silicon, 2003. 2.3, 3.3

[103] P. Lee et al., On the Ni-Si phase transformation with/without native oxide, Microelectron. Eng. **51–52**, 583 (2000). 2.3, 4.2

[104] M. Tinani et al., In situ real-time studies of nickel silicide phase formation, J. Vac. Sci. Technol. B **19**, 376 (2001). 2.3, 2.4

[105] X. Guo et al., Study of nickel silicide formation on Si(110) substrate, Appl. Surf. Sci. **257**, 10571 (2011). 2.3, 2.4

[106] D. Lishan, Personal communication, 2012. 2.3

[107] M. Qin, M. Poon, and C. Yuen, A study of nickel silicide film as a mechanical material, Sens. Actuators, A **87**, 90 (2000). 2.3

[108] L. Dubois and B. Zegarski, The activated adsorption of silane on nickel, Surf. Sci. **204**, 113 (1988). 2.3

[109] T. Gnanavel et al., Ni and W nanotips: Fabrication and characterisation, J. Phys.: Conf. Ser. **126**, 012071 (2007). 2.3

[110] M. J. Graham and M. Cohen, On the mechanism of low-temperature oxidation (23-450°C) of polycrystalline nickel, J. Electrochem. Soc. **7**, 879 (1972). 4.2

[111] S. H. Kulpa and R. P. Frankenthal, Tarnishing of nickel in air at temperatures from 23° to 200°C and relative humidities from ambient to 95%, J. Electrochem. Soc. **124**, 1588 (1977).

[112] M. R. Pinnel, H. G. Tompkins, and D. E. Heath, Oxidation of nickel and nickel-gold alloys in air at 50°–150°C, J. Electrochem. Soc. **126**, 1274 (1979). 2.3, 4.2

[113] E. J. McGuire, Photo-ionization cross sections of the elements helium to xenon, Phys. Rev. **175**, 20 (1968). 2.3

[114] M. Baldé, *Silicide Formation through Diffusion Barriers*, PhD thesis, University of Stellenbosch, 2005. 2.4

[115] O. Ozatay et al., Sidewall oxide effects on spin-torque- and magnetic-field-induced reversal characteristics of thin-film nanomagnets, Nat. Mater. **7**, 567 (2008). 2.4, 3.2

[116] X. Zhang, J. Zhao, A. V. Whitney, J. W. Elam, and R. P. Van Duyne, Ultrastable substrates for surface-enhanced raman spectroscopy: Al_2O_3 overlayers fabricated by atomic layer deposition yield improved anthrax biomarker detection, J. Am. Chem. Soc. **128**, 10304 (2006). 2.4, 3.2

[117] T. N. Ng, *Developments in Force Detection: Integrated Cantilever Magnetometry and Electric Force Microscopy of Organic Semiconductors*, PhD thesis, Cornell University, 2006. 2.4, 4.1

[118] J. Mayer, L. A. Giannuzzi, T. Kamino, and J. Michael, TEM sample preparation and FIB-induced damage, MRS Bull. **32**, 400 (2007). 2.6, 7

[119] U. Hartmann, Magnetic force microscopy, Annu. Rev. Mater. Sci. **29**, 5387 (1999). 2.6

[120] Z. Deng et al., Metal-coated carbon nanotube tips for magnetic force microscopy, Appl. Phys. Lett. **85**, 6263 (2004). 2.6

[121] M. Koblischka, U. Hartmann, and T. Sulzbach, Resolving magnetic nanostructures in the 10-nm range using MFM at ambient conditions, Mater. Sci. Eng. C **23**, 747 (2003). 2.6

[122] M. R. Koblischka, J. D. Wei, C. Richter, T. H. Sulzbach, and U. Hartmann, Advanced cantilevers for magnetic force microscopy and high frequency magnetic force microscopy, Scanning **30**, 27 (2008). 2.6

[123] S. Ingole et al., Assembly and magnetic properties of nickel nanoparticles on silicon nanowires, Appl. Phys. Lett. **94**, 223118 (2009). 2.6

[124] A. Winkler et al., Magnetic force microscopy sensors using iron-filled carbon nanotubes, J. Appl. Phys. **99**, 104905 (2006). 2.6

[125] M. Li et al., Bottom-up assembly of large-area nanowire resonator arrays, Nat. Nanotechnol. **3**, 88 (2008). 2.6

[126] J. Yang, T. Ono, and M. Esashi, Mechanical behavior of ultrathin microcantilever, Sens. Actuators, A **82**, 102 (2000). 2.6

[127] P. Panjan, D. K. Merl, F. Zupanič, M. Čekada, and M. Panjan, SEM study of defects in PVD hard coatings using focused ion beam milling, Surf. Coat. Technol. **202**, 2302 (2008). 3.1

[128] E. Beach, M. Keefe, W. Heeschen, and D. Rothe, Cross-sectional analysis of hollow latex particles by focused ion beam-scanning electron microscopy, Polymer **46**, 11195 (2005). 3.1

[129] A. Grabulov, U. Ziese, and H. Zandbergen, TEM/SEM investigation of microstructural changes within the white etching area under rolling contact fatigue and 3-D crack reconstruction by focused ion beam, Scripta Mater. **57**, 635 (2007). 3.1

[130] S. Abolhassani and P. Gasser, Preparation of TEM samples of metal–oxide interface by the focused ion beam technique, J. Microsc. **223**, 73 (2006).

[131] F. A. Stevie et al., Application of focused ion beam lift-out specimen preparation to TEM, SEM, STEM, AES and SIMS analysis, Surf. Interface Anal. **31**, 345 (2001).

[132] R. M. Langford and A. K. Petford-Long, Preparation of transmission electron mi-

croscopy cross-section specimens using focused ion beam milling, J. Vac. Sci. Technol. A **19**, 2186 (2001). 3.1

[133] E. Fawcett, Spin-density-wave antiferromagnetism in chromium, Rev. Mod. Phys. **60**, 209 (1988). 2, 4.3.2

[134] R. Hanestad, J. W. Butterbaugh, A. ben-Hamida, and I. Gelmi, Stiction-free release etch with anhydrous HF/water vapor processes, Proc. SPIE **4557**, 58 (2001). 3.8

[135] D. Vestyck, Personal communication, 2010. 3.8

[136] G. D. Fuchs et al., Spin-torque ferromagnetic resonance measurements of damping in nanomagnets, Appl. Phys. Lett. **91**, 062507 (2007). 3.9

[137] I.-C. Chen, L.-H. Chen, C. A. Orme, and S. Jin, Control of curvature in highly compliant probe cantilevers during carbon nanotube growth, Nano Lett. **7**, 3035 (2007). 3.9

[138] J. L. Hutter and J. Bechhoefer, Calibration of atomic-force microscope tips, Rev. Sci. Instrum. **64**, 1868 (1993). 4.1, 5.2.1

[139] J. A. Marohn, R. Fainchtein, and D. D. Smith, An optimal magnetic tip configuration for magnetic-resonance force microscopy of microscale buried features, Appl. Phys. Lett. **73**, 3778 (1998). 4.1, 4.4, 5.2.2, 6.4.3

[140] A. Aharoni, Demagnetizing factors for rectangular ferromagnetic prisms, J. Appl. Phys. **83**, 3432 (1998). 4.1

[141] E. S. Lambers, C. N. Dykstal, J. M. Seo, J. E. Rowe, and P. H. Holloway, Room-temerature oxidation of Ni(110) at low and atmospheric oxygen pressures, Oxid. Met. **45**, 301 (1996). 4.2

[142] W. H. Meiklejohn and C. P. Bean, New magnetic anisotropy, Phys. Rev. **102**, 1413 (1956). 4.3.2

[143] L. Smardz, U. Köbler, and W. Zinn, Oxidation kinetics of thin and ultrathin cobalt films, J. Appl. Phys. **71**, 5199 (1992). 4.3.2

[144] D. A. Shirley, High-resolution X-ray photoemission spectrum of the valence bands of gold, Phys. Rev. B **5**, 4709 (1972). 4.3.4

[145] K. J. Bruland et al., Thermal tuning of a fiber-optic interferometer for maximum sensitivity, Rev. Sci. Instrum. **70**, 3542 (1999). 5.2.1

[146] J. P. Jacky, J. L. Garbini, M. Ettus, and J. A. Sidles, Digital control of force microscope cantilevers using a field programmable gate array, Rev. Sci. Instrum. **79**, 123705 (2008). 5.2.1

[147] T. R. Albrecht, P. Grütter, D. Horne, and D. Rugar, Frequency modulation detection using high-Q cantilevers for enhanced force microscope sensitivity, J. Appl. Phys. **69**, 668 (1991). 5.2.1, 5.5

[148] J. A. Sidles, J. L. Garbini, W. M. Dougherty, and S.-H. Chao, The classical and quantum theory of thermal magnetic noise, with applications in spintronics and quantum microscopy, Proc. IEEE **91**, 799 (2003). 5.6

[149] M. Giorgio, B. Meier, R. Magin, and E. Meyer, Magnetic damping losses of tipped cantilevers, Nanotechnology **17**, 871 (2006). 5.6

[150] S. Kuehn, J. A. Marohn, and R. F. Loring, Noncontact dielectric friction, J. Phys. Chem. B **110**, 14525 (2006). 5.6

[151] J. Labaziewicz et al., Temperature dependence of electric field noise above gold surfaces, Phys. Rev. Lett. **101**, 180602 (2008). 5.6

[152] R. G. Griffin and T. F. Prisner, High field dynamic nuclear polarization — the renaissance, Phys. Chem. Chem. Phys. **12**, 5737 (2010). 6.1

[153] T.-M. Chuang et al., Nematic electronic structure in the parent state of the iron-based superconductor $Ca(Fe_{1-x}Co_x)_2As_2$, Science **336**, 181 (2010). 6.2

[154] M. P. Allan et al., Anisotropic energy gaps of iron-based superconductivity from intraband quasiparticle interference in LiFeAs, Science **336**, 563 (2012). 6.2

[155] J. E. Hoffman, *A Search for Alternative Electronic Order in the High Temperature Superconductor $Bi_2Sr_2CaCu_2O_{8+\delta}$ by Scanning Tunneling Microscopy*, PhD thesis, University of California, Berkeley, 2003. 6.2.1

[156] M. Poggio, Personal communication, 2012. 6.2.2

[157] R. C. Richardson and E. N. Smith, editors, *Experimental Techniques in Condensed Matter Physics at Low Temperatures*, Addison-Wesley, 1998. 6.3.1, 6.3.3

[158] E. W. Moore, *1. Mechanical Detection of Electron Spin Resonance from Nitroxide Spin Probes, 2. Ultrasensitive Cantilever Torque Magnetometry of Magnetization Switching in Individual Nickel Nanorods*, PhD thesis, Cornell University, 2011. 6.3.2, 6.4.5

[159] D. Rugar, H. Mamin, and P. Guethner, Improved fiber-optic interferometer for atomic force microscopy, Appl. Phys. Lett. **55**, 2588 (1989). 6.4.1

[160] A. L. Woodcraft, Recommended values for the thermal conductivity of aluminium of different purities in the cryogenic to room temperature range, and a comparison with copper, Cryogenics **45**, 626 (2005). 6.4.2

[161] E. Gmelin, M. Asen-Palmer, M. Reuther, and R. Villar, Thermal boundary resistance of mechanical contacts between solids at sub-ambient temperatures, J. Phys. D: Appl. Phys. **32**, R19R43 (1999). 6.4.2

[162] F. Xue, P. Peddibhotla, M. Montinaro, D. P. Weber, and M. Poggio, A geometry for optimizing nanoscale magnetic resonance force microscopy, Appl. Phys. Lett. **98**, 163103 (2011). 6.4.3

[163] J. A. Marohn, Magnetic resonance force microscopy tutorial, 3rd International Conference on Nano Magnetic Resonance Imaging; Le Tremblay-sur-Mauldre, France; July 12 – 16, 2010. 6.4.3

[164] S. H. Pan, International patent publication no. wo 93/19494, Technical report, 1993. 6.4.4

[165] C. Wittneven, R. Dombrowski, S. H. Pan, and R. Wiesendanger, A low-temperature ultrahigh-vacuum scanning tunneling microscope with rotatable magnetic field, Rev. Sci. Instrum. **68**, 3806 (1997).

[166] A. Gupta and K. Ng, Compact coarse approach mechanism for scanning tunneling microscope, Rev. Sci. Instrum. **72**, 3552 (2001). 6.4.4

[167] J. A. Sidles, R. Picone, J. Garbini, and J. Jacky, Transport mechanisms for inducting dynamic nuclear hyperpolarization in magnetic resonance microsystems: Dyanmical theory, design rules, and experimental protocols, Technical report, UW Quantum Systems Engineering (QSE) Group, University of Washington, Seattle, WA, 2011. 6.5

[168] D. Gill and N. Bloembergen, Linear Stark splitting of nuclear spin levels in GaAs, Phys. Rev. **129**, 2398 (1963). 7

[169] R. W. Dixon and N. Bloembergen, Electrically induced perturbations of halogen nuclear quadrupole interactions in polycrystalline compounds. II. Microscopic theory, J. Chem. Phys. **41**, 1739 (1964). 7

[170] J. A. Marohn et al., Optical Larmor beat detection of high-resolution nuclear magnetic resonance in a semiconductor heterostructure, Phys. Rev. Lett. **75**, 1364 (1995). 7

[171] J. G. Kempf, M. A. Miller, and D. P. Weitekamp, Imaging quantum confinement with optical and POWER (perturbations observed with enhanced resolution) NMR, Proc. Natl. Acad. Sci. U.S.A. **105**, 20124 (2008). 7

[172] T. G. Frey, G. A. Perkins, and M. H. Ellisman, Electron tomography of membrane-bound cellular organelles, Annu. Rev. Biophys. Biomol. Struct. **35**, 199 (2006). 7

[173] N. Urushihara et al., Three dimensional image construction and spectrum extraction from two dimensional elemental mapping in Auger electron spectroscopy, J. Vac. Sci. Technol. A **26**, 668 (2008). 7

[174] M. Hemmous, A. Layadi, A. Guittoumb, A. Bourzami, and A. Benabbas, Effect of deposition rate and thickness on the structural and electrical properties of evaporated Ni/glass and Ni/Si(100) thin films, Microelectron. J. **39**, 1545 (2008). 7

[175] Y. Wang, S. A. Boden, D. M. Bagnall, H. N. Rutt, and C. H. de Groot, Helium ion beam milling to create a nano-structured domain wall magnetoresistance spin valve, Nanotechnology **23**, 395302 (2012). 7